A Visit to Flatland

Chemistry and Photophysics of Two-Dimensional Layered Molybdenum and Rhenium Dichalcogenides

Pieter Schiettecatte

Promotor: Prof. Dr. Ir. Zeger Hens

Co-promotor: Prof. Dr. Philippe Smet

Promotor

Prof. Dr. Ir. Zeger Hens   Department of Chemistry

Co-promotor

Prof. Dr. Philippe Smet   Department of Solid State Sciences

Chairman

Prof. Dr. José Martins   Ghent University

Jury members

Dr. rer. nat. Claudia Backes   University of Heidelberg
Prof. Dr. Laurens D.A. Siebbeles TU Delft
Prof. Dr. Dirk Poelman   Ghent University
Prof. Dr. Ir. Iwan Moreels   Ghent University

Ghent University
Faculty of Science

Department of Chemistry
Krijgslaan 281 Building S3, B-9000 Gent, Belgium

Acknowledgments

For the last four years, I've had the opportunity to work among many wonderful people. I will always cherish these moments and reflect upon this time in my life with a great smile.

Pursuing a PhD is far more than writing a booklet at the end, it's a journey, an adventure. And in this respect, I couldn't have wished for a better promoter. Zeger, you offered guidance, yet at the same time you left enough room for exploration and critical reflection. Undoubtedly a difficult exercise in management, yet you balanced it perfectly. Although you are likely the most busy person in the entire building (and well beyond), your door was always open, and I could walk in to discuss an idea or to tackle a problem. In summary, you rock!

Philippe, as the project took a couple of turns in different directions, we unfortunately did not have the opportunity to work together in the way as we intended to. Nonetheless, I deeply respect your enthusiasm and passion for science and teaching. A big shout-out to Pieter G(eiregat) who provided feedback in a lot of different projects. Already since my master thesis, I had the feeling we were going to make a great team, and I am confident we can continue doing this in the future. And oh, congratulations on luring me into the realm of physics!

scientist and kudos for being a sunshine every morning. Kishu, I admire how driven you are in science and sports. Filipe (and Duda!), I cherish your hospitality and your taste for good music – the fact that you knew the absurdly obscure PF song *Several Species of Small Furry Animals Gathered Together in a Cave and Grooving with a Pict* still surprises me to this day. Also, thanks for the countless hours of looped Billy Joel songs we listened together. Margarita, as a fellow cat-and animal lover, you are always welcome to visit my cats, rabbits and the sheep! Kim Junior, I enjoyed our talks on a variety of topics (in almost perfect dutch!), and I promise that we will play a game of manillen when corona measures are relieved.

Thanks to Emile and Tangi for guiding me in my master thesis and teaching me the tricks of trade. Emile, congratulation on winning the award for being the most friendly guy in the building! Credits to Shalini for instructing me in the synthesis of 2D materials, helping me out with NMR, and for being fabulous. Pengshang, you are the most hard working person I know, and over the years you became a highly independent researcher. I enjoyed working together on the ultrafast properties of TMDs and cherish our discussions on their synthesis. Ivo, thanks for helping me out with writing code, you are a Matlab wizard.

Alessio, *caio comba!*, it is rare to find someone with whom you share so many similar interests, and from the first weeks it was crystal clear to me that we were to become very good friends! As a general word of friendly advice for the future, avoid general mailing lists. Carmelita, I appreciate your attempts in teaching me Italian and Milanese dialect (*se fem?*), and your trust in my heavily flawed horoscope readings. On Ronnie his behalf, thank you for the skype calls with Chico. Gabri(ele), an other member of the TMD crew, you are fun to talk to and I am confident your hard work will pay off soon! Jari, I like your (silly) jokes and you are without a doubt becoming the all-star and MVP of PCN. Renu, I liked your calm character and your apprecia-

tion for animals. Natalia, you are a legend.

Kim, your directness scared me a little at first, yet I soon realised how helpful and kind you are. Speaking of which, Jorick, you were always available when I needed (scientific) advice, and your chill character made it easy to hang out after work. Besides, thank you for introducing me to liquid nitrogen sports. Willem, you are the true superman and your handiness inside (and most likely outside) the lab is marvellous. I value the times we drank well-balanced beers together. Suzanne, thanks for organizing (and destroying me at) Age of Empire LAN parties. Vignesh, I enjoyed our Call of Duty games together, you sure know how to camouflage. Valeria, I like your genuine interest in my herd of sheep and I will keep you updated about Boris his adventures in neighbouring gardens. Leila, congratulations on achieving the Guinness World Record of most NMR analyses conducted in a lifetime. Jokes aside, hard work will pay off! Igor, great job on fixing spectrometers or other equipment! Chandu, you are a funny chap and without your great GPS skills we surely would never have arrived in De Vossemeren. Delphine, thanks for the many tutorials you are organizing! Ali, we had a lot of fun together on our road trip after MRS and you have a hearth of gold. Also credits to the new PCN recruits Dobromil, Ben, Ezat, Fadi, Iago, Frederick and Onur who recently strengthened the team. A nasty virus prevented me from getting to know you so far but best of luck with your research.

While group dynamics continuously change, we are fortunate at S3 to have such a solid foundation. Pierre and Kathleen, we are blessed with such helping hands at the secretary. My sincere apologies for the countless times the fox key disappeared and suddenly reappeared in the pockets of my lab coat. Pat, thank you for solving all my computer issues! Bart, great job on helping me out with the glove boxes, I appreciate it! Katrien, thanks for the TEM advice! My gratitude to other personnel and members of different research groups, Evert *the old guy*, Bernard, Ewout, Sander, Fady, Hannes, Chokri,

Jonas, Himanshu, Chidharth, Loren, Guillaume, Ilse, Jan, Jeroen, Gianmarco... for making (the hallways of) S3 such a great place to hang out.

Next, I want to express my gratitude to my friends from *Oudenaarde en omstreken* (Dries, Tom, Younes, Eline, Anke, Sander, ...) with whom I have such wonderful memories, hiking trips, weekends in the Ardennen, quizzing or simply hanging out at the bar or in a forest. You are awesome! A big shout-out to *Aldechemisten* (Hannes, Karel, Evert, Sebastiaan, Jens, Charlotte, Joke, Yentl, Annelore, Caitlin,...) for the amazing bachelor, master and PhD years. To be continued! Finally, cheers to my teammates of MVC De Pic-Nic for being a legendary team that in particular excels at the third halve of the game. All of you remind me that life is far more than chemistry alone.

Als laatste wil ik mijn dichte familie bedanken. Mama en papa, zonder jullie was niets van dit mogelijk geweest. Meer altruïstische mensen ken ik niet, jullie hebben ons opgevoed met waarden en normen, voor mémé gezorgd, en nu cijferen jullie je weg om de drie biggetjes, Eliza, Medina en Florian, op te voeden. Bedankt voor alles! Mémé, je bent een rolmodel voor ons geweest op verschillende vlakken. De laatste jaren toon je des te meer dat je nooit te oud bent om iets te leren, op je 93$^{\text{ste}}$ teken, schilder en dicht je nog, én je bent zelfs beginnen quizzen de laatste jaren! Jaspie, ook al zien we elkaar de laatste tijd spijtig genoeg iets minder, toch moet ik nog altijd even hard lachen met jouw domme lollen (PS: ik wacht op je moeilijke vragen) en voelt elk moment aan zoals vroeger. Ik ben trots om jouw grote broer te mogen zijn! Een betere schoonfamilie had ik me ook niet kunnen inbeelden. Rita, jouw enthousiasme is aanstekelijk en we kunnen altijd op je rekenen voor om het even wat, bedanktt! Luc, *onzen architect*, ondanks je drukbezet schema sta je altijd paraat om ons te helpen of van advies te voorzien! Hierbij wil ik ook Julie (Callebaut) bedanken voor het maken van deze prachtige cover.

Het beste bewaar ik voor het einde. Brenda, muizeke, je bent niet

alleen de liefde van mijn leven maar ook mijn beste vriendin en bij jou kan ik altijd mezelf zijn. De laatste 9 jaar hebben we samen fantastische momenten beleefd, en anderzijds een eindeloze lijst aan typische Pieter-Brenda stommiteiten opgebouwd waar we nu eens goed om kunnen lachen (gaande van een vermiste auto tot het vast te komen zitten in een wijngaard of op een kust bij vloed). Hiernaast heb ik ongelooflijk veel steun aan jou (en Ronneke) gehad tijdens het schrijven van dit doctoraat – *"Piiieeeeettteeeerrr, opstaan!"*. Ondanks mijn waarzeggerstatuut kan ik moeilijk voorspellen wat de toekomst zal inhouden maar ik weet wel dat ik die met jou wil beleven.

Kluisbergen, March 2021
Pieter Schiettecatte

Table of Contents

II   *Probing Ultrafast Carriers in Few-Layer Molybdenum Disulfide & Rhenium Disulfide*   99

6   Probing Carriers & Optical Nonlinearities by Pump-Probe Spectroscopy   101

7   Ultrafast Carrier Dynamics in Few-Layer Colloidal Molybdenum Disulfide   111

List of Common Acronyms

A

AFM   Atomic Force Microscopy

B

BER   Binding Energy Reduction
BGR   Band Gap Renormalization

C

CB   Conduction Band
ced   cohesive energy density
CVD   Chemical Vapor Deposition

D

DCB	1,2-Dichlorobenzene
DFT	Density Functional Density
DLS	Dynamic Light Scattering
DOS	Density of States
DOSY	Diffusion Ordered Spectroscopy

F

F	Free Energy
FFT	Fourier transform analysis
FWHM	Full Width at Half Maximum

L

LPE	Liquid-Phase Exfoliation

N

NC	Nanocrystal
nm	nanometer
NMR	Nuclear Magnetic Resonance
NMP	N-methyl-2-pyrrolidone
nOe	Nuclear Overhauser Effect
NOESY	Nuclear Overhauser Effect Spectroscopy

O

OA	Oleic Acid
OLA	Oleylamine

P

PA	Photoinduced Absorption
PL	Photoluminescence

T

TA	Transient Absorbance
TAS	Transient Absorbance Spectroscopy
TEM	Transmission Electron Microscopy
THz	Tera-Hertz
TMD	Transition Metal Dichalcogenide

U

UV-Vis	Ultraviolet-Visible Light

V

VdW	Van der Waals

X

XPS	X-ray Photoelectron Spectroscopy
XRD	X-ray Diffraction

Common Greek Symbols

δ Solubility Parameter

χ Exchange Parameter

χ_c Critical Exchange Parameter

ΔA Differential Absorbance

1

Introduction

"To inquire and to create; these are the grand centers around which all human pursuits revolve." – Wilhelm Von Humboldt

1.1   Research Context

Since prehistoric times, humankind has sought to shape and utilize the materials that nature provided. Stone tools have been made from flint, pottery from clay, and glass from sand. Throughout history, our ingenuity has shaped our civilizations.[1] In the modern age, society is changing at an unprecedented pace – for better or worse. In particular, the evolution in optics and electronics is a case in point. We went from printed books to portable electronics throughout merely a few generations, from the first telegraph to global wireless telecommunication, and from candle-lit houses to mega-cities fueled by semiconductor technology.

Technological advancements do not as much depend on the availability of materials, but more on the level of control and understanding we
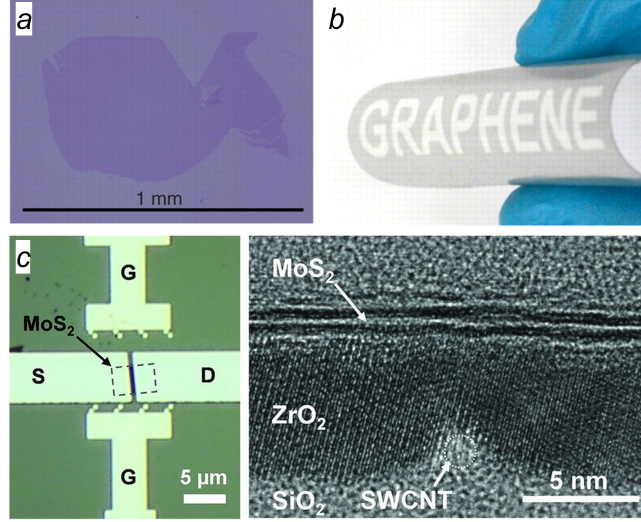
Figure 1.1: (a) Large graphene flake prepared by the scotch-tape method. (b) A printed graphene film on a flexible substrate. (c) MoS_2 transistor with a one nm-gate-length. From References 4 and 5. Reprinted with permission from AAAS.

have over their properties. Within this context, ongoing evolutions in nanoscience resonate exceptionally well with modern-age technological needs.[2] Nanotechnology opens ample opportunities for miniaturization and design of complex architectures at the fundamental limit,[3] and it provides a means to change the way materials behave. For instance, roughly half of the atoms in a three nanometer-sized crystal are at the surface. This not only renders nanocrystals (NCs) of high interest for catalysis, it also makes that a hybrid combination of bulk and surface atoms will determine the physical and chemical properties.

The layered two-dimensional (2D) materials constitute one of the more recent nanomaterial classes which are often obtained as a mono- or few-layer sheet of a three-dimensional (3D) bulk solid.[6] They are typically a few nanometers (nm) thick and have a lateral size that is one or multiple orders of magnitude larger. Such confinement in the thickness direction causes the optical, electronic, and physicochemical properties to differ significantly from the 3D bulk properties. For instance, due to its zero energy gap, graphene, a single layer of every-

day graphite, combines exceptionally high electrical and heat conductivity with optical transparency.[7–9] Discovered in 2004 by the scotch-tape method (see Figure 1.1a),[6] graphene turned out to be the tip of the iceberg. Over the last two decades, we have witnessed the (re)discovery of several classes of ultrathin 2D layered nanomaterials, such as hexagonal boron nitride (hBN), black phosphorous (BP), MXenes, and the transition metal dichalcogenides (TMDs).[10]

In particular, the study of the 2D transition metal dichalcogenides experienced a renaissance when Tony Heinz and Feng Wang independently demonstrated photoluminescence (PL) in mechanically exfoliated molybdenum disulfide (MoS_2) and direct band-edge emission in a single layer of MoS_2.[11,12] These observations surged interest in a class of relatively old materials whose peculiar structural, optical, and electronic properties have already fascinated researchers for decades.[13–18] Soon after, it was understood that the strong light-matter interaction in these ultrathin compounds results in unprecedented optical absorption coefficients up to 10^6 cm^{-1}.[19] As a result, a single TMD monolayer of ≈ 1 nm thick can absorb up to $10-20\%$ of the incident light.[11] In comparison, many of our current optoelectronic devices are based on traditional quantum well technology, containing semiconductors such as gallium arsenide or indium nitride.[20] These compounds have optical absorption coefficients of 10^{4-5} cm^{-1}, at least an order of magnitude lower than a TMD. Unsurprisingly, TMD mono- and few-layers are now widely studied as novel optoelectronic material in, for instance, LEDs and lasers.[21–23] As modern-age problems demand the development of ever-thinner flexible optoelectronic devices (we provide examples in Figures 1.1b-c),[2] atomically thin TMDs, and 2D materials in general, might occupy a central role in the transition to a post-silicon era.

1.2 Transition Metal Dichalcogenides (TMDs)

1.2.1 Structural Properties

The transition metal dichalcogenides of groups IV$_b$ to VII$_b$ feature a layered crystal structure build-up of successive ME$_2$ monolayers (see Figure 1.2a).[15] Here, M denotes a transition metal, and E a chalcogenide element (S, Se, or Te). These monolayers take the form E-M-E, with a plane of metal atoms sandwiched between two outer planes of chalcogen atoms. In such an arrangement, the lone electron pairs of
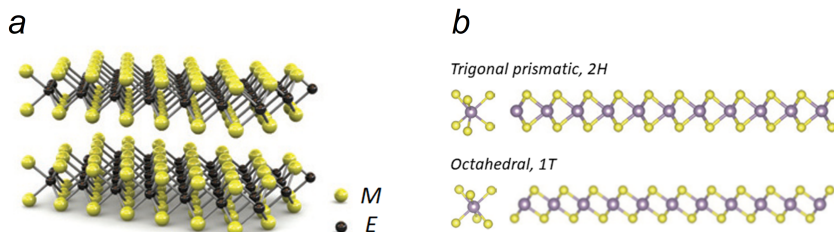
Figure 1.2: (a) Example of a layered crystal structure of a TMD. Metal cations (M) are indicated in black, chalcogen anions (E) in yellow. Reprinted by permission from Reference 26. Copyright (2012), Nature Publishing Group. (b) Schematic of a single-layer TMD with (top) a trigonal prismatic 2H and (bottom) an octahedral 1T coordination. Reprinted by permission from Reference 24. Copyright (2013), Nature Publishing Group.

the chalcogen terminate the surface, which renders the surface free of dangling bonds.[24] Within a TMD monolayer, the metal cation is coordinated by six chalcogen anions in a trigonal prismatic or octahedral arrangement, such that layered TMDs predominantly occur in two polymorphs.[25] One often refers to the trigonal prismatic arrangement as 2H in the literature and to the octahedral coordination as 1T (see Figure 1.2b).[15]

1.2.2 Optoelectronic Properties

The electronic structure of a layered TMD is dependent on the filling of the d-orbitals and the coordination of the central metal ion.[15] With over 40 transition metal/chalcogenide combinations at hand (see Figure 1.3), this leads to materials with distinct optical, electronic, and physicochemical properties.[15] For instance, the electronic properties range from metallic (*e.g.*, $NbSe_2$ and TaS_2) over semi-metallic (WTe_2) to semiconducting (*e.g.*, MoS_2, ReS_2).[11,18,27,28] Clearly, their versatility surges an interest in the fundamental sciences and fits societal needs in fields as diverse as electronics, catalysis, energy storage, and sensing.[24]

1.2.3 Semiconducting TMDs

The study of 2D semiconducting TMDs gained momentum when photoluminescence was observed in mechanically exfoliated MoS_2.[11,12]

Figure 1.3: With a diverse pallet of transition metals (M) and chalcogen atom (X) at our disposal, this results in TMDs with distinctive properties. TMDs that de facto crystallize in a layered lattice are highlighted and typically belong to group 4b to 7b. The partial highlights of group 9b and 10b elements refer to TMs that might form layered TMD structures depending on the chalcogen source. Reprinted by permission from Reference 24. Copyright (2013), Nature Publishing Group.

For one thing, the prospect of strong light-matter interaction through excitons is what stimulates research into these materials.[29]

In semiconductors, photoexcitation with photon energies exceeding the energy gap generates electrons and holes. The photogenerated carriers are either mobile or bound by Coulomb interactions in a so-called exciton, or a Coulomb-bound electron-hole pair (see Figure 1.4a). The two-dimensional character of a TMD and the reduced dielectric screening result in enhanced many-body Coulomb interactions, leading to tightly bound excitons at room temperature with unprecedented binding energies of hundreds of milli-electron volts (meV).[19, 30–37] Such a strong light-matter interaction causes a pronounced absorption of light at the exciton position(s) with an optical absorption coefficient up to 10^6 cm^{-1} (see Figure 1.4b). As a result, a 1 nm thick TMD layer can absorb up to 10% to 20% of the incident light.[11] Unsurprisingly, TMD mono- and few-layers are now widely studied as novel optoelectronic materials.[21–23] To highlight this case, we compare MoS$_2$ to CdSe by calculating the absorption coefficient a_i of CdSe in bulk and CdSe synthesized as 2D platelets (see Figure1.4c and Appendix B.1). This results in an absorption coefficient of CdSe that is at least a factor of 2 lower at the band edge and an order of magnitude lower in the blue spectral region (≈ 3 eV) in comparison
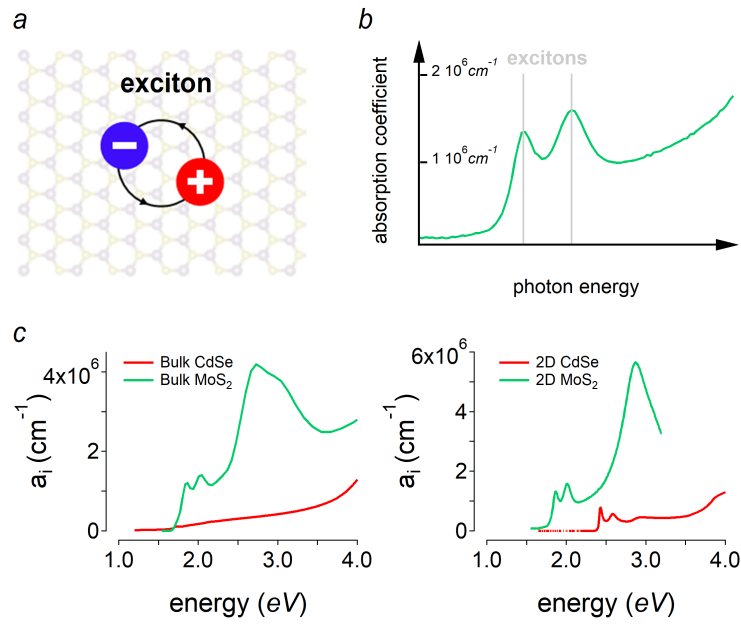
Figure 1.4: (a) Pictorial representation of an electron-hole pair bound in an exciton. (b) The calculated unscreened absorption coefficient for a MoS_2 monolayer based on experimental dielectric constants provided by Reference 38. (c) Comparison between the absorption coefficient a_i of CdSe (red) and MoS_2 (green) as bulk material and synthesized as 2D platelets.

to MoS_2.

1.2.4   Group VI_b TMDs – Molybdenum Disulfide

Molybdenum disulfide (MoS_2) is by far the most investigated member of the TMD family. As a bulk crystal, MoS_2 adopts a layered 2H crystal structure consisting of stacked S-Mo-S monolayers (see Figure 1.2). The electronic coupling between the different layers makes bulk 2H-MoS_2 an indirect semiconductor with the valence band (VB) maximum located at the Γ point, the conduction band (CB) minimum between Γ and K, and a resulting bandgap of 1.29 electron volt (eV).[39] We point out that, next to the thermodynamically stable 2H polymorph, synthetic MoS_2 crystallizes in a meta-stable metallic 1T state under specific conditions.[40]

Ab initio calculations revealed that electronic states at different wavevectors have different orbital content. The in-plane d_{xy} and $d_{x^2-y^2}$ orbitals of molybdenum predominantly make up the states at the K point and are thereby less sensitive to the interlayer coupling. On the other hand, the p_z orbitals of sulfur and d_{z^2} of molybdenum predominantly contribute to states at Γ, and the energy of those states strongly correlates with the interlayer coupling as both orbitals have a substantial out-of-plane component.[12,41] In this way, a decrease in layer number upon exfoliation disproportionately affects the Γ point and turns 2H-MoS_2 into a direct semiconductor with a bandgap of $\approx$1.8 eV in the monolayer (ML) limit.[11,12] Figure 1.5 depicts the evolution of the electronic structure from bulk to monolayer. Such behavior is reflected in an increase of the photoluminescence.[11,12,42–44] A similar crossover from indirect to direct behavior has been observed in other members of group VI_b; WS_2,[45] WSe_2[45] and $MoSe_2$.[44]

The presence of a sizeable bandgap,[11,12,39] a remarkably high absorption coefficient of 10^6 cm^{-1} due to reduced dielectric screening and band nesting,[13] carrier mobilities above 100 cm^{2}V^{-1}s^{-1},[46] a high elastic modulus combined with high mechanical strength,[47,48] makes MoS_2 appealing for a series of flexible optoelectronic devices. For instance, atomically-thin field-effect transistors with a single MoS_2 layer as conductive channel show mobilities of tens up to hundreds of cm^{2}V^{-1}s^{-1}, depending on the preparation method.[49–51] Also, the best FETs based on exfoliated MoS_2 have current on/off ratios of 10^8 and are on par with the requirements to replace silicon in CMOS-like
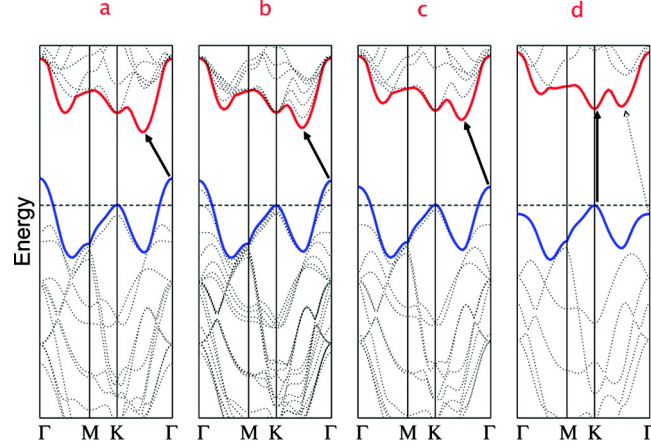
Figure 1.5: Calculated band structures of (a) bulk MoS_2, (b) quadrilayer MoS_2, (c) bilayer MoS_2, and (d) monolayer MoS_2. Reprinted with permission from Reference 12. Copyright (2010) American Chemical Society.

digital logic devices.[49,52]

Research is far from limited to single layers, as for specific purposes multi-layers have shown to be advantageous. For one thing, a larger absorption in multi-layered stacks boosts photocurrents and photovoltages in photovoltaic devices.[53] In the case of multi-layer phototransistors, a bandgap reduction extends the detection range, a higher absorption improves the responsivity, and a variable MoS_2 thickness offers wavelength-dependent photosensitivity.[54–56]

1.2.5 Group VII_b TMDs – Rhenium Disulfide

Although the earliest studies on bulk ReS_2 trace back decades ago, widespread research interest in ReS_2 only started in 2014 when Tongay and co-workers observed monolayer behavior in multilayer and bulk-like ReS_2 crystals.[28] As the interlayer coupling between the layers is relatively weak, the ReS_2 layers are electronically decoupled – theoretical work demonstrated that the coupling energy per unit cell results in a mere 18 meV per ReS_2 unit cell, compared to 460 meV per MoS_2 unit cell (see Figure 1.6c).[1] A weak layer coupling

---

[1] A weak interlayer coupling is ascribed to the extra valence electron of rhenium compared to molybdenum or tungsten. When this electron contributes to the formation of Re-Re bonds, it lowers the energy of the system, forming a distorted
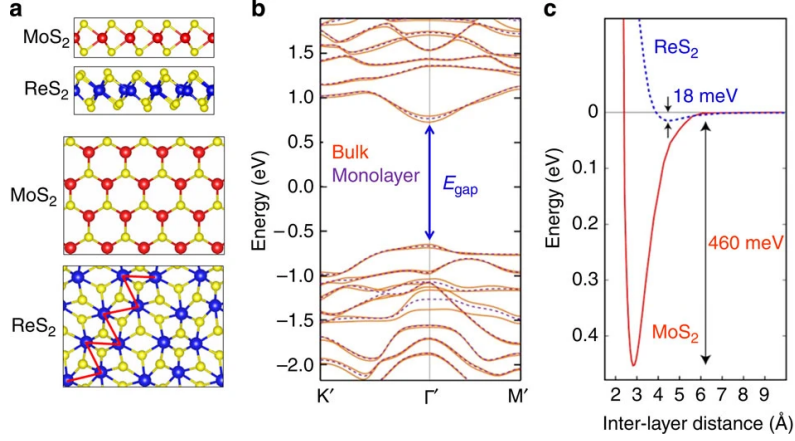
Figure 1.6: (a) Comparison between (top, red) the conventional 2H crystal structure of MoS_2 and (bottom, blue) the distorted $1T'$ structure of ReS_2. (b) Electronic structure calculations by DFT for bulk ReS_2 (solid orange lines) and a monolayer (dashed purple lines). Both have a direct bandgap at the Γ point. (c) The energy of the system as a function of the inter-layer distance, for ReS_2 and MoS_2, implying a significantly weaker inter-layer coupling energy in ReS_2. Reprinted with permission from Reference 28. Copyright (2014) Nature Publishing Group.

results in an optical and electronic response[2] (see Figure 1.6b) that is relatively independent on the layer number[28, 58–61] – opposite from group VI_b TMDs.[11, 12]

Being a relatively recent and lesser-explored member of the TMD family, there is at this point little consensus on the direct or indirect bandgap nature of ReS_2, both experimentally and theoretically. While some studies cite ReS_2 as a direct semiconductor from bulk to monolayer,[28, 60, 62] others point to a near-degenerated indirect and direct gap with the bi-and-monolayer only being direct,[63] or the bulk form being marginally indirect.[64] Even so, a common theoretical result is a valence band that is relatively flat near the Γ point

---

1T$'$ phase with zigzag Re-Re chains. Such a geometry eliminates the energy benefit that stacking provides in MoS_2 and WS_2, see Reference 28.

[2]In addition, as pointed out in Reference 57, a weak interlayer coupling results in a through-plane thermal conductivity that is the lowest observed among the 2D materials studied so far.
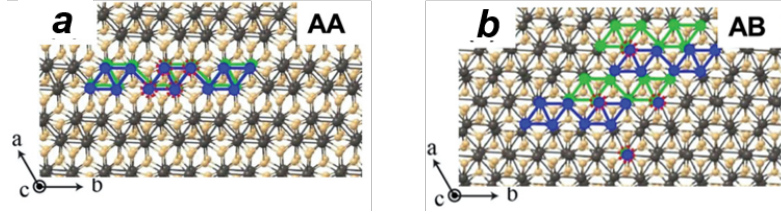
Figure 1.7: Crystal structures corresponding to (a) AA and (b) AB stacking orders. The AB stacking order is shifted along the a axis. Reprinted and adapted with permission from Reference 69. Copyright (2020) WILEY.

(similar to the one shown in Figure 1.6b) with a maximum that can be slightly off-set, depending on the level of theory, either resulting in a direct[65–67] or indirect transition.[63,68] Alternatively, it has been pointed out that these anomalies might relate to ReS_2 adopting two polytypes with different stacking orders.[69] In an isotropic stacked AA polytype, the ReS_2 layers show a negligible displacement, while in the anisotropic AB polytype consecutive layers are slightly displaced along the a-axis (see Figure 1.7). According to DFT calculations, the anisotropic AB stacking is marginally indirect[69] and is energetically more stable.[69,70] Irrespective of the conundrum mentioned above, or the presence of different stacking orders, ReS_2 differs substantially from the group VI_b TMDs whose electronic structure varies significantly with the thickness (see Figure 1.5). Such behavior is ascribed to a weak electronic interlayer coupling between the ReS_2 layers.

Besides a vanishing interlayer coupling, several distinguishable features drive research toward ReS_2. For one thing, ReS_2 adopts a distorted $1T'$ crystal structure (see Figure 1.6a) with strong in-plane anisotropy.[71] On the other hand, the sizeable bandgap in ReS_2 ($\sim 1.5\,\mathrm{eV}$), its mechanical flexibility, and high absorption coefficient ($\sim 10^6\,\mathrm{cm}^{-1}$)[72] have driven considerable research into few-layer ReS_2 devices. The viability of ReS_2 as optoelectronic material is evidenced by the development of multilayer logical circuits,[60,73] transistors,[74–78] photodetectors[79,80] and sensors,[77] mostly based on mechanically exfoliated or CVD grown few-layer ReS_2.

1.3 Synthetic Methods

In general terms, two conceptual approaches are followed to form materials with nanoscale dimensions. Either a bulk material is chopped up *top-down* in ever-smaller pieces, or atoms are assembled from the *bottom-up* to form NCs. Moreover, applied to 2D materials, nanometric crystals can be obtained in the solution phase or as flakes deposited on a substrate. In such a way, one can divide existing procedures into four broad categories: mechanical exfoliation, vapor phase deposition, liquid-phase exfoliation, and chemical synthesis (see Table 1.1). Each of these preparation methods has advantages and disadvantages and are thereby more or less suitable to prepare specific materials for certain intends.

	substrate-based	solution-based
top-down	mechanical exfoliation	liquid exfoliation
bottom-up	vapor phase deposition	chemical synthesis

Table 1.1: Tabulated overview of the different synthetic methods.

1.3.1 Mechanical Exfoliation

In a layered compound, the 2D monolayers that make up the 3D structure are held together by relatively weak out-of-plane Van der Waals (VdW) interactions, while the chemical bonds within the 2D planes are covalent and relatively strong. The unique combination of such weak out-of-plane forces with strong in-plane chemical bonds has enabled the production of ultrathin layers by mechanical exfoliation of the bulk solid using adhesive tape.

The mechanical exfoliation of layered compounds can be traced back to Robert Frindt, who started cleaving bulk MoS_2 on mica substrates.[14] In his pioneering work, he described mechanical exfoliation as a "peeling process tearing sheet after sheet from a pad of paper" (Figure 1.8 briefly illustrates mechanical exfoliation). Using this process, he was able to produce thin single-crystals of MoS_2 of several molecular layers thick.[14] Frindt already noticed that these thin cleaved specimens had absorption coefficients as high as 10^6 cm^{-1} and showed size-quantization effects.[13,16] However, it was only in 2004 when Novoselov and Geim demonstrated extraordinary physics in a
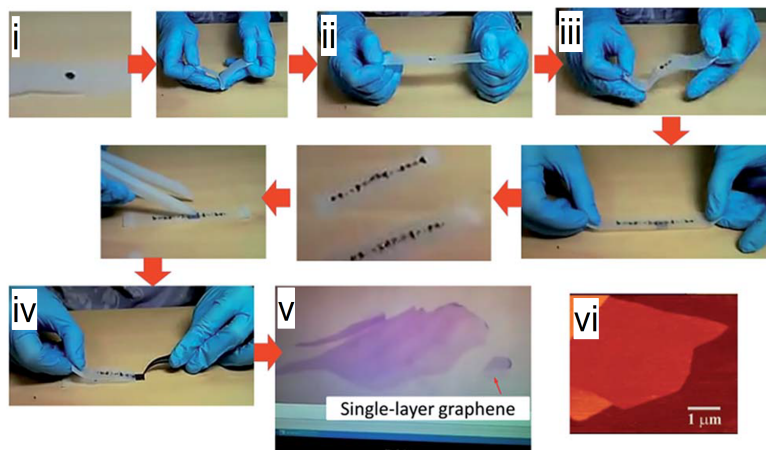
Figure 1.8: Illustrative procedure demonstrating the mechanical exfoliation of graphite. (i) Scotch-tape is applied to a piece of graphite. (ii) By exerting a normal force, it peels off N layers of graphene from the bulk graphite crystal. (iii) This procedure is repeated several times. (iv) Finally, the piece of Scotch-tape is applied to a substrate (typically SiO_2/Si). Monolayers are identified by (v) optical contrast and (vi) atomic force microscopy. Reproduced and adapted from Reference 82 with permission from The Royal Society of Chemistry.

single layer of graphite that the layered compounds started to receive the attention they deserve.[6] Merely a year later, Novoselov demonstrated the versatility of their approach by mechanically exfoliating different classes of layered materials, among them MoS_2.[81] Over the last two decades, mechanical exfoliation has been the holy grail for excavating fundamental properties, proof-of-concept studies, and fabrication of devices with superlative and unparalleled characteristics. For instance, Kis and co-workers demonstrated an atomically-thin field-effect transistor (FET) with single-layer MoS_2 as the conductive channel.[49] The FET had a current on/off ratio of 10^8; a characteristic on par with the requirements to replace silicon in CMOS-like digital logic devices.[49, 52]

While mechanical exfoliation has proven to be an excellent way to produce large-area, high-quality and crystalline flakes with atomic thickness, the method suffers from low throughput and is hardly scalable.[83] These drawbacks limit the industrial viability of mechanical exfoliation and, at the same time, restrict fundamental studies to mea-

surements on a single-flake, rather than probing the properties on a large statistical ensemble. To cope with the drawbacks of mechanical exfoliation, a plethora of synthesis methods has been proposed.

1.3.2 Vapor Phase Deposition

The compatibility of vapor phase growth approaches with the existing silicon-based technology has directed astronomical funding to this research area. Simply put, in a chemical vapor deposition (CVD) reactor, gaseous molecules (precursors) react in the vapor phase, or on a substrate, to produce a substrate-supported solid as a crystal or a continuous film.[84] For instance, the conventional route to grow graphene involves the controlled decomposition of methane gas on a metallic substrate at 1000 °C.[85] Precise control over the precursor gas concentration produces continuous graphene films with a well-defined thickness and morphology.[85–87]
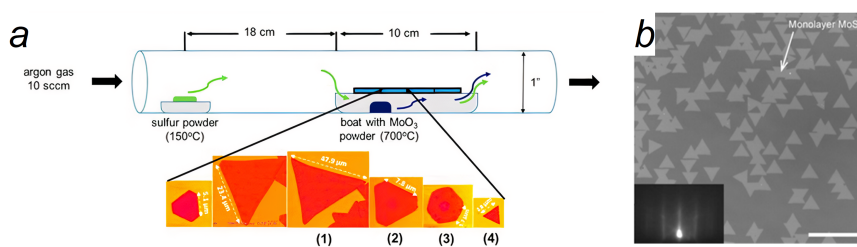
Figure 1.9: (a) Schematic depicting the growth of MoS_2 by CVD. The SEM images indicate that the shape of MoS_2 domains is highly dependent on the location on the silicon substrate. This is attributed to local changes in the ratio of the sulfur and molybdenum precursors. Adapted from References 88 and 89. (b) Optical microscopy image of monolayer MoS_2 grains grown on atomically smooth sapphire. Scale bar length is 50 μm. Reprinted from Reference 90. Copyright (2015) American Chemical Society.

In contrast to the growth of graphene, or to the existing silicon technology,[91] the conventional growth of TMDs starts from precursors in the solid-state (*e.g.*, WO_3, $MoCl_5$, S or Se), see Figure 1.9a.[45, 92, 93] As the vapor pressure of a solid is extremely sensitive to temperature fluctuations within the reactor,[94] this limits control over nucleation and growth and results in isolated domains rather than continuous films (see Figures 1.9a and 1.9b).[88] To a certain degree, this drawback could be resolved with advancements in metal-organic CVD

(MOCVD) and atomic layer deposition (ALD). Both methods result in the continuous deposition of larger film areas, albeit at the expense of the crystallinity ,and controlled stoichiometry in the case of ALD, of the deposited solid.[95, 96]

Despite the several hurdles that have to be overcome, CVD's potential for the growth of ultrathin TMDs has been demonstrated by fabricating several proof-of-concept devices.[97–99] Undoubtedly, and considering its rapid development in the last decade, we can expect vapor deposition approaches to fulfill an important role in the fabrication of high-end optoelectronic devices. Nonetheless, due to its limited scalability and high production cost, CVD might not be the optimal choice for applications that necessitate larger quantities. In such cases, solution-based methods, such as liquid-phase exfoliation (LPE)[100–103] and wet chemical synthesis,[104, 105] might be more suitable. These methods offer the prospect of scalability, and the suitability of colloidal dispersions with solution-based printing and deposition methods provides an exciting road towards their integration in devices.[106, 107]

1.3.3   Liquid-Phase Exfoliation

Liquid-phase exfoliation starts by immersing a layered bulk solid in a suitable solvent or an aqueous surfactant solution. Afterward, the liquid mixture containing the 3D vdW solid is exposed to an energy treatment, most commonly through sonication. The work supplied during sonication exfoliates the 3D bulk solid by overcoming the labile interactions between the 2D layers, and a suitable liquid medium prevents aggregation by stabilizing the exfoliated flakes. Consequently, the dispersions are centrifuged to remove the unexfoliated bulk solid from the exfoliated flakes. We depicted the exfoliation process in Figure 1.10.

Around the time of Novoselov's and Geim's work on graphene, McEuan *et al.* produced nanometric graphite flakes by sonicating natural graphite in *o*-dichlorobenzene. Fabricating devices with these exfoliated graphite layers, the authors demonstrated device mobilities up to $1900\,\mathrm{cm^2/Vs}$ and electron delocalization over the whole graphite pieces – a conclusion in line with the semi-metallic nature of graphene.[108] A few years later, Coleman and co-workers exploited sonication based exfoliation to produce carbon nanotubes and defect-free graphene in polar aprotic solvents, such as *N*-methyl-
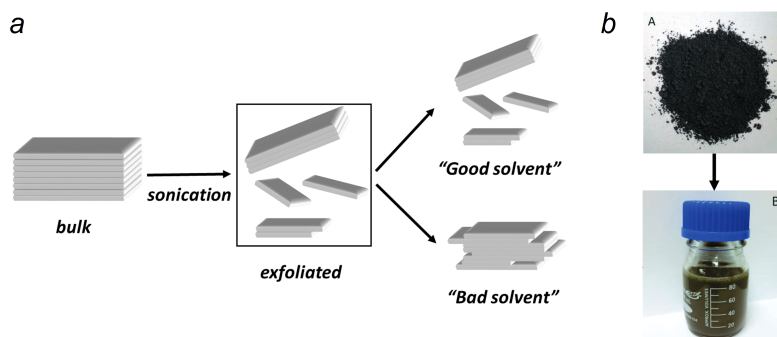
Figure 1.10: (a) Schematic depicting the liquid-phase exfoliation of a bulk solid into few-layered exfoliated flakes. (b) Photographs of A) a bulk TMD powder and B) a TMD dispersion after LPE. From Reference 101. Reprinted with permission from AAAS.

2-pyrrolidone, or in surfactant solutions (see Figure 1.11a).[101, 109–111] The birth of a broad research field coincided with the realization that LPE applies to inorganic layered crystals, *e.g.*, MoS_2 and BN (see Figure 1.11b).[100, 101] It was readily understood that the solvent occupied an essential role in promoting successful exfoliations, an observation that was understood based on Hildebrand solution theory. Applied to LPE, solution theory tells that the stability of a colloidal dispersion of exfoliated flakes correlates with the energy of mixing of the flakes/solvent mixture.[101–103, 109, 110, 112] For rigid nanomaterials, optimal conditions for mixing, and high yield exfoliation, therefore, occur when the solubility parameter of the solvent and the nanomaterial match.[113] From a practical point of view, these studies emphasize the importance of determining the layered compound's solubility parameter by screening LPE in a wide range of solvents. As solution thermodynamics occupies a central role throughout this manuscript, we elaborate solution theory in more detail in chapter 2.

While several studies illustrated the versatility of LPE by exfoliating diverse classes of layered compounds,[114] the possibility to fabricate composites or inks,[107] and the prospects for industrial scalability,[82, 115, 116] they also revealed a significant bottleneck. In general, LPE results in few-layered TMDs with a low monolayer content and offers limited control over size, morphology, and thickness.[101, 117, 118] In particular, in the case of semiconducting group VI_b TMDs – MoE_2
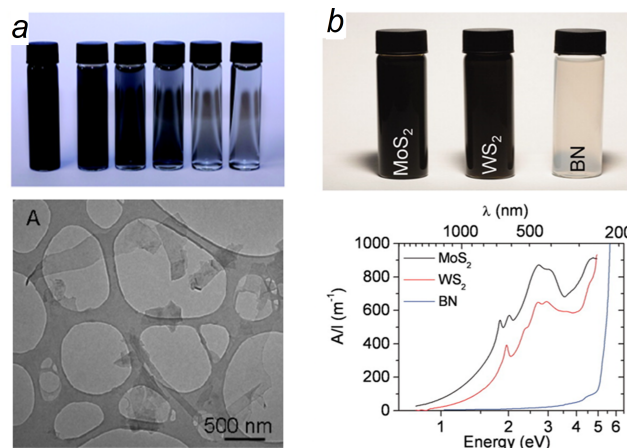
Figure 1.11: (a) Photograph of surfactant stabilized graphene dispersions together with a wide field TEM image. Adapted with permission from Reference 111. Copyright (2010) American Chemical Society. (b) Dispersions of LPE MoS_2, WS_2, and BN together with their absorbance spectra. From Reference 100. Reprinted with permission from AAAS.

and WE_2 (E=S, Se, Te), which show substantial layer-dependent properties due to a strong interlayer electronic coupling,[11,119] such limitations might be significant.

1.3.4   Colloidal Synthesis

By now, about 25 years of synthetic efforts by colloidal methods have resulted in the synthesis of nanostructures with controlled sizes and shapes. For instance, cadmium selenide (CdSe) NCs can be obtained as 0D spheres,[120–122] 1D rods and wires,[123] and 2D plates[124] with tunable dimensions. Typically, the formation of these NCs involves the decomposition of precursor molecules in a liquid environment in the presence of capping ligands. Mechanistically, such procedures follow a three-step mechanism based on Lamer and Dinegars model (see Figure 1.12a).[125] Precursors decompose at an elevated temperature – either by heating up or through injection of a precursor in a hot medium – and form reactive monomers (1) that are consumed by nucleation (2) and growth (3). Growth-control is modulated by ligands that bind to the surface of the NC. In this respect, a colloidal synthesis produces a dispersion of hybrid NCs where both the inorganic core
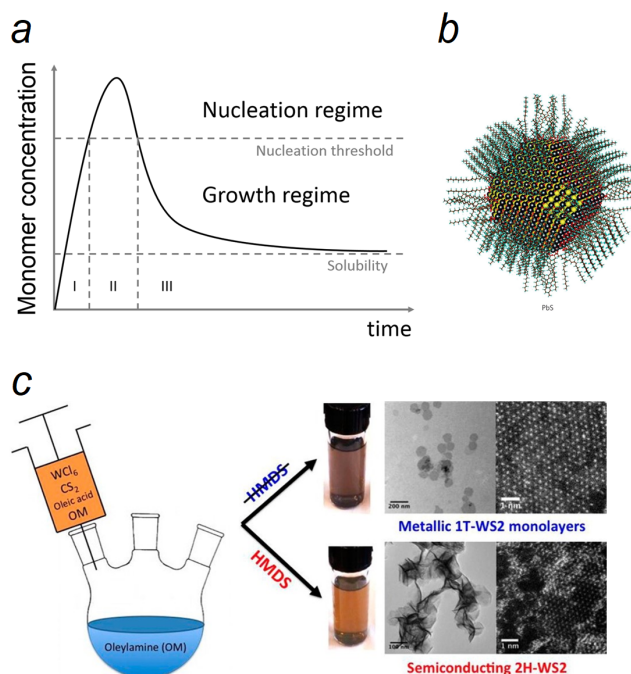
Figure 1.12: (a) Three-step LaMer and Dinegar model plotting the monomer concentration as a function of time. (b) Atomistic model of a lead sulfide NC capped with surfactant molecules (oleic acid). Reprinted with permission from Reference 128. Copyright (2016) Nature Publishing Group. (c) Reprinted with permission from Reference 104. Copyright (2014) American Chemical Society

and the organic ligand shell contribute to the NC's properties (see Figure 1.12b).[126–128] Over the past decade, the importance of the organic/inorganic interface layer has been pointed out by numerous authors. It has a pivotal role in stabilizing NC dispersion and controls the shape and the size of the nanocrystal during growth.[129, 130] As such, rational control of the interface proved indispensable to advance in research areas as diverse as optoelectronics,[131, 132] catalysis,[133] and thermoelectrics.[134]

Although these colloidal strategies are well-developed for II-VI and IV-VI quantum dots and metal oxides, knowledge of layered TMDs is still limited. Studies on group IV_b and group V_b TMDs (ME_2, M = Ti, Zr, Hf, V, and E = S, Se) assessed metal chlorides, carbon disulfide (CS_2), dodecanethiol (DDT), and selenium in an amine solvent

as viable precursors to synthesize TMD NCs.[135–138] Contrasting 0D systems, sulfur as a chalcogen source resulted in ill-defined NCs of poor quality.[135] Electron paramagnetic resonance (EPR) studies led to the conclusion that heating sulfur in amines led to the formation of reactive radicals that damage the structural integrity of the 2D layers.[135] Similar approaches were developed for group VI$_b$ TMDs. In 2014, Mahler *et al.* developed a benchmark protocol for 1T-WS$_2$ and 2H-WS$_2$ by reacting a WCl$_6$/oleic acid-complex together with CS$_2$ in oleylamine (see Figure 1.12c).[104] Their approach was later extended towards MoS$_2$ by the Hyeon group, producing MoS$_2$ NCs that are significantly more monodisperse than LPE allows.[105] Over the last years, we have witnessed a staggering growth in colloidal TMD syntheses methods, producing few-layered TMDs as a binary compound[105, 139–148] or as an alloy,[149–151] in a semiconducting[104, 105, 142–147, 150] or a semi-metallic state,[104, 141, 144, 148, 149] and having a sheet-like[104, 105, 139, 140, 144, 145] or a flower-like[104, 141–144, 146–150] morphology. In applications, the surface and layered nature of these colloidal TMDs have been exploited either as catalysts for hydrogen evolution and hydrogenation reactions,[143, 145–148, 152] as gas sensor,[145] and as battery anode materials.[139, 144, 151]

1.4 Thesis Outline

1.4.1 Objectives

The central theme of this PhD manuscript can be most concisely summarized as follows:

Following the discovery of the graphene, two-dimensional materials with diverse physical and chemical properties can now be obtained. In particular, the optoelectronic response of the transition metal dichalcogenides is increasingly sought for in next-generation devices, and their exploitable surfaces are in high demand for catalytic purposes. Generally, their production proceeds through mechanical exfoliation, where thin flakes are peeled of a bulk solid, or materials are grown on substrates from the bottom up by a vapor phase deposition methodology. Both of these fabrication methods produce materials of considerable quality, yet production volumes are limited given the material amounts practical applications may need.

In this respect, the proven viability of TMDs as optoelectronic and catalytic materials raised significant interest in more scalable production methods. In particular, solution-based methods, such as liquid-phase exfoliation and colloidal synthesis, stand out as they offer the prospect of scalability. Apart from scalability, these approaches yield colloidal dispersions of 2D flakes, which creates the additional possibility to integrate 2D materials in devices by solution-based processing or printing.

However, if solution-based methods are to become true alternatives to prepare 2D materials, (*i*) their syntheses in the liquid phase has to be thoroughly understood and, if needed, improved upon, and (*ii*) the properties of the resulting flakes, such as their physicochemical properties, surface chemistry and (ultrafast) photophysics, have to be studied and, if possible, bench-marked relative to materials produced by more established protocols through mechanical exfoliation and chemical vapor deposition.

1.4.2   Outline

With these central themes in mind, the manuscript is divided into two parts:

Part *I* narrates the story of how the thermodynamic theory of solutions and mixtures (chapter 2) holds the key to the castle and offers insights into the behavior of 2D layered materials in the liquid phase. In this tale, the protagonists are the solubility parameter δ and the exchange parameter χ. A matching of the solvent and colloid solubility parameter offers the prospect of high-yield exfoliations of bulk ReS_2 in chapter 3, and aids the formation of stable MoS_2 colloids synthesized by bottom-up chemistry in chapter 4. Chapter 5 discusses how an intricate interplay between the solubility parameter and a critical value of the exchange parameter determines the window in which stable colloids of diverse 2D materials can be obtained. Figure 1.13 provides a schematic overview of the different chapters in Part *I*.

Part *II* ventures into the realm of ultrafast physics in low dimensions. We use pump-probe spectroscopy (chapter 6) to disentangle semiconductor physics at picosecond timescales. These studies not only provide a wealth of fundamental knowledge but are at the same time of practical importance as they can pinpoint charge carrier decay through defect states. A study of the charge relaxation in colloidal
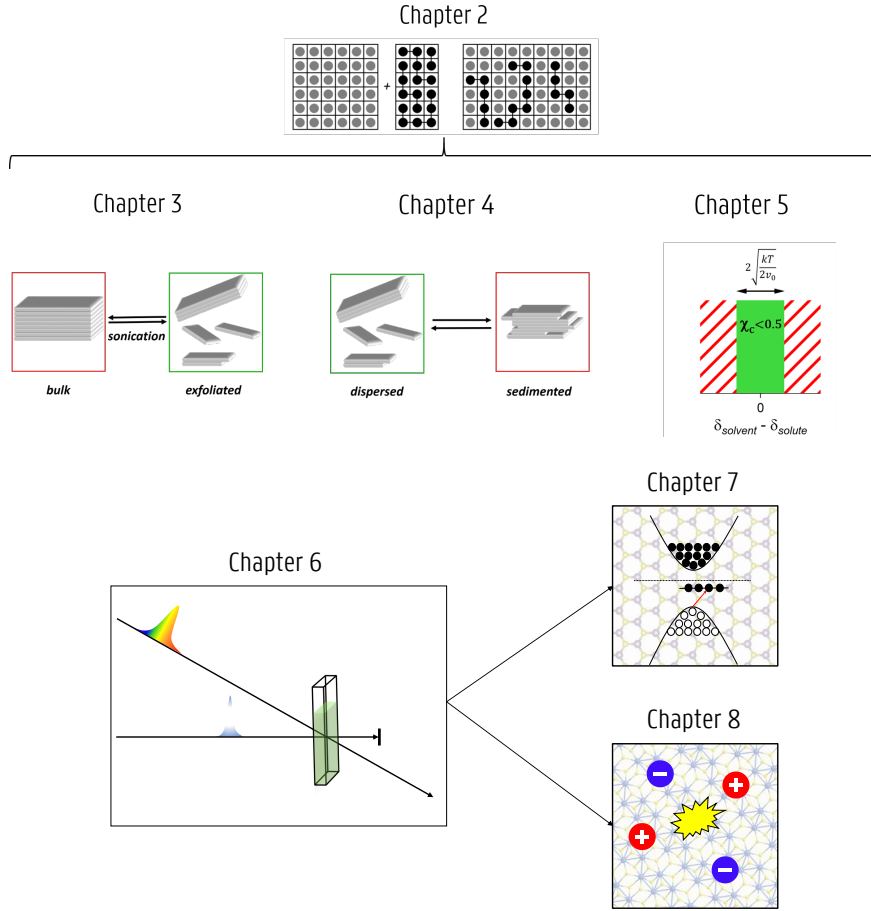
Figure 1.13: Schematic overview of the thesis.

MoS$_2$ (chapter 7) showed remarkably similar photophysics as been observed in established CVD grown MoS$_2$, even if entirely different chemistry is involved in the production process. A study of the photophysics in liquid-phase exfoliated ReS$_2$ (chapter 8) pointed to the photo-generation of mobile charges – desired for photovoltaics and photodetection – and offered insights into a maze of optical nonlinearities that are taking place on these picosecond timescales.

Part I

Solubility Parameters as Descriptors for Successful Liquid-Phase Exfoliations and Stable Colloidal Dispersions

2

Like Likes Like: Predictors for Solubility

"There is scarcely anything more important for a chemist than knowledge of solubilities, but unfortunately he finds it more difficult to predict than almost any other important property." – Joel Hildebrand[153]

2.1 Introduction

Scientific progress owed much to the use of simple conceptual models to explain complex phenomena. In physical chemistry, a lattice model provides such an example. Starting from a picture in which molecules of different types are distributed on a grid, it offers an elegant way to conceptualize the behavior of mixtures. Most notably, it relates abstract thermodynamic concepts to more tangible interactions at the molecular level. In this introductory chapter, we provide a general description of the thermodynamics of mixtures in the most general

and simplified form. Omitting a mathematical description, we reason based on the widely acknowledged solution theory predominantly developed by Joel Hildebrand throughout his life.[154] The concepts outlined here will be used throughout Part *I* of the manuscript in a modest endeavor to rationalize the behavior of 2D layered materials, processed by top-down and bottom-up methods, from a thermodynamic perspective.

2.2 Thermodynamics of Binary Mixing

2.2.1 Terminology

Mixtures By definition, mixtures are *systems consisting of two or more different chemical species that are physically combined.*[155] For instance, the fresh cup of coffee we might brew in the morning is a complex mixture containing small quantities of different chemical species dissolved in water.

Homogeneous versus heterogeneous A uniform mixture down to the microscopic scale is referred to as a homogeneous mixture or a solution. Conversely, a mixture of different phases (*i.e.*, regions with a different composition) is defined as heterogeneous.

Binary mixtures From a thermodynamic point of view, coffee already represents a complicated case as it contains multiple chemical species, each having different solubilities. For simplicity, we restrict ourselves to binary mixtures containing a solute B (*i.e.*, the dissolved substance) dissolved in a solvent A (*i.e.*, the liquid phase, typically present in large excess). A mixture of ethanol in water provides an example of such a system.

2.2.2 Solubility

Whether substances form homogeneous or heterogeneous mixtures in their equilibrium state depends on the change of thermodynamic state functions as a function of the mixture's composition.

Generally, processes tend to evolve in the direction that minimizes the free energy F of the system ($\Delta F < 0$). In the dissolution of a solute B in a solvent A, the difference in free energy between the mixed and

unmixed state sets the solubility of B, *i.e.*, the maximal amount of B in solution at equilibrium.

For a system at constant volume and temperature,[1] variations in the energy (ΔU_{mix}) and entropy (ΔS_{mix}) upon mixing dictate changes in the free energy (ΔF_{mix}) such that

$$\Delta F_{mix} = \Delta U_{mix} - T_0 \Delta S_{mix} \tag{2.1}$$

Eq 2.1 stresses that a subtle balance between energetic and entropic contributions drives dissolution processes. As we discuss below, energetic and entropic changes relate to molecular interactions and arrangements being the result of mixing.

2.2.3   Mixing within a Lattice Model

The lattice model   The relation between macroscopic state functions, such as internal energy and entropy, and microscopic interactions between individual atoms and molecules is most intuitively captured within regular solution theory, as derived by Hildebrand,[153] and its extension derived for polymers, Flory-Huggins theory.[156, 157] Both statistical theories rely on the use of a lattice model. Here, a system is represented by a grid of N cells with a fixed cell volume v_0. For pure substances, all spaces are occupied by the same molecules, while in a mixture different molecules are distributed over the lattice (see Figure 2.1). Molecules can occupy a single cell ($\nu = 1$) or they can occupy multiply cells ($\nu > 1$). The number of cells ν a substance occupies is set by its molecular (molar) volume v_m (V_m). Typically v_0 is defined so that the solvent A occupies a single cell on the grid ($\nu_A = 1$).[2]   On such a grid, molecules interact with their nearest neighbors with an interaction strength u; by definition, u is negative. In such a way, u_{AA} defines the interaction between two neighboring solvent molecules.

---

[1]Lattice models are most elegantly derived at constant volume using the Helmholtz free energy formalism. In this way, volumes are additive and both entropy and enthalpy can be written down in terms of volume fractions and molecular sizes. .

[2]Most intuitively for molecules of equal size, v_0 is equal to the molecular volume v_m. For larger solute solutions (polymers and by extension nanocrystals), the product of v_0 with the number of cells a solute occupies ν_B equals the molecular volume of the solute.
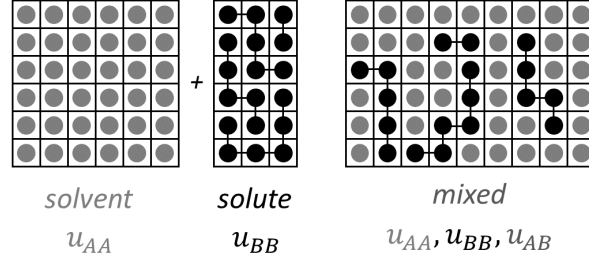
Figure 2.1: Schematic representation of a binary lattice model containing a solvent (A, grey circles) and a solute (B, black circles). We labeled the interactions following the main text as u_{AA} as solvent-solvent interaction, u_{BB} as solute-solute interaction, and u_{AB} as solvent-solute interaction.

From this perspective, mixing two pure substances involves the breaking of bonds between molecules of the same type (u_{AA} and u_{BB} in Figure 2.1), the formation of bonds between molecules of different types (u_{AB} in Figure 2.1) and molecular rearrangements that increase the combinatorial entropy. As such, molecular interactions and arrangements can be related to changes in macroscopic state functions of the mixture relative to the pure substances.

Entropy of mixing As the entropy relates to the number of ways a thermodynamic state can be realized,[158] entropic changes due to mixing can be calculated from probability theory[159] and are described by

$$\Delta S_{mix} = -\frac{k}{v_0}\left(\frac{\phi_A}{\nu_A}\ln\phi_A + \frac{\phi_B}{\nu_B}\ln\phi_B\right) \tag{2.2}$$

Here, ΔS_{mix} denotes the entropy of mixing per volume of the mixture, ϕ the volume fractions of the solvent A and solute B, ν the number of lattice sites occupied by a single solvent and solute *molecule*, and v_0 the volume of a lattice site.

Eq 2.2 provides a couple of fruitful insights:

- As in a mixture, ϕ is always smaller than 1, ΔS_{mix} is positive, and mixing is favorable as it reduces the free energy. Large and favorable entropic changes are usually significant when mixing small molecules (when $\nu_B \approx \nu_A$).

- On the other hand, for large and rigid solutes (*e.g.*, polymers or nanomaterials), the combinatorial entropy gain is assumed to decrease substantially ($\nu_B \to \infty$). For such solutes, energetic changes predominantly determine the solubility.[113, 160]

Energy of mixing and the exchange parameter   Within solution theory, the energetic cost or gain of mixing is described by the Flory-Huggins equation[155, 156, 161]

$$\Delta U_{mix} = \chi kT \phi_A \phi_B / v_0 \tag{2.3}$$

with ΔU_{mix} the energy of mixing per volume of the mixture and χ the exchange parameter.

As all other quantities in Eq 2.3 are positive, the sign of ΔU_{mix} is solely dependent on the value of the exchange parameter. In this regard, negative values for χ favor mixing.[3] The exchange parameter χ characterizes the energy change associated with the breaking of initial solvent-solvent u_{AA} and solute-solute u_{BB} bonds in favor of the formation of bonds in the mixed state between the solvent and the solute u_{AB} such that

$$\chi \propto \left(u_{AB} - \frac{u_{AA} + u_{BB}}{2} \right) \frac{1}{kT} \tag{2.4}$$

As the solubility of large solutes predominantly depends on the sign of the exchange parameter, dissolution (or exfoliation) is favored when A-B bonds are stronger than the averaged A-A and B-B interactions in the initial unmixed state – a result clearly in line with chemical intuition.

2.3   Solubility Parameters

While the theory above is appropriate for qualitative reasoning, it does not allow for a detailed and quantitative description of solubility processes. For this purpose, we rely on the solubility parameter and its relation to the exchange parameter and the energy of mixing.

---

[3]By definition, interaction parameters u are negative.

2.3.1 The Hildebrand Solubility Parameter

Hildebrand solubility parameter Analogous to the evaporation of a liquid, Eq 2.4 states that dissolution involves breaking interactions between individual molecules of the same type. The analogy between dissolution and evaporation was already highlighted by George Scatchard[162] and Joel Hildebrand[163] with the introduction of the solubility parameter δ as the square root of the cohesive energy density (ced)

$$\delta = \sqrt{ced} = \sqrt{\Delta U_v / V} \tag{2.5}$$

$$\Delta U_v = \Delta H_v - RT \tag{2.6}$$

In Eq 2.5, the cohesive energy density measures the energy needed to evaporate a liquid ΔU_v relative to the molar volume V of the liquid. Accordingly, δ^2 is indicative of the total energy required to keep the molecules of a liquid together.

Hildebrand-Scatchard equation The Hildebrand-Scatchard equation best sums up the strength of the solubility parameter as it relates the energy of mixing of a binary mixture AB to the respective difference in the solubility parameters according to

$$\begin{aligned} \Delta U_{mix} &\approx (\delta_A - \delta_B)^2 \phi_A \phi_B \\ &\approx \left(\sqrt{\frac{\Delta U_{v,A}}{V_A}} - \sqrt{\frac{\Delta U_{v,B}}{V_B}} \right)^2 \phi_A \phi_B \end{aligned} \tag{2.7}$$

According to the Hildebrand-Scatchard equation, the energy of mixing is minimized for substances with matching solubility parameters or matching cohesive energy densities.

The exchange parameter rewritten Combining Eq 2.3 and Eq 2.7, the exchange parameter χ can be expressed as a difference of solubility parameters

$$\chi \approx \frac{v_0}{kT}(\delta_A - \delta_B)^2 \approx \frac{V_s}{RT}(\delta_A - \delta_B)^2 \tag{2.8}$$

As by definition a solvent molecule occupies a single cell, v_0 equals the molecular/molar volume of the solvent v_s / V_s.

Eq 2.8 draws attention to the approximate nature of the solubility parameter. Since χ is expressed as a square of the difference in solubility parameters, χ can only attain positive values. As a consequence, χ values close to 0 associate with favorable conditions for mixing.

Equilibrium solute concentration   Often we are interested in relating the dispersed amount [of a solute] to the respective solubility parameter.

According to the literature,[4] solution theory predicts that the equilibrium concentration of a solute C is described by a Gaussian that depends on the difference in solubility parameter between the solvent δ_A and the solute δ_B according to:[112, 113, 164]

$$C \propto \exp\left(-\frac{v_B}{kT}(\delta_A - \delta_B)^2\right) \tag{2.9}$$

Here, v_B stands for the molecular volume of the dispersed phase. According to Eq 2.9, a maximal solubility is attained when the solubility parameter of the solvent δ_A matches the solubility parameter of the solute δ_B. Eq 2.9 lines up with the chemical notion *like likes like*, stating that stable solutions are expected if the mixture's constituents have compatible properties.

2.3.2 The Hansen Solubility Parameters

As during evaporation bonds of different types need to be broken, it seems intuitive to discriminate between dispersive, polar, and hydrogen-bonding contributions to the cohesive energy density. As such, Hansen divided the solubility parameter into three parameters according to[165]

$$\delta^2 = \delta_D^2 + \delta_P^2 + \delta_H^2 \tag{2.10}$$

The dispersive Hansen solubility parameter δ_D describes London dispersion interactions, the polar component δ_P permanent dipole-dipole interactions, and the hydrogen-bonding parameter δ_H groups the interactions that are not accounted for in δ_D and δ_P.

Evidently, within such a framework, stable solutions are attained when the set of Hansen solubility parameters of the solvent and the solute match.

2.4 Conclusion

We discussed the thermodynamics of mixtures within the framework of a binary lattice model. Most generally, the sign of the free energy

---

[4]We derive and debate this so-called equilibrium condition starting from the free energy of mixing in Chapter 5.

of mixing determines whether substances form homogeneous or heterogeneous mixtures (Eq 2.1). In this regard, a negative free energy promotes mixing and, therefore, favors homogeneous mixtures down to the molecular level. Both entropic and energetic effects contribute to the free energy. As the entropy relates to the number of ways a state can be realized, entropic effects promote mixing (Eq 2.2). A sizeable positive entropy favors small molecules' mixing, yet favourable entropic effects decrease when the solute size increases. As such, for large solutes, energetic effects are expected to prevail. Energetic or enthalpic changes are associated with the formation and breaking of molecular bonds. From this perspective, the sign of the energy of mixing depends on the sign of the exchange parameter which characterizes the energy change associated with breaking/forming bonds (Eq 2.3 and Eq 2.4). In this respect, negative values for χ promote mixing, *i.e.*, when bonds within the mixture are stronger than those between the pure substances.

For a more quantitative description of mixtures, we rely on the solubility parameter and its relation to the energy of mixing and the exchange parameter. The solubility parameter is indicative of the total energy required to keep the molecules of a liquid together (Eq 2.5) and therefore scales with the interaction strength between individual molecules. From this perspective, we rewrote the energy of binary mixing and the exchange parameter as the squared difference between the pure substances' solubility parameters (Eq 2.7 and Eq 2.8). Consequently, matching the solubility parameters of individual constituents within mixtures minimizes the energy of mixing and maximizes the solute's solubility (Eq 2.9). In this respect, the solubility parameter offers a quantitative description of the qualitative notion *like likes like*.

3

Liquid-Phase Exfoliation of ReS$_2$ by Solubility Parameter Matching

The proven viability of rhenium disulfide as optoelectronic material raised interest in more scalable fabrication methods. From this perspective, we introduce a method for the liquid-phase exfoliation of rhenium disulfide and provide a thermodynamic analysis of the exfoliation process within a broader context of solubility parameters as introduced in chapter 2.

Author contributions

The findings in this chapter have been published in:

Liquid-Phase Exfoliation of Rhenium Disulfide by Solubility Parameter Matching
Schiettecatte Pieter (P.S); Rousaki Anastasia (A.R.); Vandenabeele Peter (P.V.); Geiregat Pieter (P.G.); Hens Zeger (Z.H.); Langmuir, 2020, 36, 51, 15493–15500

P.S. did the experimental work, the majority of the characterization, and analyzed the data. A.R. and P.V. conducted the Raman measurements. P.S., P.G. and Z.H. discussed the results and wrote the manuscript together. Z.H. supervised the project.

Acknowledgments
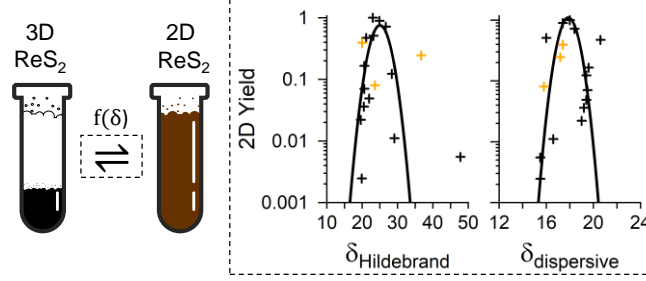
Figure 3.1: Overview of Chapter 3.

3.1   Introduction

Over the last decade, atomically thin two-dimensional (2D) transition metal dichalcogenides (TMDs) have raised an ever-increasing interest in science and technology. The development of these compounds fits the technological need for thinner functional materials in flexible optoelectronic devices and provides a platform to study the unique photophysics of low-dimensional materials.[26]   As bulk materials, TMDs are made of successive metal chalcogenide monolayers held together by relatively weak out-of-plane van der Waals interactions.[15] Such a structure enabled researchers to obtain mono- or few-layered TMD sheets using either top-down exfoliation procedures, such as micro-mechanical cleavage[11] and liquid phase exfoliation,[100] and bottom-up approaches, such as vapor phase deposition techniques[166] and chemical synthesis.[104] While micro-mechanical exfoliation and chemical vapor deposition (CVD) provide 2D materials of the highest quality, the limited scalability of these methods and the high synthesis cost prevent large-scale batch production.[83] Alternatively, solution-based processes – liquid-phase exfoliation (LPE) and wet chemical synthesis – allow for a cheaper and more scalable route to produce 2D nanomaterials.[105, 167–170] In general, however, LPE results in few-layered TMDs and offers limited control over size, morphology, and thickness. In particular in the case of semiconducting group VI_b TMDs – MoE_2 and WE_2 (E=S, Se, Te), which show substantial layer-dependent properties due to a strong interlayer electronic coupling, such limitations are a significant issue.[11, 119]

Unlike group VI_b TMDs, the electronic interlayer coupling in group VII_b TMDs, with rhenium disulfide (ReS_2) as the most prominent

constituent, is relatively weak. This leads to optoelectronic properties that are less sensitive to the layer-number.[28, 58] Additionally, ReS_2 adopts a distorted 1T$'$ crystal structure that shows strong in-plane,[71] and out-of-plane[70, 171] anisotropy. These distinguishable features have driven considerable research into few-layer ReS_2, as evidenced by the development of multilayer logical circuits,[60, 73] transistors,[74–78] photodetectors,[79, 80] and sensors[77] based on mechanically exfoliated or CVD grown few-layer ReS_2. The proven viability of few-layered ReS_2 as an optoelectronic material raised interest in a more scalable fabrication of few-layer ReS_2 flakes through liquid-phase exfoliation. Recent literature studies have highlighted the possibility to exfoliate ReS_2 in the liquid phase using lithiated agents,[172] in surfactant solutions,[173] and through a sequential bottom-up/top-down method starting from CVD grown ReS_2.[174] Besides, liquid-phase exfoliated ReS_2 has been incorporated in a TiO_2 composite, thereby enhancing the photocatalytic activity towards organic pigments,[175] and has been used as a high-Z element theranostic agent for computed tomography and photoacoustic imaging.[176]

While the aforementioned studies outline the possibility of liquid-phase exfoliation of few-layer ReS_2, the underlying physicochemistry of the liquid-phase exfoliation process and the structural and chemical properties of exfoliated ReS_2 have remained largely unexplored. A key aspect still missing involves the determination of the solubility parameters of ReS_2. From a practical point of view, these parameters are essential to identify optimal exfoliation solvents, as emphasized in seminal work on carbon nanotubes,[110] graphene,[101, 177] boron nitride,[100] transition metal dichalcogenides[112] and double-layer hydroxides.[178] Moreover, in the case of ReS_2, the solubility parameters can provide fundamental insights into the Van der Waals interactions in the group of VII$_b$ TMDs with the 1T$'$ crystal structure. Considering the recent emphasis on this peculiar interlayer stacking order in few-layer ReS_2 and the ensuing non-linear optical properties such as second harmonic generation,[179] the question arises what polymorph is adopted by liquid-phase exfoliated ReS_2.

In this study, we investigate the liquid-phase exfoliation of ReS_2 within the framework of solution thermodynamics (section 3.2) and we pursue an in-depth study of the morphological, structural, and elemental characteristics of the resulting ReS_2 (section 3.3).

3.2 Determination of Optimal Solubility Parameters and Exfoliation Conditions for ReS$_2$

3.2.1 Outline of the Experiment

As the solubility parameters of ReS$_2$ are unknown, we exfoliated ReS$_2$ in approximately 20 solvents with a known Hildebrand solubility parameter δ_s. We refer to Appendix A.1.1 for a detailed description of the experimental conditions and Table A.1 for a complete solvent list. As outlined in Schematic 3.2, we sonicated ReS$_2$ bulk powders in each of these solvents for a fixed duration using a bath sonicator. Afterward, we centrifuged the resulting dispersions to remove the unexfoliated material.
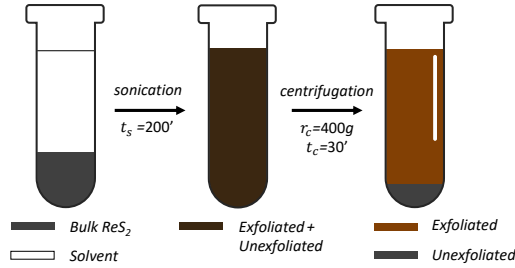
Figure 3.2: Schematic representing the liquid-phase exfoliation process for ReS$_2$.

3.2.2 A Description of Exfoliation using the Hildebrand Solubility Parameter

Visual Inspection For an initial visual inspection, we arranged the different dispersions from a small to a large δ_s, see Figure 3.3. Some ReS$_2$/solvent combinations yield brown, translucent dispersions, while others remained colorless. Since the band-edge exciton transition in ReS$_2$ is found at 820 nm,[180, 181] we interpreted the brown color as evidence of successful exfoliation. In this way, three regimes in rough agreement with the variation of the solubility
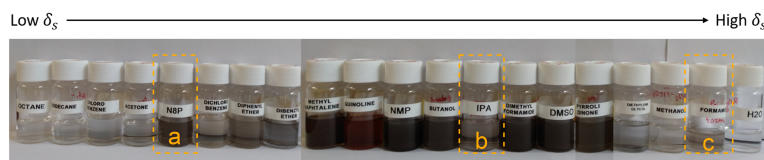
Figure 3.3: (a) Photograph of ReS_2 dispersions after LPE in different solvents. The dispersions are arranged from a small to a large Hildebrand solubility parameter δ_s. Solvents from left to right read: octane, dodecane, chlorobenzene, acetone, 1-octyl-2-pyrrolidone (N8P), o-dichlorobenzene, diphenylether, dibenzylether, 1-methylnaphtalene, quinoline, N-methyl-2-pyrrolidone (NMP), 1-butanol, isopropanol (IPA), N,N-dimethylformamide, dimethylsulfoxide (DMSO), 2-pyrrolidone, diethyleneglycol, methanol, formamide, water (H_2O). Solvents indicated with an orange box substantially deviate from the observed trend in δ_s, but are accounted for when considering the trend in $\delta_{s,D}$ (see later).

parameter can be distinguished. First, exfoliation in solvents with the smallest solubility parameter, such as octane and acetone, results in transparent to nearly transparent dispersions. The same applies to solvents with the largest solubility parameter, such as water and methanol. Clearly, both categories of solvents result in negligible or non-existent exfoliation. On the other hand, brown dispersions – indicative of significant ReS_2 exfoliation – are obtained for solvents with an intermediate solubility parameter. Such a trend is in line with predictions of solution thermodynamics presented in Section 2.2. For the small δ_s solvents, solvent/ReS_2 interactions are too weak to overcome the van der Waals interactions between the ReS_2 layers. On the other hand, with large δ_s solvents, the solvent/ReS_2 interactions are too weak to compensate for the breaking of the solvent-solvent interactions upon exfoliation. For the intermediate case, however, the formation of solvent/ReS_2 interaction balances out with the breaking of the initial interactions. Examples of suitable exfoliation solvents include lactams (*e.g.*, N-methyl-2-pyrrolidone), polar aprotic solvents (*e.g.*, dimethylformamide), and certain alcohols (*e.g.*, 1-butanol).

Quantitative analysis For a more quantitative analysis of the exfoliation yield in different solvents, we measured the at-

tenuance D[1] of each dispersion after exfoliation using UV-Vis
spectroscopy[2].[101, 102, 109, 112, 183–186]   The attenuance of a dispersion
in N-methyl-2-pyrrolidone (NMP), a representative solvent that
results in a high exfoliation yield, is plotted in Figure 3.4a. The
spectrum features a distinctive resonance at approximately 820 nm,
a wavelength that agrees with the band-edge exciton of ReS$_2$.[180, 181]
We, therefore, assigned the measured attenuance to the presence of
ReS$_2$. As transitions at higher energy are typically less influenced
by size quantization effects,[187] we used the attenuance D_{400} at
400 nm to measure the amount of dispersed ReS$_2$. As outlined
in Appendices B.2.1 and B.2.2, the choice of probe wavelength, or
whether raw or baseline subtracted data are used, has no substantial
influence on the quantities determined below. Also, a statistical
analysis through the Pearson correlation coefficient suggest the
absence of any correlation between the measured attenuance and the
solvent viscosity, see Appendix B.2.3. Figure 3.4b summarizes the
main results of this analysis by plotting D_{400} as a function of δ_s. In
line with the visual inspection, D_{400} varies substantially throughout
the range of solvents – over three orders of magnitude – and the
distribution peaks at around $24 - 25\,\mathrm{MPa}^{1/2}$.

As a first quantitative assessment of the average ReS$_2$ solubility pa-
rameter $\bar{\delta}$, we calculate the weighted arithmetic mean using the at-
tenuance D_i in a given solvent with solubility parameter $\delta_{s,i}$ as a
weighing factor according to

$$\bar{\delta} = \frac{\sum_i D_i \times \delta_{s,i}}{\sum_i D_i} \tag{3.1}$$

This is a standard methodology in descriptive statistics and has been
used, for example, to estimate the solubility parameters of graphene
and carbon nanotubes.[161, 177]   Using the recorded data for each
ReS$_2$/solvent combination in Figure 3.4b, the solubility parameter of
ReS$_2$ measures $24.2\,\mathrm{MPa}^{1/2}$ on average.

Alternatively, we relied on the prediction of solution theory that the
equilibrium concentration of a solute C is described by a Gaussian

---

[1]The absorbance, typically denoted as A, denotes "the logarithm of the ra-
tio of incident to transmitted radiant power through a sample". Analogous to
absorbance, attenuance also takes into account the effects due to scattering and
luminescence.Attenuance was formerly called extinction. The use of the term
extinction is no longer recommended by IUPAC.[182]

[2]In such an experiment, we detect the directly transmitted light.
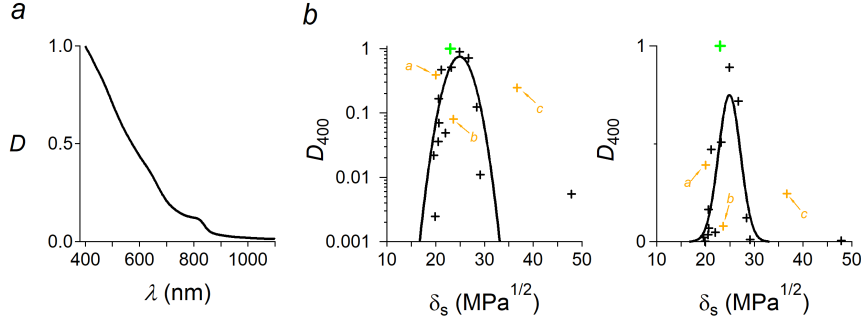
Figure 3.4: (a) Attenuance D of ReS_2 in NMP, normalized at 400 nm. (b) A plot of the attenuance at 400 nm D_{400} (markers), that serves as a metric for the dispersed concentration of ReS_2 nanosheets as a function of the Hildebrand solubility parameter of the solvent δ_s. Attenuance values for different ReS_2/solvent combinations are normalized to the ReS_2/NMP dispersion. The solid line is a fit to a Gaussian function.

that depends on the difference in solubility parameter between the solvent δ_s and the solute $\bar{\delta}$ according to:[112, 113, 164]

$$C \propto \exp\left(-\frac{\bar{v}}{kT}(\delta_s - \bar{\delta})^2\right) \tag{3.2}$$

Here, $\bar{v}$ stands for the unit volume of the dispersed phase. According to Eq 3.2, this distribution peaks when δ_s equals $\bar{\delta}$. Following Eq 3.2, we fit the experimental data in Figure 3.4b to a Gaussian function using the width and the central position of the Gaussian as fit parameters. Such a fit reproduces the observations (black line in Figure 3.4b), and the respective Gaussian is centered at a value $\bar{\delta} = 24.9 \pm 0.5\,\mathrm{MPa}^{1/2}$. Clearly, the estimate for the average ReS_2 solubility parameter from solution theory agrees with the weighted arithmetic mean determined above and is in line with the solubility parameters found for other layered materials, such as graphene[177] ($23\,\mathrm{MPa}^{1/2}$), boron nitride[100] ($22.5\,\mathrm{MPa}^{1/2}$), molybdenum disulfide[112] ($22\,\mathrm{MPa}^{1/2}$) and tungsten disulfide[112] ($21.5\,\mathrm{MPa}^{1/2}$). These data suggest that ReS_2 tends to exfoliate better in solvents with a slightly higher solubility parameter than those that allow for efficient exfoliation of molybdenum and tungsten chalcogenides. The best fit of D_{400} to Eq 3.2 yields a volume $\bar{v}$ of $3.7 \times 10^{-22}\,\mathrm{cm}^3$ and a concomitant full-width-at-half-maximum (fwhm) of $5.5 \pm 1.2\,\mathrm{MPa}^{1/2}$. This result agrees well with figures reported for MoS_2[112] (fwhm

= 6.5 MPa$^{1/2}$) and for WS$_2$[112] (fwhm = 4.5 MPa$^{1/2}$). Even so, $\bar{v}$ strongly underestimates the volume of the dispersed material, *i.e.*, a single ReS$_2$ flake. This discrepancy was already highlighted by Hughes *et al.*[164] in their study on dispersions of carbon nanotubes. Maybe, the systematic observation of this deviation can aid further theoretical work in the solution thermodynamics of van der Waals solids. We debate this discrepancy further on in Chapter 5.

3.2.3 A Description of Exfoliation using Hansen Solubility Parameters

Although the trend in the exfoliation yield of ReS$_2$ correlates with the Hildebrand solubility parameter, some noticeable exceptions exist. Isopropanol, for example, has a much lower exfoliation yield than its nearly ideal solubility parameter of 23.6 MPa$^{1/2}$ predicts, whereas 1-octyl-2-pyrrolidone (δ_s= 20.0 MPa$^{1/2}$) and formamide (δ_s= 36.7 MPa$^{1/2}$) exhibit better exfoliation yields than expected (see specific markers in Figures 3.3 and 3.5b). Additionally, NMP (green marker in Figure 3.4b) shows higher exfoliation yields compared to other solvents with a δ_s near the optimum. Since the Hildebrand solubility parameter does not discriminate between dispersive, polar and hydrogen-bonding contributions to the cohesive energy density (see Section 2.3.2,[165] we also analyzed the attenuance of each dispersion as a function of the dispersive $\delta_{s,D}$, polar $\delta_{s,P}$ and hydrogen-bonding $\delta_{s,H}$ contributions to the Hansen solubility parameter, see Figure 3.5.

Analogous to the method described above, we first calculate average values for the Hansen solubility parameters using a weighted arithmetic mean, and those values amount to $\bar{\delta}_D$= 18.0 MPa$^{1/2}$, $\bar{\delta}_P$= 11.2 MPa$^{1/2}$ and $\bar{\delta}_H$= 9.6 MPa$^{1/2}$. From Figure 3.5a, the yield correlates with $\delta_{s,D}$ through a similar Gaussian relation, while correlation in $\delta_{s,P}$ and $\delta_{s,H}$ are less evident. These figures indicate that Hildebrand solubility parameter trend originates mostly from a correlation between the exfoliation yield and the dispersive component of the Hansen solubility parameter. Notably, and in line with the existing literature on other two-dimensional materials,[100, 112, 177] solvents with a dispersive solubility parameter $\delta_{s,D}$ at around 18 MPa$^{1/2}$ (Table 3.1) favor exfoliation.[3] Such a value

---

[3]The observation that $\delta_{s,D}$ seems material independent suggests that vdW-

is typical for polar aprotic solvents or solvents with an aromatic functionality. The aforementioned discrepancies in δ_s are thereby a consequence of solvents having a too-small dispersive contribution despite a matching solubility parameter (isopropanol) or with a matching dispersive contribution despite a deviating solubility parameter (1-octyl-2-pyrrolidone and formamide), see specific markers in Figures 3.5a.
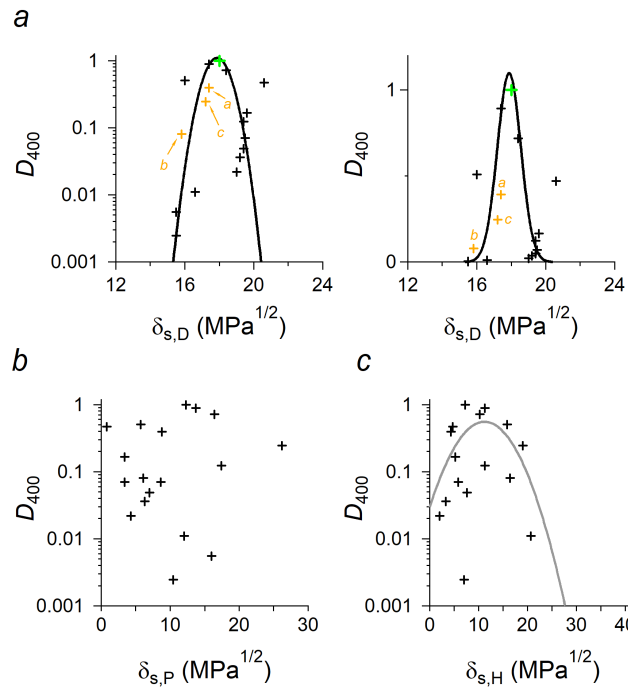
Figure 3.5: Plot of the attenuance at 400 nm as a function of the (a) dispersive $\delta_{s,D}$, (b) polar $\delta_{s,P}$ and (c) hydrogen-bonding $\delta_{s,H}$ components of the Hansen solubility parameter.

As already pointed out, our data suggest that group VII_b $1T'$ ReS_2 tends to exfoliate better in solvents with a slightly higher Hilderbrand solubility parameter δ_s than those that allow for efficient exfoliation of isotropic 2H molybdenum and tungsten chalcogenides of group VI_b. A comparison to MoS_2 and WS_2 in Table 3.1 learns that ReS_2 has

---

layered solids, independent of their elemental composition or crystal structure, have similar polarizabilities.

	$\bar{\delta}$ (MPa$^{1/2}$)	$\bar{\delta}_{\mathrm{D}}$ (MPa$^{1/2}$)	$\bar{\delta}_{\mathrm{P}}$ (MPa$^{1/2}$)	$\bar{\delta}_{\mathrm{H}}$ (MPa$^{1/2}$)
ReS$_2$	24.2/24.9	18.0/17.9	11.2/NA	9.6/NA
MoS$_2$[112]	22.0	17.8	9	7.5
WS$_2$[112]	21.5	18	8	7.5

Table 3.1: (first row) Optimal values for the Hildebrand solubility parameter ($\bar{\delta}$) and the dispersive, hydrogen-bonding and polar Hansen solubility parameters ($\bar{\delta}_{\mathrm{D}}$, $\bar{\delta}_{\mathrm{P}}$, $\bar{\delta}_{\mathrm{H}}$) for ReS$_2$ as obtained using, respectively, the weighted arithmetic mean/a Gaussian fit. (second row) Comparison with literature values for MoS$_2$ and WS$_2$.[112]

a similar $\bar{\delta}_{\mathrm{D}}$, but has a larger polar and hydrogen-bonding solubility parameters. Alternatively, as there is no difference in dispersive interactions, the equivalence between the Hildebrand and the set of Hansen solubility parameters ($\delta_{\mathrm{s}}^2 = \delta_{\mathrm{s,D}}^2 + \delta_{\mathrm{s,P}}^2 + \delta_{\mathrm{s,H}}^2$)[165] points indeed towards a more considerable contribution of polar interactions in ReS$_2$. Possibly, this difference reflects the larger dipole moment stemming from the distorted 1T$'$ phase of ReS$_2$.

3.3 Liquid-Phase Exfoliation of ReS$_2$

3.3.1 Optimization of the Exfoliation Conditions

Following the screening of different exfoliation solvents, we decided to use N-methyl-2-pyrrolidone as an exemplary solvent for an in-depth characterization of the exfoliated ReS$_2$. For details concerning the experimental procedure, we refer to the Experimental Section in Appendix A.1.2.

First, we optimize our exfoliation method according to a common sequential procedure.[183, 188] We first optimize the parameters related to the separation of the unexfoliated bulk material and the exfoliated nanosheets after sonication. In practice, we sonicated ReS$_2$ in NMP and centrifuged the final mixture at progressive centrifugation times t_c, while keeping the centrifugation rate fixed. We recorded the supernatant's attenuance (Figure 3.6a) and plotted the attenuance (Figure 3.6b, left axis) as a metric for the concen-

tration. Alternatively, the relative attenuance above the band-gap and below the band-gap (Figure 3.6b, right axis), a metric for the absorbance relative to the scattering, encodes similar information. The sedimentation decay can be fit to a biexponential fit function with time constants of 1 minute and 11 minutes, representing the decay of two unstable phases. To remove the majority of unexfoliated bulk material ($\approx$ 95%) while preserving the exfoliated material, we decided to set the centrifugation time at $3\tau_2 = 30$ minutes.

Once the centrifugation time was optimized, ReS_2/NMP dispersions were centrifugated at different centrifugation rates r_c, while keeping the centrifugation time fixed (Figure 3.6c). Here again, the extinction reaches a steady-state regime for rates exceeding 500g and can be fit to a biexponential decay with decay constants of 12g and 180g. Following our considerations outlined above, the centrifugation rate is fixed at $3\tau_2 = 540g$ (Figure 3.6d).

To track exfoliation kinetics, we took aliquots at different sonication times t_s, ranging from 10 minutes to roughly 24 hours. Consequently, we subjected each aliquot to an identical centrifugation cycle (540g, 30 minutes), and measured the supernatant by UV-vis spectrophotometry. As evident in Figure 3.6e, the yield of exfoliation increases sub-linearly, *i.e.*, defining the yield after 24 hours as 100%, we reach roughly 30% yield after 3 hours, 45% after 6 hours, and 75% after 12 hours of sonication. In line with the literature, the evolution follows a square-root dependence on the sonication time.[183, 186] Therefore, striving for the highest output in a reasonable experimental time window, we decided to fix the sonication time t_s at 6 hours.

Finally, we varied the initial concentration c_i of ReS_2 bulk powder in Figure 3.6f. Initially, we observe a linear increase, as evidenced by a 4-fold increase in the yield when changing to initial loading from 0.5 mg/L to 2 mg/L. However, raising the initial concentration further from 2 mg/L to 15 mg/L only results in a mere 3-fold increase. Based on these considerations, we fix the initial concentration c_i at 2 g/L.

3.3.2 Analysis of the Morphology

We assessed the morphology of the ReS_2 nanosheets through transmission electron microscopy, atomic force microscopy, and dynamic
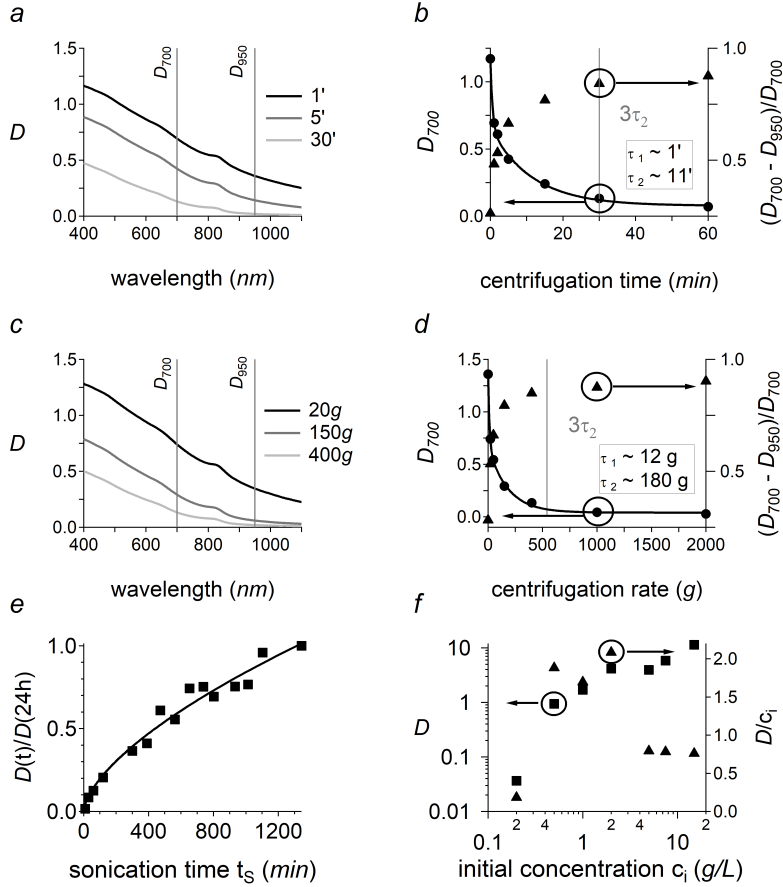
Figure 3.6: Optimization of (a-b) the centrifugation time t_c, (c-d) the centrifugation rate r_c, (e) sonication time t_s, and (f) the initial concentration c_i of bulk ReS$_2$. (a) Attenuance spectra at different t_c. (b) Plot of the attenuance (markers) as a function of t_c. (c) Attenuance spectra at different r_c. (d) Plot of the attenuance (markers) as a function of r_c. The solid lines in (b) and (d) are fits to biexponential functions. (e) Plot of the attenuance (markers) as a function of t_s. The solid line is a fit to a square-root dependence on the time $t^{1/2}$. (f) Plot of the attenuance (markers) as a function of c_i. The right axis plots the attenuance normalized by the initial ReS$_2$ concentration.

light scattering (DLS). According to the TEM image in Figure 3.7a, exfoliation in NMP yields two-dimensional flakes with lateral sizes of approximately 50 to 100 nm, not unlike individual grains observed in the bulk powder (see Appendix B.2.4). This assessment is corroborated by dynamic light scattering (Figure 3.7b), which shows a monomodal size distribution centered at 109 nm. Using data for various non-spherical and exfoliated nanomaterials, the Coleman group developed a framework to estimate the average size from the particle size distribution peak in DLS.[189] Using their empirical relation, the average length of a flake measures 80 nm, a value in good agreement with interpretations from TEM measurements. To estimate the
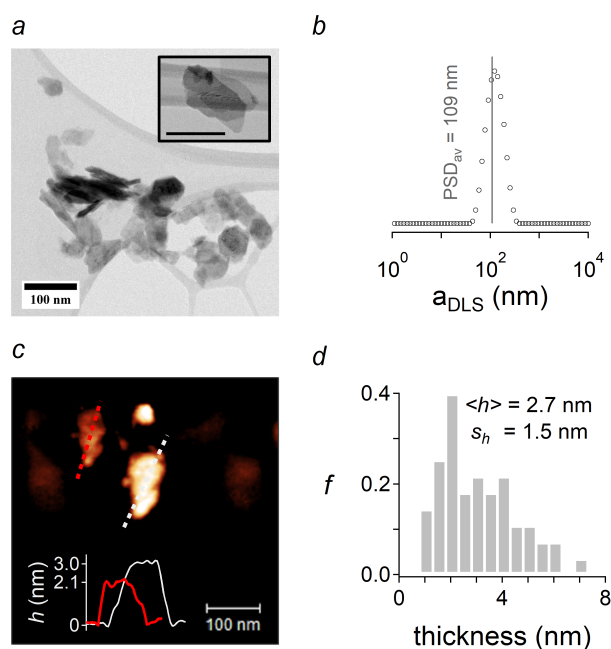
Figure 3.7: Overview of the most relevant morphological characteristics of the ReS_2 nanosheets produced in NMP. (a) Low-resolution TEM image. (b) DLS particle size distribution (markers) of ReS_2. The PSD average (PSD_{av}) for the calculation of the average length is marked with a vertical line. (c) AFM image with height profiles (solid lines) corresponding to slices across two particles (dashed lines). (d) AFM histogram showing the distribution of the nanosheet thickness (grey bars).

thickness of the ReS_2 flakes, we cast a dispersion on a SiO_2 wafer and

imaged the deposited flakes by atomic force microscopy. Figure 3.7c provides an AFM image, and the inset of Figure 3.7c depicts height profiles that correspond to slices across two particles. According to these profiles, the particles have a thickness of ≈ 2.1 nm and ≈ 3.0 nm at the center. As a ReS$_2$ monolayer has a thickness of 0.7 nm,[28] these flakes consist of, respectively, 3 and 4 ReS$_2$ monolayers. We refer to Appendix B.2.5 for additional AFM images. Figure 3.7d summarizes the main results of the AFM analysis by plotting the distribution of the thickness, which measures 2.7 nm on average and has a standard deviation of 1.5 nm, corresponding to approximately 4 ± 2 ReS$_2$ monolayers.

3.3.3 Analysis of the Interlayer Stacking Order

For ReS$_2$, the Raman features allow us to discriminate between the two ReS$_2$ polymorphs that solely differ in the interlayer stacking order. One refers to either as an isotropic or an anisotropic stacking between the ReS$_2$ layers in the literature. Additionally, there are sizing curves reported for both stacking orders.[70, 190]

Figure 3.8a plots the Raman spectrum for a ReS$_2$ film on glass. We observe a rich Raman response at small wavenumbers, from 120 to 450 cm^{-1}, where the 18 A_g vibrational modes of 1T$'$ ReS$_2$ are expected.[191] We labeled the 18 Raman vibrations in Figure 3.8a following the literature.[191] Besides, the spectrum is flat between 800 and 1100 cm^{-1}, a region that is characteristic for Re-O stretch vibrations (see inset Figure 3.8a).[192] This qualitative observation already points to a surface free of surface ReO$_x$ species (*vide infra*). Figure 3.8b plots the fingerprint region of ReS$_2$. Here, we draw attention to the A_g^1 and A_g^4 modes as the peak difference $\Delta\omega$ between both modes serves as a metric for the interlayer stacking order.[70, 190] We are aware that doping can influence the position of the Raman peaks, as observed in doped MoS$_2$.[193] In the case of intentionally p- and n-doped ReS$_2$,[194, 195] it has been reported that all of the Raman modes exhibited a slight shift in the same direction with a mere 2 cm^{-1} shift at the highest doping densities. While the absolute peak positions might not be as reliable, these studies suggest that even in the event of unintentional doping, the frequency difference $\Delta\omega$ between the two modes will still be a robust metric to distinguish between the aforementioned stacking orders. Determining the peak positions using a second derivative analysis, we find a value for $\Delta\omega$
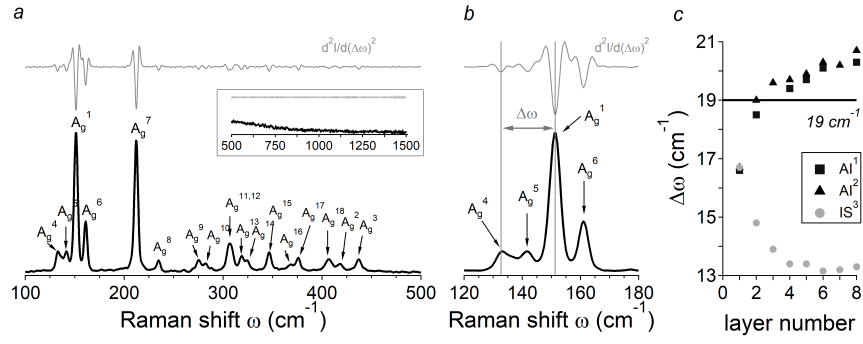
Figure 3.8: Overview of the Raman analysis of a representative ReS_2/glass film (excitation wavelength: 532 nm). (a) Raman spectrum covering wavenumbers from 100 to $500 \, \text{cm}^{-1}$ with the assignment of the Raman response following the reports by the Terrones group.[191] The inset covers the wavenumbers from 500 to $1500 \, \text{cm}^{-1}$. (b) Zoom of the Raman spectrum (black) together with the second derivative (grey). The vertical lines at A_g^1 and A_g^4 serve as a guide to the eye. (c) Sizing curves for ReS_2 relating $\Delta\omega(A_g^1 - A_g^4)$, the frequency difference between A_{1g} and A_g^4, with the layer number and for an anisotropic (AI) and isotropic (IS) stacking order. Sizing curve AI^1 (squares) was reported in Reference 190, AI^2 (triangles), and IS^2 (grey dots) in Reference 70.

of 19 cm^{-1}. As shown in Figure 3.8c, such a number is indicative of anisotropically stacked few-layer ReS$_2$ with a layer number of $N \approx 2 - 3$ depending on the sizing method. We can rationalize this result based on a simple thermodynamic argument; an anisotropic stacking order has a lower free energy,[70] and during exfoliation, there is ample time to relax into the thermodynamically most stable polymorph. Based on such an argument, it is likely that few-layer ReS$_2$ produced by bottom-up wet chemistry would also result in the anisotropically stacked polymorph.[145, 196, 197]

3.3.4   Elemental Analysis and Oxidation

We assessed the chemical purity of the exfoliated ReS$_2$ using X-ray photoelectron spectroscopy (XPS). Besides signals associated with adsorbed carbon and oxygen,[198] the XPS survey spectrum (Figure 3.9a) features different transitions from the core electrons of rhenium and sulfur. Besides, the distinctive N1s signal at ≈ 400 eV, indicative of NMP solvent residues, is entirely absent in the survey spectrum. The high-resolution XPS spectrum in Figure 3.9b gives a more detailed account of the chemical states of rhenium and sulfur. In particular, we find the characteristic peaks associated with the Re^{4+} 4f states at a binding energy of 42.8 eV and 45.3 eV and the S^{2-} 2p states at a binding energy of 163.4 and 164.4 eV. As a quantitative analysis by XPS gave a rhenium to sulfur ratio of 1:1.99, there are virtually no signs of oxidation.

This interpretation lines up with the qualitative Raman assessment described above. Interestingly, even aged samples (≈ 1 year) stored under ambient conditions retain their chemical purity as evidenced by a near-stoichiometric Re:S ratio of 1:1.97 (see Figure 3.9c). In a similar case, exfoliation of TiS$_2$ in a pyrrolidone solvent (cyclohexyl-pyrrolidone) suppressed oxidation, likely through the formation of an ordered solvent monolayer on the surface of TiS$_2$, and facilitated their use in lithium storage applications.[199] In summary, these figures outline that the liquid phase exfoliation, presented here, produces few-layer, anisotropically stacked, and chemically pure ReS$_2$ platelets with long-term stability.
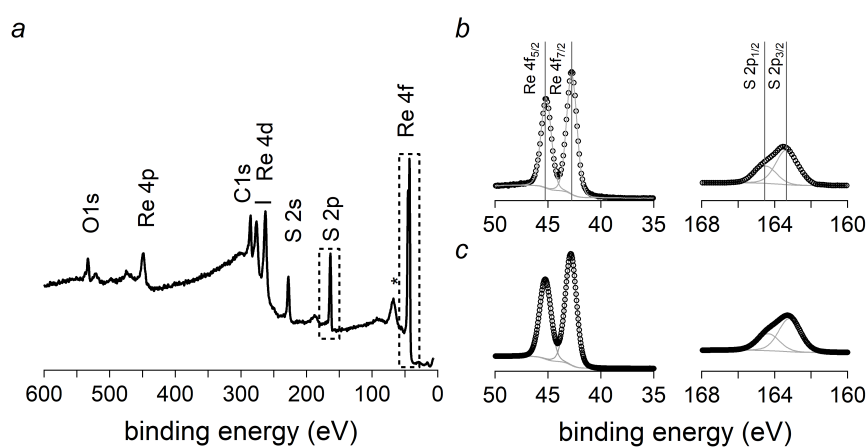
Figure 3.9: Overview of the X-ray photoelectron (XPS) analysis of a representative ReS_2/glass film (X-ray source: $Al\,K\alpha$). (a) XPS survey spectrum. The signals related to either rhenium (Re), sulfur (S), oxygen (O), and C (carbon) are marked. The asterisk (*) denotes the residual signal from the conductive copper tape applied to the sample to avoid charging during the measurement. The fingerprint regions for Re 4f and S 2p shown in panel b are highlighted. (b-c) High-resolution XPS analysis of the core level spectra of the rhenium 4f peaks (Re $4f_{7/2}$, Re $4f_{5/2}$), and the core level spectra of the sulfur 2p peaks (S $2p_{3/2}$, S $2p_{1/2}$) of (b) a fresh ($\approx 1\,week\,old$) sample and (c) an aged ($\approx 1\,year$) sample. The markers represent experimental data points, and the solid line represents a fit of a Lorentzian line shape and a background.

3.4 Conclusion

In summary, this work provides physicochemical insights into the liquid-phase exfoliation process of ReS_2, a promising 2D nanomaterial for various optoelectronic applications. By screening liquid-phase exfoliation in a wide range of solvents, we observe that conditions for high yield exfoliations can be understood from polymer solution thermodynamics, where the most optimal solvents are characterized by similar Hildebrand and Hansen solubility parameters of $25\,\mathrm{MPa}^{1/2}$ and $18\,\mathrm{MPa}^{1/2}$, respectively. Accordingly, N-methyl-2-pyrrolidone and N,N-dimethylformamide are recommended exfoliation solvents, as they result in the highest exfoliation yields, and 1-butanol is convenient due to its lower boiling point. Next, we carried out a detailed analysis of the exfoliated ReS_2 using N-Methyl-2-pyrrolidone as an exemplary solvent. Combining transmission electron microscopy, atomic force microscopy, and dynamic light scattering, we established the exfoliated nanomaterial as few-layered ($N \approx 4 \pm 2$) with lateral sizes ranging from tens to a hundred nanometer. According to Raman analysis, the liquid-phase exfoliated ReS_2 adopts the anisotropically stacked and thermodynamically most stable polymorph. Elemental analysis based on X-ray photoelectron spectroscopy verifies that the ReS_2 flakes are chemically pure and are stable against oxidation. Accordingly, we conclude that liquid-phase exfoliation is suitable to batch produce few-layer and pristine ReS_2 flakes in solvents with a solubility parameter close to $25\,\mathrm{MPa}^{1/2}$.

4

Solubility Parameters as Descriptors for Stable Colloidal MoS$_2$ Dispersions

"God made the bulk; surfaces were invented by the devil.
– Wolfgang Pauli

Chapter 3 outlined that similar solubility parameters characterized optimal exfoliation solvents for rhenium disulfide. We rationalized this finding based on solution theory (see chapter 2). Similar to LPE, a colloidal synthesis relies on a tight interplay between the inorganic and organic interface. Provided that most proof-of-concept applications of colloidal TMDs to-date exploit the surface, typically as a catalyst, we study the interface science of molybdenum disulfide produced by colloidal chemistry.

Acknowledgments

4.1   Introduction

The remarkable optoelectronic properties and high surface areas of layered 2D nanomaterials have sparked widespread research interest.[200] Most notably, the TMDs are intensively investigated as next-generation semiconductors with potential applications in the field of optoelectronics, catalysis, sensing, or energy storage, to name a few.[10, 11, 26, 201, 202] Molybdenum disulfide (MoS_2) is by far the most investigated member of the TMD family. As a bulk crystal, MoS_2 adopts a layered crystal structure consisting of stacked S-Mo-S monolayers. The relatively weak dispersion forces between the layers favor the production of ultrathin mono-and few-layered TMDs through various methods.[26] Currently, vacuum deposition and mechanical exfoliation are the most commonly used techniques to manufacture high-quality transition metal dichalcogenides,[95] yet their high synthesis cost and limited scalability remain key issues. These drawbacks have raised interest in more scalable production methods. From these perspectives, solution-based methods, such as top-down liquid-phase exfoliation (LPE) and bottom-up wet chemical synthesis, have attracted significant research interest. These methods offer the prospect of scalability and the suitability of colloidal nanocrystals for solution-based processing via a variety of deposition methods, *e.g.*, dip-and spin-coating, which offers an exciting road towards their integration in devices.

Both LPE and colloidal synthesis rely on a tight interplay between the inorganic and the organic interface. On the one hand, seminal studies on layered 2D materials systematically demonstrated that stable dispersions of exfoliated nanomaterials are only obtained in solvents with well-defined solubility parameters δ_s at around $20 - 27\,\text{MPa}^{1/2}$.[101–103, 109, 112] These results have been rationalized within a broader context of solution thermodynamics where a matching of the solubility parameter of the solvent and the nanomaterial minimizes the energy of mixing. In this respect, knowledge of solubility parameters proved essential to determine suitable conditions for high-yield exfoliations and offered the prospect of post-processing 2D materials in solution. For instance, solvent-exfoliated dispersions can be processed into printable inks and used to fabricate printed devices, such as thin-film transistors.[106]

A colloidal synthesis, on the other hand, produces dispersions of hybrid nanocrystals where both the inorganic core and the organic sur-

factant shell contribute to the properties of the nanocrystal.[126–128] Over the past decade, the importance of the surfactant/inorganic interface layer has been pointed out by numerous authors. It not only has a pivotal role in the stabilization of NC dispersion,[203] but also controls the shape[129] and the size[130] of the nanocrystal during growth. In a similar way as it did for LPE nanomaterials, rational control of the interface proved indispensable to advance in research areas as diverse as optoelectronics,[131, 132] catalysis,[133] and thermoelectrics.[134]

Clearly, in both fields, insights in the inorganic-organic interface layer proved essential to improving the material's performance. Despite the staggering growth in colloidal TMD synthesis recipes,[104, 105, 137, 139–141, 143–148, 204] the interface between the NC and the surrounding organic medium is barely understood. Most remarkably, nearly all proof-of-concept applications involving those colloidal TMDs, exploit the surface of these compounds either as a catalyst for hydrogen evolution reactions,[145–148, 152] as gas sensor,[145] as hydrogenation catalyst[143] or as battery materials.[139, 144] Besides, to enhance their performance, colloidal TMDs are often processed as composite materials. In such a composite, they are typically mixed with other low-dimensional materials.[104, 144, 145]

From these perspectives, we use colloidal MoS_2 as a model system to gain insight into the inorganic/organic interface of colloidal TMDs materials. We first synthesize and characterize MoS_2 in section 4.2. In sections 4.3 and 4.4, we study the interactions between ligands and NCs by solution NMR spectroscopy.[205] Lastly, we investigate their stability within a framework of solubility parameters in section 4.5.

4.2 Colloidal Synthesis of MoS$_2$

4.2.1 Description of the Synthesis Protocol

We synthesized MoS$_2$ NCs based on a recent publication by Son *et. al.*[105] Figure 4.1 depicts the set-up for such a synthesis. We refer to Appendix A.2 for a detailed description of the experimental procedure. In brief, we prepared a precursor solution containing molybdenum chloride, oleic acid (OA), and oleylamine (OLA). After introducing anhydrous carbon disulfide (CS$_2$) into the mixture, the precursor solution (indicated as 1 in Figure 4.1b) was loaded into a glass syringe and slowly injected into a hot oleylamine (shown as 2 in Figure 4.1b) using a syringe pump. The reaction temperature was kept at 320°C and the reaction time was 2 hours. Afterward, the reaction product was purified through a standard purification protocol and taken for characterization.
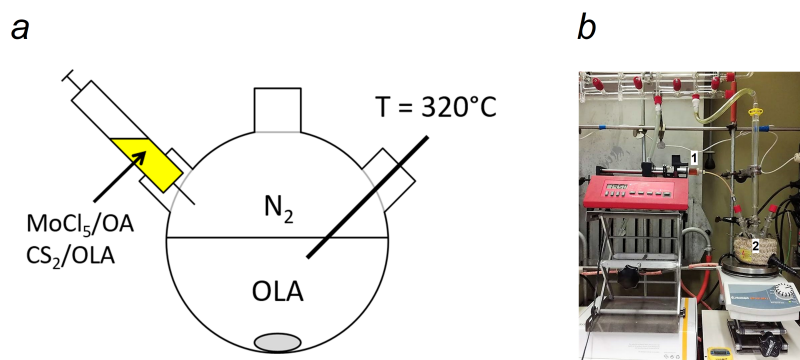
Figure 4.1: Set-up of a colloidal MoS$_2$ synthesis, including (a) a pictorial representation and (b) an image of the reaction. A precursor solution containing MoCl$_5$, oleic acid (OA), carbon disulfide (CS$_2$), and oleylamine (OLA) (a mixture labeled as 1) is slowly injected into oleylamine (a solution labeled as 2) at a temperature of 320 °C using a syringe pump.

4.2.2 Material Characteristics of Colloidal MoS$_2$

In this section, we use different characterization methods to study the synthesized product. In particular, we emphasize procedures that allow us to identify the compound and to investigate whether colloidal chemistry produces the desired semiconducting 2H phase. Addition-

ally, we use different approaches to quantify the layer number.

Sections 4.2.2.1, 4.2.2.2, and 4.2.2.3 deal with Ultraviolet-Visible (UV-Vis) spectroscopy, Raman spectroscopy, and X-ray Diffraction (XRD) as macroscopic characterization methods that probe billions of nanoparticles simultaneously. Sections 4.2.2.4 and 4.2.2.5 address transmission electron microscopy (TEM) and atomic force microscopy (AFM) as microscopic methods that probe individual nanoparticles on a nanometric scale.

4.2.2.1   UV-Vis Spectroscopy

Principle   UV-Vis spectroscopy is a straightforward yet powerful method to characterize semiconductor NC dispersions. The absorption of electromagnetic radiation by semiconductors provides essential information about their electronic structure and optical response.[187] In practice, we record the attenuance D of a dispersion for incident light with different energies (or wavelengths) and summarize the results in a so-called attenuance spectrum.

In the case of MoS_2, the optical response depends on the crystal phase and the layer number. The semiconducting 2H phase has distinctive exciton bands, denoted as A, B, and C.[11, 15] Alternatively, size quantization results in a layer-dependence of the A exciton position.[11] Provided that sizing curves for MoS_2 exist, the layer number can be estimated from the A exciton position.[117]

Results   The attenuance spectrum of the purified reaction product is given in Figure 4.2a. We observe three features that are characteristic of the semiconducting 2H phase of MoS_2. At approximately 665 nm (1.865 eV) and 615 nm (2.016 eV), the features labeled A and B correspond to the excitonic transitions between the spin-orbit split valence-band maxima and the conduction-band minimum at the K point. We refer to Figure 4.2b for a simplified sketch of the electronic band structure of MoS_2.[11, 19, 206] As outlined in Appendix B.3.1, we assigned the wavelength to these resonances using a derivative analysis of the attenuance spectrum. The prominent feature C at around 420 nm, on the other hand, originates from transitions between the valence and conduction band along the direction from K to Γ, where these bands are mostly parallel.[207]

As emphasized in the introductory chapter, the electronic structure
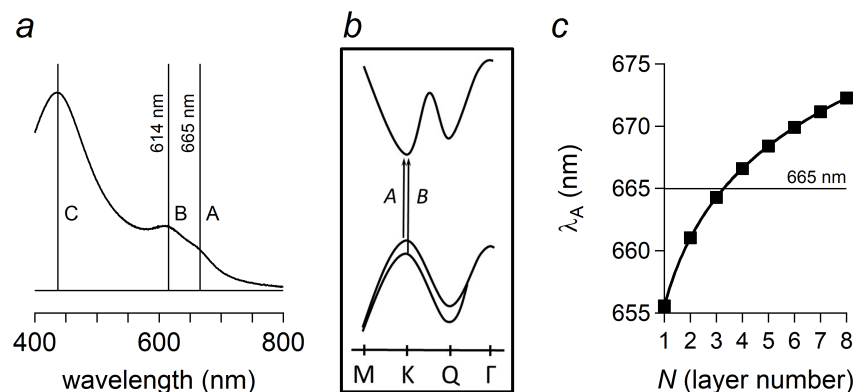
Figure 4.2: (a) Attenuance spectrum of a dispersion of MoS$_2$ nanosheets in *o*-DCB, indicating the characteristic *A*, *B* and *C* transitions. (b) Simplified sketch of the electronic band structure of monolayer MoS$_2$ along the direction M to Γ. (c) Sizing curve for MoS$_2$ relating the A exciton position λ_A to the layer number *N* reported in Ref. 117.

of a MoS$_2$ crystal depends on the number of monolayers it contains. Backes *et al.* reported a sizing curve for liquid-phase exfoliated MoS$_2$ that allows the determination of the layer number *N* from the A exciton position (see Figure 4.2c).[117] For the A exciton situated at 665 nm, we expect a synthesized MoS$_2$ sheet to contain approximately 3 monolayers on average.[1]

4.2.2.2 Raman Spectroscopy

Principle Raman spectroscopy has proven to be an indispensable tool to analyze two-dimensional materials since their earliest discoveries.[119, 208] For one thing, characteristic vibrations related to the compound in question and its crystal phase are typically imprinted in the Raman spectrum. Regarding layered crystals, the frequency of the vibrational modes often changes as a function of their layer number.[209]

---

[1]Given the difference in synthesis method, some care must be taken not to overinterpret this result. Nonetheless, the authors reported that the experimental position of the *A* exciton in mechanically exfoliated MoS$_2$, supported on a substrate, agreed with their sizing curve. We believe this strongly validates the use of their sizing curve.
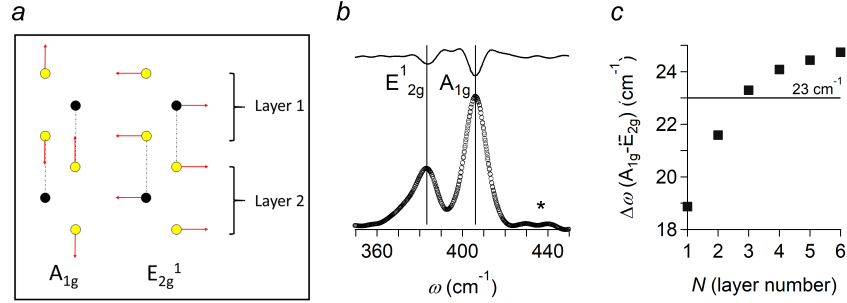
Figure 4.3: (a) Schematic of the atomic displacements of A_{1g} and E_{2g} in MoS_2 as viewed along the [100] direction.[119] The sulfur and molybdenum atoms are indicated in yellow are black, respectively. (b) Raman spectrum (532 nm excitation) of a dispersion of MoS_2 nanosheets in o-DCB. The distinctive A_{1g} and E_{2g} Raman modes of 2H MoS_2 are highlighted. The asterisk marks a residual signal from the solvent o-dichlorobenzene, see Appendix B.3.2. (c) Sizing curve for MoS_2 relating $\Delta\omega(A_{1g} - E_{2g})$, the frequency difference between A_{1g} and E_{2g}, with the layer number N reported in Ref. 119.

Here, the presence of the A_{1g} and E_{2g} vibrational modes in the Raman spectrum between wavenumbers of $350 - 450\,\mathrm{cm}^{-1}$ (see schematic in Figure 4.3a) characterizes the 2H crystal phase of MoS_2. Besides, the frequency difference between A_{1g} and E_{2g} serves as a metric for the layer number.[119]

Results   The finding that the synthesis yields few-layer, 2H MoS_2 presented above is corroborated by the Raman spectrum, which shows the characteristic A_{1g} and E_{2g} vibrations of hexagonal 2H MoS_2 separated by a frequency difference of $23\,\mathrm{cm}^{-1}$ (Figure 4.3b). According to the sizing curve reported by Tony Heinz *et al.*, such a Raman shift is representative of few-layer MoS_2 containing roughly 3 monolayers on average (Figure 4.3c).[119]

4.2.2.3   X-ray Diffraction

Principle   When an x-ray hits an object, the atoms within the object have a small but finite probability to elastically scatter the incident wave. In a periodically oriented crystal, the scattered waves can undergo constructive interference for specific directions determined
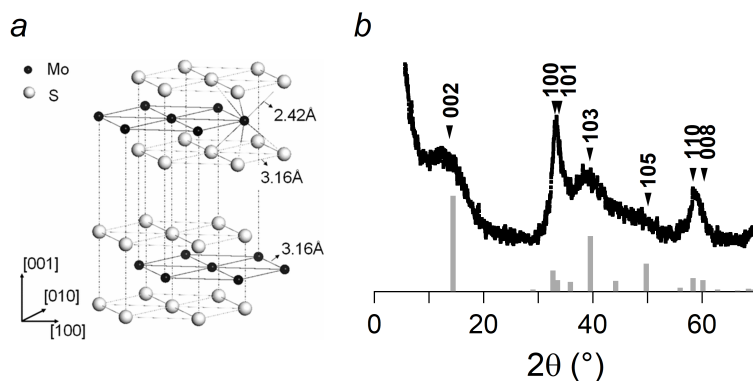
Figure 4.4: (a) Crystal structure of bulk MoS$_2$. Reprinted from Ref. 211. (b) x-ray diffractogram of a glass substrate coated with the reaction mixture and a reference pattern for bulk hexagonal (2H) MoS$_2$ according to JCPDS 75-1539 (vertical bars).

by the spacing between the lattice planes of the crystal.[210] X-ray diffraction thereby provides crystallographic information on a macroscopic scale by mapping the intensity of diffracted x-rays at different angles 2θ.

Bulk MoS$_2$ crystallizes in a hexagonal lattice ($\alpha = \beta = 90°$, $\gamma = 120°$) with lattice parameters a = b = 0.3161 nm and c = 1.229 nm (see Figure 4.4a). As emphasized in the introduction, synthesized MoS$_2$ occurs in 2 hexagonal polytypes that solely differ in the complexation of the central metal. Unfortunately, the XRD patterns of both phases only show subtle changes.[40] For nanocrystallites with broadened XRD peaks, differentiating between 2H and 1T poses a challenge. Nonetheless, we see XRD as an integral asset in our toolbox as it provides information on whether colloidal MoS$_2$ is crystallized in its typical hexagonal arrangement.

Results The x-ray diffractogram in Figure 4.4b and Table 4.1 summarize the results of the analysis. We assigned the 2θ reflections according to the reference pattern for hexagonal bulk MoS$_2$ (JCPDS-75-1539 indicated with vertical bars in Figure 4.4b). At small 2θ values, we observe a broad feature that corresponds to the (002) c-plane reflection. Making use of Bragg's law, the inter-planar spacing d_{hkl} amounts to $\approx 7\text{Å}$, a value in agreement with the distance between two successive MoS$_2$ layers in the bulk crystal (c/2). At large 2θ values,

reflection	$2\theta_{exp}$ (°)	$2\theta_{ref}$ (°)	d_{hkl} (Å)
(002)	12.9	14.4	6.9
(101),(100)	33.3	32.7	2.7
(103)	39.2	39.5	2.3
(105)	48.6	49.8	1.9
(110)	58.9	58.3	1.6

Table 4.1: Assignment of the 2θ reflections in the x-ray diffractogram (left column). Comparison with 2θ reflections of the corresponding diffraction planes in bulk 2H-MoS_2 according to JCPDS 75-1539 (middle and right columns).

an envelope containing multiple reflections that belong to hexagonal MoS_2 extends from 30° up to 60°. Here, the interlayer (100) and (110) reflections, at 33° and 59°, respectively, are most intense. Weak and broad c-plane reflections combined with intense and sharp reflections of lateral planes are typically associated with thinner crystals having a less-ordered stacking in the vertical direction.[212, 213]

4.2.2.4   Transmission Electron Microscopy

Principle   The discovery of the wave-like nature of electrons[214] provided intriguing opportunities to study materials at the fundamental limit. From a practical point of view, it prompted the invention of the electron microscope, an invaluable experimental tool in nanocrystal research.[215] Conceptually, as electrons pass through a thin specimen, for example, a layer of MoS_2, they undergo a wide variety of possible electron-matter interactions. It should be no surprise that these interactions provide important morphological and crystallographic information about the specimen. In a conventional bright-field TEM, the transmitted and low-angle scattered electron beams are used to create an image through a Fourier transformation of an interference pattern.

For ultrathin two-dimensional materials, the information provided by low-resolution TEM is rather limited as TEM doesn't provide a reliable quantification of the thickness, and materials tend to wrinkle or aggregate due to drying effects, impeding a reliable size determination. High-resolution TEM, on the other hand, provides complementary information to XRD on a microscopic scale.
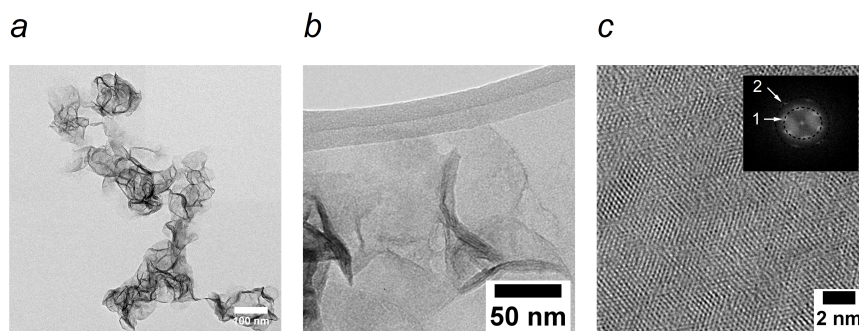
Figure 4.5: (a,b) Low-resolution TEM images. (c) High-resolution TEM image accompanied by the corresponding FFT pattern in the inset. The reciprocal patterns labeled as 1 and 2 are respectively spaced at 0.27 nm and 0.15 nm to the origin.

Results Figure 4.5 shows bright-field TEM images of the sample after it has been cast on a thin copper foil. The low-resolution TEM images, in Figures 4.5a and 4.5b, indicate that the synthesis method yields two-dimensional and partly folded nanosheets with dimensions of about 100 nm.

The high-resolution TEM and the corresponding fast Fourier transform analysis (FFT) in Figure 4.5c reveal crystalline domains with a hexagonal symmetry and reciprocal patterns spaced at 0.27 nm and 0.15 nm. These patterns correspond to the (101) and (110) lateral planes of MoS$_2$, a result in line with the XRD analysis presented above.[216]

4.2.2.5 Atomic Force Microscopy

Principle Since its development in 1989, atomic force microscopy (AFM) emerged as a powerful tool to image and study surfaces at the nanoscale.[217] A cantilever with a sharp tip is the most vital part of an AFM. In essence, while scanning the specimen, deflections of the cantilever tip enable surface reconstruction and thickness determination.[218]

Results After casting the MoS$_2$ dispersion on a silicon substrate, the nanosheets could be imaged by atomic force microscopy, see Figure 4.6a. As shown in Figure 4.6b, such an AFM analysis yields
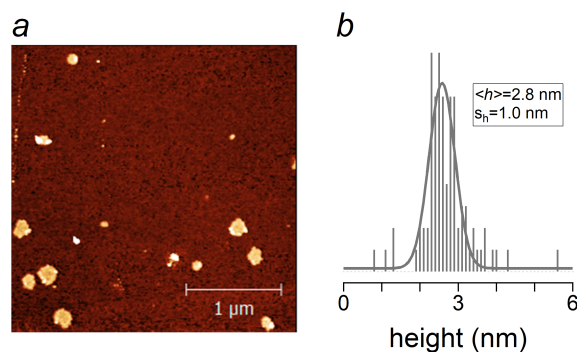
Figure 4.6: (a) AFM analysis of a spin-coated MoS_2 sample on a SiO_2 wafer. (b) AFM height histogram showing the distribution of the nanosheet thickness ($N = 85$). The solid line is a fit to a Gaussian function.

the nanosheet thickness distribution, which measures 2.8 nm on average and has a standard deviation of $\pm$ 1.0 nm. Alternatively, we fit the height distribution to a Gaussian function using the width and the central position of the Gaussian as fit parameters. The respective Gaussian is centered at 2.5 nm and has a full-width at half maximum (FWHM) of 0.8 nm. Using 0.7 nm as the thickness of a monolayer (see Section 4.2.2.3), these figures indicate that the MoS_2 sheets analyzed here consist of approximately 3 to 4 MoS_2 monolayers. Importantly, the numbers extracted following indirect methods (UV-VIS spectroscopy and Raman spectroscopy) agree well with the quantification done by AFM. Such an observation could suggest that the top and bottom facets are in fact ligand-free (see later).

4.2.3   Conclusion

We have carried out a detailed analysis of MoS_2 synthesized through colloidal bottom-up chemistry using molybdenum chloride and carbon disulfide as chemical precursors. Different analyzes of the synthesized product (see Table 4.2 for an overview) indicate that colloidal MoS_2, as synthesized here, contains 3 monolayers on average and adopts the 2H semiconducting phase.

Technique	Results	Layer thickness
UV-Vis	Excitonic absorption related to 2H phase	$N \approx 3$ according to position of A exciton
Raman	A_{1g} and E_{2g} modes of 2H phase present	$N \approx 3$ according to frequency difference
XRD	Hexagonal pattern of bulk 2H MoS$_2$	Few-layer (less stacking in c-direction)
(HR)TEM	Lateral size in order of hundreds of nanometer Hexagonal planes (100) and (101) in FFT	-
AFM	-	$N \approx 3 - 4$ according to height statistics

Table 4.2: Summary of the material characteristics of colloidal MoS$_2$. (left column) Characterization technique. (Middle column) Short description of the major results. (Right column) Estimation of the layer thickness.

4.3 Surface Chemistry of As-Synthesized MoS$_2$ Nanocrystals

4.3.1 Observations and Motivation

It is a common practice to purify colloidal nanocrystal dispersions by a sequence of successive precipitation and redispersion.[205] However, we observe that such a practice renders the colloidal MoS$_2$ dispersions unstable. Progressive purification leads to rapid aggregation of the colloids in (cyclo)hexane, toluene, or chloroform, commonly used solvents in nanocrystal syntheses.[104, 105, 150] A similar observation had already been reported by Mahler et al. in the case of the synthesis of 2H-WS$_2$ nanosheets.[104] In this study, 2H-WS$_2$ tended to aggregate over time and additional washing steps by precipitation render the product less dispersible in hexane. Nonetheless, we noticed that redispersion of MoS$_2$ in o-dichlorobenzene resulted in stable dispersions that show little to no sedimentation over time – we address the solubility of TMD nanocrystals in sufficient detail further on. These

observations motivated us to study the binding of the capping ligands
to MoS_2.

4.3.2   The Solution ^{1}H NMR Toolbox

Over the last decades, Nuclear Magnetic Resonance (NMR) spec-
troscopy has arisen as a key method to study the interface between an
inorganic nanocrystal and its organic ligand shell. Studies on distinct
classes of NCs demonstrated that a combination of one-dimensional
(1D) ^{1}H NMR with two-dimensional (2D) techniques such as dif-
fusion ordered spectroscopy (DOSY) and nuclear Overhauser effect
spectroscopy (NOESY) provides researches with a powerful *toolbox*
to elucidate ligand binding. Most notably, the combination of these
techniques enables bound ligands to be distinguished from free ligands
and dynamic ligands, *i.e.*, ligands involved in a dynamic exchange be-
tween a free and a bound state.[205]

*Instead of providing a detailed description of each method, we rather
highlight what each technique offers from this perspective.*

4.3.3   1D ^{1}H NMR Spectroscopy

Principle   A ligand that is tightly bound to the surface of a
nanocrystal typically experiences an excessive transverse T_2 relax-
ation[219] and a different chemical environment compared to a freely
tumbling species in solution. As such, surface-binding is reflected
in a severe broadening of the linewidth.[220–223]   Throughout the
literature, linewidth broadening has been rationalized as a sign of
surface-bound ligands.[220, 221, 224–226]

Conversely, dynamic ligands engaging in a fast adsorption/desorp-
tion equilibrium, only show moderate changes in their linewidth and
chemical shift.[227, 228] Nonetheless, as we discuss below, to elucidate
tightly bound ligands from dynamic ligands 2D techniques are gener-
ally more conclusive.

Results   Figure 4.7b shows a ^{1}H NMR spectrum of a dispersion
containing MoS_2 nanosheets in deuterated *o*-dichlorobenzene. Apart
from the resonances associated with the solvent *o*-DCB at 7 ppm (†),
the spectrum is dominated by a series of resonances ascribed to the
different protons in the oleyl-chain of oleylamine and oleic acid – the
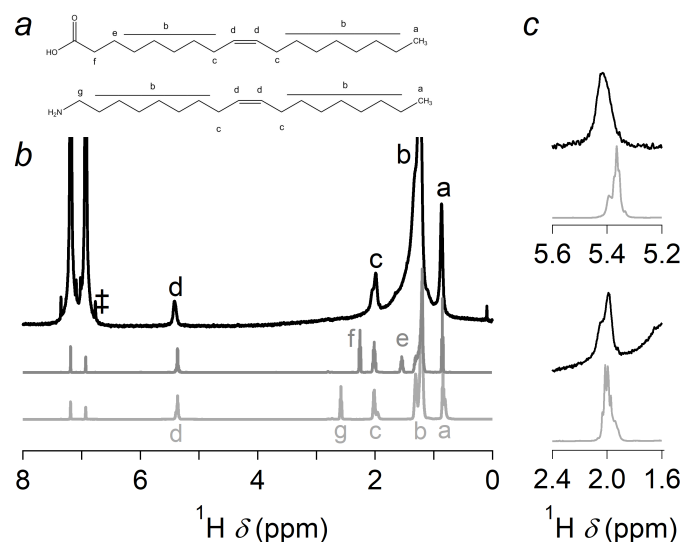
Figure 4.7: Overview of the 1D ^{1}H NMR analysis of a representative colloidal MoS$_2$ dispersion (solvent: o-dichlorobenzene-d$_4$). (a) Shorthand formula of oleic acid and oleylamine. (b) ^{1}H NMR spectrum (black) of a colloidal MoS$_2$ dispersion in o-dichlorobenzene-d$_4$. The labeled resonances are associated with (a-d) the ligands oleylamine and oleic acid, (‡) o-dichlorobenzene-d$_4$, and (†) silicon grease. (c) Zooms of (top) alkene protons **d** and (bottom) α-methylene protons **c** for (black) the dispersion containing MoS$_2$ nanosheets and (grey) a reference sample containing oleylamine.

ligands present in the chemical synthesis. The two prominent resonances in the spectrum at 0.9 ppm and spanning the region between 1.0-1.8 ppm are, respectively, associated with the protons in the terminal methyl moiety **(a)** and with the methylene proton pool **(b)**, while the resonances at 2.0 ppm and 5.4 ppm are, respectively, assigned to protons in the α-methylene **(c)** and the alkene **(d)** group.

The resonances in the ^{1}H NMR spectra of the sample are moderately broadened and lack fine-structure. Besides, resonances are slightly shifted towards higher δ values (*i.e.*, down-field). For instance, the α-methylene resonance shifts a mere ≈ 0.005 ppm, while the alkene resonance shifts ≈ 0.04 ppm. For clarity, we provide zooms of both resonances in Figure 4.7c.

These figures point to an interaction of the ligands with the NC sur-
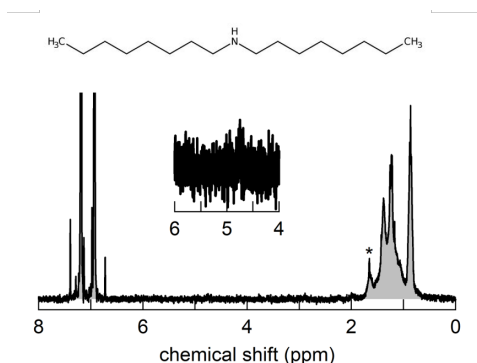
Figure 4.8: Overview of the 1D ^{1}H NMR analysis of a colloidal MoS_2 dispersion synthesized with oleic acid and diocylamine instead of oleylamine (solvent: o-dichlorobenzene-d$_4$). The inset shows a zoom around the alkene resonance and highlights that the alkene protons of oleic acid are absent.

face. Nonetheless, the limited chemical shift changes and linewidth broadening line up with the characteristic behavior of a dynamic (labile) ligand rather than that of a tightly bound moiety.

To identify if the resonances present after work-up are attributed to oleylamine or oleic acid, we exchanged oleylamine for dioctylamine in the synthesis. In contrast to oleylamine and oleic acid, dioctylamine is a saturated amine and thereby lacks alkene protons. The 1D 1H spectrum of such a dispersion is shown in Figure 4.8. Most importantly, the absence of the alkene resonance, typically retrieved at around 5.5 ppm (see inset), suggests the absence of oleic acid in the dispersions.

4.3.4   2D ^{1}H Spectroscopy

Principle   The combination of NOESY and DOSY offers a unique framework to study the ligand binding motive by monitoring the diffusion coefficient and the nOE build-up of the species in solution. Compared to a 1D spectrum, it allows for a more straightforward distinction between a tightly bound, a free, and a dynamic ligand.[205]

DOSY measures the molecular diffusion coefficient D as a function of the chemical shift. Typically, diffusion coefficients in the order of 10^{-9} m^2/s mark free ligands. Alternatively, surface-bound species tend to diffuse slower with D values in line with the NC's solvo-
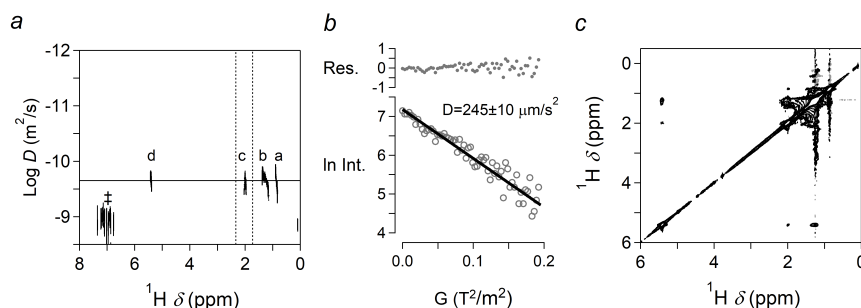
Figure 4.9: Overview of the 2D ^{1}H-^{1}H NMR analysis of a representative colloidal MoS_2 dispersion (solvent: o-dichlorobenzene-d$_4$). (a) DOSY NMR spectrum and (b) the decay of the intensity to the gradient field strength at chemical shift values around the α-methylene group (resonance c, dashed lines). The markers represent data points, the solid line is a fit to the Stejkal-Tanner equation. The labeled resonances are associated with (a-d) the ligands oleylamine and oleic acid, ($\ddagger$) o-dichlorobenzene-d$_4$. (c) NOESY NMR spectrum of the dispersion. The negative nOEs are indicated in black and the positive nOEs in grey.

dynamic size.[224] For instance, ligands tightly bound to QDs of a few nm in size yield diffusion coefficients of 10^{-10} m^2/s as a rule of thumb[220, 224, 229–231] while tightly packed ligands on ≈ 30 nm long 2D CdSe platelets tended to diffuse D values of 3.5 10^{-11} m^2/s.[226]

Alternatively, in the case of dynamic ligands, an average diffusion coefficient is measured.[227, 228, 232] In such cases, NOESY spectroscopy can ascertain ligand interaction as bound and free species develop different signatures in a NOESY spectrum. Importantly, only bound ligands develop strong nOEs (*i.e.*, off-diagonal resonances with a similar sign as the diagonal) due to a reduction in rotational correlation time.[233]

Results As shown in the DOSY spectrum in Figure 4.9a, the resonances associated with the different protons in the oleyl-chain appear at the same value of the diffusion coefficient at approximately $10^{-9.6}$ m^2/s, or 250 μm^2/s. For instance, using established procedures, the decay of the intensity at the position of the α-methylene group, to the applied gradient can be well described using a mono-exponential fit to the Stejkal-Tanner equation (for more information

on the Stejkal-Tanner equation, we refer to Appendix B.3.3). Such a fit yields an average value of the diffusion coefficient of 245±10 μm^2/s.

The Stokes-Einstein equation relates the diffusion coefficient to the solvodynamic radius r_{H} through the friction coefficient f

$$D = \frac{k_B T}{f} \tag{4.1}$$

In this most simple case, *i.e.*, for spherical particles, f equals $6\pi r_{\mathrm{H}}\eta$, with η the viscosity of the solvent. In this case, this yields a solvodynamic radius of 1.3 ± 0.1 nm. Alternatively, we calculated the apparent dimensions of the ligands for a disc-shaped geometry (f=$12r_{\mathrm{H}}\eta$), resulting in r_{H}=2.1 $\pm$ 0.1 nm. Irrespective of the exact functional dependence of r_{H} on D, these numbers differ significantly from the expected diffusion coefficient of a large nanosheet with TEM dimensions of 100 nanometers. Based on the Stokes-Einstein Equation, we rationalize that such an object's diffusion coefficient is several orders of magnitude smaller, and falls in the order of $\sim 1\mu$m^2/s.

Off-diagonal cross-peaks with weak negative nOE intensities appear in the NOESY spectrum of the MoS$_2$ dispersion (Figure 4.9c) and provide proof for an interaction of the ligands with the surface of the NC. The intensity a cross peak attains during such an experiment depends on the spin polarization transfer from the initially polarised resonance to the other resonances in the chain. For instance, polarizing the alkene protons (**6**), the initial magnetization of the 2 alkene protons is transferred to the (n-2) other protons in the chain (for instance, n=37 for oleylamine). In this way, if every molecule has spent time on the surface during the mixing phase, (n-2)/n of the initial polarization is transferred. We would expect a total polarization transfer of 90-95% for long-chained molecules at sufficiently long mixing times. Opposite from this prediction, the sum of the integrated cross-peaks only contains a mere 5% of the the diagonal intensity, a low number that points to a weak interaction.

4.3.5   Conclusion

A moderate resonance broadening and limited changes in chemical shift, a fast ligand diffusion coefficient, and weak, albeit negative, nOEs imply that the ligands are not tightly bound to the surface of the MoS$_2$ NC, yet, they are in a dynamic exchange between a bound
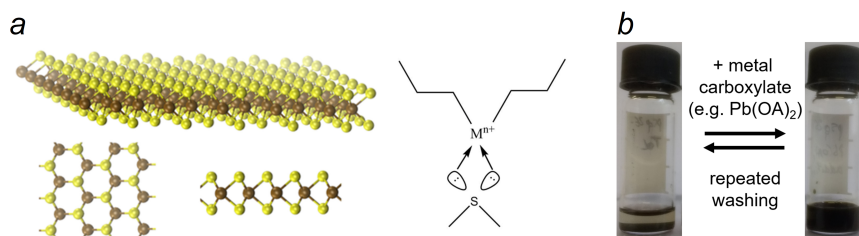
Figure 4.10: (a) Crystal structure of MoS_2 showing extended sulfur-rich (yellow) top-and-bottom facets. Schematic of a donor-acceptor interaction between sulfur and a metal complex. (c) (left) A dispersion of MoS_2 in toluene and (right) the same dispersion after adding the lead oleate complex. After homogenizing, both dispersions were centrifugated.

and a free state.[205, 228] Most likely, such a dynamic interaction is responsible for the limited colloidal stability of MoS_2 in commonly used NC solvents (*e.g.*, hexane, chloroform, toluene). As a side-note, we observed a similar weak ligand binding in colloidal WSe_2 (submitted work, see publication 4, section 9.4).

4.4 Addition of Metal Complexes

4.4.1 Motivation and Exploratory Experiments

One could think of alternative ligands that are compatible with the surface of MoS_2. An appealing option are metal carboxylate salts that could act as lewis acids and coordinate to the sulfur atoms in the top and bottom planes of a MoS_2 layer (see Figure 4.10a). Based on the Pearson hardness/softness principle,[234] we might expect soft metal complexes to adhere stronger to the relatively soft S^{-2} ions present in the top and bottom facets. In this respect, Pb^{2+} complexes might be good candidates.

As an exploratory experiment, we add lead oleate to an unstable dispersion of MoS_2 in toluene. Both the dispersions with and without lead oleate are homogenized and centrifuged. While the native dispersion is colloidally unstable, supplying a metal carboxylate salt proves efficient to stabilize the dispersion to a great extend, see Figure 4.10b. However, a subsequent purification with ethanol as the non-solvent readily destabilizes the dispersion. This exploratory ex-

periment already points to a labile interaction between the capping
ligand and the nanocrystal.

4.4.2 ^{1}H NMR Toolbox Analysis
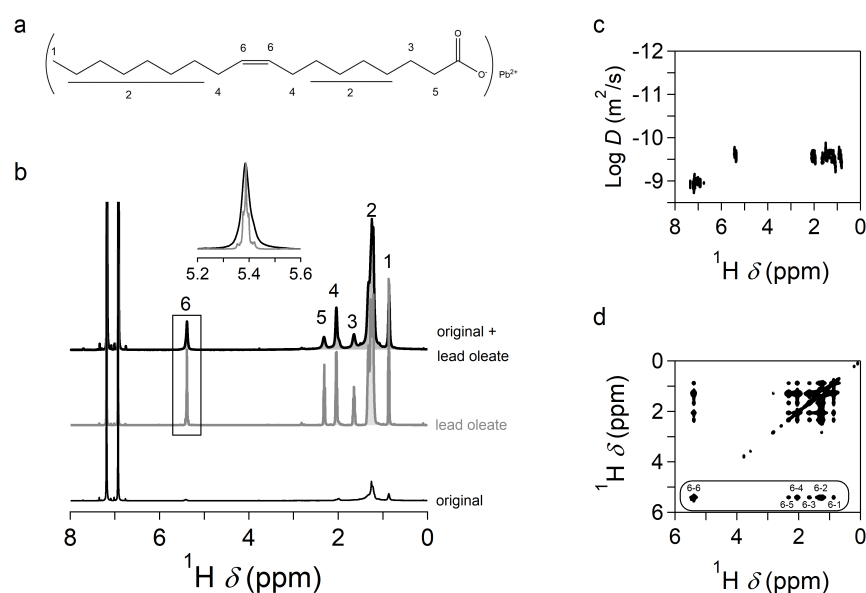
Figure 4.11: Overview of the NMR toolbox analysis on a sample that contains
MoS_2 dispersed in o-dichlorobenzene-d$_4$ after the addition of lead oleate, hence-
forth denoted as $MoS_2/Pb(OA)_2$. (a) The chemical formula of lead oleate with
the resonances labeled as indicated in the NMR spectra. (b) ^{1}H NMR spectra
of (bottom) the MoS_2 dispersion before the addition of lead oleate, (middle,
grey) a blank reference containing lead oleate, and (top, black) a MoS_2 dis-
persion after lead oleate has been added. The inset shows a comparison of
the broadened alkene resonance of the lead oleate. (c) DOSY NMR spectrum
of $MoS_2/Pb(OA)_2$. (d) NOESY NMR spectrum of $MoS_2/Pb(OA)_2$. Negative
nOEs are indicated in black, positive nOEs in grey.

We apply the solution NMR toolbox to elucidate the ligand-binding
of the metal carboxylate complex to the MoS_2 surface. To do so,
lead oleate was added in a ten-fold excess with respect to the amount
of oleylamine still present in the dispersion, see Appendix A.2 for
experimental details. The sample containing lead oleate (see Fig-
ure 4.11a for the chemical formula) and MoS_2 is henceforth denoted

as $MoS_2/Pb(OA)_2$. The ^1H NMR spectrum of the $MoS_2/Pb(OA)_2$ dispersion (Figure 4.11b, top black curve) shows a series of moderately broadened resonances in comparison to the sharp resonances of a blank lead oleate solution (Figure 4.11b, middle grey curve). Additionally, the DOSY spectrum in Figure 4.11c only shows a single value for the lead oleate diffusion coefficient ($\approx 200 \pm 10$ $\mu m^2/s$), a value that hardly differs relative to the one of free lead oleate (see Appendix B.3.4). Both observations hint at a loosely bound ligand in a fast exchange between a free and a bound state. Nuclear Overhauser effect spectroscopy confirms this assumption. The NOESY spectrum in Figure 4.11d shows off-diagonal cross-peaks with strongly negative nOEs arising from ligands interacting with the surface of the NCs. The combination of ^1H NMR, DOSY, and NOESY thus ambiguously points to lead oleate being in a fast exchange between a free and a bound state. Here again, the manifestation of a ligand which readily attaches and detaches from the surface is in line with the observation that colloidally stable dispersions are only obtained in the presence of an excess of free ligand, as well as the fact that extensive washing renders the dispersion to its original colloidal instability.

4.4.3   nOE Build-up Curves

Principle   To study the ligand binding in more detail, we constructed an nOE build-up curve by analyzing the intensity of the nOE cross-peaks as a function of the nOE mixing time. The intensity I_{ij} that a cross peak attains during such an experiment depends on the transfer of the spin polarization from the initially polarised resonance i to the resonance j and the loss of initial polarization during the mixing phase due to longitudinal T_1 relaxation. As such, the build-up curve can be described by[228]

$$\frac{I_{ij}(t)}{I_{ii}(0)} = C_{ij} \exp\left(-R_L t\right)(1 - \exp\left(-R_C t\right)) \tag{4.2}$$

with $I_{ij}(t)$ being the intensity of the cross peak between resonance i and j and $I_{ii}(0)$ the intensity of the diagonal peak of the polarised resonance i at $t = \tau_{mix} = 0$. The rate constant R_C describes cross-relaxation of spin polarization from resonance i to j and R_L describes the longitudinal T_1 relaxation rate. In the absence of longitudinal T_1 relaxation (R_L equal to zero), the relative intensity that an nOE cross peak would attain is equal to the pre-factor C_{ij}. In this way, the sum of the pre-factors equals the amount of spin polarization transferred

Cross peak 6-j	C	R_C (s^{-1})
6-2	0.45 ± 0.03	4.2 ± 0.4
6-4	0.11 ± 0.01	10.6 ± 1.1
6-3	0.04 ± 0.01	5.8 ± 1.3
6-1	0.04 ± 0.01	2.1 ± 0.7
6-5	0.03 ± 0.01	4.1 ± 1.7
$\sum$	0.67 ± 0.07	

Table 4.3: Fit parameters obtained by fitting the nOE build-up curves in Figure 4.12 to Eq 4.2.

from resonance i to all the other resonances in the chain. As the build-up of a negative nOE intensity is solely due to ligands that reside on the surface, summing C_{ij} over all possible resonances j allows us to estimate the fraction of bound ligands. For instance, starting from an initial polarization of the alkene protons (6), the initial magnetization of the 2 alkene protons is transferred to 32 other protons. In this way, if every molecule has spent time on the surface, *i.e.*, under conditions of fast exchange, 32/34 of the initial polarization is transferred, and we expect a total polarization transfer of 94% or approximately 3% per hydrogen nucleus.

Results   In practice, we measured NOESY spectra at different mixing times ranging from 10 ms up to 500 ms. For simplicity, we focus on the alkene resonance as it is isolated from the rest. At each mixing time, we integrated the diagonal alkene resonance and each off-diagonal cross peak, yielding the respective intensities $I_{6-6}(t)$ and $I_{6-i}(t)$. For instance, $I_{6-4}(t)$ denotes the cross peak intensity ascribed to the spin transfer from the alkene (6) to the α-CH$_2$ (4). We summarized this analysis by plotting the $I_{6-i}(t)$ relative to $I_{6-6}(0)$ in Figure 4.12a. As the value for $I_{6-6}(0)$, the initial intensity present in the diagonal before mixing, we used the value at the shortest mixing time of 10 ms. At such short mixing times, barely any cross-relaxation has occurred, and most of the intensity is present in the diagonal.

Knowledge of the longitudinal relaxation rate is required to fit the experimental data-set to Eq 4.2. However, it is not straightforward to determine this parameter from a nOE build-up curve as the dynam-
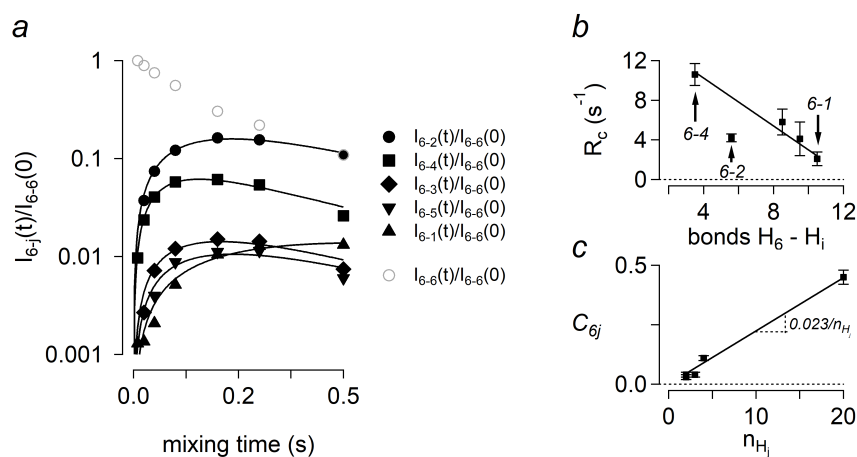
Figure 4.12: (a) nOE build-up curve for a MoS_2-lead oleate dispersion for mixing times ranging from 10 ms up to 500 ms for different resonances (markers). The solid lines represent fits to Equation 4.2 with fit parameters as listed in Table 4.3. (b) cross-relaxation rate R_C corresponding with the spin transfer from the polarized alkene resonance 6 to other resonances in the chain j as a function of the number of bonds between 6 and j. (c) Prefactor C as a function of the number of hydrogen nuclei of the resonance n_{H_j}.

ics are a function of both the cross-relaxation and the longitudinal relaxation rate (see Eq 4.2). For this purpose, we measured the T_1 relaxation rates for all the resonances in the lead oleate complex (see Appendix B.3.5 for the tabulated values). Such an analysis yielded values for R_L that vary between 0.6 s^{-1} and 2.5 s^{-1}, with the relaxation of the methyl group being the slowest. During fitting (to Eq 4.2), we allowed R_L to vary between these limits. We found that, apart from the cross peak associated with the methyl resonance (I_{6-1}), all resonances can be well-described with a fixed R_L of 2.5 s^{-1} and yield a set of fit parameters listed in Table 4.3. In Figure 4.12b, we map the cross-relaxation rate R_C, corresponding with the spin transfer from the polarized alkene resonance 6 to other resonances j in the chain, as a function of the number of bonds spaced between the alkene protons and the protons of resonance j. In line with intuition, polarization transfer happens faster to resonances in closer proximity to the alkene protons (*e.g.*, to the α-CH$_2$, see marker 6-4). Besides, the trend appears linear, a finding hinting at a cascade mechanism. As we expect a larger transfer to resonances that contain more hydrogen nuclei, we plot the pre-factor C_{6j} in Eq 4.2 to the number of hydrogen nuclei in resonance j. In this way, we obtain a linear plot with a slope of 0.023, corresponding with a transfer of 2.3% per hydrogen nuclei or a total polarization transfer of 74%. Note that this value agrees well with the sum of the pre-factors listed in Table 4.3. Although these numbers are slightly lower than the predicted value of 94%, their high value suggests that every ligand in the dispersion contributes to the negative nOE build-up while lead oleate rapidly exchanges between a free and a bound state during the mixing phase.

4.4.4 Comparison between Oleylamine and Lead Oleate

NOESY spectra for both ligands have been measured at identical mixing times of 300 ms. Such spectra suggested larger polarization transfers, evidenced by more intense off-diagonal peaks, in case of lead oleate (Figure 4.11d) compared to oleylamine (Figures 4.9c). Following the line of thought presented in section 4.4.3, the ratio of the integrated off-diagonal to the diagonal resonances $I_{ij}(300\text{ms})/I_{ii}(300\text{ms})$, provides a means to compare the relative binding strength of both ligands to the MoS$_2$ surface. In this respect, we integrate the diagonal alkene resonance and each off-diagonal cross peak, which yields respective the intensities $I_{6-6}(300\text{ms})$ and $I_{6-i}(300\text{ms})$. Finally, the

ratio $I_{6-i}(300\text{ms})/I_{6-6}(300\text{ms})$ yields a value that is roughly 23 larger in case lead oleate which might suggest a 23 times stronger relative binding strength of lead oleate compared to oleylamine.

4.4.5   Conclusion

An NMR toolbox analysis and a more detailed analysis using nOE build curves ambiguously showed that lead oleate is dynamically interacting with the surface, fastly exchanging between a free and a bound state. Due to the dynamic nature of such a bond, stable dispersions could only be obtained in the presence of an excess of the lead oleate complex. Nonetheless, by supplying an excess of a metal carboxylate that acts as a Lewis acid, we can stabilize MoS_2 NCs in more-conventional and apolar solvents such as toluene.

4.5   Solubility Parameter Matching

4.5.1   Observations and Hypothesis

We pointed out that progressive purification of the as-synthesized MoS_2 NCs leads to rapid aggregation in apolar solvents, and we ascribed this behavior to highly dynamic ligand passivation (section 4.3). The supply of an excess of a metal carboxylate salt, acting as a Lewis acid, offered stability, yet the stabilization was again highly dynamic (section 4.4). Certainly, such behavior would hamper the post-processing of MoS_2 and colloidal 2D TMDs in general.

In this respect, two additional observations are worth mentioning here. For one thing, redispersion of MoS_2 in *o*-dichlorobenzene resulted in stable dispersions with little to no sedimentation over time. Also, after a routine purification cycle involving the removal of the native reaction mixture by centrifugation and two additional washing steps with ethanol, we were able to redisperse the MoS_2 pallet in polar solvents under mild sonication. For instance, MoS_2 dispersed in N,N-dimethylformamide, a common exfoliation solvent (*vide supra*), forms stable colloids for months. These observations contrast the behavior of nanocrystals synthesized in an apolar reaction mixture by hot-injection. For instance, 2D CdSe nanoplatelets packed with organic surfactant molecules are most stable in cyclohexane,[226, 235] while QDs are usually dispersed in hexane or toluene.[205] Additionally, a nanocrystal transfer from an apolar to a polar solvent typically

involves the laborsome exchange of the native apolar surfactant layer to a polar ligand shell using a two-phase system.[236]

Conceivably, these observations point to a similar stabilization mechanism as we used to exfoliate bulk ReS_2 crystals in layered ReS_2 colloids in chapter 3. Here, we interpreted conditions for high yield exfoliations of ReS_2 as a matching of the solvent and the ReS_2 solubility parameter. In another study, Cunningham *et al.*[112] estimated the solubility parameter of bare MoS_2 as $\approx 22\,\mathrm{MPa}^{1/2}$ by screening LPE in a wide range of solvents. Interestingly, *o*-dichlorobenzene has a closely matching solubility parameter ($20.5\,\mathrm{MPa}^{1/2}$) to the one of a bare MoS_2 surface. On the other hand, typical apolar solvent solubility parameters range from $15 - 18\,\mathrm{MPa}^{1/2}$ and match those of usual apolar surfactant molecules used in hot-injection syntheses.[237]

In this respect, the question stands out as to whether the concepts developed for rational liquid-phase exfoliations transfer nanomaterials synthesized through hot-injection.

4.5.2   Outline of the Experiment

We pursue a similar approach as in chapter 3. First, we purify the MoS_2 colloid through a regular purification cycle (2 washing cycles), we disperse the precipitated MoS_2 pallet in a series of solvents with known solubility parameters (Figure 4.13, step a). We rationally chose solvents with diverse solubility parameters in the range of ≈ 15 to $30\,\mathrm{MPa}^{1/2}$. We included the most common *nanocrystal* solvents (*e.g.*, hexane, cyclohexane, chloroform, toluene) and non-solvents (*e.g.*, acetonitrile, ethanol, methanol) in our study. Besides, we incorporated typical solvents known to result in high yield exfoliations (*e.g.*, NMP, DMF, butanol), see chapter 3. Next, we solubilize the resulting mixtures under mild sonication in a bath sonicator (Figure 4.13, step b). We leave the dispersions untouched for 48 hours, and subsequently, we carefully separate the supernatant from the sediment (Figure 4.13, step c) for visual inspection and quantitative analysis by UV-vis spectroscopy. We refer to Appendix A.2 for a more detailed description of the experimental procedure, and Table A.2 for a full solvent list.
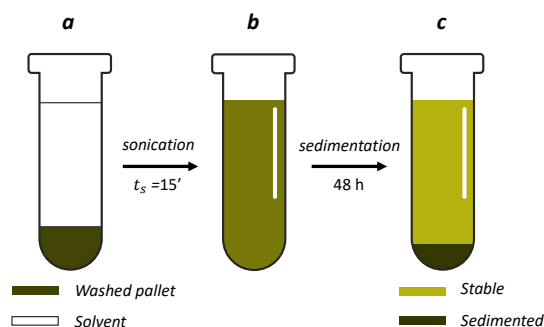
Figure 4.13: Schematic representing the outline of the experiment.

4.5.3 Visual Inspection and Basic Quantitative Analysis

After sonication (Figure 4.13, step b), we immediately notice that MoS_2 rapidly aggregates in hexane and methanol, solvents with the smallest and largest δ_s, respectively. In other solvents, clear sedimentation occurs within hours, yet a colored supernatant is still visible after 48 hours. As already stated, dispersions in o-dichlorobenzene are stable without any visible sedimentation.

For a visual inspection after 48 hours, we carefully decant the supernatant from the sediment and arrange the supernatants of the dispersions from a small to a large solubility parameter in Figure 4.14a. For a better visual comparison, we dilute each supernatant further in the same manner. In this way, we distinguish three regimes in agreement with the solubility parameter of the solvent. As MoS_2 rapidly aggregated in aliphatic hydrocarbons with the smallest solubility parameter, such solvents result in optically transparent to nearly transparent supernatants. Strikingly,, those are common laboratory solvents to disperse NCs. The same holds for solvents with the largest solubility parameter, such as ethanol and methanol. In contrast, colored dispersions are obtained in solvents with an intermediate solubility parameter.

As stated in chapter 3, UV-vis spectroscopy allows us to compare dispersions in different solvents quantitatively. Hence, we record the attenuance D of MoS_2 in each dispersion after sonication (step b)
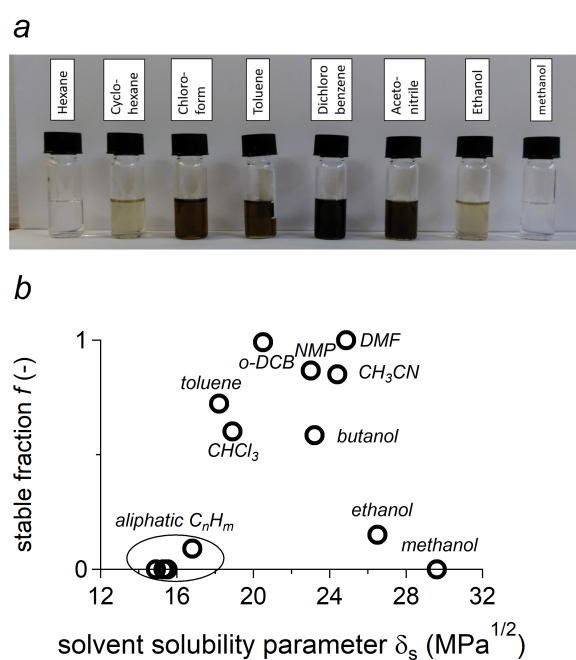
Figure 4.14: (a) Photograph of the supernatant of colloidal MoS_2 flakes dispersed in solvents with an increasing solvent solubility parameter after 48 hours of standing. (b) Plot of the stable fraction after 48 hours f (attenuance after 48 hours normalized by the initial attenuance after sonication) as a function of the solvent solubility parameter δ_s. The different solvents are marked.

and after 48 hours (step c). As a metric for the dispersion stability, we use the ratio of D after 48 hours by the initial attenuance. We denote this metric as f. As higher energy transitions are typically less influenced by size quantization effects, we use the attenuance at 400 nm. Given this definition, $f = 0$ characterizes a *non-solvent* (100% sedimentation), and values for f close to 1 are distinctive for stable dispersions.

Figure 4.14b summarizes this analysis's main result by plotting f for each MoS$_2$-solvent combination as a function of the solvent solubility parameter. In line with the visual inspection, we record low values for f in low and high δ_s solvents, and f approaches 1 for intermediate δ_s solvents with solubility parameters at around $20 - 25 \, \mathrm{MPa}^{1/2}$. The distribution appears Gaussian in shape – as predicted by solution theory – and appears to reach a maximum at a position in-between the experimental data points of *o*-DCB and NMP. Applying the weighted arithmetic mean (Eq 3.1) to the recorded data, the average solubility parameter of synthesized MoS$_2$ measures $21.5 \, \mathrm{MPa}^{1/2}$.

4.5.4 Analysis within Solution Theory

Equilibrium solute concentration as a function of the solubility parameter δ Following the line of thought presented in Chapter 3, we rely on regular solution theory that predicts a Gaussian dependence of the equilibrium solute concentration C on the difference in solubility parameters between the solvent δ_s and the solute δ_0:

$$C \propto \exp\left(-\frac{\bar{v}}{kT}(\delta_s - \delta_0)^2\right) \tag{4.3}$$

Fitting a Gaussian function to the experimental data in Figure 4.15a, yields a value for δ_0 of $21.5 \pm 0.3 \, \mathrm{MPa}^{1/2}$. The optimal MoS$_2$ solubility parameter determined by solution theory agrees well with the weighted arithmetic mean determined above. Most important, this number corresponds with the reported solubility parameter of liquid-phase exfoliated MoS$_2$[112] ($22 \, \mathrm{MPa}^{1/2}$, see Table 4.4) stabilized only by solvent interactions, *i.e.*, in the absence of surfactant molecules. Importantly, the fact that remaining ligands in the dispersion hardly influence the physicochemical properties of the surface agrees well with the NMR experiments conducted earlier.

As the Gaussian fit function has a fwhm of $6.5 \pm 0.8 \, \mathrm{MPa}^{1/2}$, MoS$_2$ has a solute volume $\bar{v}$ of $2.7 \times 10^{-22} \, \mathrm{cm}^3$. Once more, this result

	δ_0 $(MPa^{1/2})$	fwhm $(MPa^{1/2})$
colloidal MoS_2	21.5 ± 0.3	6.5 ± 0.9
exfoliated MoS_2[112]	22.0	6.5

Table 4.4: Summary of the through solution thermodynamics and comparison with literature values listed in Reference 112.
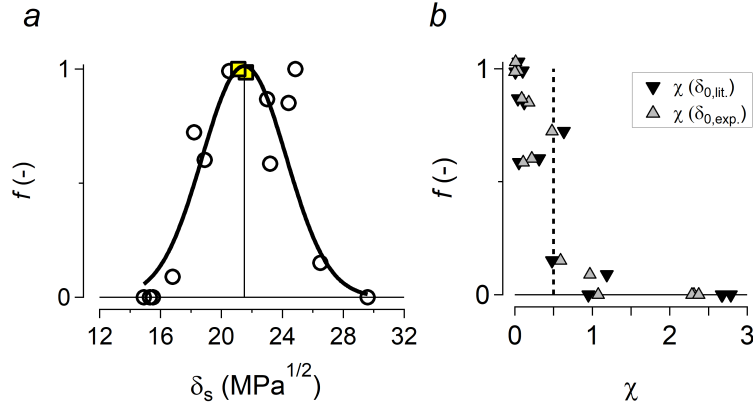
Figure 4.15: (a) Plot of f as a function of δ_s. The solid line is a fit to Eq 4.3. The yellow squares mark solvents with a δ_s close to δ_0, and were used to validate the model (b) f plotted against χ.

agrees well with reports on LPE MoS_2[112] (fwhm $= 6.5\,MPa^{1/2}$). As stated earlier, this value strongly underestimates the volume of the dispersed material. Considering the excellent agreement between materials prepared by two very different methods with different architectures, this observation hints at similar underlying physicochemistry. From this perspective, we address this conundrum in sufficient detail in chapter 5.

Equilibrium solute concentration as a function of the exchange parameter χ In a similar way, we can relate the equilibrium solute concentration C to the exchange parameter χ.

First, we calculate the exchange parameter according to Eq 2.8 for each data point and summarize those values in Figure 4.15b. As a

value for the solute solubility parameter, we either used the number we determined earlier according to Eq 4.3 ($\delta_0 = 21.5 \, \mathrm{MPa}^{1/2}$) (grey markers) or the parameter of exfoliated MoS_2 reported by Cunningham[112] ($\delta_0 = 22 \, \mathrm{MPa}^{1/2}$) (black markers). In both cases, the trend encodes similar information and agrees with the predictions made by solution theory as discussed below. As low values for χ are associated with a favorable energetic cost of mixing, f converges to 1 in small χ solvents and plunges steadily to 0 in large χ solvents. Conspicuously, the solubility of MoS_2 plunges when χ exceeds 0.5. Similar behavior has been observed in polymer solutions – an observation that we address at length in the next chapter.[155]

4.5.5 Validation using Optimal δ Solvents

A prerequisite to any successful model is its predictability. Based on the results outlined above, we expect that MoS_2 forms stable dispersions in solvents with solubility parameters of approximately $21.5 \, \mathrm{MPa}^{1/2}$. Using the Hansen database,[165] we identified pyridine[2] ($\delta_s = 21.5 \, \mathrm{MPa}^{1/2}$) and 1-methylnaphthalene ($\delta_s = 21.1 \, \mathrm{MPa}^{1/2}$) as potential candidates; we marked those solvents with yellow squares in Figures 4.15a. Most importantly, both solvents result in stable dispersions without any noticeable sedimentation after 2 days ($f \approx 1$),[3] and thereby follow the predictions made by solution theory. We believe that these results strongly validate our approach.

4.6 Conclusion

Starting from a series of observations, supplemented by extensive analysis, we extended the solution thermodynamics approach to colloidal TMD systems. In doing so, we touched upon a series of topics, starting with the synthesis of MoS_2 by colloidal chemistry (section 4.2). In this respect, we carried out a detailed analysis of the reaction product using a combination of UV-Vis absorbance spectroscopy, Raman spectroscopy, XRD, TEM, and AFM. By combining these tools, we assessed that the synthesized MoS_2 flakes contained 3

---

[2]Besides providing thermodynamic stabilization, pyridine might also provide additional steric stabilization as has been previously observed in case of CdSe quantum dots.[228]

[3]While dispersions in 1-methylnaphthalene are still stable after a month of storage, disperions in pyridine appear to sediment faster over time.

monolayers on average and adopted the 2H semiconducting phase – the desired phase for optoelectronic applications.

Starting from the empirical observation that the MoS_2 dispersions were colloidally unstable, we first studied their surface by NMR spectroscopy (section 4.3). Combining 1D and 2D NMR techniques, we observed that ligands are not tightly bound to the MoS_2 surface yet engage in a dynamic adsorption/desorption equilibrium, exchanging between a free and a bound state. Accordingly, we concluded that this behavior is likely to cause their limited colloidal stability in conventional solvents, such as hexane and toluene. Based on their crystal structure, which features extended sulfur planes, we speculated that soft metal complexes might stabilize the dispersions through adhesion by donor-acceptor interactions (section 4.4). While supplying a metal salt in excess stabilized the dispersions in conventional solvents, removing the excess by a standard sequence of successive precipitation and redispersion easily destabilized the colloid. By NMR spectroscopy, we again interpreted these observations as a manifestation of dynamic ligand interaction.

Reasoning from the observation that the stability is heavily dependent on solvent choice, we screened the stability of colloidal MoS_2 NCs in a wide range of solvents (section 4.5). Similar to our work on the LPE of ReS_2 in chapter 3, we show that this behavior can be understood from solution thermodynamics, where the solubility parameter of the solvent is a successful descriptor to predict the *solubility* of colloidal MoS_2 NCs. The ensuing matching of the solubility parameter enabled us to compare colloidal MoS_2 to MoS_2 produced by LPE. The excellent agreement between materials produced by very different methods underscored that the stability of synthesized flakes correlates with the energy of mixing of the flakes/solvent mixture, rather than being an effect of electrostatic ligand repulsion. These findings complemented our NMR analyses, which demonstrated ligands with a minimal affinity toward the NC surface, engaged in a highly dynamic adsorption/desorption equilibrium. Notably, these findings contrasted other low-dimensional systems synthesized by hot-injection where steric/electrostatic ligand repulsion is the main driving force that prevents aggregation. As a result, colloidal MoS_2 NCs are stable in solvents with higher solubility parameters than those typically used to disperse NCs prepared by hot-injection. Suitable solvents resulting from this include aromatic solvents with polar groups, such as *o*-dichlorobenzene, or even polar aprotic solvents, such as DMF.

We thus conclude that hot-injection yields MoS$_2$ NCs with comparable interfaces as those produced by LPE. This finding might offer the prospect of using established procedures developed for LPE nanomaterials to post-process TMD dispersions as processable inks.

5

Why is Exfoliation of Van der Waals Layered Solids Possible in a Broad Spectrum of Solvents?

"I understand HOW. I do not understand WHY." – George Orwell, 1984

Experimental data on various 2D materials, including our experimental studies in chapters 3 and 4, suggest that exfoliation is possible in a much broader range of solvents than solution theory seemingly predicts. With knowledge about top-down and bottom-up systems at hand, we attempt to describe these findings from a thermodynamic perspective. Derived from Flory-Huggins theory, we introduce a straightforward criterion that judges suitable exfoliation solvents for liquid-phase exfoliation and colloidal stability based on their exchange parameter.

Author Contributions

The findings in this chapter are currently under review:

A Thermodynamic Perspective on the Broad Solvent Window for Liquid Phase Exfoliation of Two Dimensional Van der Waals Solids Schiettecatte, Pieter; Hens, Zeger.

P.S and Z.H. discussed the results and wrote the manuscript together.
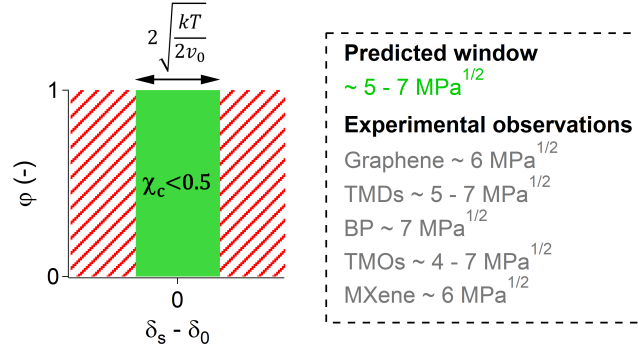
Figure 5.1: Overview of Chapter 5.

5.1 Introduction

Over the past years, studies on organic and inorganic layered nanomaterials demonstrated that liquid-phase exfoliation could be described within a solution thermodynamics framework.[101–103, 109, 112] This approach interprets high-yield exfoliation and the formation of stable colloids of exfoliated flakes in terms of the energy of mixing of the flakes/solvent mixture. The main prediction of solution thermodynamics is that exfoliation works best when the solubility parameter of the solvents and the exfoliated flakes match, a point that found ample experimental support in the literature on liquid-phase exfoliation. On the other hand, several studies highlighted that the set of good exfoliation solvents corresponds to a solubility parameter window that is considerably larger than solution thermodynamics would allow based on the size of the dispersed, exfoliated flakes. For example, strong discrepancies between theory and experiment have been described for carbon-based nanomaterials,[164] layered transition metal dichalcogenides,[112] and layered oxides.[188] In all those studies, the good exfoliation solvent window would correspond to solute volumes of $\approx 10^{-22}$ cm^3, which can be up to 5 orders of magnitude smaller than the dispersed colloid volume. In this regard, the question arises whether such experimental results can be reconciled with solution theory, and, if yes, what thermodynamic quantities would effectively describe the experimental window of good exfoliation solvents.

To address these points, we first list our experimental observations and complement those with relevant literature data (section 5.2).

Next, we derive the most commonly applied equilibrium condition, which builds on Flory-Huggins theory to express the fraction of dispersed or exfoliated material as a Gaussian function of the solubility parameter difference, and links the width of the Gaussian to the volume of an individual dispersed flake (section 5.3). In particular, we point out certain spurious approximations, and we debate the use of this relation. Lastly, based on Flory-Huggins theory, we introduce the critical exchange parameter χ_c as a metric for good exfoliation solvents (section 5.4). Reasoning from this perspective, we answer the question *why exfoliation is possible in such a broad spectrum of solvents*, and we argue that experimental data acquired on different classes of 2D materials are in excellent agreement with our assessment.

5.2 Experimental Observations and Literature Survey

When optimizing the liquid phase exfoliation of a Van der Waals solid, a typical first step has become the analysis of the exfoliation yield for a range of solvents with different solubility parameters δ_{sol}. The outcome of such screening studies is then represented by plots showing the amount of material obtained after exfoliation as a function of δ_{sol}. Such experiments showed that liquid-phase exfoliation works best for solvents within a limited range of solubility parameters for very different materials. A common interpretation of this outcome is based on solution thermodynamics,[101, 112, 178, 183, 188, 238–243] through the statement that the equilibrium concentration of a solute B is a Gaussian function of the difference in solubility parameter of the solvent and the solute:[112, 113, 164]

$$[B] \propto \exp\left(-\frac{\bar{v}}{k_B T}(\delta_B - \delta_{sol})^2\right) \tag{5.1}$$

Here, $\bar{v}$ stands for the solute's unit volume, *i.e.*, the exfoliated flakes or tubes. According to Eq 5.1, the concentration of exfoliated flakes will peak when the solubility parameters δ_{sol} and δ_B match, a condition we will refer to as solubility parameter matching.

Table 5.1 and Figure 5.2 provide an overview of different materials of which exfoliation has been analyzed using the solution-thermodynamics approach. Clearly, a broad range of materials
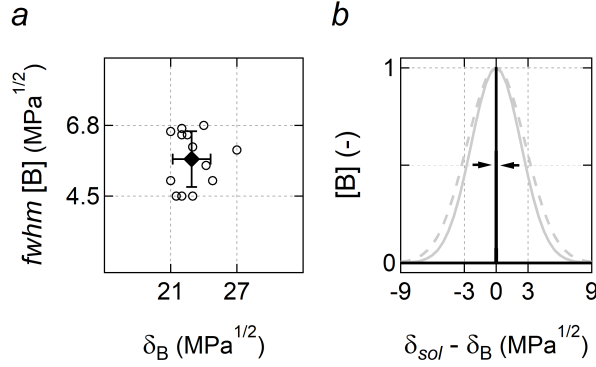
Figure 5.2: Overview of the literature survey of experimental observations. (a) Scatter plot summarizing the literature survey, the open circles are individual data points as listed in Table 5.1 and the filled square plots the sample mean. (b) Plots of the equilibrium solute concentration [B] as a function of the difference in solubility parameters between solvent δ_{sol} and solute δ_B. The grey lines mark the Gaussian using fits for (solid line) ReS_2 (chapter 3) and (dashed line) MoS_2, compared to (black line) a reconstructed Gaussian using the hypothetical volume of a disc with the dimensions listed in the main text.

has been covered, including graphene,[177] graphene oxide,[244] black phosphorous (BP),[238] transition metal dichalcogenides (TMDs),[100, 112, 239] transition metal oxides (TMOs)[240–242] and MXenes.[243] Moreover, despite major differences in elemental composition, crystallography, and morphology, these layered compounds showed good exfoliation in similar solvents, with matching solubility parameters in the range $21 - 27 \, \mathrm{MPa}^{1/2}$. On the other hand, stable dispersions of exfoliated flakes could be systematically obtained in solvents with solubility parameters deviating roughly $\pm 3 \, \mathrm{MPa}^{1/2}$ from the matching condition. This point was evidenced in many studies by plots of the dispersed amount of exfoliated material as a function of δ_{sol}, which could be fitted to a Gaussian having a full-width-at-half-maximum (fwhm) in the range $4.5 - 6.8 \, \mathrm{MPa}^{1/2}$ for the different materials analyzed, with an average of $5.7 \, \mathrm{MPa}^{1/2}$.

Referring to Eq 5.1, a good exfoliation solvent window of $6 \, \mathrm{MPa}^{1/2}$ corresponds to solute volumes $\bar{v}$ of the order $10^{-22} \, \mathrm{cm}^3$. However, approximating a single TMD flake as a disc of 100 nm in diameter and 2.5 nm in thickness, the solute volume would rather amount to

	δ_{B} $(\mathrm{MPa}^{1/2})$	[B] fwhm $(\mathrm{MPa}^{1/2})$	reference
ReS_2	24.2/24.9	5.5^a	Ch. 3
c-MoS_2	21.5	6.5^a	Ch. 4
MoS_2	22	6.5^a	Ref. 112
WS_2	21.5	4.5^a	Ref. 112
GeS	23	4.5^b	Ref. 239
$MoSe_2$	22.5	6.5^a	Ref. 112
$MoTe_2$	21	5^a	Ref. 112
Graphene	23	6.1^b	Ref. 177
rGO	22.0	4.5^c	Ref.244
GO	25.4	NA	Ref.244
MoO_2	22	6.7^b	Ref. 240
V_2O_5	24	6.8^b	Ref. 242
MnO	24.8	4.1^a	Ref. 241
BP	21	6.6^b	Ref. 238
$Ti_3C_2T_x$	27	6.0^b	Ref. 243
$\bar{x} \pm s$	22.9 ± 1.7	5.7 ± 0.9	

Table 5.1: Overview of the literature survey of experimental observations. Tabulated values for (second column) optimal solubility parameter of the layered compound δ_{B}, (third column) good solvent window as characterized by the fwhm of the Gaussian fit functions. [a] reported by the authors, [b] values extracted from fits reported by the authors, [c] values extracted by fitting the reported dataset to a Gaussian function.

2×10^{-17} cm^3 – five orders of magnitudes larger than expected based on the good exfoliation window. To highlight the underlying issue, we used a flake volume of 2×10^{-17} cm^3 to predict the dependence of [B] on δ_{sol} by means of Eq 5.1. As shown in Figure 5.2b, the thus obtained Gaussian has a fwhm of a mere 0.2 MPa$^{1/2}$. This result would suggest that liquid phase exfoliation is only possible in an extremely tight range of solvents, a prediction at odds with the overview given in Table 5.1, and with the experimental data added to Figure 5.2b for comparison. This conundrum has already been identified in the literature,[112, 164, 188] but no attempts to reconcile the successful identification of solubility parameter matching with the failure to predict the width of the good exfoliation window by solution thermodynamics were made.

5.3 Describing Liquid Phase Exfoliation Through Solution Thermodynamics

Eq 5.1 underlies the identification of solubility parameter matching as the central requirement of good exfoliation solvents. One obtains this expression starting from the assumption that Flory-Huggins theory provides an apt description of the free energy of the dispersion of the exfoliated flakes – referred henceforth as the exfoliated colloid – and that the exfoliated colloid is in physical equilibrium with the to-be-exfoliated material. Following this idea, we first derive conditions for physical equilibrium (section 5.3.1) and apply those conditions within the framework of a Flory-Huggins lattice model (section 5.3.2).

5.3.1 Physical Equilibrium between Two Phases

Physical equilibrium refers to systems whose composition can change by exchanging components between the different phases of the system. In other words, it deals with equilibrium phenomena that do not involve chemical reactions. Generally, we can derive equilibrium conditions at constant pressure and constant temperature, or at constant volume and constant temperature. As lattice models are typically derived at a constant volume, we describe the system under volume-temperature control. As such, equilibrium is reached when the (Helmholtz) free energy F of the system is minimal

$$(dF)_{V,T} = 0 \tag{5.2}$$
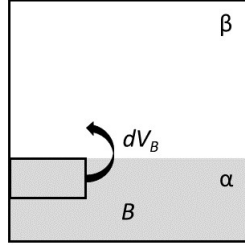
Figure 5.3: Schematic representation of physical equilibrium.

In the most simple case, we will assume a system containing a single component B. As shown in Figure 5.3, component B can exchange between two phases α and β. For instance, phase α can represent the pure substance B (*e.g.*, a solid powder), and β can represent B in solution. The free energy of such a system is the sum of the free energy of B in each separate phase ($F_B = F_{B,\alpha} + F_{B,\beta}$). In such a way, the transfer of a volume V_B from α to β (see Figure 5.3) changes the free energy ($dF_B = dF_{B,\alpha} + dF_{B,\beta}$) such that we can write at equilibrium

$$\frac{\partial F_B}{\partial V_B}dV_B = \frac{\partial F_{B,\alpha}}{\partial V_B}dV_{B,\alpha} + \frac{\partial F_{B,\beta}}{\partial V_B}dV_{B,\beta} = 0 \qquad (5.3)$$

For a closed system kept at constant volume, and in the absence of chemical changes, $V_{B,\alpha}$ equals $-V_{B,\beta}$, and equilibrium is expressed as a matching of the partial derivatives of F_B to V_B in each separate phase

$$\frac{\partial F_{B,\alpha}}{\partial V_B} = \frac{\partial F_{B,\beta}}{\partial V_B} \qquad (5.4)$$

Importantly, this equilibrium condition can be extended towards systems containing multiple components. Fof binary mixtures AB, the equilibrium conditions are retrieved by solving the set of coupled differential equations for both components in the mixture according to

$$\begin{cases} \dfrac{\partial F_{B,\alpha}}{\partial V_B} = \dfrac{\partial F_{B,\beta}}{\partial V_B} \\[4mm] \dfrac{\partial F_{A,\alpha}}{\partial V_A} = \dfrac{\partial F_{A,\beta}}{\partial V_A} \end{cases} \qquad (5.5)$$

5.3.2 The Free Energy Within a Lattice Model Description

Referring to Figure 5.3**a**, the total free energy F_{tot} of a system consisting of (1) to-be-exfoliated material and (2) an exfoliated colloid can be written as

$$F_{tot} = F_\alpha + F_\beta = V_{B,\alpha}\mathcal{F}_B + V_{B,\beta}\mathcal{F}_B + V_{sol}\mathcal{F}_{sol} + \Delta_{mix}F(V_{sol}, V_{B,\beta}) \tag{5.6}$$

Here, $\mathcal{F}_B$ and $\mathcal{F}_{sol}$ are the free energy per unit volume of the to-be-exfoliated material and the solvent, respectively, whereas $V_{B,\alpha}$ is the volume of the to-be-exfoliated material, $V_{B,\beta}$ is the volume of the exfoliated flakes in the colloid and V_{sol} is the volume of the solvent. Furthermore, $\Delta_{mix}F(V_{sol}, V_{B,\beta})$ is the free energy of mixing of the exfoliated colloid, which can be written by means of Flory-Huggins theory as:

$$\Delta_{mix}F = \frac{k_B T}{v_0}\left(V_{sol}\ln\phi_{sol} + \frac{V_{B,\beta}}{\nu_B}\ln\phi_{B,\beta} + \frac{V_{sol}V_{B,\beta}}{V_\beta}\chi\right) \tag{5.7}$$

Here, v_0 is the volume occupied by an individual solvent molecule, ν_B is the ratio between the volume of a single solute particle and v_0, V_β is the sum of $V_{B,\beta}$ and V_{sol}, and χ is the so-called exchange parameter. In terms of the solubility parameters of the solvent and the solute, χ can be expressed as:

$$\chi = \frac{v_0}{k_B T}(\delta_{sol} - \delta_B)^2 \tag{5.8}$$

5.3.3 Physical Equilibrium Within a Lattice Model Approach

As stated by Eq 5.2 and Eq 5.3, physical equilibrium can be expressed through the requirement that F_{tot} is invariant under the transfer of an infinitesimal volume $dV_{B,\beta}$ from phase α to phase β. Inspecting Eq 5.6, the equilibrium condition in Eq 5.4 can be rewritten most concisely as

$$\frac{d\Delta_{mix}F}{dV_{B,\beta}} = 0 \tag{5.9}$$

Hence, by means of Eq B.5, we obtain that the following relation should hold at equilibrium (see mathematical detail below) that

$$k_B T\left(\chi\phi_{sol}^2 - \phi_{sol} + \frac{1}{\nu_B}\ln\phi_{B,\beta} + \frac{1}{\nu_B}\phi_{sol}\right) = 0 \tag{5.10}$$

For solutions of large particles ($\nu_B \gg 1$) with low solubility, Eq 5.10 reduces to

$$\chi - 1 + \frac{1}{\nu_B} \ln \phi_{B,\beta} = 0 \tag{5.11}$$

In that case, we indeed find that the volume fraction $\phi_{B,\beta}$ can be written as:

$$\phi_{B,\beta} \propto \exp\left(-\nu_B \frac{v_0}{k_B T}(\delta_{sol} - \delta_B)^2\right) \tag{5.12}$$

According to Eq 5.12, the volume fraction of exfoliated particles will be largest when the solubility parameter δ_{sol} and δ_B are equal, in line with the experimentally observed solubility parameter matching. However, as mentioned before, relating the width of the accessible solubility parameter window with $1/\sqrt{\nu_B v_0}$, Eq 5.12 strongly underestimates the experimental good exfoliation solvent window.

Considering Eq 5.10 in the limit $\nu_B \gg 1$, it follows that an equilibrium volume fraction $\phi_{B,\beta}$ is only obtained for cases where the exchange parameter exceeds 1. Indeed, since $\phi_{B,\beta}$ is a number between 0 and 1, solutions are only found when $\chi \phi_{sol}^2 - \phi_{sol}$ is a positive number, which can be the case as soon as $\chi > 1$. Therefore, Eq 5.12 will only apply under conditions of low solute solubility, related to a considerable solubility parameter mismatch. This is not the case when describing optimal exfoliation conditions in terms of solubility parameter matching; a condition that corresponds to an exchange parameter $\chi = 0$.

To explore a more consistent interpretation of liquid-phase exfoliation and the stability of exfoliated colloids based on solution thermodynamics, we return to the Flory-Huggins expression for the free energy of mixing of small solvent molecules and large solute particles (Eq B.5). This relation predicts that such systems will only exhibit a miscibility gap, and therefore a limited solubility of solute particles in a given solvent, when the exchange parameter exceeds a critical value χ_c as given by:

$$\chi_c = \frac{(1 + \sqrt{\nu_B})^2}{2\nu_B} \tag{5.13}$$

This point can be demonstrated by requiring that the second derivative and the third derivative of $\Delta_{mix}F$ to ϕ_B are zero simultaneously. One sees that for cases where $\nu_B \gg 1$, χ_c tends to a lower limit of 0.5. Moreover, under such conditions, the solubility of the solute in the solvent will become vanishingly small once χ exceeds 0.5. Taking

the above considerations into account, the link between solubility and
exchange parameter for the case $\nu_B \gg 1$ is better expressed in terms
of the critical exchange parameter χ_c as:

$$
\begin{cases}
\text{miscibility } (\phi_B = 1) & \text{if} \quad \chi < 1/2 \\
\text{immiscibility } (\phi_B \approx 0) & \text{if} \quad \chi > 1/2
\end{cases}
\tag{5.14}
$$

Mathematical detail: $\dfrac{\partial}{\partial V_{B,\beta}} \Delta_{\text{mix}} F$

$$
\begin{aligned}
\frac{\partial}{\partial V_{B,\beta}} \Delta_{\text{mix}} F &= k_B T \frac{\partial}{\partial V_{B,\beta}} \left(\chi \frac{V_{sol} V_{B,\beta}}{V_{sol} + V_{B,\beta}} + \frac{1}{\nu_A} V_{sol} \ln \left(\frac{V_{sol}}{V_{sol} + V_{B,\beta}} \right) \right. \\
&\quad \left. + \frac{1}{\nu_B} V_{B,\beta} \ln \left(\frac{V_{B,\beta}}{V_{sol} + V_{B,\beta}} \right) \right) \\
&= k_B T \left(\chi \frac{V_{sol}^2}{(V_{sol} + V_{B,\beta})^2} - \frac{V_{sol}}{\nu_A} \frac{V_{sol}}{(V_{sol} + V_{B,\beta})^2} \frac{V_{sol} + V_{B,\beta}}{V_{sol}} \right. \\
&\quad + \frac{1}{\nu_B} \ln \left(\frac{V_{B,\beta}}{V_{sol} + V_{B,\beta}} \right) \\
&\quad \left. + \frac{V_{B,\beta}}{\nu_B} \frac{V_{sol}}{(V_{sol} + V_{B,\beta})^2} \frac{V_{sol} + V_{B,\beta}}{V_{B,\beta}} \right) \\
&= k_B T \left(\chi \phi_{sol}^2 - \frac{1}{\nu_A} \phi_{sol} + \frac{1}{\nu_B} \ln \phi_{B,\beta} + \frac{1}{\nu_B} \phi_{sol} \right)
\end{aligned}
$$

5.4 The Critical Exchange Parameter as Determinant for the Exfoliation Window

In line with the idea that solution thermodynamics helps to under-
stand optimal exfoliation, we hypothesize that the condition for full
miscibility of the solvent/solute mixture as expressed by Eq 5.14 de-
scribes the good exfoliation solvent window. In that case, apt ex-
foliation solvents would be characterized by an exchange parameter
$\chi < 0.5$, whereas poor exfoliation solvents would yield exchange pa-
rameters outside of the full miscibility range. Given the relation be-
tween χ and the solubility parameters δ_{sol} and δ_B, this description
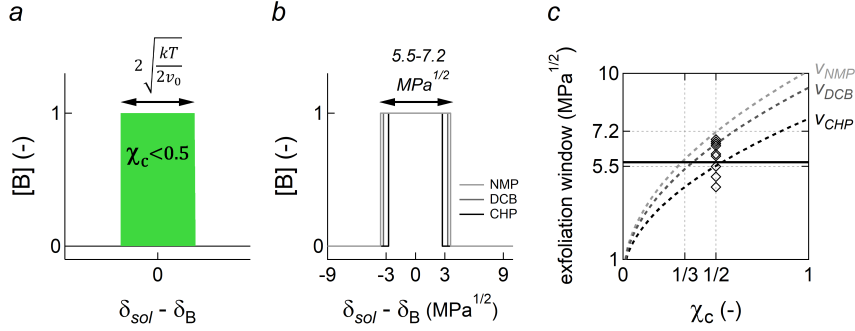
Figure 5.4: (a) Rectangular distribution calculated according to Eq 5.15 high-lighting that good exfoliation is possible within a solubility parameter range characterized by a width of $2\sqrt{k_BT/2v_0}$. (b) Rectangular distributions calculated for a set of common exfoliation solvents, including N-cyclohexyl-2-pyrrolidone (CHP),[161, 245] 1,2-dichlorobenzene (DCB)[118, 246] and N-methyl-2-pyrrolidone (NMP).[100, 101, 110] The plots span a solubility parameter window of $5.5\,\mathrm{MPa}^{1/2}$ to $7.2\,\mathrm{MPa}^{1/2}$ for solvents with molecular volumes ranging from $1.6\,10^{-22}\,\mathrm{cm}^3$ to $2.7\,10^{-22}\,\mathrm{cm}^3$. (c) The window for good exfoliation solvents was calculated for the solvents listed in panel b for different values of the exchange parameter χ_c. For comparison, we plotted (open circles) the individual data points and (black horizontal line) the average value of the literature survey in Table 5.1.

corresponds to a rectangular good exfoliation solvent window, the depends as follows on the solubility parameter mismatch:

$$
\begin{cases}
\phi = 1 & \forall \, \delta_s \in \left[\left(\delta_\mathrm{B} - \sqrt{\dfrac{k_BT}{2v_0}} \right), \left(\delta_\mathrm{B} + \sqrt{\dfrac{k_BT}{2v_0}} \right) \right] \\
\phi = 0 & \text{otherwise}
\end{cases}
\tag{5.15}
$$

As depicted in Figure 5.4a, good exfoliation and stable exfoliated colloids are expected according to Eq 5.15 under conditions where the solvent has a solubility parameter that deviates by less than $\pm\sqrt{k_BT/2v_0}$ from the matching condition $\delta_{sol} = \delta_\mathrm{B}$ or, equivalently, good exfoliation is possible within a solubility parameter range characterized by a width of $2\sqrt{k_BT/2v_0}$.

To validate the hypothesis that the critical exchange parameter outlines the good exfoliation solvent window, we calculated the rectangular distributions as predicted by Eq 5.15 for different exfoliation

solvents, as characterized by the molecular volume v_0. Figure 5.4b depicts such plots for a set of common exfoliation solvents that feature molecular volumes ranging from $1.6 \, 10^{-22} \, \mathrm{cm}^3$ to $2.7 \, 10^{-22} \, \mathrm{cm}^3$. As evident in Figure 5.4b, the boxcar plots span a solubility parameter window of $\approx 5.5 - 7.2 \, \mathrm{MPa}^{1/2}$. Returning to Table 5.1, one sees that such widths are consistent with the survey of experimental data acquired on a broad set of 2D materials, which yields an average width of $5.7 \pm 0.9 \, \mathrm{MPa}^{1/2}$. We thus conclude that the identification of the limits of the good exfoliation solvent window with solvent/solute combinations having an exchange parameter equal to the critical value for immiscibility yields a consistent interpretation of liquid phase exfoliation in terms of solution thermodynamics.

Considering the significant simplifications underlying the Flory-Huggins expression for the free energy of mixing of the solvent/solute mixture, the close correspondence between experimental exfoliation studies and predictions based on Eq 5.15 is quite remarkable. For example, the assumption that the total volume does not change upon mixing, or that mixing is a statistically random process, poses considerable issues for the description of solutions and blends of polymers by means of Flory-Huggins theory. To account for deviations such as volume changes and local packing effects, the exchange parameter is typically modified by the addition of a temperature-independent empirical constant.[155] Similar effects in the case of exfoliated colloids may be difficult to capture by the analysis introduced here. Given the relatively weak dependence of the solubility parameter window on the critical exchange parameter, any value of χ_c in the range $1/2$ to $1/3$ would make the average window width of $5.7 \pm 0.9 \, \mathrm{MPa}^{1/2}$ fit within the predicted width based on a range of solvents (see Figure 5.4c). On the other hand, Eq 5.15 suggests that, in particular local packing effects, could be studied through a temperature-dependent analysis of the good solubility window.

5.5   Conclusion

In this study, we addressed the question of the good exfoliation solvent window starting from an overview of literature data. Irrespective of the characteristics of the exfoliated material, we found that this good solvent window corresponds to a solubility parameter range of $4.5 - 6.8 \, \mathrm{MPa}^{1/2}$ around the optimal matching value. Next, we red-

erived the most commonly applied good exfoliation condition, which builds on Flory-Huggins theory to express the fraction of dispersed or exfoliated material as a Gaussian function of the solubility parameter difference, and links the width of the Gaussian to the volume of an individual dispersed flake. In doing so, we highlighted that this relation only applies when the Flory-Huggins free energy yields a miscibility gap between the solvent and the solute. Since any colloid of exfoliated material should be stable when solvent/solute mixtures are predicted to be stable at all compositions, we therefore introduced the critical exchange parameter $\chi_c = 0.5$ above which a miscibility gap arises as a metric for the experimental exfoliation window. Interestingly, we found that the resulting solubility parameter range corresponds closely to experimentally observed good exfoliation solvent windows. We therefore concluded that solution thermodynamics is apt to describe good exfoliation solvents, provided that the solubility parameter range is linked to the critical exchange parameter for solvent/solute immiscibility.

Part II

Probing Ultrafast Carriers in Few-Layer Molybdenum Disulfide & Rhenium Disulfide

6

Probing Carrier & Optical Nonlinearities by Pump-Probe Spectroscopy

6.1 Introduction

For several millennia, we have been limited by the response time of our senses. Processes happening beyond the blink of an eye were simply immeasurable, and anything faster than tens of milliseconds was perceived as a continuous motion.[1] Rapid technological changes starting in the 19$^{\text{th}}$ century surpassed our senses' natural limitations and offered the tantalizing opportunity to freeze a continuous motion as a sequence of discrete frames.

In this respect, the development of high-speed photography and time-resolved spectroscopy are cases in point. Using a complex arrange-

---

[1] The response time of the eye is $\approx 50\,\text{ms}$ or 20 Hz.

ment of high-speed cameras with short millisecond shutter times, Eadweard Muybridge (1878) captured the slow-motion of a galloping horse and resolved the conundrum of whether all four hooves were lifted during the gallop (Figure 6.1).[247] The experiments conducted by Muybridge pointed out that an even faster probe is needed to resolve a seemingly continuous motion. Merely two decades later, Abraham and Lemoine (1899) pioneered the *pump-probe* measurement principle.[248] In an experiment with carbon disulfide, they used two synchronized light pulses. An optical *pump* excitation induced a change in the refractive index of carbon disulfide, and a delayed *probe* pulse measured the photo-induced change.
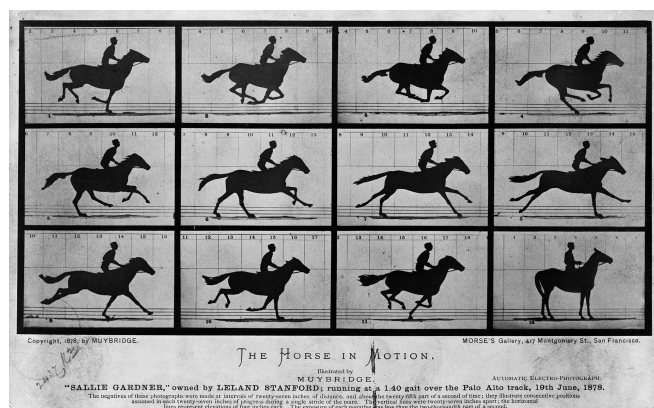
Figure 6.1: Sequential series of photographs taken by Muybridge of a horse at Stanford's Palo Alto Stock Farm. The shutters of 12 cameras set along the race track were automatically triggered when a horse tripped the wires connected to a circuit.

Continuous improvements in electronics gradually shifted the experimental time resolution in pump-probe measurements from milliseconds to the microseconds[2].[249] The largest paradigm shift coincides with the invention of the laser in the 1960s,[250] shortening the *arrow of time* to the nanosecond,[251] picosecond,[252] and femtosecond[253] regime. With the development of solid-state Ti-sapphire lasers in 1991,[254] chemists and physicists were finally able to venture a century-old dream and visualize the motion within atoms, molecules, and solids with femtosecond precision.

---

[2]The experimental resolution is limited by the duration of the pulse.
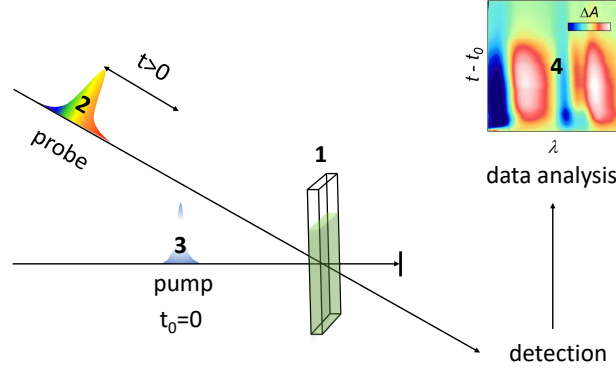
Figure 6.2: Schematic depicting the principles behind ultrafast pump-probe spectroscopy.

6.2   White-Light Pump-Probe Spectroscopy

Modern transient absorbance spectroscopy (TAS), and white-light pump-probe spectroscopy in general, is conceptually not very different from the pioneering experiments conducted by Abraham and Lemoine. We illustrate pump-probe spectroscopy in Figure 6.2. A material (**1**) is pumped with an ultrafast laser pulse (**2**), thereby inducing a change in the the material's absorbance. A delayed probe pulse (**3**) monitors changes in absorbance ΔA. Photo-induced changes, and, to a certain extent, the *motion* of photo-excited carriers, are mapped by tracking changes in the differential absorbance ΔA as a function of time and wavelength/energy (**4**).

Figure 6.3 provides a schematic of the TAS setup available at our facilities in PCN. We record transient absorbance spectra by exciting dispersions (**7**) using 110 femtosecond pump pulses with variable wavelengths. Pump pulses are created from the 800 nm fundamental of a 1 kHz Ti:sapphire laser system (**1**) (Spitfire Ace, Spectra Physics) through non-linear conversion in an OPA (**2**) (Light Conversion, TOPAS). We vary the pump's photon flux through a neutral density wheel (**3**) and determine the photon flux using a Thorlabs CCD camera beam profiler and a thermal power sensor. Probe pulses in the visible and near-infrared window are generated by passing the
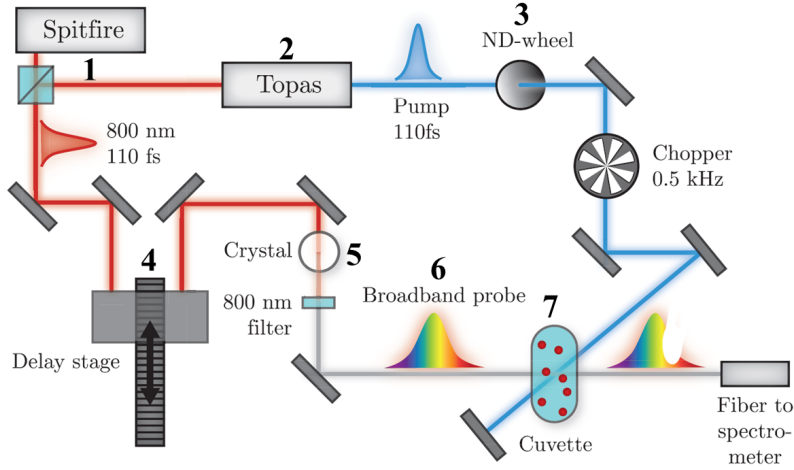
Figure 6.3: Schematic of the ultrafast TAS setup available at PCN.

800 nm fundamental through a thin CaF_2 and YAG crystal (**5**), respectively.[3] The spectral density of the pump pulses is in the order of µJ/nm. The probe pulses, on the other hand, are several orders less intense and fall in the order of pJ/nm. The pulses are delayed relative to the pump using a mechanical delay stage (**4**) with a maximum delay of 6 nanoseconds. In our experiments, the probe spectrum (**6**) covers the UV-Vis window from 350 nm up to 700 nm and the near-infrared window from 850 nm up to 1300 nm.

6.3   Pump-Induced Optical Nonlinearities

6.3.1   Introduction

The creation of charge carriers after pump excitation alters the absorption of a semiconductor, leading to distinct pump-induced optical

---

[3]Broadband probe pulses are generated through the mechanism of white-light continuum (WLC) generation. White light is generated when a high-intensity (monochromatic) light source is focused on a transparent medium.[255] Both the efficiency of the process and resulting spectra depend critically on the bandgap E_g of the medium.[256] Generally, larger bandgap media result in higher energy probes. We used calcium fluoride ($E_g \approx 12$ eV) for the generation of visible probe pulses and YAG ($E_g \approx 7$ eV) for near-IR probe pulses.

nonlinearities. Understanding how characteristic features in the differential absorbance can be assigned to typical nonlinearities observed in semiconductors will prove essential in Chapters 7 and 8.

Omitting a mathematical description, we opt for a simplified picture and consider a semiconductor with a parabolic valence band (VB) and conduction band (CB), and a free particle band-gap $E_0 = E_c - E_v$. We describe the ground-state absorption between CB and VB states by a simple Gaussian absorption profile A_0. The absorption is centered around E_0 and is characterized by a linewidth Γ (Figure 6.4a). For instance, Γ can represent the homogeneous line broadening of an optical transition due to its finite lifetime.

6.3.2   Interband Bleach and Intraband Absorption

Interband bleach   In the simplest case, photo-excitation with energies exceeding E_0 generates VB-holes and CB-electrons. After cooling, these charge carriers at the band edges (Figure 6.4b) *bleach* the absorption by filling states. As the density of states (DOS) is finite, the occupation of CB or VB states by a population of electrons or holes reduces the absorption at the band-edges. As depicted in Figure 6.4b, the effect of state-filling is reflected in a negative differential absorbance ΔA, or a *bleach*, at the position of the transitions connecting the CB minimum or VB maximum.

Intraband absorption   Alternatively, the accumulation of CB electrons and VB holes at local band minima/maxima opens additional absorption channels within a band. As a photon has no momentum ($k=0$), intraband absorption in bulk semiconductors involves the coupling to phonons (see Figure 6.4c, top) and therefore typically results in low transition probabilities. Yet, for low-dimensional structures, size quantization is known to relax k-selection rules, enhancing the transition probability of intraband absorption.[257] Importantly, such a process can only occur in the excited-state and yields a net positive ΔA or photoinduced absorption (PA) (Figure 6.4c, bottom).

6.3.3   Linewidth Broadening

The linewidth of an optical transition tends to broaden after photo-excitation. In a simple absorption picture, an increased carrier density decreases the time $\Delta\tau$ between particle collisions (see pictorial representation in the top panels of Figure 6.5). An increase in scattering
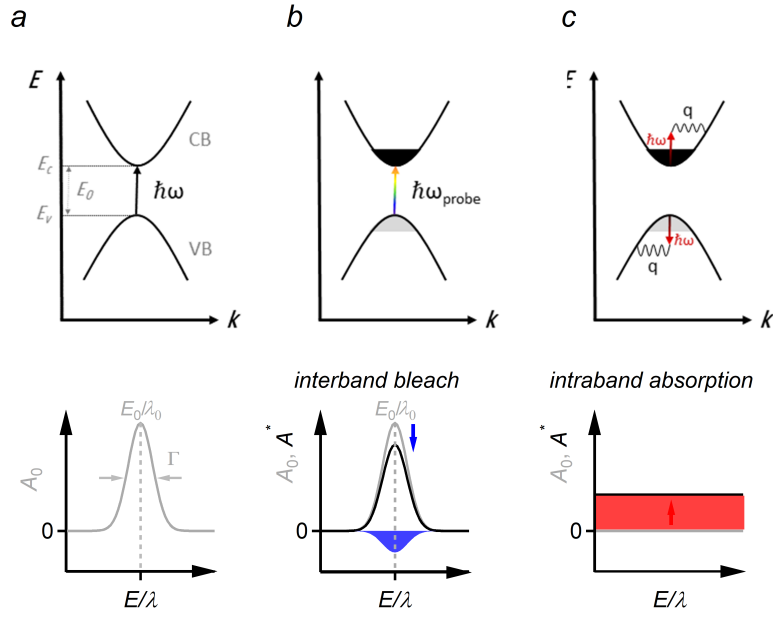
Figure 6.4: (a) (top) Simplified energy diagram and (bottom) ground-state absorption profile (A_0, grey) of a semiconductor as described in the main text. (b) (top) Illustration of interband bleach due to carriers at the band edges. (bottom) The excited-state absorption ($A^\star$, black) is bleached with an amount ΔA (filled in blue, $\Delta A < 0$). (c) (top) Illustration of intraband absorption. (bottom) The excited-state absorption ($A^\star$, black) increases with an amount ΔA (filled in red, $\Delta A > 0$). In the ΔA spectrum, positive and negative values are respectively indicated in red and blue – we use the same color code in Figures 6.5 and 6.6.
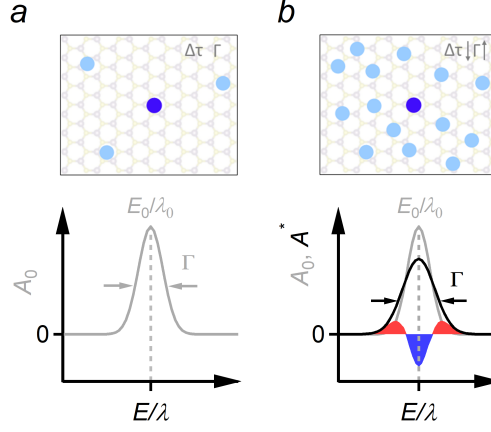
Figure 6.5: Illustration of the optical linewidth in (a) a low-density regime and (b) a high-density regime. A high carrier concentration broadens the excited-state absorption ($A^\star$, black), yielding a second derivative-like ΔA (filled).

events between particles yields a concomitant increase in the linewidth Γ of the transition[4].[259, 260] For a Gaussian-shaped absorption profile, a broadening results in a characteristic second-derivative-like ΔA spectrum having a minimum at E_0. We illustrate this effect in the lower panel of Figure 6.5b.

6.3.4   Photoinduced Spectral Shifts

As a description of spectral shifts requires a multi-particle view, we extend our conceptual approach by introducing an exciton state at a binding energy $E_{\mathrm{b,X}}$ below the free particle bandgap E_0, see Figure 6.6a. Within such a framework, the optical gap now reads $E_0' = E_0 - E_{\mathrm{b,X}}$.

In particular, in low-dimensional TMDs where Coulomb effects dominate the optical response, photogenerated charge carriers can alter

---

[4]Following the uncertainty principle $\Delta E \Delta \tau \geq \hbar/2$, the energy spread on a transition (the linewidth) is correlated with the lifetime of that transition. For an exciton, two mechanisms can result in a loss of coherence (a decrease in the dephasing time τ): (i) scattering with phonons; hence the temperature dependence of the linewidth, or (ii) scattering with carriers; hence the dependence on the carrier concentration n.[258]
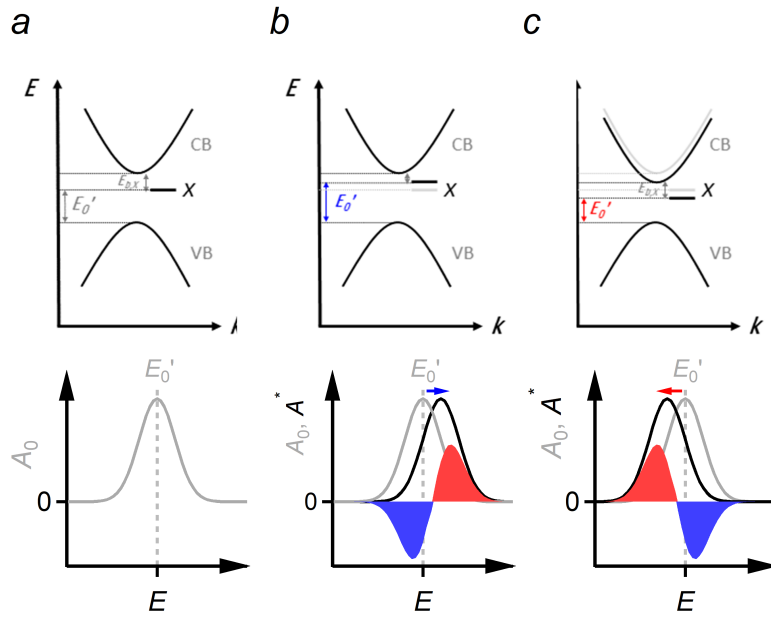
Figure 6.6: Schematic representing (a) the ground state energy landscape of an excitonic semiconductor with an optical gap $E_0^{'}$ and an exciton at binding energy $E_{b,X}$. The ground-state absorption A_0 (grey) at the exciton transition is Gaussian in shape. (b,c) Illustration of the effect of (b) binding energy reduction causing blueshifts and (c) bandgap renormalization causing redshifts.

the Coulomb potential experienced by electrons and holes. This can cause a renormalization of the exciton binding energy (Figure 6.6b) and the bandgap (Figure 6.6c). Binding energy reduction (BER) results in a blueshifted exciton absorption (Figure 6.6b, middle and bottom panels). On the other hand, bandgap renormalization (BGR) redshifts the absorption edge, leading to a shrinkage of the optical gap (Figure 6.6c, middle and bottom panels).

Hence, the overall energy shift of an exciton resonance originates from an interplay between both effects. For a Gaussian-shaped absorption profile, a spectral shift yields a sinusoidal (first-derivative-like) ΔA spectrum, where the sign of ΔA is dependent on the direction of the shift. We illustrate the effect of a blueshift and a redshift on ΔA pictorially in the bottom panels of Figure 6.6.

6.3.5   Summary
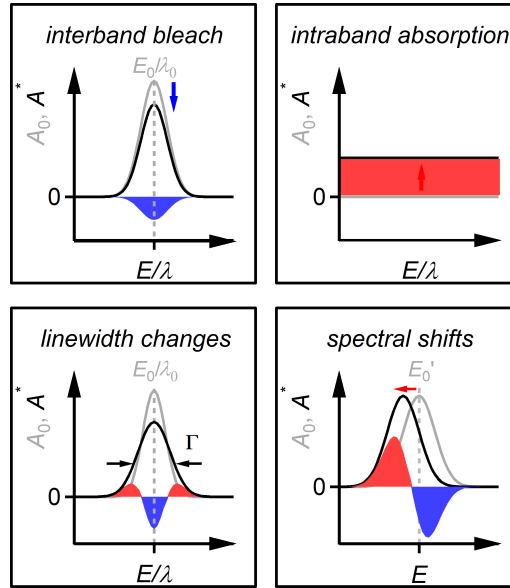
Figure 6.7: Summary of optical nonlinearities observed in semiconductor physics. The transient absorbance signatures are filled in blue ($\Delta A < 0$) and red ($\Delta A > 0$).

Figure 6.7 summarizes typical optical nonlinearities observed in semiconductor physics and how they are manifested in the differential

absorbance spectrum.

6.4   Conclusion

We reviewed the principles behind ultrafast pump-probe spectroscopy. While the roots of pump-probe spectroscopy can be traced back to the late 1800s, the birth of a broader research field is more recent and coincided with the development of *stable* solid-state Ti:sapphire lasers with femto- to picosecond time resolution (section 6.1). At our facilities, we have access to a white-light transient absorbance spectrometer with $\approx$100 fs time resolution. Such a set-up allows us to map changes in the absorbance of a material as a function of energy and time and summarizes this information in a so-called differential absorbance map (section 6.2). In such a way, we can disentangle semiconductor physics at otherwise inaccessible time scales. An essential aspect here involves the assignment and interpretation of optical nonlinearities encrypted in differential absorbance maps. While a detailed description is outside the scope of this work, we reviewed the most characteristic effects, and we discussed how they are manifested in the transient absorbance measurement from a phenomenological point of view (section 6.3).

7

Ultrafast Carrier Dynamics in Few-Layer Colloidal Molybdenum Disulfide

Chapter 4 showed how stable dispersions of colloidal MoS_2 flakes are obtained by solubility parameter matching. In this chapter, we address the ultrafast properties of such MoS_2 flakes. If colloidal synthesis is to become a genuine alternative to produce TMD nanocrystals, the optoelectronic characteristics of colloidal TMDs must be understood and benchmarked. We evaluate colloidal MoS_2 nanosheets from these perspectives using broadband transient absorption spectroscopy.

Author Contributions

The findings in this chapter have been published in:

Ultrafast Carrier Dynamics in Few-Layer Colloidal Molybdenum Disulfide Probed by Broadband Transient Absorption Spectroscopy Schiettecatte, P.; Geiregat, P.; Hens, Z.

P.S did the synthesis, a part of the TA measurements and the data analysis. P.G. guided the TA experiments and performed the initial measurements. P.S., P.G. and Z.H. discussed the results and wrote the manuscript together.

Acknowledgments

I want to thank Ivo Tanghe for providing Matlab scripts and for his help with Matlab programming.
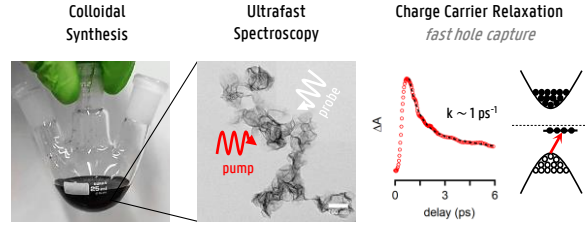
Figure 7.1: Overview of chapter 7.

7.1 Introduction

Over the past years, much work has been devoted to understand the photophysics of MoS_2 flakes made by exfoliation or CVD. These studies highlighted the central role of the enhanced many-body Coulomb interactions, leading to strongly bound excitons and excitonic molecules, resulting from the two-dimensional character of these materials and the reduced dielectric screening by the low-permittivity environment.[33, 261–267] These studies contributed to a deeper understanding of TMDs and advanced the use of MoS_2 in a broad range of applications in fields as diverse as optoelectronics[49, 268] and photocatalysis.[269] On the other hand, the photophysical properties of MoS_2 produced by direct colloidal synthesis are still unexplored. However, if colloidal synthesis is to become a true alternative to produce TMDs, the optoelectronic characteristics of colloidal TMDs must be understood and benchmarked relative to CVD-grown and exfoliated TMDs.

Using the established colloidal synthesis detailed in chapter 4, we address charge carrier relaxation in photoexcited colloidal MoS_2 sheets through femtosecond transient absorption spectroscopy at visible and near-infrared wavelengths.

7.2 Photoinduced Bandgap Renormalization

As stated in the introduction, we study the charge carrier relaxation in colloidal few-layer ($N \approx 3$) MoS_2 sheets by means of femtosecond
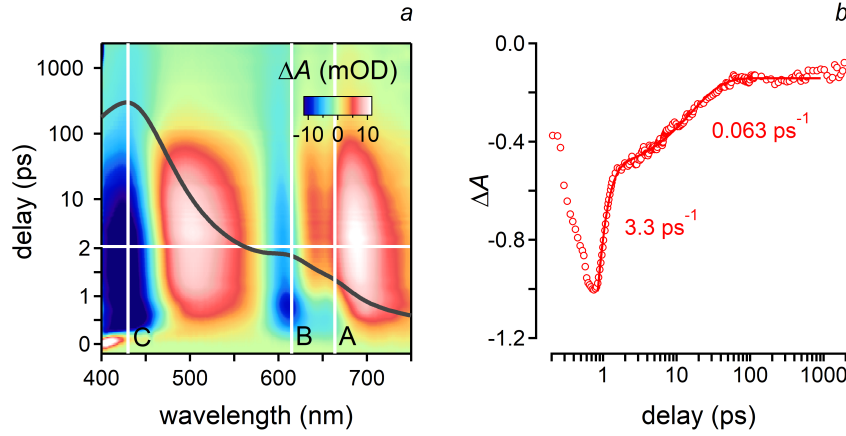
Figure 7.2: (a) 2D wavelength-delay map of ΔA measured on colloidal MoS_2 nanosheets after photoexcitation with 400 nm ($\hbar\omega$=3.1 eV), 110 fs pulses (fluence: $470\,\mu J/cm^2$). The full black line represents the linear absorbance spectrum A_0. The position of (vertical white lines) the A and B exciton and the C band have been indicated. (b) Transient absorbance (normalized to the bleach maximum) at the B exciton wavelength after photo-excitation at 400 nm using an excitation fluence of 235 $\mu J/cm^2$. The markers represent experimental data, and the solid line is a fit to a combination of a biexponential decay and a fixed background. The value of the fast (k_1, circles) and slow (k_2, squares) component has been indicated.

TA spectroscopy at visible and near-infrared probe wavelengths. For experimental details concerning the synthesis, we refer the reader to Chapter 4 and Appendix A.2. For a description of the conditions under which we conducted the TAS experiments, we refer the reader to Appendix A.3.

7.2.1 General Description and Kinetic Analysis of the Transient Absorbance

Figure 7.2a shows a 2D transient absorbance (TA) map covering the wavelength range 400–750 nm (3.1–1.65 eV) and pump delays up to 2.5 ns. We identified two different regimes in this ΔA map. At early pump-probe delays, ΔA features two short-lived bleach features ($\Delta A < 0$) close to the A and B exciton resonances, which disappear within 2 ps after photoexcitation. At longer time delays, ΔA shows
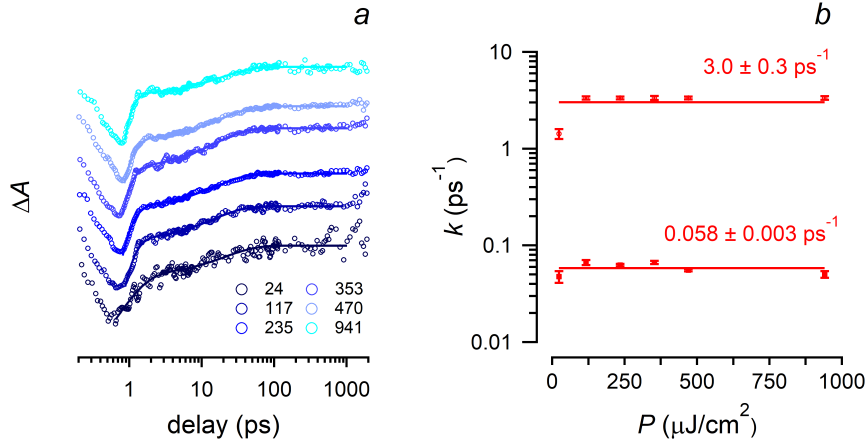
Figure 7.3: (a) Transient absorbance at the B exciton wavelength (610 nm) after photoexcitation at 400 nm using for excitation fluences ranging from 24 to 941 μJ/cm^2. The markers represent experimental data points. The solid line is a fit to a combination of a biexponential decay and a fixed background. (b) Decay rates obtained from biexponential fits. Error bars on the values of the fast (circles) and slow (squares) components as well an estimated error on the average values have been indicated.

multiple bands that decay on a similar time scale. An analysis of the transient absorbance around, for example, the spectral region of the B exciton (≈ 610 nm) provides a more quantitative view of both regimes. As shown in Figure 7.2b, the decay of ΔA exhibits two different rates that can be well described using a fit to a biexponential decay and a fixed background C according to:

$$\Delta A = A_1 \exp^{-k_1(\mathrm{t-t_0})} + A_2 \exp^{-k_2(\mathrm{t-t_0})} + C \qquad (7.1)$$

Here, k_1 and k_2 are the rate constants associated with the faster and slower decay process and amount to $3.3\,\mathrm{ps}^{-1}$ and $0.063\,\mathrm{ps}^{-1}$ for an excitation fluence of 235 μJ/cm^2.

Figure 7.3 summarizes this initial survey by plotting the transient absorbance at the B exciton wavelength for different excitation fluences P ranging from 24 to 941 μJ/cm^2. Importantly, the decay traces and the corresponding decay rates obtained by a fit to Equation 7.1, are largely independent of the pump fluence and amount to $3.0 \pm 0.3\,\mathrm{ps}^{-1}$ and $0.058 \pm 0.003\,\mathrm{ps}^{-1}$, see Figure 7.3b.
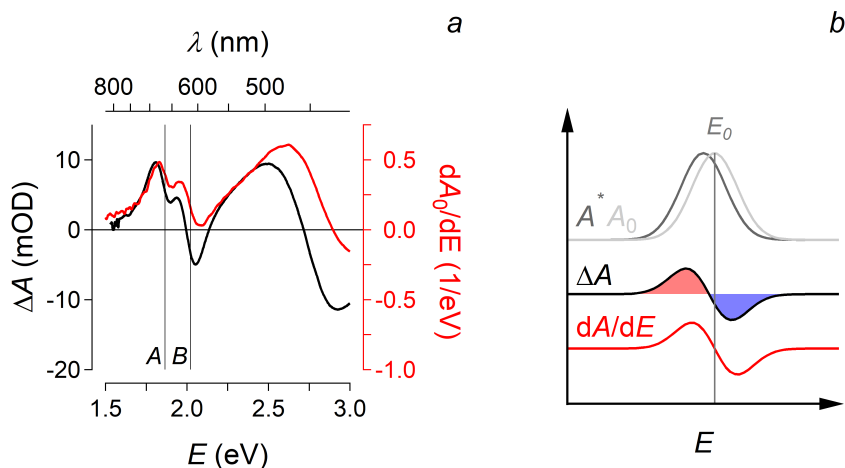
Figure 7.4: (a) Comparison of (black) transient absorbance spectrum (400 nm, $470\,\mu\mathrm{J/cm^2}$ photo-excitation) at a delay of 10 ps and (red) the derivative $\mathrm{d}A_0/\mathrm{d}E$ of the attenuance spectrum. The spectral positions of the A and B exciton are indicated in solid vertical lines. (b) Pictorial representation showing the relationship between a derivative and a spectral shift. A spectral shift closely resembles a derivative-like spectrum except that the inflection point is being slightly off-set. (top) attenuance A_0 and the attenuance spectrum of the excited-state $A^\star$. (middle) Differential absorbance ΔA, positive and negative values are respectively indicated in red and blue. (bottom) Derivative of the attenuance $\mathrm{d}A_0/\mathrm{d}E$.

7.2.2   Derivative   Analysis   of   the   Transient   Absorbance

Focusing on the second, more slowly decaying regime, we noticed that the alternation between bleach and photoinduced absorption ($\Delta A > 0$) at a given delay closely resembles the derivative of the absorbance spectrum. For comparison, Figure 7.4a represents a spectral cut of the TA spectrum after a pump-probe delay of 10 ps and the derivative $\mathrm{d}A_0/\mathrm{d}E$ of the attenuance spectrum to the photon energy E. Both show a similar behavior where features in the TA spectrum coincide with local minima and maxima in $\mathrm{d}A_0/\mathrm{d}E$. It is well-known that small spectral shifts δE give rise to a transient absorbance ΔA that mimicks $\mathrm{d}A_0/\mathrm{d}E$,[270] see Figure 7.4b for a conceptual representation and Appendix S2 for a mathematical description. From the

correspondence between ΔA and dA_0/dE, the spectral shift δE can be readily deduced according to:

$$\Delta A \approx \frac{dA_0}{dE}\delta E \qquad (7.2)$$

The deviations from this one-to-one correlation apparent in Figure 7.4a at high photon energy (short wavelengths) are likely caused by light scattering contributing to A_0 but not to ΔA. This leads to an overestimation of positive and an underestimation of negative slopes. As scattering is less important at longer wavelengths, one sees a better resemblance between ΔA and dA_0/dE at photon energies around the A exciton. From Equation 7.2 we can estimate a spectral redshift of around 20 meV for this specific example. This value lines up with recent reports of redshifts observed in TMD systems.[204, 271]

7.2.3 Photoexcitation using Different Excitation Energies

To further support the interpretation that the long-delay ΔA spectra merely reflect spectral shifts, we pumped a dispersion of MoS_2 nanosheets using different excitation energies, see Figure 7.5a. As shown in Figure 7.5b, we obtained highly similar ΔA spectra showing a pronounced bleach near the C transition even for excitation photon energies near the B ($\hbar\omega$=2.07 eV) and A ($\hbar\omega$=1.88 eV) exciton. As different single-particle states give rise to the A exciton, the B exciton, and the C band, such behavior cannot be explained by a state filling argument.[206] We thus conclude that at delays longer than 2 ps, a spectral shift of the transition energies dominates the transient absorbance after photo-excitation. This finding is consistent with the current literature on CVD grown and exfoliated TMDs, where a similar behavior was observed and assigned to a photoinduced renormalization of the bandgap, which concomitantly shifts transition energies, see Figure 7.5c for a conceptual representation.[261, 262, 271]

7.2.4 On the Origin of a Spectral Redshift

As pointed out in chapter 6, the central position of an exciton line E_X depends on the exciton binding energy E_b and the free-particle bandgap E_g such that $E_X =$ equals $E_g - E_b$.[29] The presence of photoexcited carriers alters the Coulomb potential experienced by
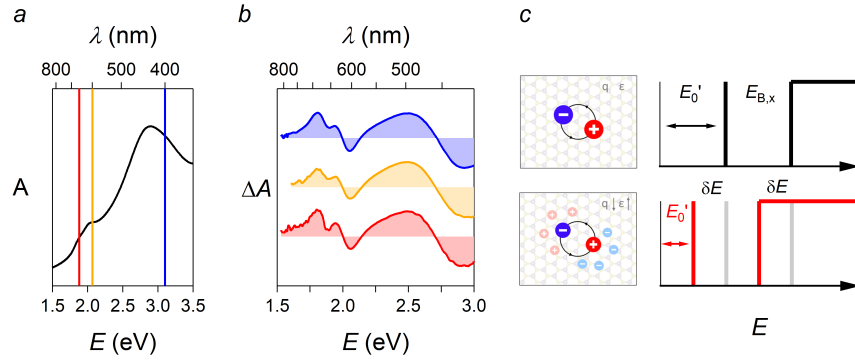
Figure 7.5: Summary of the experiments that involved photoexcitation using different excitation energies. (a) attenuance spectrum A_0 (black) with the excitation energies indicated as follows: (blue) excitation near the C exciton ($\hbar\omega$=3.1 eV, 400 nm), (orange) near the B exciton ($\hbar\omega$=2.07 eV, 600 nm) and (red) in the proximity of the A exciton ($\hbar\omega$=1.88 eV, 660 nm). (b) Transient absorbance spectra recorded at a delay of 10 ps for different pump excitation energies, including (blue) $\hbar\omega$=3.1 eV (400 nm), (orange) $\hbar\omega = 2.07\,\mathrm{eV}$ (600 nm) and (red) $\hbar\omega = 1.88\,\mathrm{eV}$ (660 nm). c) Pictorial representation of a renormalization of the transition energies. The optical bandgap $E_0^{'}$ is red-shited with an amount of δE due to screening.
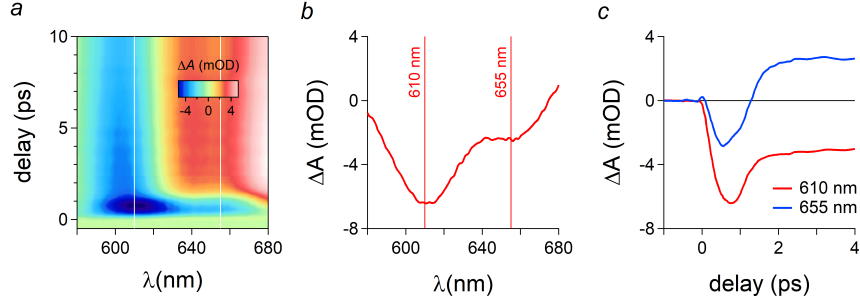
Figure 7.6: Transient absorbance at short pump-probe delays. (a) ΔA delay-wavelength map after photoexcitation with a 400 nm ($\hbar\omega$=3.1 eV) pump pulse (fluence: $470\,\mu\mathrm{J/cm}^2$). (b) ΔA spectrum after a 1 ps delay taken from the ΔA map. The wavelength of the bleach features around the A (655 nm) and B (610 nm) exciton have been indicated. (c) Evolution of ΔA with pump-probe delay at the wavelengths indicated.

electrons and holes, and thereby screens attractive electron-hole interactions and repulsive electron-electron interactions.[272] The former decreases the exciton binding energy (binding energy reduction, BER) and causes blueshifts, while the latter renormalizes the bandgap (bandgap renormalization, BGR) and causes redshifts.[273] Both mechanisms work in spectrally opposite directions, yet do not fully compensate in quasi-2D systems.[259] As such, the direction of the spectral shift depends on an intricate balance between BER and BGR.

7.3   Exciton Dynamics

7.3.1   Transient Absorbance at Early Pump-Probe Delays

In the previous sections, we addressed the transient at pump-probe delays that are longer than 10 picoseconds. Here, different analyses of the ΔA maps, including a derivative analysis of the absorbance spectra and experiments where we optically excited at different energies, attested that a spectral redshift of the transition energies dominates the transient dynamics at long pump-probe delays. At early pump-probe delays, we, however, noticed two short-lived bleach bands cen-
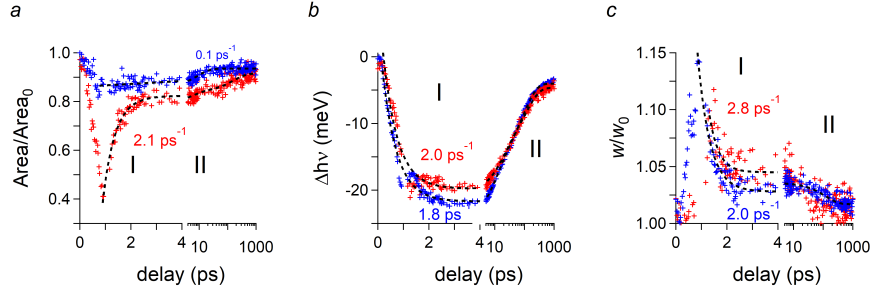
Figure 7.7: Parameters obtained from fitting the ΔA map to a sum of two Gaussians and a background as a function of the pump-probe delay (markers), including (a) evolution of the area, (b) energy shift, and (c) line-width of the Gaussians that describe the A (red) and B (blue) feature. The dashed line is a fit to an exponential decay and a fixed background.

tered at ~ 655 nm and ~ 610 nm in the ΔA map (see Figure 7.6a). Interestingly, these wavelengths appear slightly blueshifted relative to the A and B exciton wavelengths that we extracted from the attenuance spectrum. Both bleach bands build up within a few hundred femtoseconds after photoexcitation and decay within 1-2 picoseconds (see Figures 7.6b and 7.6c). After this rapid picosecond decay, the transient absorbance of both bands reaches a value in line with the respective spectral shift bands, which yield a net photoinduced absorbance at around the A exciton and a remaining bleach at the B exciton (see Figure 7.2a).

7.3.2 Spectral Deconvolution of the Excited-State Spectrum

The net bleach (or reduced absorbance) of a transition can be quantified by comparing the area of its respective absorption profile before and after photoexcitation. For this reason, we decided to fit the absorbance spectrum of the excited-state rather than the differential absorbance. The excited-state spectrum $A^\star(E, t)$ at each time delay was calculated by summing the attenuance $A_0(E)$ and the differential absorbance $\Delta A(E, t)$. The resulting spectrum was fit to a sum of two Gaussian fit functions that account for the absorption profiles of the A and B exciton bands and a polynomial background that describes

any residual absorption of the broad C feature and scattering:

$$A^{\star}(E,t) = A_A \exp^{-\left(\frac{E-E_A}{w_A}\right)^2} + A_B \exp^{-\left(\frac{E-E_B}{w_B}\right)^2} + \sum_{i=0}^{5} K_i E^i \quad (7.3)$$

with A_A and A_B being the amplitude, E_A and E_B the central position, and w_A and w_B the width of the A and B exciton band of the excited-state absorbance, and K_i being the pre-factor in the polynomial background function.

Figure 7.7 summarizes the main results of this analysis by plotting the evolution of the area, spectral position, and width of the Gaussians that are used to describe both exciton bands. Each parameter is normalized to the value obtained at zero time delay. We analyzed the time-dependence of these parameters through fits to a multi-exponential decay, which yields a set of fitting parameters that have been listed in Table 7.1.

It can be seen that photoexcitation rapidly induces a notable decrease in the area of both Gaussians, hereby reflecting a true bleach of both exciton bands. We assign these bleaches to state-filling brought about by the presence of a photogenerated carrier population at the band edges.[274] During the next picosecond, the area of the Gaussian used to describe the A exciton band quickly recovers with a rate constant of $2.1\,\mathrm{ps}^{-1}$ (Figure 7.7a, stage I), while the area of the B band hardly changes and recovers with a notable slower rate of $0.1\,\mathrm{ps}^{-1}$. Concomitantly, peaks broaden, and the spectra shift to lower energies. The recovery of the A exciton bleach, the ingrowth of a spectral redshift, and the rapid changes in linewidth take place on a remarkably similar time scale with matching rate constants as indicated in Figure 7.7b, stage I and listed in Table 7.1. These processes line up with the rapid rate constant already identified in the transient absorbance at 610 nm (see Figure 7.2b and Figure 7.6c) and reflect a carrier loss process. At longer time delays (Figure 7.7, stage II), the A exciton bleach, the changes in line-width and the spectral shift recover at a much slower rate, defined by two rate constants in the order of $0.1\,\mathrm{ps}^{-1}$ and $0.01\,\mathrm{ps}^{-1}$. The aforementioned B bleach band recovers at a rate of $0.1\,\mathrm{ps}^{-1}$ over the entire time window.

Parameter	k_1 (ps^{-1})	k_2 (ps^{-1})	k_3 (ps^{-1})
$A_A/A_{A,0}(t)$	2.08 ± 0.12	0.172 ± 0.066	0.0060 ± 0.0014
$A_B/A_{B,0}(t)$	NA^a	0.112 ± 0.012	NA^a
$\Delta E_A(t)$	2.00 ± 0.11	0.089 ± 0.011	0.0096 ± 0.0005
$\Delta E_B(t)$	1.75 ± 0.09	0.103 ± 0.007	0.0109 ± 0.0003
$w_A/w_{A,0}(t)$	2.78 ± 0.60	NA^b	NA^b
$w_B/w_{B,0}(t)$	1.96 ± 0.12	NA^b	0.0087 ± 0.0012
ΔA_{NIR}	1.64 ± 0.07	0.179 ± 0.012	0.0070 ± 0.0005

Table 7.1: Rate constants associated with the temporal evolution of the energy shift $\Delta E_A(t)$, the normalized area $A/A_0(t)$, and normalized line width $w/w_0(t)$ of the Gaussians used to describe the A and B exciton band as described, see Figure 7.7. The rate constants associated with the dynamics at near-infrared wavelengths (1.25 μm), denoted as ΔA_{NIR}, see later on, are listed for comparison. The values indicated with NA are either absent or could not be fit within the noise level. NA^a the B bleach band decays monoexponentially without showing the rapid decay described by the rate constant k_1. NA^b the changes in line width drop within the noise after the initial decay stage which makes the long delay challenging to fit, see Figure 7.7.
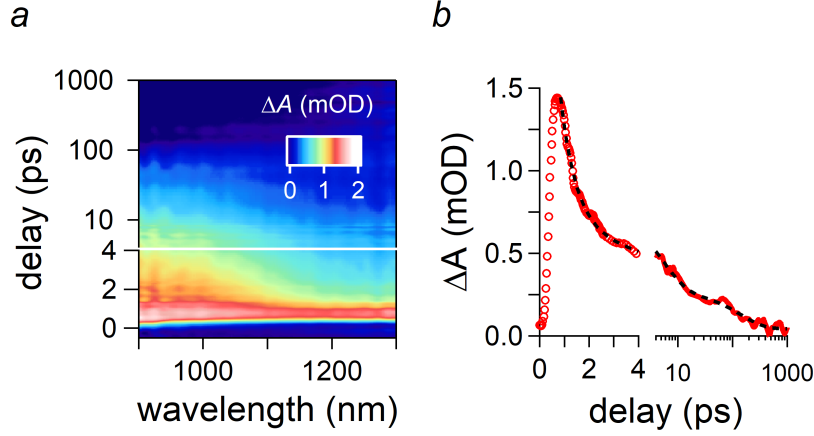
Figure 7.8: (a) 2D transient time delay-wavelength map upon 400 nm ($\hbar\omega$=3.1 eV), 110 fs, 470 μJ/cm^2 photoexcitation in the wavelength range from 900 nm to 1.3 μm. b) Temporal dependence of the transient probed at 1.25 μm. The dashed line is a fit to a combination of an exponential decay and a fixed background.

7.4   Probing Near-Infrared Wavelengths

7.4.1   Non-Resonant Excitation

In the case of CVD grown MoS$_2$, TA spectra were presented in the literature that strongly resemble the ΔA maps shown in Figures 7.2a and 7.6a.[262] In that case, however, the initial bleach features were assigned to the broadening of the exciton transitions, rather than to a net bleach. We, therefore, extended our analysis to infrared wavelengths to ascertain the initial accumulation of charge carriers after photoexcitation. At those wavelengths, neither spectral shifts nor line broadening can affect the transient absorbance since A_0 will be zero at wavelengths longer than the indirect gap of 1.2 eV, *i.e.*, 1000 nm.[26] Opposite from this prediction, the experimental ΔA spectrum shown in Figure 7.8a exhibits a featureless yet pronounced photoinduced absorption in the entire wavelength range between 900 and 1300 nm. Moreover, as shown in Figure 7.8b, the transient absorbance at a fixed probe wavelength of 1.25 μm features a decay with a fast stage decaying at a rate of $1.64 \, \text{ps}^{-1}$ and two slower stages decaying with rates of $0.18 \, \text{ps}^{-1}$ and $0.007 \, \text{ps}^{-1}$, as was obtained by

a fit to three exponential functions and a fixed background, see Table 7.1.[1] Importantly, the observation of sub-bandgap photoinduced absorption confirms that ΔA is not a mere combination of broadened and shifted exciton lines. Typically, this increased absorption is attributed to intraband transitions that involve conduction-band electrons or valence-band holes.[265] In that case, the sub-bandgap transient probes changes in the population of these charge-carriers, hence the similar decay behavior of ΔA above and below the MoS_2 bandgap.

7.4.2 Resonant Excitation
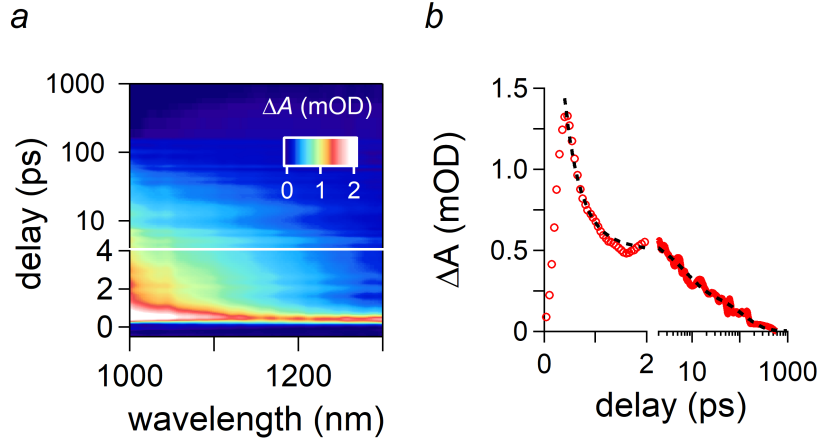
Figure 7.9: (a) 2D transient time delay-wavelength map upon 650 nm ($\hbar\omega$=1.91 eV), 110 fs, 587 $\mu J/cm^2$ photoexcitation in the wavelength range from 1000 nm to 1300 nm. b) Temporal dependence of the transient probed at 1.20 μm. The dashed line is a fit to a combination of an exponential decay and a fixed background.

Using resonant excitation near the A exciton, we observe a featureless yet pronounced photoinduced absorption at near-infrared wavelengths as shown in Figure 7.9a. The transient absorbance at a fixed probe wavelength indicates a fast stage decaying with a rate

---

[1]The decay rates extracted from the fits slightly depend on the probe wavelength. For instance, evaluating the decay at 1.05 μm yields a fast stage decaying at a rate of 1.11 ps^{-1} and two slower stages decaying with rates of 0.15 ps^{-1} and 0.008 ps^{-1}.

of $3.27 \pm 0.15\,\text{ps}^{-1}$ and two slower stages described by rate constants of $0.141 \pm 0.013\,\text{ps}^{-1}$ and $0.0083 \pm 0.0010\,\text{ps}^{-1}$, as were obtained by a fit to three exponential functions and a fixed background see Figure 7.9b. The observation of three distinctive decay stages lines up with the measurements at non-resonant photoexcitation, see Figure 7.8. Slight discrepancies with the estimated rate constants are to be expected as the transient dynamics at non-resonant excitation are being compounded by cooling effects, while those at resonant excitation are less. Similarly, we observe slightly faster decay rates for resonant excitation at visible wavelengths, see Appendix B.5.2.

7.5 A Model for Charge Carrier Decay in Colloidal MoS$_2$

Based on the acquired data and analysis, we propose that photoexcited carriers in colloidal MoS$_2$ nanosheets decay through a model as outlined in Figure 7.10. This involves cooling of photoexcited carriers towards the band-edge extrema, followed by the trapping of one of the band-edge carriers and a subsequent series of slower non-radiative capture events. Cooling induces the initial net bleach of the A and B exciton absorption and a notable build-up of the sub-bandgap photoinduced absorption. Accordingly, the rapid loss of this net bleach reflects the depletion of band-edge carriers. Given the fluence independent, first-order decay, we attribute this depletion to a defect-related trapping process rather than to a higher-order Auger mechanism, as was previously observed in exfoliated MoS$_2$ flakes.[263, 275] While the different analyses of the TA spectra confirm the presence of this rapid trapping process, estimated decay rates range from 1.6 to $3\,\text{ps}^{-1}$ depending on the probe wavelength and the analysis method. Discrepancies are caused by the transient dynamics in the visible being compounded by simultaneous spectral shifts and line-width broadening effects, while those in the near-infrared are not. Even so, the presence of a rapid decay of the A exciton bleach, during which the area of the B exciton band hardly changes, suggests that hole carriers are trapped, since both transitions share the same conduction-band states, yet different valence band states. Note that the rapid loss of a hole population also accounts for the first, rapid decay component of the sub-bandgap photoinduced absorption within this model.

The second stage in the transient absorbance predominantly involves
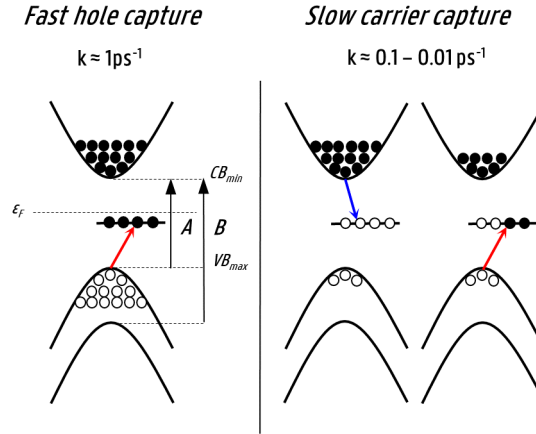
Figure 7.10: Schematic representation of the proposed photo-excited carrier decay in colloidal MoS_2. Upon cooling towards the band-edge extrema, (left) photoexcited holes are captured by mid-gap defect states, (right) followed by a series of slower recombination events involving trapping of conduction band electrons and an eventual remaining hole population. The so-called A and B exciton states, originating from transitions between the spin-orbit split valence band and the conduction-band minimum, are indicated for clarity.

the relaxation of the spectral shift or band-gap renormalization created by substantial carrier loss after photoexcitation; a phenomena which takes place over two distinctive time regimes, with estimated decay rates of $\sim 0.1\,\mathrm{ps}^{-1}$ and $\sim 0.01\,\mathrm{ps}^{-1}$. Note that the sub-bandgap transient shows a highly similar decay behavior. According to the proposed model, this mirrors the non-radiative recombination of remaining carrier populations through a series of processes that bring the photo-excited MoS_2 nanosheets back to equilibrium. For one thing, this involves the relaxation of a remaining electron population, as advocated by the presence of a $\sim 0.1\,\mathrm{ps}^{-1}$ decay on both the A and B exciton bleach bands – both transitions share the same conduction band states. The $\sim 0.01\,\mathrm{ps}^{-1}$ relaxation appears to be associated with the decay of eventual remaining hole carriers due to its absence
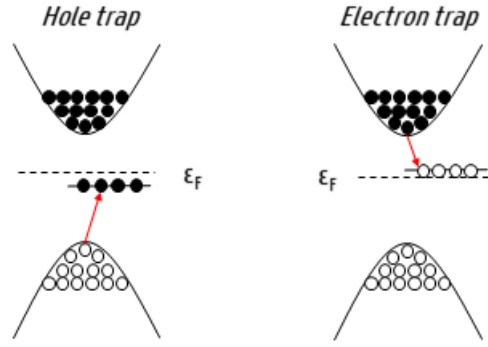
Figure 7.11: Schematic representation of an electron trap or a hole trap. Whether a trap acts an electron or hole scavenger depends on the position of the Fermi level ε_F with respect to the energy of the trap state.

from the B exciton trace. This interpretation lines up with a model proposed by Wang *et. al.*[265] who found a similar sequence of first order processes in exfoliated MoS$_2$ and with the work by Docherty et al.[276] on CVD grown MoS$_2$ and WSe$_2$ where it was shown that one type of carrier is predominantly captured at surface states in the first few picoseconds, while the other carrier is captured over a much longer time scale. Again, this interpretation accounts for the concomitant slower decay components in the sub-bandgap photoinduced absorption. The fact that this recombination is also observed for resonant pumping suggests that carriers are trapped by in-gap defect states. As depicted in Figure 7.11, the position of the Fermi level with respect to the energy of the trap state sets whether a trap acts acts an electron or hole scavenger. Reasoning from this perspective, hole trapping concurs with filled mid-gap trap states. While no STM studies on defects have been performed on colloidally synthesized 2D TMDs, vacancies, edge states, and grain boundaries[277] are prominent defects in CVD grown and exfoliated MoS$_2$ flakes.[278–280] Our spectroscopic studies call for an enhanced effort to understand the defect landscape of colloidal 2D TMD nanomaterials, for instance by combining pump-probe spectroscopy with detailed microscopic characterization.

7.6 Conclusion

We have presented a detailed study on the charge carrier relaxation in photoexcited colloidal MoS_2 nanosheets using femtosecond transient absorption spectroscopy at visible and near-infrared wavelengths. We demonstrate that the transient absorbance after photoexcitation is caused by both a reduction in oscillator strength of the transitions making up the direct gap, and a shift of the entire absorbance spectrum towards lower energy. We attribute these features to state filling and bandgap renormalization, respectively. Through spectral deconvolution, we find that in particular, the A exciton bleach exhibits a sub-picosecond decay, which we attribute to rapid hole capture in midgap defect states. The disappearance of spectral shifts at longer delay times reflects the relaxation of the charge carrier distribution by further charge trapping and recombination events. A comparison between the dynamics of photogenerated charge carriers in the case of colloidal MoS_2 nanosheets as measured here and existing literature on CVD grown MoS_2 nanosheets points towards a very similar sequence of rapid trapping of one carrier type, followed by capture of the remaining carrier on a longer time scale. Accordingly, we conclude that colloidal synthesis yields MoS_2 nanosheets of comparable quality, even if an entirely different chemistry is involved in the TMD production.[262] This shows that TMDs fabricated with both approaches may benefit from similar defect passivation strategies to enhance the lifetime of photogenerated excitons.

8

Free Carrier Generation and Optical Nonlinearities in Rhenium Disulfide

Thriving on the methodologies introduced in chapter 7, we study charge carrier decay in photoexcited ReS_2 by combining broadband femtosecond transient absorbance spectroscopy and optical pump terahertz (THz) probe spectroscopy (OPTP). The addition of pump-probe THz spectroscopy to our toolbox allows us to distinguish between photoexcited electron-hole pairs bound in an exciton or those moving freely through the crystal. Where excitons are typically desired for light emission, mobile carriers are preferred for photovoltaics or photodetection.

Author Contributions

This study has been done in collaboration with the Optoelectronic Materials Section Group at Delft University of Technology.

The findings in this chapter are being summarized in:

Unraveling the Peculiar Photophysics of Liquid-Phase Exfoliated ReS_2 **Nanoflakes** Pieter Schiettecatte, Deepika Poonia, Ivo Tanghe, Sourav Maiti, Michele Failla, Sachin Kinge, Laurens D.A. Siebbeles, Zeger Hens, and Pieter Geiregat.

P.S. and D.P. contributed equally to this work. Both contributed to the spectroscopy and synthesis, data analysis and wrote the paper. I.T. wrote the analysis code for the spectral deconvolution. Michele Failla helped in the THz measurements. Sourav Maiti participated in the discussions. Laurens D.A. Siebbeles and Zeger Hens supervised the research. P.G. initiated and supervised the research, and wrote the manuscript.

Acknowledgments

I want to thank Arjan Houtepen for the opportunity to conduct the exploratory measurements at their facilities, and Gianluca Grimaldi and Indy du Fosse for their help with the experiments. I thank Jaco Geuchies for the electrochemical characterization (still ongoing and not part of the manuscript).
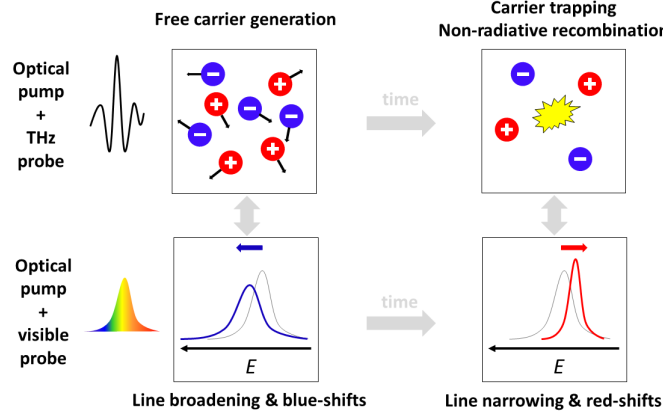
Figure 8.1: Overview of chapter 8.

8.1 Transient Absorbance Spectroscopy

8.1.1 Material Description

We study the charge carrier decay in few-layer liquid-phase exfoliated ReS_2 by transient absorbance spectroscopy and optical pump tera-hertz (THz) probe (OPTP) spectroscopy. For experimental details concerning the preparation of the few-layer ReS_2 dispersions, we refer the reader to chapter 3 and appendix A.1.2. As a thin film on a substrate is required for OPTP spectroscopy, every measurement is done on a film of deposited ReS_2 on a quartz substrate.

8.1.2 General Description and Assignment of Photo-induced Nonlinearities

Figure 8.2 provides a general overview of the transient absorbance ΔA of a ReS_2 film after the film has been photoexcited with a 530 nm ($\hbar\omega = 2.34$ eV) pump pulse and interrogated by a broadband probe spanning the wavelength range from 510 nm up to 910 nm. In the top panel, we present a two-dimensional wavelength-delay map of ΔA plotted together with the linear absorbance spectrum A_0 (black solid line). The bottom panel shows spectral slices of ΔA at distinctive pump-probe time delays.

Immediately after photo-excitation (spectrum i, t=200 fs), the spectrum yields a negative bleach band centered around the exciton line
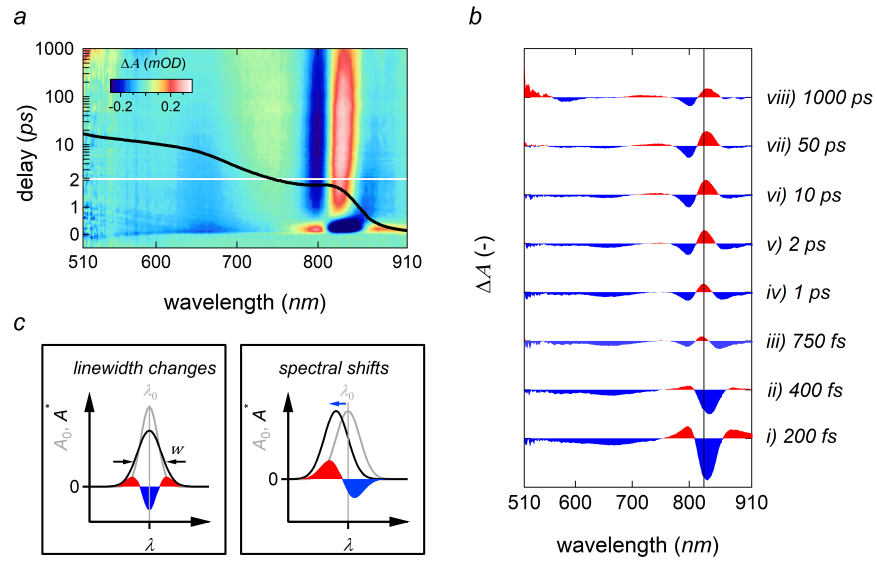
Figure 8.2: Overview of the transient absorbance ΔA recorded after a film of $\mathrm{ReS_2}$ was photoexcited with a 180 fs pump pulse. ($\hbar\omega_{\mathrm{pump}} = 2.34$ eV, $1.2 \times 10^{13}\,\mathrm{photons\,cm^{-2}}$) (a) (top) 2D wavelength-delay map of ΔA recorded for probe wavelengths from 510 up to 910 nm. The solid black line represents the linear absorbance spectrum A_0 of the $\mathrm{ReS_2}$ film. (b) Transient absorbance spectra recorded at fixed time delays. The spectra of ΔA are plotted at an offset, negative values of ΔA are filled in blue, positive values of ΔA in red. (c) Schematics representing the effect of (left) a broadening and (right) a spectral blueshift. Positive values for $\Delta A = A^\star - A_0$ are filled in red, negative values in blue.

sided by two positive bands of photoinduced absorption (PA). We recognize such a second-derivative-like line shape as a broadening of a Gaussian absorption profile (see section 6.3.3, Figure 6.5b for a pictorial representation of a linewidth change). The minimum of the bleach is slightly off-set toward longer wavelengths and the PA band appears more intense at the higher energy side. These asymmetries are likely due to a broadened and blueshifted exciton absorption line (see section 6.3.4, Figure 6.6c for a pictorial representation of a blueshift). At higher energies, the transient yields a net negative signal where the linear absorbance A_0 has a relatively uniform slope. Considering the extent of the negative band, it is unlikely to result from state-filling but rather reflects a blueshift of the higher-lying energy states.

Most remarkably, while decaying, the signal at the band edge switches sign over the next few hundreds of femtoseconds (spectra ii-iv) and yields a clear photoinduced absorption sided by two bleach bands at a delay of 1 ps (spectrum iv). Strikingly, such a line shape reflects a narrowed exciton, *i.e.*, an exciton with a narrower linewidth in the excited-state than in the ground state. Here again, we want to stress differences in the (a)symmetry of the signal. At a delay of 750 fs (spectrum iii), the line shape is asymmetric with the PA maximum slightly off-set toward the blue (*i.e.*, higher energy) side of the exciton line and has a more intense negative tailing at lower energy. In this regard, it reflects a blueshift superimposed on the narrowed line. At a delay of 1 ps (spectrum iv), the line is symmetric, while at pump-probe delays longer than 1 ps (spectra v-vi), the symmetry is reversed, and the initial blueshift has decayed into a redshift; a process that is evidenced by a less intense tailing at longer wavelengths (see section 6.3.4, Figure 6.6b for a pictorial representation of a redshift). The blueshifted absorption at high energy has mostly decayed and even yields a slight redshift at decays longer than $\approx 10\,\mathrm{ps}$ (spectrum vi), a signature we recognize through the rise of a positive absorption band between 700-750 nm. In contrast, the signature at the band edge decays over a much longer time scale. While decaying (spectra vi-viii), the peak maximum progressively shifts to the red side of the exciton line and is more alike to the sinusoidal shape characteristic for a redshift.

A first and general interpretation of the ΔA map marks a complex interplay between spectral shifts and linewidth changes. We recognize two major regimes in the ΔA map. (Regime I) After photoexcitation, the exciton band broadens and blueshifts. At the same time, photoex-

citation induces a blueshift of the higher-lying energy states. (Regime *II*) Peculiarly, during the first picoseconds, the initially broadened and blueshifted exciton transition decays into its mirror image, *i.e.*, it narrows down and shifts to the red.

8.1.3 Understanding Width Changes and Spectral Shifts via a Derivative Analysis

Taylor approximations For a transient spectrum ΔA that is determined by a spectral shift δE[270] or a change in the linewidth $\Delta\sigma$, we expect a proportionality between, respectively, the first and second derivative of the linear absorbance A_0 to the energy E

$$\Delta A \approx \frac{\mathrm{d}A_0}{\mathrm{d}E}\delta E \qquad (8.1)$$

$$\Delta A \approx \frac{\mathrm{d}^2 A_0}{\mathrm{d}E^2}\sigma_0\Delta\sigma \qquad (8.2)$$

We point out that eq 8.1 and eq 8.2 are derived by expanding $\Delta A(x + \delta x)$ $(x = E, \sigma)$ as a Taylor series up to the first order, and thereby only hold for infinitesimal increments δx. For a more detailed description of the formulas presented above, we refer to Appendix B.6.1.

Regime *I* – linewidth broadening and blueshifts Figures 8.3a and 8.3b plot ΔA after a pump-probe delay of 200 fs (solid red curve) and the averaged ΔA between t_0 and 500 fs (dashed red curve) together with the first derivative $\frac{\mathrm{d}A_0}{\mathrm{d}E}$ (black, panel a) and second derivative $\frac{\mathrm{d}^2 A_0}{\mathrm{d}E^2}$ (black, panel b). As evident in Figure 8.3a, the transient has a one-to-one correspondence with $\frac{\mathrm{d}A_0}{\mathrm{d}E}$ between $1.6 - 1.9$ eV. Notably, the ratio of ΔA to the first derivative $\frac{\mathrm{d}A_0}{\mathrm{d}E}$ is negative and thereby reflects a blueshift of the higher energy states. By eq. 8.1, the blueshift δE, for instance, evaluated at a 1.75 eV probe energy equals ≈ 0.2 meV.

Around the band-edge, the transient coincides relatively well with minima and maxima in the second derivative $\frac{\mathrm{d}^2 A_0}{\mathrm{d}E^2}$ to the photon energy E, and the sign of this correspondence marks a broadening of the exciton. For clarity, we plot both the second derivative of A_0 (solid black line) and the second derivative of a fitted Gaussian absorption profile to A_0 (black dashed line). For an isolated Gaussian, the second derivative is symmetric, that is, a linewidth change has
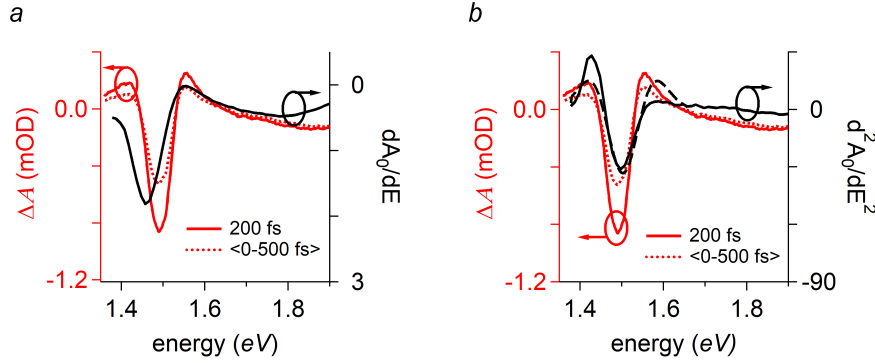
Figure 8.3: Overview of the derivative analysis in regime I. Comparison of (red) the transient absorbance at a delay of (red, solid line) 200 fs and of (red, dashed line) the averaged signal between t_0 and 500 fs to (black, panel a) the first derivative $\frac{\mathrm{d}A_0}{\mathrm{d}E}$ and to (black, panel b) the second derivative $-\frac{\mathrm{d}^2 A_0}{\mathrm{d}E^2}$ to the energy. Take note that the right axis in panel a runs from positive to negative values.

an identical effect at lower and higher energy (black dashed line). In the case of an A_0 spectrum consisting of an exciton superimposed on a step-like background (see Figure 8.2a, solid black line), a broadening of the exciton line is more pronounced at lower energy (see black solid line). Irrespective of these considerations, the line symmetry of ΔA is opposite from both predictions and is consistent with the presence of an additional blueshift. As signified by its correspondence to $-\frac{\mathrm{d}A_0}{\mathrm{d}E}$, such a blue shift would decrease/increase the intensity at lower/higher energy. Although shifts also contribute to the transient, we can, nonetheless, make a rough estimate on the order of magnitude of the relative broadening $\delta\sigma/\sigma_0$ using eq. 8.2. In this respect, evaluating ΔA at different energies, we retrieve values for $\delta\sigma/\sigma_0$ of $0.3 - 0.7\%$

Regime II – linewidth narrowing and redshifts Figures 8.4a and 8.4b plot ΔA after a pump-probe delay of 2 ps (solid red line) and the averaged ΔA between 1 ps and 1.5 ns (dashed red line) together with the second derivative $\frac{\mathrm{d}^2 A_0}{\mathrm{d}E^2}$ (black line in Figures 8.4a) and the first derivative $\frac{\mathrm{d}A_0}{\mathrm{d}E}$ (black line in Figures 8.4b).

At longer time delays, the band edge feature has switched sign and is similar in shape to the mirror image of a second derivative, see Fig-
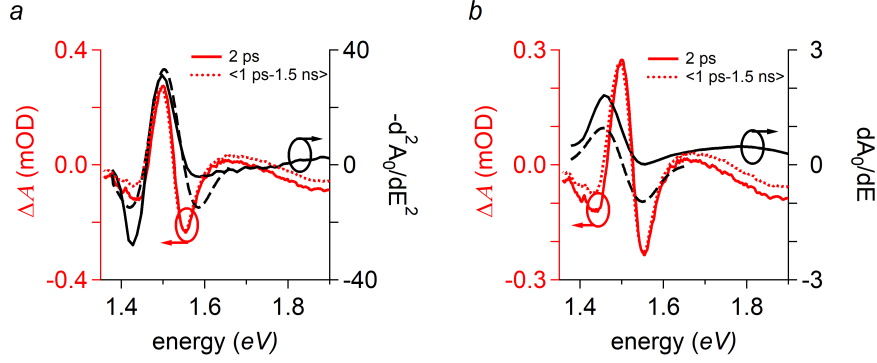
Figure 8.4: Overview of the derivative analysis in regime II. Comparison of (red) the transient absorbance at a delay of (red, solid line) 2 ps and of (red, dashed line) the averaged signal between 1 ps and 1.5 ns to (black, panel a) the second derivative $-\frac{\mathrm{d}^2 A_0}{\mathrm{d}E^2}$ and to (black, panel b) the first derivative $\frac{\mathrm{d}A_0}{\mathrm{d}E}$ to the energy.

ure 8.4a. Importantly, such a correlation implies a counter-intuitive narrowing of the exciton band. In a similar way as we pointed out above, the shape deviates from a purely narrowed line shape. Given that at those time delays ΔA is asymmetric with the lower energy feature being less intense, it also marks a superimposed redshift. As marked by its correspondence to $\frac{\mathrm{d}A_0}{\mathrm{d}E}$, such a redshift would indeed increase ΔA at longer wavelengths and decrease ΔA at shorter wavelengths, see Figure 8.4b.

8.1.4   Spectral Deconvolution

A first visual interpretation of the spectra and a comparison of the transients to derivatives of A_0 to E marked a complex interplay between shifts and linewidth changes. To better quantify the parameters that govern the transient signal, we fit $\Delta A(E, t)$ to a Gaussian fit function $G(h, E_{\mathrm{exciton}}, w)$, which accounts for the exciton absorption, and a background absorbance attributed to higher energy states $C(E)$. Using this procedure, we extract, for each pump-probe time delay, the amplitude h, the spectral position E_{exciton}, and the width w of the Gaussian that describes the exciton band, and a shift of the background absorbance ΔE_{bck}.

The main results of this analysis are summarized in Figure 8.5 and
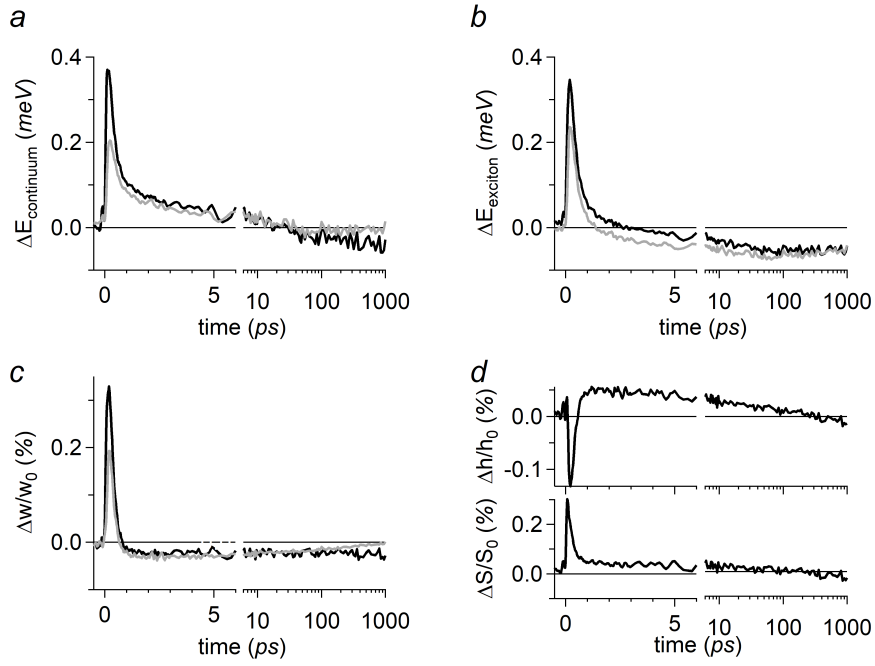
Figure 8.5: Evolution of the fit parameters (markers) that were obtained from a fit to a Gaussian $G(h, E_{\mathrm{exciton}}, w)$ and a background absorbance $C(E)$ to the ΔA in Figure 8.2a, including (a) the shift of the background absorbance ΔE_{bck} and, (b) the energy shift of the exciton $\Delta E_{\mathrm{exciton}}$, (c) the normalized change in the width $\Delta w/w_0$, (c) and (d) the normalized change in the amplitude $\Delta h/h_0$ of the Gaussian that describes the exciton band.

show the evolution of the parameters mentioned above as a function of the pump-probe delay. In conjunction with a visual interpretation and a derivative analysis, we observe a blueshift of the higher energy states (Figure 8.5a, $\Delta E_{\mathrm{bck}} > 0$), and the values agree with estimates based on eq. 8.1. Around the band edge, the exciton line is blueshifted (Figure 8.5b, $\Delta E_{\mathrm{exciton}} > 0$) and broadened (Figure 8.5c-d, $\Delta w/w_0 > 0$ and $\Delta h/h_0 < 0$). Both results are in line with a slightly asymmetric second-derivative-like line shape having a more intense PA band at the higher energy side (see Figure 8.2b, spectrum i).

Around a time delay of $\approx 1-2\,\mathrm{ps}$, the exciton has decayed into its narrowed (Figure 8.5c-d, $\Delta w/w_0 < 0$ and $\Delta h/h_0 > 0$) and red-shifted (Figure 8.5b, $\Delta E_{\mathrm{exciton}} < 0$) mirror image. Concomitantly, a large fraction of the blueshifted background (Figure 8.5a) has decayed. Over time, the exciton redshift reaches a maximum around $\approx 50\,\mathrm{ps}$, where the background shift starts to fluctuate around zero or even becomes slightly negative. On the other hand, the narrowed exciton line shows little to no decay.

While the agreement between the quantitative fit and the qualitative analyses presented above is remarkable, we also want to point out a shortcoming of our approach. We implemented the Gaussian amplitude and width as two different fit parameters to account for possible areal changes. In this respect, the area is proportional to the product of the width and the amplitude. As shown in Figure 8.5d (bottom panel), the Gaussian area seemingly increases after photo-excitation. Likely, this is due to the compensation of overestimated blueshifts. In this respect, we refitted the data-set while constraining the Gaussian area, and we plotted those fit parameters in Figure 8.5a-c in grey. Most importantly, the trend of the fit parameters is similar, yet the initial blueshifts and line broadening are slightly reduced in intensity, while at a longer delay, the exciton redshift gained in intensity and the narrowed line shows a decay over time.

8.2   Optical   Pump   Terahertz   Probe   Spectroscopy

For expertise in Optical Pump Terahertz (THz) Probe (OPTP) spectroscopy, we rely on a collaboration with the Laurens Siebbeles Group (Optoelectronic Materials Section, Department of Chemical Engineering, Delft University of Technology).
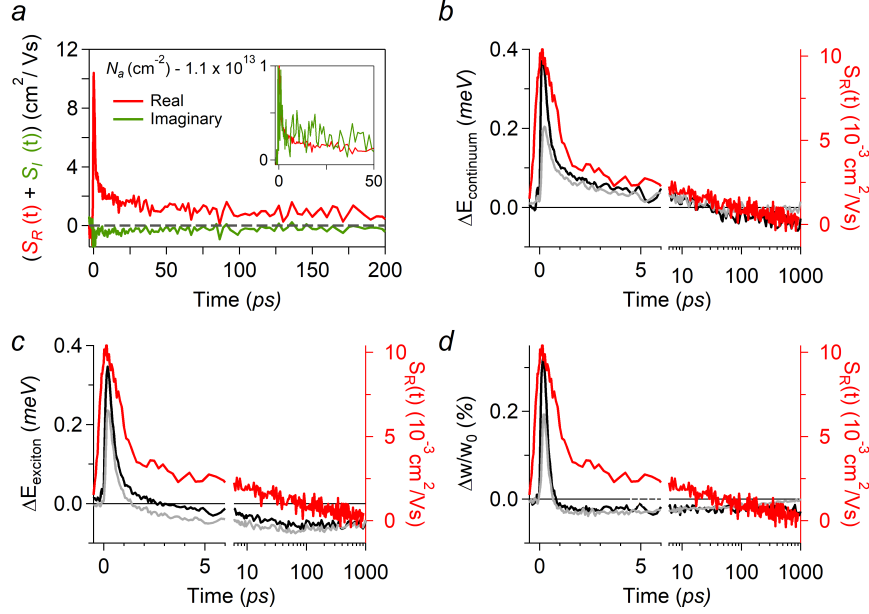
Figure 8.6: (a) Real and imaginary THz conductivity signal as a function of time obtained after photoexcitation ($\hbar\omega = 3.1\,\mathrm{eV}$, 1.1×10^{13} photons $\mathrm{cm^{-2}}$). (b-d) Evolution of the fit parameters (markers) that were obtained from a fit to a Gaussian $G(h, E_{\mathrm{exciton}}, w)$ and a background absorbance $C(E)$ to the ΔA, including (b) the shift of the background absorbance ΔE_{bck} and, (c) the energy shift of the exciton $\Delta E_{\mathrm{exciton}}$, (d) the normalized change in the width $\Delta w/w_0$.

Principle OPTP spectroscopy offers the possibility to distinguish between electron-hole pairs bound in a neutral exciton or charge carriers that are moving freely through the lattice. We are particularly interested in ascertaining whether the spectral signatures in TAS can be reconciled with the generation and decay of free charge carriers and/or neutral excitons.

Results Figure 8.6a plots the real ($S_R(t)$, red trace) and imaginary components ($S_I(t)$, green trace) of the photoinduced THz conductivity $S(t)$, measured on a $\mathrm{ReS_2}$ film after photoexcitation with a 3.1 eV pump pulse[1]. Generally, photoexcitation generates free charges and/or excitons. From this perspective, a real THz conductivity can

---

[1]$S(t)$ is averaged over the frequency domain $0.5 - 1.1$ THz

be assigned to the motion of free (mobile) charges with an in-phase velocity to the THz field.[281, 282] The real THz conductivity is directly proportional to the time-dependent quantum yield of electrons and holes $\Phi(t)$ weighted by the real component of the sum of the electron and hole mobility μ_R

$$S_R(t) = \Phi(t)\mu_R \tag{8.3}$$

In Figure 8.6a, $S_R(t)$ (assigned to free charges) exhibits a fast decay on a time scale of 2 picoseconds at an absorbed photon density of 1.1×10^{13} photons cm^{-2}. The remaining signal decays on a much longer time scale of several hundreds of picoseconds in the second stage.

On the other hand, an imaginary conductivity signal relates to the motion of free charges with an out-of-phase velocity. In addition to back-scattered free charges, a polarized exciton also yields an imaginary conductivity signal.[281–283] The exciton polarizability, α, measures how easily an applied electric field induces a dipole moment and is assessed by $\alpha_{theory} = \frac{2e^2a_B^2}{E_1-E_0}$.[284] In this expression, the summation over all higher exciton states is reduced to the first order, and the transition dipole moment equals the 2D exciton Bohr radius, $a_B = 1$ nm,[285] and $E_1 - E_0$ is set to the exciton binding energy of ReS$_2$.[285] This yields an exciton polarizability α_{theory} of 0.24×10^{-35} Cm^{2}V^{-1}; a value lower than the experimental detection limit. As α_{theory} is below the detection limit, the observation of a small, albeit detectable, imaginary conductivity is attributed to back-scattering of free charges on randomly oriented stacks of ReS$_2$ flakes. Indeed, after normalization, $S_R(t)$ and $S_I(t)$ follow a similar decay (see inset Figure 8.6a), which strongly confirms the presence of free charges after photoexcitation.

Returning the to spectral deconvolution of the ΔA maps presented in section 8.1.4, we plot the real THz photoconductivity together with the evolution of the fit parameters as assessed by TAS, and summarize this information in Figures 8.6b-d.

8.3   A Mechanistic Picture of the Ultrafast Photophysics in ReS$_2$

Different analyses on the ΔA maps, including a derivative analysis and a spectral deconvolution, along with THz data, mark a peculiar inter-
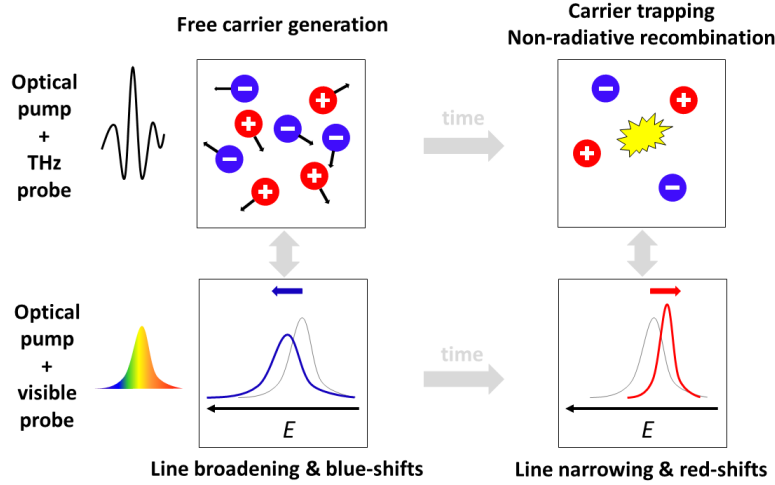
Figure 8.7: Schematic representing the ultrafast response of ReS$_2$.

play between line width changes and spectral shifts whose evolution coincides with the decay of the real component of the THz conductivity. In particular, we list the following set of observations:

- As evidenced by a pronounced real THz conductivity signal, photoexcitation generates mobile free charge carriers.

- After photoexcitation, the width of the exciton band is broadened. Also, at early delays, we observe an instantaneous blueshift ΔE (toward higher energy) of the entire absorbance spectrum, both of the exciton and the higher-lying energy states. The evolution of both the shift and broadening corresponds remarkably well to the dynamics of the real THz conductivity and reflects a similar origin. In other words, free charge carriers blueshift and broaden the absorbance spectrum.

- During the next ≈ 2 ps, the real THz conductivity plunges, and this decrease coincides with the decay of the exciton linewidth, the exciton blueshift, and the background blueshift. While the background remains slightly blueshifted, the exciton line has decayed into its mirror image, it is redshifted and narrowed, and this spectrum decays slowly over the next hundreds of picoseconds where the real THz conductivity remains fairly constant.

Based on the acquired data, we outline two dominant regimes, which

we discuss in sufficient detail afterward

1. (Regime I) The optical pump generates free charge carriers that initially broaden the exciton resonance due to collision broadening and blueshift the absorbance due to a free carrier screening mechanism. We discuss the consistency of our data-set with two possible explanations (i) screening of Coulomb forces, resulting in binding energy reduction (BER) and bandgap renormalization (BGR), and (ii) screening of an internal electric field.

2. (Regime II) Free charges decay through a non-radiative recombination mechanism, presumably defect-assisted trapping. Lattice heating or bandgap renormalization induces a cross-over from a blue to a redshift, and trapping reduces the (in)homogeneous linewidth. In particular, we outline a series of mechanisms that might explain a reduction in the exciton linewidth.

8.3.1 Regime I – free carrier excitation, linewidth broadening and blueshifts

Collisional broadening   Collisional broadening is responsible for broadening spectral lines in atoms and molecules and absorption and emission lines in semiconductors.[260, 286–288] In this context, it's worth mentioning that scattering between an exciton and a free carrier is more efficient than the mutual scattering between excitons.[288] Both mechanisms are also more pronounced in 2D compared to 3D.[289] As a blueshift accompanies the broadened line, it likely rules out a temperature-induced effect (*i.e.*, exciton-phonon scattering). As such, when the probe generates an exciton, scattering with free charge carriers dephases the exciton state, causing a broadening following the uncertainty principle $\Delta E \Delta \tau \sim \hbar/2$.

Bandgap renormalization (BGR) and binding energy reduction (BER)   The central position of an exciton resonance E_X depends on the exciton binding energy E_b and the free-particle bandgap E_g such that $E_X = E_g - E_b$.[29] It is well-known that the presence of carriers alters the Coulomb potential experienced by electrons and holes. Screening of attractive electron-hole and repulsive electron-electron interactions decreases the exciton binding energy (binding energy reduction, BER), causing blueshifts, and renormalizes the bandgap (bandgap renormalization, BGR), causing

redshifts.[273] Both mechanisms work in spectrally opposite directions, yet do not fully compensate in quasi-2D systems. As such, screening either results in a blue or a redshift of the exciton line.[259] For instance, blueshifted exciton transitions resulting from screening have been observed in quasi-2D QWs,[259, 287, 288, 290] atomically-thin TMDs,[260, 291, 292] and 2D layered perovskites.[293] In MoS$_2$[260] and WS$_2$,[291, 292] blueshifts at early delays were always accompanied by a broadening, similar to our observations.

It is worth mentioning that studies typically focus on the lowest-lying exciton state within this context and rarely address the higher-lying energy levels. This makes it more challenging to rationalize a blueshift of the absorption of the higher-lying energy states. Theoretical work addressing the broadband optical response of MoS$_2$ in the presence of excited carriers showed a clear difference between the excitonic response and the higher energy C band absorption. While the excitons engaged in a distinctive competitive behavior between the BGR and BER, the C peak was relatively stable against increasing carrier densities and even showed signs of a small blueshift, see Reference 294, figure 5. In this regard, the work by Steinhoff *et al.* suggests that an interpretation of higher-lying energy states is far from trivial. We are not aware of any experimental work that addresses the evolution of energy states at high energy in the presence of photoexcited carriers.

On the other hand, it has been reported that the energy states of 2D materials are quite sensitive to their dielectric environment. Rigid band shifts have been observed when TMDs were embedded in a matrix with a different permittivity.[295] For instance, Heinz and co-workers observed a blueshift of the lowest-lying exciton levels (n=1, n=2) and the higher-lying C-band absorption when embedding WS$_2$ in a low κ/ε environment (h-BN).[295] Considering that, in our experiments, the exciton state $\Delta E_{\text{exciton}}$ and the background absorbance ΔE_{bck} shift in a similar manner, it is not unexpected that a strong photo-excitation density alters the dielectric environment of the sheet leading to a rigid shift of the entire absorbance.

Internal field screening An alternative interpretation could involve the screening of an internal electric field. In this regard, let us first review the influence of an applied electric field on the optoelectronic properties of a quantum well. Numerous authors have studied such effects.[296–299] An applied field results in a pronounced

redshift and a broadening of the exciton line. For parallel fields to the QW, the dominant effect is broadening due to field ionization that shortens the exciton lifetime (Stark Broadening),[297] while perpendicular fields give rise to a dominant redshift,[272, 296–299] an effect labeled as the Quantum Confined Stark Effect (QCSE).[297] Besides redshifting the lowest-lying exciton, an electric field also shifts higher energy levels to lower energy,[300, 301] and allows forbidden transitions to occur.[272, 302, 303]

The opposite case, in which an internal field is screened by photogenerated charge carriers has been addressed by pump-probe experiments on epitaxially grown quantum wells. In these studies, a blueshift of the excitonic absorption and/or a narrowing of the resonance dominates the ultrafast response.[304–308] The observations are explained as follows. Excitons that are generated by the pump are dissociated under the influence of the internal field. The electrons and holes are pushed toward the opposite sides of the well. As long as the carriers stay in the well, the intrinsic field strength is screened. Consequently, the exciton line sharpens and blueshifts through a reduction of the QCSE, and, its oscillator strength increases due to an enhanced overlap of the electron and hole wavefunctions.[272, 297, 309] Although Shikanai et al.[304] mentioned that this would also lead to a blueshift of the continuum states – such an interpretation would be in line with the PC spectroscopy studies addressed above[300–302] – no experimental TA studies are addressing this claim; as generally, if not exclusively, the lowest-lying exciton is probed.

As addressed above, extensive research conducted by Miller and co-workers[297] outlined that, for parallel fields to the QW, field ionization predominantly produces changes in the line width, while in the case of perpendicular fields a shift dominates the optoelectronic response. As such, a blueshift suggests the screening of a perpendicular field along the c-axis of ReS_2. Such a spontaneous polarisation would require a polar crystal structure or a dipole moment with its vector direction pointing perpendicular to an individual sheet. Unlike 2H TMDs, such as $MoS(e)_2$ and $WS(e)_2$, ReS_2 crystallizes in a distorted 1T'-$CdCl_2$ lattice-type, similar to WTe_2. Although a ReS_2 monolayer (unit cell) is centrosymmetric, as it has no inversion center, exfoliated multi-layered stacks of ReS_2 are known to favor an anisotropic AB stacking order where one layer shifts with respect to the other.[70, 171] We, indeed, observed such a stacking order by Raman spectroscopy. In a similar case, Cobden and co-workers reported the presence of

ferroelectricity in bilayer 1T'-WTe$_2$, while it was absent in a mono-layer.[310] This distinctive behavior stemmed from surface dipoles which arise due to the uniquely distorted 1T'-phase. In this respect, this literature survey suggests that an internal field in ReS$_2$ is not unlikely.

8.3.2   Regime II: free carrier decay, linewidth narrowing and redshifts

Lattice heating and bandgap renormalization A cross-over from a blue to a redshift has been observed in WS$_2$.[291,292] In these studies, the cross-over was attributed to an initial blueshift due to BER, followed by a redshift due to lattice heating, arising from non-radiative recombination of carriers. On the other hand, as outline above, a sudden change in carrier population would also alter the intricate interplay between BER and BGR. Irrespective of whether the redshift is induced by a temperature effect or by a variation in carrier density, tipping the fragile balance between BER and BGR, both mark a similar underlying trapping event, an interpretation in line with a sudden drop in the real THz conductivity.

Linewidth narrowing As carrier-carrier scattering induces a broadening of the line, carrier loss inevitably reduces the width. While such a process accounts for the decay in broadening, it does not explain the small, albeit measurable, narrowing we observe afterward. A line narrowing might occur due to different mechanisms. Nonetheless they all reflect a non-radiative capture event

1. As pointed out above, a line narrowing can be interpreted as screening of in-plane electric fields that could arise from local potentials, for instance, as a result of charged or ionized defects.[258,311] As such, localization of charge carriers, for instance, by defect-assisted trapping, screens local potentials and narrows the linewidth of the exciton

2. Alternatively, the linewidth of a transition narrows when the energy landscape is homogenized. Heinz and co-workers outlined that dielectric disorder is the dominant source of inhomogeneities in 2D materials.[312] Dielectric disorder originates from local fluctuations in the permittivity of the dielectric environment. Fluctuations on ε introduce a spatial modulation of the Coulomb interaction, which strongly affects the exciton's

     linewidth. As such, it is not unsurprising that, charge carriers capture homogenizes the energy landscape by reducing dielectric disorder.

3. An alternative interpretation relates to the stacking order in ReS_2, leading to two dominant polytypes, labeled as AB (anisotropic) and AA (isotropic). Recently, it has been reported that spectral lines in the AB polytype are broader and blueshifted with respect to AA.[69] These differences are associated with a stronger interlayer coupling between stacked ReS_2 layers in the AB polytype – the dominant polytype present in LPE ReS_2 (see chapter 3). In this respect, a sudden carrier capture event would locally polarize/charge the sheet and reduce the interlayer attraction – thereby partially undoing differences between AB and AA. As a result, the exciton transition redshifts and narrows.

8.4 Conclusion

We have presented a detailed study on the charge carrier decay in photoexcited ReS_2 by combining broadband femtosecond transient absorbance spectroscopy and femtosecond THz spectroscopy. By THz spectroscopy, we demonstrated that optical excitations generate free charge carriers in ReS_2. In particular, we found a peculiar interplay between different optical nonlinearities observed in the TA spectrum – linewidth changes and spectral shifts – and the evolution of the photoexcited free charge carrier population. From a phenomenological perspective, we discussed the consistency of our data-set with different mechanisms that could lead to such rich spectra. For one thing, the presence of free charges initially broadened the exciton resonance due to collision broadening and blueshifted the absorbance due to free carrier screening. In a second stage, the free carrier population decayed, and this decay coincided with a cross-over from a blue to a redshift associated with lattice heating or bandgap renormalization and reduction in the inhomogeneous linewidth of the exciton. Besides providing insights into a series of optical nonlinearities, the generation of mobile charges in such ultrathin materials is equally interesting from a practical point of view, as mobile charges are highly desired in any photovoltaic device or photodetector.

9

General Conclusion

As central objective throughout this work, we studied solution-based methodologies to prepare two-dimensional transition metal chalcogenides. Doing so, we touched on a series of topics, of which knowledge in one domain proved key to advance in an other domain. In this manuscript's final chapter, we summarize the main findings in each chapter, and we provide directions for further research.

9.1 Conclusions to Part *I*

Chapter 2: Like Likes Like, Descriptors for Solubility

Scientific progress owed much to the use of simple conceptual models to explain complex phenomena; a mental picture often goes a long way. In the first chapter of Part *I*, we introduced a binary lattice model to conceptualize the behavior of mixtures (section 2.2) and provided a general overview of solution theory within the framework

of a lattice model. Using such a model, we related abstract thermo-dynamic concepts, (free) energy and entropy, to tangible interactions at the molecular level. As entropy relates to the number of ways a state can be realized, entropic effects typically promote mixing. In particular, we emphasized that energetic changes are associated with the formation and breaking of molecular bonds. As such, solubility depends on a trade-off between those effects – a result clearly in line with chemical intuition.

Most conveniently for experimental inquiry energetic effects can be expressed in terms of the solubility parameter difference of the pure substances (section 2.3). Consequently, matching the solubility parameters of individual constituents within mixtures minimizes the energy of mixing, thereby maximizing the solubility of a solute in a solvent. In such a way, the solubility parameter offers a quantitative description of the qualitative notion *like likes like*. The simple notion of *solubility parameter matching* as a central requirement for forming stable mixtures will be used throughout the first part of the manuscript on numerous occasions.

Chapter 3: Liquid-Phase Exfoliation of ReS_2 by Solubility Parameter Matching

Using the concepts outlined in chapter 2, we investigated the factors that determine the successful liquid-phase exfoliation of ReS_2, and we analyzed the main characteristics of the resulting ReS_2 flakes. By screening LPE in a wide range of solvents, we showed that conditions for high yield exfoliations could be understood from (polymer) solution thermodynamics, where the most optimal solvents are characterized by similar Hildebrand and Hansen solubility parameters (section 3.2). The ensuing matching of Hildebrand or Hansen solubility parameters enabled us to compare LPE of ReS_2 with more established exfoliated 2D materials such as graphene or MoS_2. Using N-methyl-2-pyrrolidone as a good exfoliation solvent, we undertook a detailed analysis of the exfoliated ReS_2, which showed that the LPE procedure proposed by us produces few-layer, anisotropically stacked, and chemically pure ReS_2 platelets with long-term chemical stability (section 3.3). Accordingly, we concluded that LPE is a suitable method to produce few-layer and pristine ReS_2 flakes that are apt for post-processing and device incorporation.
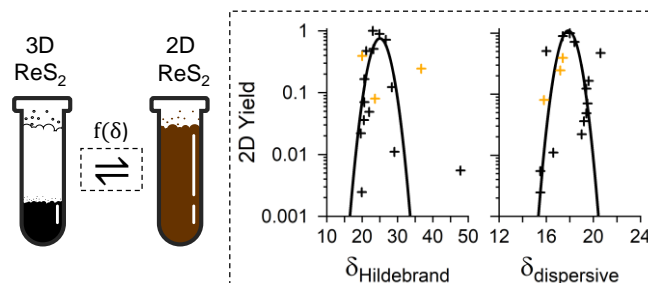
Figure 9.1: Overview of chapter 3.

Chapter 4: Solubility Parameters as Descriptors for Stable Colloidal MoS_2 Dispersions

Starting from a series of observations, supplemented by extensive analysis, we extended the solution thermodynamics approach to colloidal TMD systems. In doing so, we touched upon a series of topics, starting with the synthesis of MoS_2 by colloidal chemistry (section 4.2). In this respect, we carried out a detailed analysis of MoS_2 produced by colloidal chemistry using a combination of UV-Vis absorbance spectroscopy, Raman spectroscopy, XRD, TEM, and AFM. By combining these tools, we assessed that the synthesized MoS_2 flakes contained 3 monolayers on average and adopted the 2H semiconducting phase – the desired phase for optoelectronic applications.

Starting from the empirical observation that the MoS_2 dispersions were colloidally unstable, we first studied their surface by NMR spectroscopy (section 4.3). Combining 1D and 2D NMR techniques, we observed that ligands are not tightly bound to the MoS_2 surface yet engage in a dynamic adsorption/desorption equilibrium, exchanging between a free and a bound state. Accordingly, we concluded that this behavior is likely to cause their limited colloidal stability in conventional solvents, such as hexane and toluene. Based on their crystal structure, which features extended sulfur planes, we speculated that soft metal complexes might stabilize the dispersions through adhesion by donor-acceptor interactions (section 4.4). While supplying a metal salt in excess stabilized the dispersions in conventional solvents, removing the excess by a standard sequence of successive precipitation and redispersion easily destabilized the colloid. By NMR spectroscopy, we again interpreted these observations as a manifestation

of dynamic ligand interaction.

Lastly, reasoning from the observation that the stability is heavily dependent on solvent choice, we screened the stability of colloidal MoS_2 NCs in a wide range of solvents (section 4.5). Similar to our work on the LPE of ReS_2 in chapter 3, we show that this behavior can be understood from solution thermodynamics, where the solubility parameter of the solvent is a successful descriptor to predict the *solubility* of colloidal MoS_2 NCs. The ensuing matching of the solubility parameter enabled us to compare colloidal MoS_2 to MoS_2 produced by LPE. The excellent agreement between materials produced by very different methods underscored that the stability of synthesized flakes correlates with the energy of mixing of the flakes/solvent mixture rather than being an effect of electrostatic ligand repulsion. These findings complemented our NMR analyses, which demonstrated ligands with a minimal affinity toward the NC surface, engaged in a highly dynamic adsorption/desorption equilibrium. Notably, these findings contrast other low-dimensional systems synthesized by hot-injection where steric/electrostatic ligand repulsion is the main driving force that prevents aggregation. As a result, colloidal MoS_2 NCs are stable in solvents with higher solubility parameters than those typically used to disperse NCs prepared by hot-injection. Suitable solvents resulting from this include aromatic solvents with polar groups, such as *o*-dichlorobenzene, or even polar aprotic solvents, such as DMF. We thus conclude that hot-injection yields MoS_2 NCs with comparable interfaces as those produced by LPE. This finding might offer the prospect of using established procedures developed for LPE nanomaterials to post-process TMD dispersions as processable inks.

Chapter 5: Why is Exfoliation of Van der Waals Layered Solids Possible in a Broad Spectrum of Solvents?

Experimental data on a variety of Van der Waals solids, including our studies presented in chapters 3 and 4, marked that exfoliation is possible in a much broader range of solvents than solution theory would allow, based on the size of the dispersed, or exfoliated flakes. Currently, we defined this range of suitable solvents as the *window for good exfoliation solvents*. In this regard, the question arises if such experimental results can be reconciled with solution theory, and, if yes, what thermodynamic quantities would effectively describe the experimental window of good exfoliation solvents?

Figure 9.2: Overview of Chapter 5.

Reasoning from these perspectives, we first complemented our experimental observations with relevant literature data (section 5.2). Irrespective of the exfoliated material characteristics, we found that this window of good exfoliation solvents corresponds to a solubility parameter range of $4.5 - 6.8\,\mathrm{MPa}^{1/2}$ around the optimal matching value. To apprehend the discrepancies between theory and experiment, we rederived the most commonly applied good exfoliation condition, which builds on Flory-Huggins theory to express the fraction of dispersed or exfoliated material as a Gaussian function of the solubility parameter difference, and links the width of the Gaussian to the volume of an individual dispersed flake (section 5.3). In doing so, we highlighted that this relation only applies when the Flory-Huggins free energy yields a miscibility gap between the solvent and the solute. Since any colloid of exfoliated material should be stable when solvent/solute mixtures are predicted to be stable at all compositions, we introduced the critical exchange parameter $\chi_c = 0.5$, above which a miscibility gap arises, as a metric for the experimental exfoliation window. Interestingly, we found that the resulting solubility parameter range corresponds closely to experimentally observed good exfoliation solvent windows. We therefore concluded that solution thermodynamics is apt to describe good exfoliation solvents, provided that the solubility parameter range is linked to the critical exchange parameter for solvent/solute immiscibility.

9.2   Conclusions to Part *II*

Chapter 6: Probing Carriers & Optical Nonlinearities by Pump-Probe Spectroscopy

In the introductory chapter to part *II*, we reviewed the principles behind ultrafast *pump-probe* spectroscopy. By highlighting a couple of historical experiments, we emphasized that an even faster shutter is needed to measure a seemingly continuous motion (section 6.1). Modern pump-probe spectroscopy thrives on this idea and uses two synchronized light pulses to map changes in material properties (section 6.2). An optical *pump* excitation induces a change in a material property, *e.g.*, the absorbance, and a delayed *probe* pulse measures the photo-induced change as a function of energy and delay time. In such a way, using femtosecond lasers, we can disentangle semiconductor physics at otherwise inaccessible time scales. As will become apparent in chapters 7 and 8, an essential aspect will involve interpreting spectral effects, induced by photoexcited carriers, that are encrypted in the experimental data. With this idea in mind, we reviewed a series of spectral effects, and we discussed how they are manifested in a transient absorbance measurement (section 6.3).

Chapter 7: Ultrafast Carrier Dynamics in Few Layer Colloidal Molybdenum Disulfide

Using the established colloidal synthesis procedure detailed in chapter 4, we presented a detailed study on the charge carrier relaxation in photoexcited colloidal MoS_2 nanosheets using femtosecond transient absorption spectroscopy at visible and near-infrared wavelengths. We demonstrated that the transient absorbance after photoexcitation is caused by both a reduction in oscillator strength of the transitions making up the direct gap, and a shift of the entire absorbance spectrum towards lower energy. We attributed these features to state filling and bandgap renormalization, respectively. Through spectral deconvolution, we find that in particular, the *A* exciton bleach exhibits a sub-picosecond decay, which we attribute to rapid hole capture in midgap defect states. The disappearance of spectral shifts at longer delay times reflects the relaxation of the charge carrier distribution by further charge trapping and recombination events. A comparison between the dynamics of photogenerated charge carriers in the case of colloidal MoS_2 nanosheets as measured here and exist-
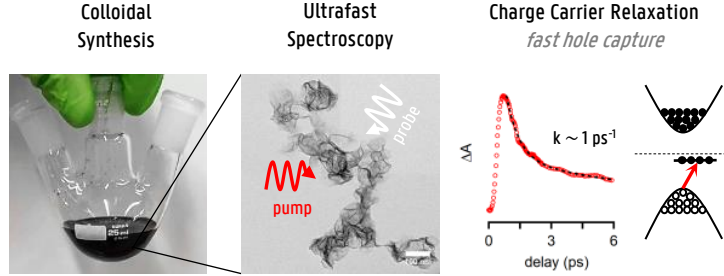
Figure 9.3: Overview of chapter 7.

ing literature on CVD grown MoS_2 nanosheets points towards a very similar sequence of rapid trapping of one carrier type, followed by capture of the remaining carrier on a longer time scale. Accordingly, we conclude that colloidal synthesis yields MoS_2 nanosheets of comparable quality, even if an entirely different chemistry is involved in the TMD production.[262] This shows that TMDs fabricated with both approaches may benefit from similar defect passivation strategies to enhance the lifetime of photogenerated excitons.

Chapter 8: Free Carrier Generation and Optical Non-linearities in Rhenium Disulfide

Thriving on the concepts outlined in chapter 7, we studied the charge carrier decay in photoexcited ReS_2 by combining broadband femtosecond transient absorbance spectroscopy and femtosecond THz spectroscopy. By THz spectroscopy, we demonstrated that optical excitations generate free charge carriers in ReS_2. In particular, we observed a peculiar interplay between different optical nonlinearities observed in the TA spectrum – linewidth changes and spectral shifts – and the evolution of the photoexcited free charge carrier population. From a phenomenological perspective, we discussed the consistency of our data-set with different mechanisms that could lead to such rich physics. For one thing, the presence of free charges initially broadened the exciton resonance due to collisional broadening and blueshifted the absorbance due to free carrier screening. In a second stage, the free carrier population decayed, and this loss co-
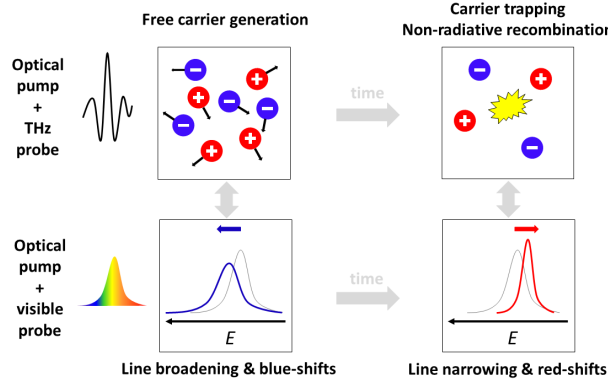
Figure 9.4: Overview of chapter 8.

incided with a cross-over from a blue to a redshift associated with lattice heating or bandgap renormalization and reduction in inhomogeneous exciton linewidth. Besides providing insights into a series of optical nonlinearities, the generation of mobile charges in such ultra-thin materials is equally interesting from a practical point of view as mobile charge carriers are highly desired for photovoltaic devices or photodetectors.

9.3 Perspectives

Extending the Solution Thermodynamics Approach to Other Colloidal Systems

According to the solution thermodynamics approach, optimal dispersion occurs in solvents with solubility parameters that match the colloid solubility parameter (chapters 3 and 4). Besides, the exchange parameter χ of the solvent-solute system determines the window for miscibility, and solutions of large solutes are attained as long as χ is below 0.5 (chapter 5). Reasoning from these perspectives, the use of solubility parameters offered an experimental framework to describe the exfoliation of VdW bulk solids and the stability of colloidal layered TMD systems.

Extending this approach beyond layered systems, 2D CdSe and CdSe/CdS nanoplatelets might be interesting study objects as they suffer from colloidal instability at elevated concentrations. A tightly packed
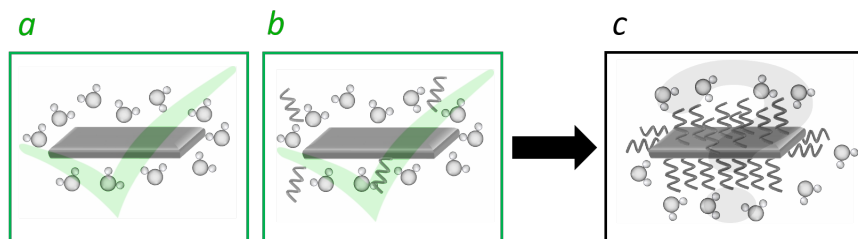
Figure 9.5: Extending the solution thermodynamics approach to other colloidal TMD systems. (a-b) Applying solution thermodynamic to (a) LPE systems and (b) colloidal TMD systems, as narrated in chapter 3-5. (c) Extending the solution thermodynamics approach to other colloidal nanoplatelets passivated by tightly packed ligands?

aliphatic ligand shell passivates such objects, and apolar aliphatic solvents are typically preferred over aromatic solvents.[226, 235] Considering a tight ligand packing without solvent penetration (the solvent only *sees* the ligand shell), the energetic cost associated with mixing a platelet capped with aliphatic ligands is more favorable in aliphatic solvents compared to aromatic solvents due to a more suitable solubility parameter match. Such a simple thought-experiment suggests that solubility parameter matching could apply to other classes of nanomaterials, provided that the solubility parameter is linked to the surface composition. Depending on the geometry and ligand density, the solubility parameter might be a hybrid combination of the ligand packing and the NC composition. From a more general perspective, knowledge of those solubility parameters could aid more rational post-processing of NC dispersions as inks or composites.

Liquid-Phase Exfoliation of $ReSe_2$

Over the last decades, a growing environmental awareness has started an ongoing evolution towards more sustainable technology. Next to the generation of electrical power using renewable sources, for example, solar energy, this also involves using non-toxic materials and the deployment of an environmentally friendly production process. Within this respect, the top-down production of two-dimensional materials in the liquid phase could fit multiple socio-economical needs. Layered transition metal dichalcogenides are promising candidates for applications that involve the absorption of light due to their excep-
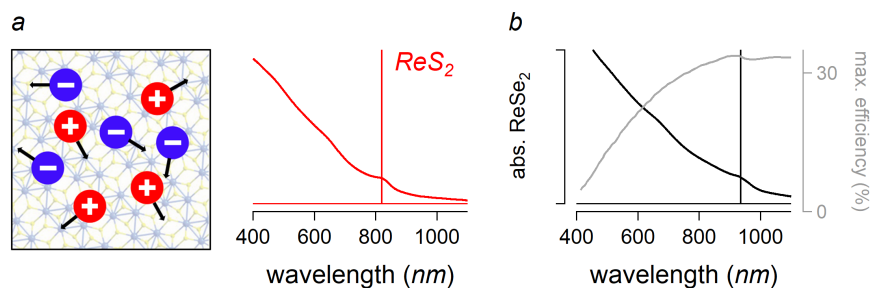
Figure 9.6: Liquid-Phase Exfoliation of $\mathrm{ReSe_2}$. (a) Free charge carrier generation in $\mathrm{ReS_2}$ in chapter 8. (b) Absorbance spectrum of $\mathrm{ReSe_2}$ with an optical bandgap close to the Shockley-Queisser efficiency limit.

tionally high absorption coefficient. Provided that photoexcitation generates free charge carriers in $\mathrm{ReS_2}$ (see chapter 8 and Figure 9.6a), rhenium diselenide ($\mathrm{ReSe_2}$) might be an appealing candidate to explore given its suitable near-infrared bandgap ($\approx 1.3\,\mathrm{eV}$) close to the Shockley-Queisser efficiency limit. In fact, exfoliation of $\mathrm{ReSe_2}$ proved possible in the liquid phase (an absorbance spectrum of $\mathrm{ReSe_2}$ is provided in Figure 9.6b), and a preliminary analysis yielded an optimum solvent solubility parameter of $25.7\,\mathrm{MPa^{1/2}}$ for $\mathrm{ReSe_2}$.

9.4   Scientific Output

Publications in International Journals

1. **Schiettecatte, P.**; Geiregat, P.; Hens, Z. Ultrafast Carrier Dynamics in Few-Layer Colloidal Molybdenum Disulfide Probed by Broadband Transient Absorption Spectroscopy. *The Journal of Physical Chemistry C*, **2019**, *123*(16), 10571-10577.
   * Basis of Chapter 7

2. Zhou, P.; Tanghe, I.; **Schiettecatte, P.**; Van Thourhout, D.; Hens, Z.; Geiregat, P. Ultrafast Carrier Dynamics in Colloidal $\mathrm{WS_2}$ Nanosheets Obtained Through a Hot Injection Synthesis. *The Journal of Chemical Physics*, **2019**, *151*(16), 164701.

3. **Schiettecatte, P.**; Rousaki, A.; Vandenabeele, P.; Geiregat, P.; Hens, Z. Liquid-Phase Exfoliation of Rhenium Disulfide by Solubility Parameter Matching. *Langmuir*, **2020**.
   * Basis of Chapter 3

4. Zhou, P.; **Schiettecatte, P.**; Vandichel, M.; Rousaki, A.; Vandenabeele, P.; Hens, Z.; Singh, S. Synthesis of Colloidal WSe$_2$ Nanocrystals: Polymorphism Control by Precursor-Ligand Chemistry *Crystal Growth & Design*, **2021**.

Conference Contributions

1. **Schiettecatte, P.**; Zhou, P.; Singh, S.; Martins, J.; Hens, Z. The Surface Chemistry and Stabilization of Colloidal Molybdenum Disulfide Nanosheets. *nanoGe September meeting*, Barcelona, Spain, **2017**.

2. **Schiettecatte, P.**; Zhou, P.; Singh, S.; Hens, Z. What's the Role of Ligands in the Synthesis of 2D Materials? *ChemCYS*, Blankenberge, Belgium, **2018**.

3. **Schiettecatte, P.**; Zhou, P.; Singh, S.; Hens, Z. What's the Role of Ligands in the Synthesis of 2D Materials? *Inorganic and Environmental Materials, International symposium*, Ghent , Belgium, **2018**.

4. **Schiettecatte, P.**; Geiregat, P.; Hens, Z. Ultrafast Carrier Dynamics in Colloidally Synthesized Molybdenum Disulfide Probed by Transient Absorption Spectroscopy. *Optical Spectroscopy Workshop*, Ghent, Belgium, **2018**.

5. **Schiettecatte, P.**; Geiregat P.; Hens Z. Ultrafast Carrier Dynamics in Few-Layer Colloidal Molybdenum Disulfide Probed by Broadband Transient Absorption Spectroscopy, *MRS spring meeting*, Phoenix, AZ, USA, **2019**.

A

Experimental Section

A.1   Experimental Section of Chapter 3

A.1.1   Determination of Optimal Solubility Parameters and Exfoliation Conditions for ReS_2

Chemicals. Rhenium disulfide bulk powder (ReS_2, $\geq$ 99%, Alfa Aesar,89482.04), N-methyl-2-pyrrolidone (NMP, $\geq$ 99.0 %, Merck), N, N-dimethylformamide (DMF, $\geq$ 99.0 %, Acros Organics), dimethyl sulfoxide (DMSO, $\geq$ 99.0 %, Merck), 1-butanol ($\geq$ 99.5 %, Merck), 1-methylnaphtalene ($\geq$ 96.0 %, Acros Organics), 1-octyl-2-pyrrolidone (N8P, 98 %, Sigma Alrich), formamide ($\geq$ 99.5 %, VWR), dibenzylether (98.0 %, Sigma Aldrich), diphenylether ($\geq$ 98 %, Merck), quinoline ($\geq$ 99.0 %, Acros Organics), isopropanol (IPA, $\geq$ 99.0 %, ChemLabs), o-dichlorobenzene (o-DCB,$\geq$ 99.0 %, Acros Organics), chlorobenzene ($\geq$ 99.0 %, Merck), diethyleneglycol ($\geq$ 99.0 %, Merck), acetone ($\geq$ 99.0 %, Acros Organics), methanol ($\geq$ 99.9 %, Merck), n-octane (technical $\geq$ 95 % ,VWR chemicals), dodecane ($\geq$ 99.0 %, Merck).

Experimental Procedure. ReS_2 bulk powder was dispersed and sonicated in a broad range of solvents with known Hildebrand and Hansen solubility parameters. We refer to Table A.1 for a detailed account of the solvents used in this study. We prepared the dispersions as follows: 15 mg ReS_2 bulk powder is mixed with 10 mL of solvent and sonicated for a total duration of 3 hours using a bath sonicator (brand: USC-THD, VWR). After sonication, the dispersions are subjected to centrifugation (brand: Eppendorf model 5804) for 30 minutes at a relative centrifugal force of $400g$ (equivalent to 1.5 krpm). The top part of the supernatant ($\approx$ 75%) was carefully removed with a Pasteur pipette and stored for further UV-vis analysis.

Characterization. Attenuance spectra were recorded on a PerkinElmer Lambda 365 UV-vis spectrophotometer in quartz cuvettes with a path length of 1 cm and were baseline-corrected at $\lambda = 1100$ nm.

A.1.2   Liquid phase exfoliation of ReS_2

Optimization of the Centrifugation Time. Bulk ReS_2 was dissolved in NMP at a concentration of 1.5 mg/mL and sonicated for

solvent	δ_{s} $(\text{MPa}^{1/2})$	$\delta_{\text{s,D}}$ $(\text{MPa}^{1/2})$	$\delta_{\text{s,P}}$ $(\text{MPa}^{1/2})$	$\delta_{\text{s,H}}$ $(\text{MPa}^{1/2})$
NMP	23.0	18.0	12.3	7.2
DMF	24.9	17.4	13.7	11.3
DMSO	26.7	18.4	16.4	10.2
1-Butanol	23.2	16.0	5.7	15.8
Methylnaphtalene	21.1	20.6	0.8	4.7
N8P	20.0	17.4	8.8	4.3
Formamide	36.7	17.2	26.2	19.0
Dibenzylether	20.6	19.6	3.4	5.2
2-pyrrolidone	28.4	19.4	17.4	11.3
IPA	23.6	15.8	6.1	16.4
Diphenylether	20.6	19.5	3.4	5.8
Quinoline	22.0	19.4	7.0	7.6
o-DCB	20.5	19.2	6.3	3.3
Chlorobenzene	19.6	19.0	4.3	2.0
Diethyleneglycol	29.1	16.6	12.0	20.7
Water	47.8	15.5	16.0	42.3
Acetone	19.9	15.5	10.4	7.0
Methanol	29.6	15.1	12.3	22.3
Octane	15.1	15.1	0.0	0.0
Dodecane	16.0	16.0	0.0	0.0

Table A.1: List of screened solvents including (second column) the solvent Hilderbrand solubility parameter δ_{s}, (third column) the dispersive Hansen solubility parameter $\delta_{\text{s,D}}$, (fourth column) the polar Hansen solubility parameter $\delta_{\text{s,P}}$, (fifth column) the hydrogen bonding Hansen solubility parameter $\delta_{\text{s,H}}$.

200 minutes. The resulting dispersion was divided over 4 mL aliquot vials and centrifuged at different centrifugation times t_c ($0'$, $1'$, $2'$, $5'$, $15'$, $30'$, $60'$) while keeping the centrifugation rate fixed at $r_c = 400g$ (equivalent to roughly 1500 rpm). The colored supernatant was carefully decanted and measured by UV-Vis spectroscopy.

Optimization of the Centrifugation Rate. Bulk ReS$_2$ was dissolved in NMP at a concentration of 1.5 mg/mL and sonicated for 200 minutes. The resulting dispersion was divided over 4 mL aliquot vials and centrifuged at different centrifugation rates r_c ($0g$, $20g$, $50g$, $150g$, $400g$, $1000g$, $2000g$) while keeping the centrifugation time fixed at $t_c = 30$ minutes. The colored supernatant was carefully decanted and measured by UV-Vis spectroscopy.

Optimization of the Initial Concentration. Bulk ReS$_2$ was dissolved in NMP at concentrations of 0.2 mg/mL, 0.5 mg/mL, 1 mg/mL, 2 mg/mL, 4 mg/mL, 8 mg/mL and 15 mg/mL. and sonicated for 3 hours, centrifugation at 540 g. The resulting dispersion was sonicated for 3 hours and subjected to centrifugation for 30 minutes at a relative centrifugal force of $540g$ (equivalent to 1700 rpm). The colored supernatant was carefully decanted and measured by UV-Vis spectroscopy.

Optimized Experimental Procedure. ReS$_2$ bulk powder was stored in a nitrogen-filled glove box. All other operations were performed under ambient conditions. Our optimized protocol reads as follows: 50 mg rhenium disulfide bulk powder was mixed with 25 mL N-methyl-2-pyrrolidone, and was sonicated for 6 hours using a bath sonicator. During sonication, the temperature was kept below $40 - 45°$C to avoid autoxidative transformations of NMP.[313] The unexfoliated bulk material was separated from the exfoliated flakes by centrifugation for 30 minutes at a relative centrifugal force of $540g$ (equivalent to 1700 rpm). The colored supernatant containing the exfoliated ReS$_2$ flakes was carefully decanted and stored for further analysis. We quantified the amount of dispersed ReS$_2$ from the Lambert-Beer law (A/l $= \varepsilon$C). Using the optical extinction coefficient ε of ReS$_2$ reported by Kang $et\ al.$,[173] the amount of dispersed ReS$_2$ after sonication and centrifugation amounts to $\approx$0.1 g/L. Such numbers line up with literature reports on layered compounds produced by LPE.[100, 173, 183, 314] The dispersions of ReS$_2$ in N-methyl-

2-pyrrolidone were colloidally stable for months with only little sedimentation.

Characterization Samples for TEM were prepared by diluting a ReS_2/NMP dispersion in 2-propanol, and drop-casting this nearly-transparent dispersion on a Holy Carbon-Cu grid (200 mesh, 50 micron). Traces of volatile components were removed by drying the sample overnight in a vacuum tube connected to a schlenk line, or in the antechamber of a glove box. Subsequently, TEM images were taken using a Cs-corrected JEOL 2200-FS TEM operated at an acceleration voltage of 200 kV. For the height analysis, the ReS_2 flakes were imaged by AFM after we cast a diluted dispersion in 2-propanol on a preheated SiO_2 wafer.[186] All measurements were carried out on a Bruker Dimension Edge equipped with a NCHV probe using tapping mode in air. Afterward, the height of a single flake was determined by a fit of the corresponding height profile to a step function in Gwyddion. To measure the particle size distribution, we diluted dispersions further in NMP, and recorded Dynamic Light Scattering (DLS) on a Malvern Nano ZS zetasizer equipped with a He-Ne laser operated at 633 nm. Samples for X-ray photoelectron spectroscopy (XPS) and Raman analysis were prepared by casting a dispersion of ReS_2 in NMP on a glass slide, and removing the solvent under vacuum in the antechamber of a glove box. X-ray photoelectron spectroscopy (XPS) spectra were recorded on an S-Probe Monochromatized XPS spectrometer using a monochromatized Al Kα source operated at 1486 eV as a probe. Further data treatment was carried out in the Casa XPS software. Raman measurements were conducted on a Bruker Optics Senterra dispersive Raman spectrometer attached to an Olympus BX51 microscope and coupled to a thermoelectrically cooled CCD detector, operating at $-65°C$. The spectrometer has an XYZ motorized (automatic) stage for positioning and focusing. The samples were studied as dried films on glass slides. Spectra were obtained in the spectral range of 60 to 1560 cm^{-1} and with a spectral resolution of $3 - 5$ cm^{-1} using a green Nd:YAG (532 nm) laser. The experimental conditions were set at 5 accumulations of 10 seconds, and sufficiently low laser power (0.1 mW) was used. All the samples were measured under a $\times 50$ magnification objective (numerical aperture (NA) of 0.75) with a spot size of 4 μm.

A.2   Experimental Section of Chapter 4

Chemicals   The following chemicals were used in this work: oleic acid (OA, 90%, Alfa Aesar), oleylamine (OLA, 80-90%, Acros Organics), carbon disulfide (CS_2, $\geq$ 99%, Sigma Aldrich), molybdenum(V) chloride ($MoCl_5$, 99.99%, Sigma Aldrich) 1,2-dichlorobenzene (o-DCB, 99%, Acros Organics), 1,2-dichlorobenzene-d_4 for NMR (o-DCB-d_4, 98% atom D, Acros Organics), hexane (normapur, VWR), heptane (99.8%, VWR), octane (99.5%+, Chem-Lab Analytical), cyclohexane (99.5%+, Chem-Lab Analytical), toluene (technical, VWR), acetonitrile (ACN, normapur, VWR), N-methyl-2-pyrrolidone (NMP, $\geq$ 99.0 %, Merck), N,N-dimethylformamide (DMF, $\geq$ 99.0 %, Acros Organics), , 1-methylnaphtalene ($\geq$ 96.0 %, Acros Organics), 1,2-dichlorobenzene (o-DCB,$\geq$ 99.0 %, Acros Organics), ethanol (technical, VWR), methanol ($\geq$ 99.9 %, Merck), pyridine (99.0 %+, VWR) n-octane (technical $\geq$ 95 % ,VWR chemicals)

Colloidal Synthesis of MoS_2 We synthesized MoS_2 nanosheets according to a recent publication by Son *et. al.*[105] To prepare the precursor solution, $MoCl_5$ (54 mg, 0.2025 mmol), OA (2.25 mL) and OLA (15 mL) were mixed together (denoted as mixture 1) in inert atmosphere. At the same time, OLA (15 mL) was loaded into another three-neck round bottom flask (denoted as mixture 2) and degassed at an elevated temperature. Both solutions were flushed with consecutive nitrogen-vacuum cycles to remove traces of residual volatile components. Subsequently, mixture 2 was heated to 320 °C under an inert nitrogen atmosphere. Meanwhile, CS_2 (0.1 mL, in excess) was introduced in mixture 1 at room temperature. This viscous precursor solution was rapidly introduced in a nitrogen-flushed glass syringe and injected over 30 minutes into mixture 2 at 320 °C. After injection, we kept the reaction mixture at 320 °C for another 90 minutes. The MoS_2 sheets were precipitated by adding butanol, collected by centrifugation (10000 g), and redispersed in toluene under mild sonication. Afterward, the sample was subjected to successive washing steps with ethanol as the non-solvent and toluene as the solvent as follows: to a MoS_2 dispersion in toluene, ethanol was added as a non-solvent in a 1:1 ratio with respect to toluene. The dispersion was centrifuged at 5000 rpm for 5 minutes (brand: Eppendorf model 5804). The cloudy supernatant was discarded, and the precipitate was redispersed in the same amount of toluene.

solvent	δ_s (MPa$^{1/2}$)	$f = D_{48}/D_0$ (-)
Hexane	14.9	0.00
Heptane	15.3	0.00
Octane	15.5	0.00
Cyclohexane	16.8	0.09
Toluene	18.2	0.72
Chloroform	18.9	0.60
1,2-dichlorobenzene	20.5	0.99
Methylnaphtalene	21.1	1.03
Pyrridine	21.6	0.99
N-methyl-2-pyrrolidone	23.0	0.87
1-Butanol	23.2	0.59
Acetonitrile	24.4	0.85
DMF	24.9	1.00
Ethanol	26.5	0.15
Methanol	29.6	0.00

Table A.2: List of screened solvents including (second column) the solvent Hilderbrand solubility parameter δ_s, (third column) the ratio between the attenuance after 48 hours D_{48} and the initial attentuance D_0 in each solvent.

For the solubility study, 0.5 mL of MoS$_2$ in toluene (washed once as described above) was divided over 4 mL vials. To each vial, we added 0.5 mL ethanol, centrifuged the dispersion at 5000 rpm for 5 minutes and discarded the clear and colourless supernatant. We added 2 mL solvent (a full solvent list is provided in Table A.2) to each MoS$_2$ pallet, and solubilized the mixture under mild sonication in a bath sonicator for 15 minutes (brand: USC-THD, VWR). Once solubilized, we measured the attenuance of a dilution immediately. After 48 hours, we measured the attenuance D_{48} of stable fraction present in the supernatant in a similar manner.

UV-Vis Spectroscopy Attenuance spectra were recorded on either a PerkinElmer Lambda 950 or a PerkinElmer Lambda 365 spec-

trometer. The samples were studied as diluted dispersions in o-DCB in quartz cuvettes with a path length of 1 cm.

Raman Spectroscopy Raman spectra were recorded on a KAISER dispersive RXNI spectrometer (operating at 532 nm) equipped with a non contact probe. The samples were studied as concentrated dispersions in o-DCB.

X-ray Diffraction X-ray diffraction measurements were carried out on a Thermo Scientific ARM X′tra X-ray diffractometer with the Cu Kα ($\lambda = 0.154$ nm) line as primary source. The samples were studies as films on glass.

Transmission Electron Microscopy Bright-field TEM images were taken on a Cs-corrected JEOL 2200-FS TEM operated at an acceleration voltage of 200 kV. Samples for TEM were prepared by diluting dispersions in toluene, and drop-casting the nearly transparent dispersion on a Holy Carbon-Cu grid (200 mesh, 50 micron). Traces of volatile components were removed by drying the sample overnight in a vacuum tube connected to a schlenk line, or in the antechamber of a glove box.

Atomic Force Microscopy For the height analysis, the particles were imaged by atomic force microscopy (AFM) after we cast a dispersion in o-DCB on a SiO_2 wafer. All measurements were carried out on a Bruker Dimension Edge equipped with a NCHV probe using tapping mode in air.

Nuclear Magnetic Resonance Spectroscopy The samples used in the Nuclear magnetic resonance (NMR) experiments were prepared by drying a purified dispersion containing colloidal MoS_2 in o-dichlorobenzene under a mild nitrogen flow, followed by re-dispersion in deuterated 1,2-dichlorobenzene, henceforth denoted as o-dichlorobenzene-d$_4$. The Nuclear magnetic resonance (NMR) spectra were recorded at a ^{1}H frequency of 500.13 MHz, either on a Bruker Avance III Ascend Spectrometer equipped with a BBI-Z probe or on a Bruker Avance II Spectrometer equipped with a TXI-Z probe. All spectra were measured at a temperature of 298.15 K using standard pulse sequences from the Bruker pulse program library. Quantitative ^{1}H spectra were recorded with a 20s delay between the

scans to ensure a full relaxation of all the NMR signals. Afterwards, the quantification was done using the Digital ERETIC method. Diffusion-Ordered Spectroscopy (DOSY) experiments were recorded using a double stimulated echo sequence to account for convection and a bipolar gradient pulse program to minimize signal loss due to T_2 relaxation. In such an experiment, the diffusion decay was recorded in 64 steps while the squared gradient strength was varied from 95% up to 2% of the probes maximum value. The gradient pulse duration and diffusion delay were optimized to guarantee that at least 90% of the signal decayed at the highest gradient strength. In a Nuclear Overhauser Effect Spectroscopy (NOESY) experiment, the parameters were set as follows: 4096 and 512 time domain points in the direct and indirect dimension respectively, a spectral width of 12 ppm, the number of scans varied from 8 to 32 depending on the signal intensity. The mixing time was 300 ms unless otherwise specified. Afterwards, the data was processed in Bruker TopSpin 4.0.6 and IgorPro 6.

NMR experiments involving lead oleate   Lead oleate was prepared according to the literature.[315] A stock solution was prepared by dissolving lead oleate in o-dichlorobenzene-d$_4$ (27.2 mg in 500 μL). Subsequently, lead oleate was added in a ten-fold excess with respect to the amount of the original ligands (determined by ERETIC) to the dispersion that contains the MoS_2 in o-dichlorobenzene-d$_4$.

A.3   Experimental Section of Chapter 7

Chemicals   The following chemicals were used in this work: oleic acid (OA, 90%, Alfa Aesar), oleylamine (OLA, 80-90%, Acros Organics), carbon disulfide (CS$_2$, $\geq$ 99%, Sigma Aldrich), molybdenum(V) chloride (MoCl$_5$, 99.99%, Sigma Aldrich) 1,2-dichlorobenzene (o-DCB, 99%, Acros Organics).

Colloidal Synthesis of MoS$_2$ We synthesized MoS$_2$ nanosheets based on a recent publication by Son *et. al.*[105] To prepare the precursor solution, MoCl$_5$ (18 mg, 0.0675 mmol), OA (750 μL) and OLA (5 mL) were mixed together (denoted as mixture 1) and degassed under a reduced atmosphere. At the same time, OLA (5 mL) was loaded into another three-neck round bottom flask (denoted as mixture 2) and degassed at an elevated temperature. Both solutions were flushed with consecutive nitrogen-vacuum cycles to remove traces of residual volatile components. Subsequently, mixture 2 was heated to 320 °C under an inert nitrogen atmosphere. Meanwhile, CS$_2$ (0.1 mL, in excess) was introduced in mixture 1 at room temperature. This viscous precursor solution was rapidly introduced in a nitrogen-flushed syringe and injected over 30 minutes into mixture 2 at 320 °C. After injection, we kept the reaction mixture at 320 °C for another 90 minutes. The reaction was cooled down using a heated water bath, and we added a small amount of o-DCB, typically 4 mL, to ensure proper miscibility. The MoS$_2$ sheets were precipitated by adding butanol as a non-solvent, collected by centrifugation (10000 g), and redispersed in o-DCB under mild sonication. Afterward, the sample was subjected to successive washing steps with ethanol as the non-solvent and o-DCB as the solvent. We stored our samples in o-DCB for further analysis.

UV-Vis Spectroscopy   Attenuance spectra were recorded on either a PerkinElmer Lambda 950 or a PerkinElmer Lambda 365 spectrometer. The samples were studied as diluted dispersions in o-DCB in quartz cuvettes with a path length of 1 cm.

Raman Spectroscopy   Raman spectra were recorded on a KAISER dispersive RXNI spectrometer (operating at 532 nm) equipped with a non contact probe. The samples were studied as concentrated dispersions in o-DCB.

X-ray Diffraction X-ray diffraction measurements were carried out on a Thermo Scientific ARM X′tra X-ray diffractometer with the Cu Kα ($\lambda = 0.154$ nm) line as primary source. The samples were studies as films on glass.

Transmission Electron Microscopy Bright-field TEM images were taken on a Cs-corrected JEOL 2200-FS TEM operated at an acceleration voltage of 200 kV. Samples for TEM were prepared by diluting dispersions in toluene, and drop-casting the nearly transparent dispersion on a Holy Carbon-Cu grid (200 mesh, 50 micron). Traces of volatile components were removed by drying the sample overnight in a vacuum tube connected to a schlenk line, or in the antechamber of a glove box.

Atomic Force Microscopy For the height analysis, the particles were imaged by atomic force microscopy (AFM) after we cast a dispersion in o-DCB on a SiO_2 wafer. All measurements were carried out on a Bruker Dimension Edge equipped with a NCHV probe using tapping mode in air.

Transient Absorbance Spectroscopy We recorded transient absorbance spectra by exciting dispersions of MoS_2 nanosheets using 110 femtosecond pump pulses with varying wavelength. Pump pulses were created from the 800 nm fundamental of a 1 kHz laser system (Spitfire Ace, Spectra Physics) through non-linear conversion in an OPA (Light Conversion, TOPAS). Probe pulses in the visible and in the near-infrared window were generated by passing the 800 nm fundamental through a thin CaF_2 or YAG crystal, respectively. Both crystals are translated along one axis to avoid photo-damage from the fundamental. The pulses were delayed relative to the pump using a delay stage with a maximum delay of 6 nanoseconds. The probe spectrum in our experiments covers the UV-VIS window from 350 nm up to 700 nm and the near-infrared window from 850 nm up to 1300 nm. The sheets were dispersed in o-DCB and continuously stirred to avoid charging or photo-degradation. Photon fluxes were determined using a Thorlabs CCD camera beam profiler and a thermal power sensor.

A.4 Experimental Section Chapter 8

Liquid Phase Exfoliation and Film Preparation Dispersions of ReS_2 were produced by liquid phase exfoliation in N-methyl-2-pyrrolidone as reported by us previously. In brief, we mixed 50 mg ReS2 bulk powder ($\geq$99%, Alfa Aesar, 89482.04) together with 25 mL N-methyl-2-pyrrolidone (NMP,$\geq$ 99.0%, Merck) in a centrifugation tube. We sonicated the resulting mixture for a total duration of 6 hours in a sonication bath (USC-THD, VWR) while keeping the bath temperature below 40°C. Subsequently, we subjected the dispersion to centrifugation (Eppendorf model 5804, 30 minutes, 1700 rpm) to separate exfoliated flakes from unexfoliated material. The experimental parameters were optimized in our previous work. The supernatant that contains exfoliated ReS_2 flakes was decanted from the sediment and stored for further use. Such dispersions of ReS_2 in N-methyl-2-pyrrolidone were colloidally stable for months with only little sedimentation over time. ReS_2 films were prepared by dropcasting an ReS_2 dispersion on a quartz substrate, followed by annealing the substrate at 30°C for 20 minutes.

Transient Absorbance Spectroscopy We recorded 2D of the transient absorbance experiments by optically exciting ReS_2/quartz films with 180 fs pump pulses. Pump pulses of variable wavelength (310-1330 nm) were generated from the 1028 nm fundamental of a 5 kHz frequency laser system (Yb:KGW oscillator, Light Conversion, Pharos SP) through non-linear conversion in an Optical Parametric Amplifier (OPA) equipped with a second harmonic module (Light conversion, Orpheus). The pump photon flux was determined with a thermopile sensor (Coherent, PS19Q). Broadband probe pulses (500-1600 nm) are generated by passing the fundamental through a sapphire crystal.

Optical Pump-THz Probe (OPTP) Spectroscopy The OPTP laser system consists of a Micra Oscillator and a Legend HE-USP regenerative amplifier (by Coherent Inc). OPTP measurements were performed by photoexciting ReS_2/quartz films by 60 fs pump pulses, and probing photogenerated charge carriers using single cycle THz pulses generated in a non-linear zinc telluride (ZnTe) crystal via optical rectification.[316] The detection takes place in a ZnTe crystal by spatially overlapping single cycle THz pulses with a chirped optical laser pulse centered at 800 nm such that the entire THz waveform is

detected by a single laser shot. The photogeneration quantum yield of charge carriers, ϕ, and decay kinetics of charge carriers are obtained from the difference, $\Delta E(t_p, t) = E_{excited}(t_p, t) - E_0(t_p)$, of the maximum amplitude of the THz electric field at time t succeeding the optical pump pulse, $E_{excited}(t_p, t)$, and the maximum amplitude of the THz waveform at time, t_p, after generation of the THz waveform, $E_0(t_p)$,in absence of a pump pulse.

B

Supporting Information

B.1   Supporting Information of Chapter 1

B.1.1   Calculation of the Absorption Coefficient of CdSe and MoS_2

We calculated the absorption coefficient of bulk and monolayer[317] molybdenum disulfide[318] and bulk cadmium selenide[319] starting from experimentally determined values of the refractive index n and the extinction coefficient k (see Figures B.1a and B.1c) according to:[187]

$$a_i = \frac{2\pi}{\lambda}Im(\epsilon) = \frac{2\pi}{\lambda}2nk \tag{B.1}$$

To compare a 2D monolayer of MoS_2 to a 2D platelet of CdSe, we convert an absorption spectrum recorded on a dispersion of CdSe nanoplatelets (see Figure B.1c) into an absorption coefficient through an established procedure.[187] Since high energy transitions are less influenced by size quantization, we use the optical constants of bulk CdSe at high energy (4 eV) to rescale the absorption spectrum according to:

$$a_i(E) = \frac{A_{2D}(E)a_{bulk}(4eV)}{A_{2D}(4eV)} \tag{B.2}$$

The results of such an analysis are summarized in Figure 1.4c of the main text. Importantly, the absorption coefficient of CdSe is a factor of 2 lower at the band edge and an order of magnitude lower around 3 eV.
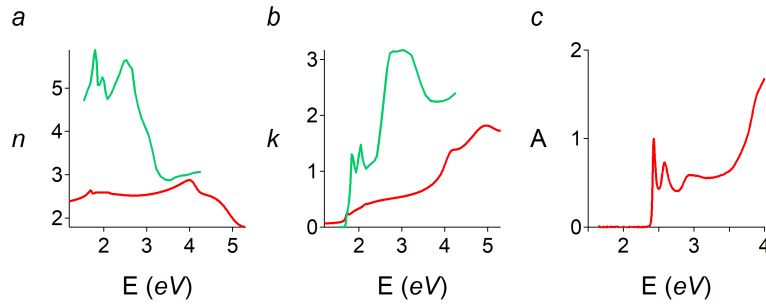
Figure B.1: (a) Extinction coefficient and (b) refractive index of MoS_2 (green) and CdSe (red). (c) Absorption spectrum of CdSe nanoplatelets provided by Alessio Di Giacomo.

B.2　Supporting Information of Chapter 3

B.2.1　Determination of the Solubility Parameters of ReS$_2$ at a Different Wavelength

We determined optimal values for the ReS$_2$ solubility parameters using the attenuance D_{400} at 400 nm and D_{700} at 700 nm. As summarized in Table B.1, the choice of wavelength has no substantial influence on the result.

	$\bar{\delta}$ (MPa$^{1/2}$)	$\bar{\delta}_{\mathrm{D}}$ (MPa$^{1/2}$)	$\bar{\delta}_{\mathrm{P}}$ (MPa$^{1/2}$)	$\bar{\delta}_{\mathrm{H}}$ (MPa$^{1/2}$)
using D_{400}	24.2/24.9	18.0/17.9	11.2/NA	9.6/NA
using D_{700}	24.1/24.8	18.2/18.0	10.4/NA	9.5/NA

Table B.1: Optimal values for ($\bar{\delta}$, $\bar{\delta}_{\mathrm{D}}$, $\bar{\delta}_{\mathrm{P}}$, $\bar{\delta}_{\mathrm{H}}$) for ReS$_2$ determined using (first row) the attenuance D_{400} at 400 nm and (second row) the attenuance D_{700} at 700 nm. Consistent with the main text, we obtained values for the solubility parameters using a weighted arithmetic mean (Eq 1, main text)/a Gaussian fit (Eq 2, main text).

B.2.2 Determination of the Solubility Parameters of ReS_2 With and Without a Baseline Substraction

We determined optimal values for the ReS_2 solubility parameters using the attenuance D_{400} at 400 nm with and without a baseline subtraction at 1100 nm. As summarized in Table B.2, such an approach has no substantial influence on the result.

	$\bar{\delta}$ (MPa$^{1/2}$)	$\bar{\delta}_D$ (MPa$^{1/2}$)	$\bar{\delta}_P$ (MPa$^{1/2}$)	$\bar{\delta}_H$ (MPa$^{1/2}$)
baseline corrected	24.2/24.9	18.0/17.9	11.2/NA	9.6/NA
raw data	24.0/25.1	18.0/18.0	11.2/NA	9.6/NA

Table B.2: Optimal values for $(\bar{\delta}, \bar{\delta}_D, \bar{\delta}_P, \bar{\delta}_H)$ for ReS_2 determined using the attenuance D_{400} at 400 nm (first row) with a baseline subtraction at 1100 nm and (second row) using the raw spectra. Consistent with the main text, we obtained values for the solubility parameters using a weighted arithmetic mean (Eq 1, main text)/a Gaussian fit (Eq 2, main text).

B.2.3 Effect of the Solvent Viscosity

Alzakia *et al.*[320] pointed out that the sedimention velocity is influenced by the viscosity of the solvent η, resulting in overestimated exfoliation yields in viscous solvents. To access whether such effects could influence our results, we plot the attenuance as a function of the solvent viscosity, and we calculate the Pearson correlation coefficient ρ as the ratio between the co-variance σ_{XY} and the product of the standard deviations σ as follows:

$$\rho(D, \eta) = \frac{\sigma_{XY}(D, \eta)}{\sigma_Y(D)\sigma_X(\eta)} \tag{B.3}$$

Values for ρ close to ± 1 predict a perfect correlation, while values near zero imply no correlation. As such, if both variables are positively correlated, we would expect the Pearson correlation coefficient ρ to attain positive values near 1. On the contrary, the correlation coefficient attains a number close zero and thereby points to the absence of a linear correlation between the exfoliation yield and the solvent viscosity.
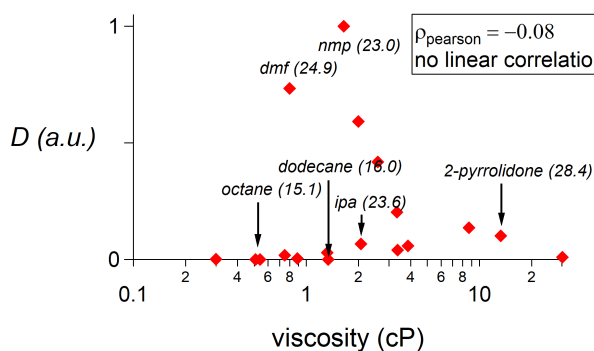
Figure B.2: Plot of the attenuance as a function of the solvent viscosity. The Pearson correlation coefficient calculated for such a data-set amounts to -0.08 and points to the absence of a linear correlation.

B.2.4 SEM Images of $\mathrm{ReS_2}$ Bulk Powder

Rhenium disulfide bulk powder ($\mathrm{ReS_2}$, $\geq 99\%$) was purchased from Alfa Aesar. According to the scanning microscopy (SEM) images provided in Figure B.3, the powder consists of particles with a platelet-like geometry, as expected for TMD bulk powders.[100] Although the powder is relatively poly-disperse and consists of micrometric sized conglomerates, most individual particles have a lateral size of a few hundreds of nanometer at most (see arrows in Figure B.3).
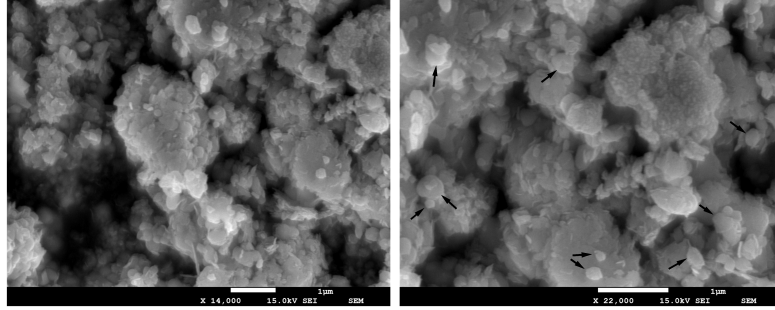
Figure B.3: SEM images of $\mathrm{ReS_2}$ bulk powder. The arrows indicate individual particles observed within larger conglomerates are indicated.

B.2.5   Additional Information on AFM

To estimate the thickness of the ReS_2 platelets, we diluted the dispersion in 2-propanol, cast this dispersion on a pre-heated SiO_2 wafer[186] and imaged the sample by atomic force microscopy (AFM). Figures B.4a-B.4c provide examples of AFM images of exfoliated ReS_2. We have drawn lines along the particles and extracted the height of these profiles, see Figures B.4d-B.4f. The height of a single particle was determined by a fit of the corresponding height profile to a step function in Gwyddion; examples are shown in Figures B.4g-B.4i. We measured the height of 50 particles on different areas on the substrate, and Figure 3.7d in the main text shows the main results of this analysis by plotting the distribution on the thickness.
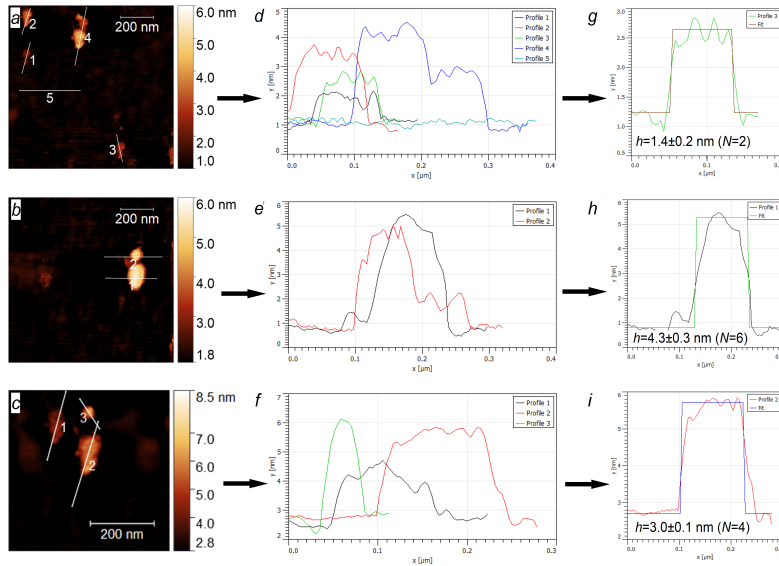
Figure B.4: (a-c) AFM images with a field of view of (a,b) $1\mu m$ by $1\mu m$ and (c) $0.5\mu m$ by $0.5\mu m$. (d-f) Height profiles as outputted by the Gwyddion software along the lines in panels a-c. (g-i) Examples of representative height profiles shown in (d-f) are fit to a step function in Gwyddion, and the height h ($\pm$ error) and the approximate layer number N are indicated accordingly.

B.3 Supporting Information of Chapter 4

B.3.1 Determination of the spectral positions of the A and B resonances

The central wavelength assigned to the A and B exciton was determined from (i) the inflection points of the first derivative of the attenuance spectrum, $\mathrm{d}D/\mathrm{d}\lambda$ (see Figure B.5a) and (ii) a fit of the second derivative $\mathrm{d}^2D/\mathrm{d}\lambda^2$ (see Figure B.5b). As can be seen in Figure B.5, both approaches lead to similar spectral positions.
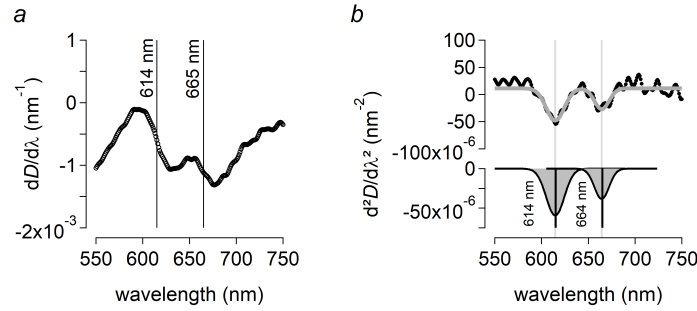
Figure B.5: Determination of the A and B spectral position from a) the first derivative of the attenuance $\mathrm{d}D/\mathrm{d}\lambda$ and b) a global fit to the second derivative $\mathrm{d}^2D/\mathrm{d}\lambda^2$. (top) Data points (black markers), fit (grey). (bottom) Gaussian fit functions describe the A and B exciton features, respectively at 614.4 $\pm$ 0.5 nm and 664.2 $\pm$ 0.7 nm.

B.3.2 Additional Information on Raman Spectroscopy

The Raman spectra are corrected by subtracting the signals related to the solvent, see Figure B.6. The resonances assigned to the solvent o-dichlorobenzene were determined using a blank measurement. The frequency assigned to the A_{1g} and E_{2g}^1 vibrational modes of MoS_2 was determined from the inflection point of the first derivative of the Raman spectrum to the frequency, $dI/d\omega$ (see Figure B.6c) and the local minima of the second derivative to the frequency $d^2I/d\omega^2$ (see Figure B.6d). The values calculated using both approaches lead to similar spectral positions listed in Table B.3.

	$dI/d\omega$ (inflection point)	$d^2I/d\omega^2$ (minimum)
E_{2g}^1	383 cm^{-1}	$383.5 \pm 0.2 \text{ cm}^{-1}$
A_{1g}	406 cm^{-1}	$406.1 \pm 0.1 \text{ cm}^{-1}$
$\Delta\omega$	23 cm^{-1}	$22.6 \pm 0.2 \text{ cm}^{-1}$

Table B.3: Assignment of the spectral positions of the A_{1g} and E_{2g}^1 vibrational modes of MoS_2 in the Raman spectrum using the inflection point of $dI/d\omega$ and the local minimum of $d^2I/d\omega^2$.
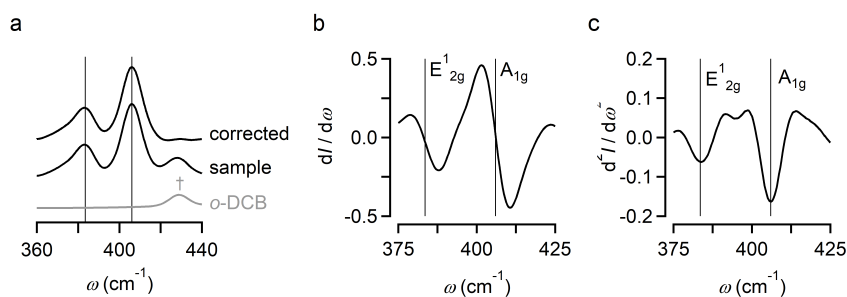
Figure B.6: (a) Raman spectra of (bottom, grey) the solvent o-dichlorobenzene (middle, black) the sample and (top, black) the sample after subtraction. (b-c) The first and second derivatives of the Raman spectrum.

B.3.3 Determining the Diffusion Coefficient from DOSY and the Stejkal-Tanner Equation

A series of 1D NMR spectra are recorded at an increasing gradient field strength in a diffusion NMR experiment. The Stejkal-Tanner equation describes the attenuation of the signal intensity due an increase in the magnetic field gradient, see Equation B.4, for which the different parameters are listed in Table B.4:

$$I = I_0 \exp(-D\gamma_{\text{eff}}^2\delta^2\sigma^2\Delta'G^2) \qquad (B.4)$$

A fit to Equation B.4 holds a value for the translational diffusion coefficient listed in the main text.

parameter	description
D	translational diffusion coefficient
γ_{eff}	gyromagnetic ratio of the nuclei
δ	duration of the pulse field gradient
σ	gradient shape factor
Δ'	corrected diffusion delay for the pulse sequence and the gradient shape
G	gradient field strength

Table B.4: A description of the different parameters that appear in the Stejkal-Tanner equation, see Equation B.4.

B.3.4 Diffusion Coefficient of Lead Oleate

The lead oleate diffusion coefficient was determined according to the same procedure outlined in Section 4.3.4. The DOSY decays are fit to the Stejkal-Tanner equation, see Figure B.7. The diffusion coefficient of the free lead oleate and $MoS_2/Pb(OA)_2$ amount to 206.3 $\pm$ 0.2 $\mu m^2/s$ and 202.7 $\pm$ 1.6 $\mu m^2/s$, respectively.
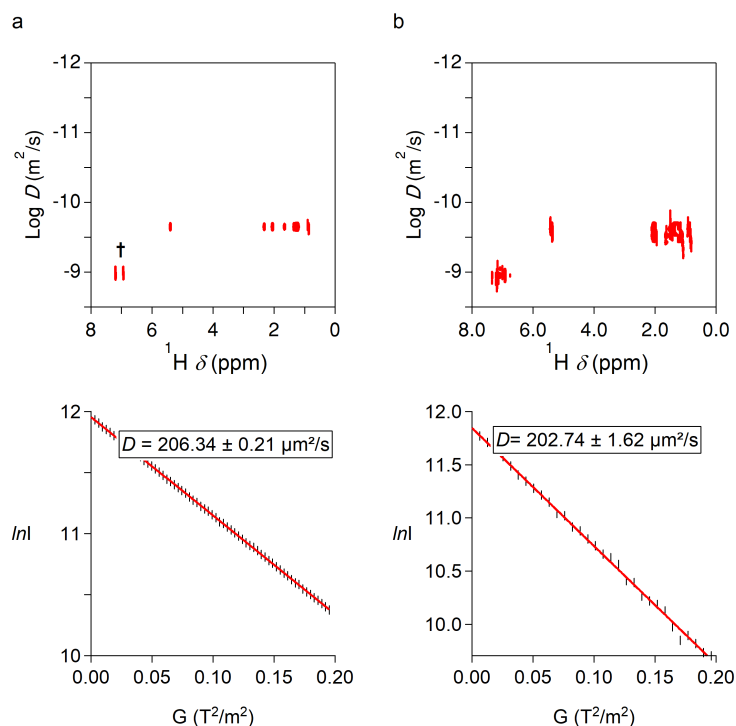
Figure B.7: (a) (top) DOSY NMR spectrum and (bottom) the decay of the intensity to the gradient field strength of a reference sample only containing lead oleate. b) (top) DOSY NMR spectrum and (bottom) the decay of the intensity to the gradient field strength of the sample containing MoS_2 and lead oleate.

B.3.5 T_1 relaxation time and rates of lead oleate

The T_1 relaxation times and corresponding longitudinal relaxation rates R_L were determined through an inverse recovery experiment, yielding values listed in Table B.5.

Resonance	T_1 (s)	R_L (s^{-1})
1	1.6	0.6(3)
2	0.6	1.6(7)
3	0.4	2.5(0)
4	0.6	1.6(7)
5	0.4	2.5(0)
6	1.0	1.0(0)

Table B.5: T_1 relaxation (second column) times and (third column) rates of the different resonances of lead oleate labeled following the main text.

B.4   Supporting Information of Chapter 5

B.4.1   Critical Exchange Parameter for a Regular Mixture

Omitting a (rather tedious) mathematical description, we instead graphically describe mixtures with exchange parameters below, above and equal to the critical exchange parameter χ_c. In doing so, we arrive at the requirement that the second and third derivative of ΔF_{mix} to ϕ_B are zero simultaneously at χ_c. For the sake of simplicity, we describe a regular solution with molecules of type A (solvent) and B (solute) of equal size ($\nu_A = \nu_B = 1$). For such systems, the critical exchange parameter amounts to 2 (Eq 5.13).

Most generally, the free energy of mixing ΔF_{mix} can be written as follows:

$$\Delta F_{mix} = \frac{k_B T}{v_0} \left(\phi_A \ln \phi_A + \phi_B \ln \phi_B + \phi_A \phi_B \chi \right) \qquad \text{(B.5)}$$

Figure B.8a plots ΔF_{mix} as a function of the volume fraction of the solute ϕ_B and for different values of the exchange parameter χ.

The green curve in Figure B.8a signifies an ideal mixture ($\chi = 0$). Such a mixture forms a homogeneous phase at any composition due to a favourable entropy of mixing. As is apparent in Figure B.8b, this condition can be mathematically expressed as a positive second derivative throughout its entire domain.

On the other hand, for an unfavourably large exchange parameter (for instance, $\chi = 3$, red curve), local minima appear and the mixture separates into a phase rich in A and a phase rich in B with respective compositions ϕ' and ϕ''. Such cases are recognized by a second derivative that crosses zero at the inflection points of $\Delta F_{\mathrm{mix}}(\phi_B)$ (see Figure B.8c).

In-between both extremes, one arrives at a limiting condition where the mixture transitions from being completely miscible into a state of limited miscibility. Such a cross-over takes place at an exchange parameter equal to the critical exchange parameter χ_c. Here, $\Delta F_{\mathrm{mix}}(\phi_B)$ has a near zero slope at intermediary compositions (Figure B.8a, orange curve) and the second and third derivative are zero simultaneously (Figure B.8d). Note that for any value of χ, the third derivative
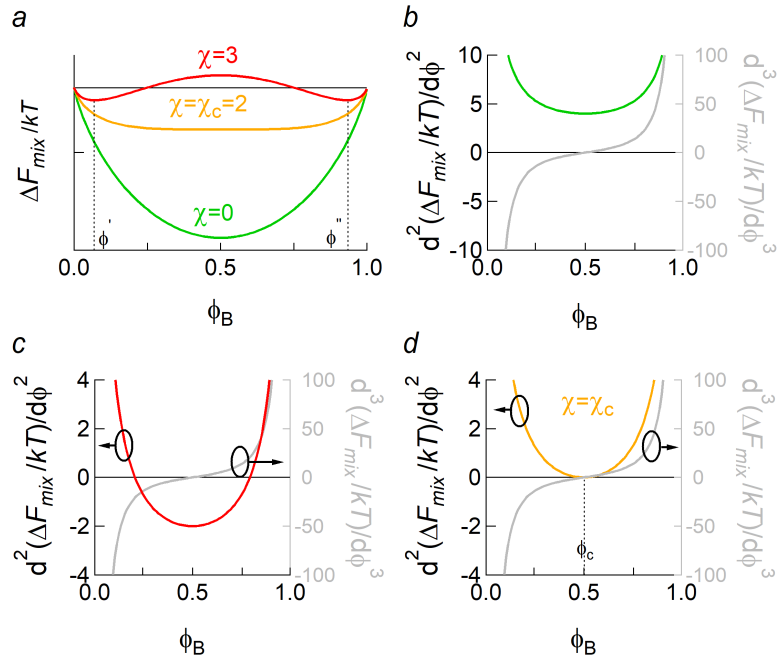
Figure B.8: (a) Plots of ΔF_{mix} as a function of the volume fraction of the solute ϕ_B for $\chi = 0$ (green), $\chi = 2$ (orange) and $\chi = 3$ (red). (b-d) The second (left axis) and the third (right axis, grey) derivatives of ΔF_{mix} to ϕ_B.

is zero at the critical composition ϕ_c, but only at $\chi = \chi_c$ the second and third derivative are zero simultaneously at $\phi = \phi_c$.

B.5   Supporting Information of Chapter 7

B.5.1   Proportionality between ΔA and dA_0/dE in Case of a Spectral Shift $\delta\sigma$

In the case of a pure spectral shift δE, the non-linear absorbance after photoexcitation $A^\star$ will be a function of δE that can be expanded through a Taylor series around the linear absorbance A_0:

$$A^\star = A_0 + \frac{dA_0}{dE}\delta E + \frac{1}{2}\frac{d^2 A_0}{dE^2}\delta E^2 + ...$$

For a δE that is sufficiently small, a Taylor expansion up to the first order yields a direct proportionality between the transient ($\Delta A = A^\star - A_0$) and the derivative of the linear absorbance dA_0/dE:

$$\Delta A \approx \frac{dA_0}{dE}\delta E \tag{B.6}$$

According to Equation B.6, the spectral shift δE can be obtained from the ratio between the transient absorbance and the derivative of the linear absorbance spectrum. Figure B.9 illustrates this proportionality between dA_0/dE and ΔA in the case of a pure spectral shift.
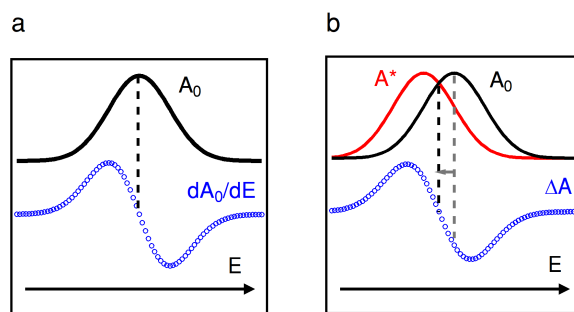
Figure B.9: Pictorial representation showing the relationship between a derivative (a) and a spectral shift (b). A spectral shift closely resembles a derivative-like spectrum except that the inflection point is being slightly off-set. The linear absorption A_0 is indicated in black, and the excited state absorption $A^\star$ in red.

B.5.2   Resonant Excitation at Visible Wavelengths

Similar to the measurements that involve non-resonant photoexcitation and visible probing (Figure 7.6), we observe two short bleach features at the band edge when resonantly exciting near the A exciton around 660 nm (Figure B.10a). The transient absorbance at a fixed probe wavelength indicates a fast stage decaying with a rate of 4.0 ps^{-1}. Similar to the experiments that involve resonant photoexcitation and near-infrared probing (Section 7.4.2), decay rates are slightly accelerated compared to conditions of non-resonant photoexcitation.
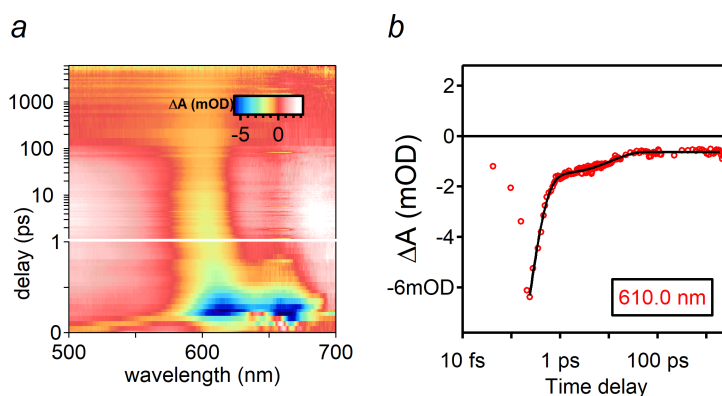
Figure B.10: (a) 2D transient time delay-wavelength map upon 660 nm ($\hbar\omega$=1.88 eV), 110 fs photoexcitation in the wavelength range from 500 nm to 700 nm. b) Temporal dependence of the transient probed at 610 nm. The black line is a fit to a combination of an exponential decay and a fixed background.

B.6 Supporting Information of Chapter 8

B.6.1 Proportionality between ΔA and $\mathrm{d}^2 A_0/\mathrm{d}E^2$ in Case of a Change in Linewidth $\Delta\sigma$

In the case of a pure spectral broadening or narrowing $\Delta\sigma$, the nonlinear absorbance after photoexcitation $A^\star(\sigma)$ can be expanded as a Taylor series around the linear absorbance $A_0(\sigma_0)$

$$A^\star(\sigma_0 + \Delta\sigma) = A_0(\sigma_0) + \frac{\mathrm{d}A_0}{\mathrm{d}\sigma}\Delta\sigma + \frac{1}{2}\frac{\mathrm{d}^2 A_0}{\mathrm{d}\sigma^2}\Delta\sigma^2 + ...$$

Here again, for small values of $\Delta\sigma$, the transient $(\Delta A = A^\star - A_0)$ is directly proportional to the derivative of the linear absorbance to the linewidth $\mathrm{d}A_0/\mathrm{d}\sigma$

$$A^\star(\sigma_0 + \delta\sigma) \approx A_0(\sigma_0) + \frac{\mathrm{d}A_0}{\mathrm{d}\sigma}\Delta\sigma \tag{B.7}$$

Approximating the absorbance spectrum A_0 by a Gaussian function characterized by a spectral position E_0 and a linewidth σ_0, the respective derivatives of A_0 to σ_0 and E are given by

$$\frac{\mathrm{d}A_0}{\mathrm{d}\sigma} = A_0 \frac{E_0^2 - \sigma_0^2}{\sigma_0^3} \tag{B.8}$$

$$\frac{\mathrm{d}^2 A_0}{\mathrm{d}E^2} = A_0 \frac{E_0^2 - \sigma_0^2}{\sigma_0^4} \tag{B.9}$$

Combining Equations B.8 and B.9, the equivalence between $\frac{\mathrm{d}A_0}{\mathrm{d}\sigma}$ and $\frac{\mathrm{d}^2 A_0}{\mathrm{d}E^2}$ reads

$$\frac{\mathrm{d}A_0}{\mathrm{d}\sigma} = \frac{\mathrm{d}^2 A_0}{\mathrm{d}E^2}\sigma_0 \tag{B.10}$$

Using Equations B.7 and B.10, the transient ΔA, expressed as the difference between the nonlinear absorbance $A^\star(\sigma_0 + \Delta\sigma)$ and the linear absorbance $A_0(\sigma_0)$, reads

$$A^\star(\sigma_0 + \Delta\sigma) - A_0(\sigma_0) \approx \frac{\mathrm{d}^2 A_0}{\mathrm{d}E^2}\sigma_0\Delta\sigma \tag{B.11}$$

According to Equation B.11, a transient absorbance that results from changes in linewidth has a one-to-one correlation with the second
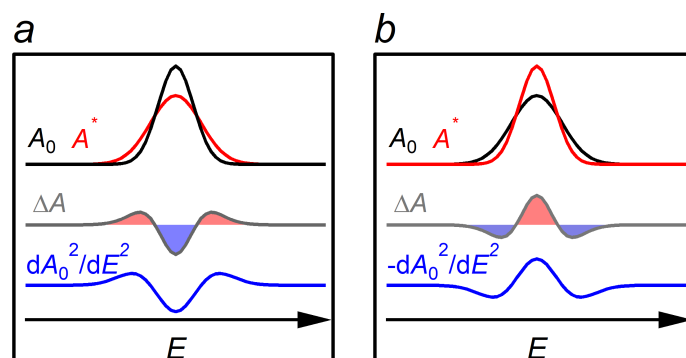
Figure B.11: Pictorial representation showing the relationship between (a) the broadening and (b) the narrowing of a Gaussian resonance, the difference spectrum ΔA and the second derivative of A_0 to E. The linear absorbance A_0 is indicated in black, the excited state absorbance $A^\star$ in red and the transient absorbance ΔA in grey.

derivative of the linear absorbance spectrum to the energy, and the ratio between both functions yields a value for $\sigma_0 \Delta \sigma$. Figure B.11 illustrates this proportionality in the case of the broadening and the narrowing of a Gaussian.

References

[1] Erwin Schrodinger and Erwin Schrödinger. *'Nature and the Greeks' and 'Science and Humanism'.* Cambridge University Press, 1996.

[2] Gordon E Moore et al. *Cramming More Components Onto Integrated Circuits*, 1965.

[3] Richard P Feynman. *There's Plenty of Room at the Bottom.* California Institute of Technology, Engineering and Science Magazine, 1960.

[4] Sujay B Desai, Surabhi R Madhvapathy, Angada B Sachid, Juan Pablo Llinas, Qingxiao Wang, Geun Ho Ahn, Gregory Pitner, Moon J Kim, Jeffrey Bokor, Chenming Hu, et al. *MoS_2 Transistors with 1-nanometer Gate Lengths.* Science, 354(6308):99–102, 2016.

[5] Andre Konstantin Geim. *Graphene: Status and Prospects.* Science, 324(5934):1530–1534, 2009.

[6] Kostya S Novoselov, Andre K Geim, Sergei V Morozov, D Jiang, Y_ Zhang, Sergey V Dubonos, Irina V Grigorieva, and Alexandr A Firsov. *Electric Field Effect in Atomically Thin Carbon Films.* Science, 306(5696):666–669, 2004.

[7] Kirill I Bolotin, K J Sikes, Zd Jiang, M Klima, G Fudenberg, J Hone, Ph Kim, and HL Stormer. *Ultrahigh Electron Mobility in Suspended Graphene.* Solid State Commun., 146(9-10):351–355, 2008.

[8] Alexander A Balandin, Suchismita Ghosh, Wenzhong Bao, Irene Calizo, Desalegne Teweldebrhan, Feng Miao, and Chun Ning Lau. *Superior Thermal Conductivity of Single-layer Graphene.* Nano Lett., 8(3):902–907, 2008.

[9] Rahul Raveendran Nair, Peter Blake, Alexander N Grigorenko, Konstantin S Novoselov, Tim J Booth, Tobias Stauber, Nuno MR Peres, and Andre K Geim. *Fine Structure Constant Defines Visual Transparency of Graphene.* Science, 320(5881):1308–1308, 2008.

[10] Ganesh R Bhimanapati, Zhong Lin, Vincent Meunier, Yeonwoong Jung, Judy Cha, Saptarshi Das, Di Xiao, Youngwoo Son, Michael S Strano, Valentino R Cooper, et al. *Recent Advances in Two-Dimensional Materials beyond Graphene.* ACS Nano, 9(12):11509–11539, 2015.

[11] Kin Fai Mak, Changgu Lee, James Hone, Jie Shan, and Tony F Heinz. *Atomically Thin MoS_2: a New Direct-gap Semiconductor.* Phys. Rev. Lett., 105(13):136805, 2010.

[12] Andrea Splendiani, Liang Sun, Yuanbo Zhang, Tianshu Li, Jonghwan Kim, Chi-Yung Chim, Giulia Galli, and Feng Wang. *Emerging Photoluminescence in Monolayer MoS_2.* Nano Lett., 10(4):1271–1275, 2010.

[13] RF Frindt and AD Yoffe. *Physical Properties of Layer Structures: Optical Properties and Photoconductivity of Thin Crystals of Molybdenum Disulphide.* Proceedings of the Royal Society of London. Series A. Mathematical and Physical Sciences, 273(1352):69–83, 1963.

[14] RF Frindt. *Single Crystals of MoS_2 Several Molecular Layers Thick.* J. Appl. Phys., 37(4):1928–1929, 1966.

[15] Jl A Wilson and AD Yoffe. *The Transition Metal Dichalcogenides Discussion and Interpretation of the Observed Optical, Electrical and Structural Properties.* Adv. Phys., 18(73):193–335, 1969.

[16] F Consadori and RF Frindt. *Crystal Size Effects on the Exciton Absorption Spectrum of WSe_2.* Phys. Rev. B, 2(12):4893, 1970.

[17] RF Frindt. *Superconductivity in Ultrathin $NbSe_2$ Layers.* Phys. Rev. Lett., 28(5):299, 1972.

[18] Jl A Wilson, FJ Di Salvo, and S Mahajan. *Charge-density Waves and Superlattices in the Metallic Layered Transition Metal Dichalcogenides.* Adv. Phys., 24(2):117–201, 1975.

[19] Tawinan Cheiwchanchamnangij and Walter RL Lambrecht. *Quasiparticle Band Structure Calculation of Monolayer, Bilayer, and Bulk MoS_2*. Phys. Rev. B, 85(20):205302, 2012.

[20] Shuji Nakamura, Takashi Mukai, and Masayuki Senoh. *Candela-class Gigh-brightness InGaN/AlGaN Double-heterostructure Blue-light-emitting Diodes*. Appl. Phys. Lett., 64(13):1687–1689, 1994.

[21] Yu Ye, Zi Jing Wong, Xiufang Lu, Xingjie Ni, Hanyu Zhu, Xianhui Chen, Yuan Wang, and Xiang Zhang. *Monolayer Excitonic Laser*. Nat. Photonics, 9(11):733, 2015.

[22] Jason S Ross, Philip Klement, Aaron M Jones, Nirmal J Ghimire, Jiaqiang Yan, DG Mandrus, Takashi Taniguchi, Kenji Watanabe, Kenji Kitamura, Wang Yao, et al. *Electrically Tunable Excitonic Light-Emitting Diodes Based on Monolayer WSe_2 p–n Junctions*. Nat. Nanotechnol., 9(4):268–272, 2014.

[23] Rui Cheng, Dehui Li, Hailong Zhou, Chen Wang, Anxiang Yin, Shan Jiang, Yuan Liu, Yu Chen, Yu Huang, and Xiangfeng Duan. *Electroluminescence and Photocurrent Generation from Atomically Sharp WSe_2/MoS_2 Heterojunction p–n Diodes*. Nano Lett., 14(10):5590–5597, 2014.

[24] Manish Chhowalla, Hyeon Suk Shin, Goki Eda, Lain-Jong Li, Kian Ping Loh, and Hua Zhang. *The Chemistry of Two-Dimensional Layered Transition Metal Dichalcogenide Nanosheets*. Nat. Chem., 5(4):263–275, 2013.

[25] Per Joensen, RF Frindt, and S Roy Morrison. *Single-layer MoS_2*. Mater. Res. Bull., 21(4):457–461, 1986.

[26] Qing Hua Wang, Kourosh Kalantar-Zadeh, Andras Kis, Jonathan N Coleman, and Michael S Strano. *Electronics and Optoelectronics of Two-dimensional Transition Metal Dichalcogenides*. Nat. Nanotechnol., 7(11):699–712, 2012.

[27] KK Kam and BA Parkinson. *Detailed Photocurrent spectroscopy of the Semiconducting Group VIB Transition Metal Cichalcogenides*. J. Phys. Chem., 86(4):463–467, 1982.

[28] Sefaattin Tongay, Hasan Sahin, Changhyun Ko, Alex Luce, Wen Fan, Kai Liu, Jian Zhou, Ying-Sheng Huang, Ching-Hwa Ho, Jinyuan Yan, et al. *Monolayer Behaviour in Bulk ReS_2 due to*

Electronic and Vibrational Decoupling. Nat. Commun., 5:3252, 2014.

[29] Gang Wang, Alexey Chernikov, Mikhail M Glazov, Tony F Heinz, Xavier Marie, Thierry Amand, and Bernhard Urbaszek. *Colloquium: Excitons in Atomically Thin Transition Metal Dichalcogenides.* Rev. Mod. Phys., 90(2):021001, 2018.

[30] Zhiyong Y Zhu, Yingchun C Cheng, and Udo Schwingenschlögl. *Giant Spin-orbit-induced Spin Splitting in Two-dimensional Transition-metal Dichalcogenide Semiconductors.* Phys. Rev. B, 84(15):153402, 2011.

[31] Chendong Zhang, Amber Johnson, Chang-Lung Hsu, Lain-Jong Li, and Chih-Kang Shih. *Direct Imaging of Band Profile in Single Layer MoS_2 on Graphite: Quasiparticle Energy Gap, Metallic Edge States, and Edge Band Bending.* Nano Lett., 14(5):2443–2447, 2014.

[32] Heather M Hill, Albert F Rigosi, Cyrielle Roquelet, Alexey Chernikov, Timothy C Berkelbach, David R Reichman, Mark S Hybertsen, Louis E Brus, and Tony F Heinz. *Observation of Excitonic Rydberg States in Monolayer MoS_2 and WS_2 by Photoluminescence Excitation Spectroscopy.* Nano Lett., 15(5):2992–2997, 2015.

[33] Keliang He, Nardeep Kumar, Liang Zhao, Zefang Wang, Kin Fai Mak, Hui Zhao, and Jie Shan. *Tightly Bound Excitons in Monolayer WSe_2.* Phys. Rev. Lett., 113(2):026803, 2014.

[34] Alexey Chernikov, Timothy C Berkelbach, Heather M Hill, Albert Rigosi, Yilei Li, Ozgur Burak Aslan, David R Reichman, Mark S Hybertsen, and Tony F Heinz. *Exciton Binding Energy and Nonhydrogenic Rydberg Series in Monolayer WS_2.* Phys. Rev. Lett., 113(7):076802, 2014.

[35] Bairen Zhu, Xi Chen, and Xiaodong Cui. *Exciton Binding Energy of Monolayer WS_2.* Sci. Rep., 5:9218, 2015.

[36] Soohyung Park, Niklas Mutz, Thorsten Schultz, Sylke Blumstengel, Ali Han, Areej Aljarb, Lain-Jong Li, Emil JW List-Kratochvil, Patrick Amsalem, and Norbert Koch. *Direct Determination of Monolayer MoS_2 and WSe_2 Exciton Binding Energies on Insulating and Metallic Substrates.* 2d. Mater., 5(2):025003, 2018.

[37] AR Klots, AKM Newaz, Bin Wang, D Prasai, H Krzyzanowska, Junhao Lin, D Caudel, NJ Ghimire, J Yan, BL Ivanov, et al. *Probing Excitonic States in Suspended Two-dimensional Semiconductors by Photocurrent Spectroscopy.* Sci. Rep., 4:6608, 2014.

[38] Yilei Li, Alexey Chernikov, Xian Zhang, Albert Rigosi, Heather M Hill, Arend M Van Der Zande, Daniel A Chenet, En-Min Shih, James Hone, and Tony F Heinz. *Measurement of The Optical Dielectric Function of Monolayer Transition-metal Dichalcogenides: MoS_2, $MoSe_2$, WS_2, and WSe_2.* Phys. Rev.B, 90(20):205422, 2014.

[39] Th Böker, R Severin, A Müller, C Janowitz, R Manzke, D Voß, P Krüger, A Mazur, and J Pollmann. *Band Structure of MoS_2, $MoSe_2$, and $\alpha - MoTe_2$: Angle-resolved Photoelectron Spectroscopy and Ab Initio Calculations.* Phys. Rev. B, 64(23):235305, 2001.

[40] Fernando Wypych and Robert Schöllhorn. *1T-MoS_2, a New Metallic Modification of Molybdenum Disulfide.* Journal of the Chemical Society, Chem. Comm., (19):1386–1388, 1992.

[41] Eugene S Kadantsev and Pawel Hawrylak. *Electronic Structure of a Single MoS_2 Monolayer.* Solid State Commun., 152(10):909–913, 2012.

[42] Goki Eda, Hisato Yamaguchi, Damien Voiry, Takeshi Fujita, Mingwei Chen, and Manish Chhowalla. *Photoluminescence from Chemically Exfoliated MoS_2.* Nano Lett., 11(12):5111–5116, 2011.

[43] Weijie Zhao, Zohreh Ghorannevis, Leiqiang Chu, Minglin Toh, Christian Kloc, Ping-Heng Tan, and Goki Eda. *Evolution of Electronic Structure in Atomically Thin Sheets of WS_2 and WSe_2.* ACS Nano, 7(1):791–797, 2013.

[44] Philipp Tonndorf, Robert Schmidt, Philipp Böttger, Xiao Zhang, Janna Börner, Andreas Liebig, Manfred Albrecht, Christian Kloc, Ovidiu Gordan, Dietrich RT Zahn, et al. *Photoluminescence Emission and Raman Response of Monolayer MoS_2, $MoSe_2$, and WSe_2.* Opt. Express, 21(4):4908–4916, 2013.

[45] Yu Zhang, Yanfeng Zhang, Qingqing Ji, Jing Ju, Hongtao Yuan, Jianping Shi, Teng Gao, Donglin Ma, Mengxi Liu, Yubin Chen,

et al. *Controlled Growth of High-quality Monolayer WS_2 Layers on Sapphire and Imaging its Grain Boundary*. ACS Nano, 7(10):8963–8971, 2013.

[46] Branimir Radisavljevic and Andras Kis. *Mobility Engineering and a Metal–Insulator Transition in Monolayer MoS_2*. Nat. Mater., 12(9):815–820, 2013.

[47] Andres Castellanos-Gomez, Menno Poot, Gary A Steele, Herre SJ Van Der Zant, Nicolás Agraït, and Gabino Rubio-Bollinger. *Elastic Properties of Freely Suspended MoS_2 Nanosheets*. Adv. Mater., 24(6):772–775, 2012.

[48] Simone Bertolazzi, Jacopo Brivio, and Andras Kis. *Stretching and Breaking of Ultrathin MoS_2*. ACS Nano, 5(12):9703–9709, 2011.

[49] Branimir Radisavljevic, Aleksandra Radenovic, Jacopo Brivio, I V Giacometti, and A Kis. *Single-layer MoS_2 Transistors*. Nat. Nanotechnol., 6(3):147, 2011.

[50] Atresh Sanne, Rudresh Ghosh, Amritesh Rai, Maruthi Nagavalli Yogeesh, Seung Heon Shin, Ankit Sharma, Karalee Jarvis, Leo Mathew, Rajesh Rao, Deji Akinwande, et al. *Radio Frequency Transistors and Circuits based on CVD MoS_2*. Nano Lett., 15(8):5039–5045, 2015.

[51] Kirby KH Smithe, Saurabh V Suryavanshi, Miguel Munoz Rojo, Aria D Tedjarati, and Eric Pop. *Low Variability in Synthetic Monolayer MoS_2 Devices*. ACS Nano, 11(8):8456–8463, 2017.

[52] Semiconductor Industry Association et al. *International Technology Roadmap for Semiconductors*. http://www. itrs. net, 2009.

[53] Sungjin Wi, Hyunsoo Kim, Mikai Chen, Hongsuk Nam, L Jay Guo, Edgar Meyhofer, and Xiaogan Liang. *Enhancement of Photovoltaic Response in Multilayer MoS_2 Induced by Plasma Doping*. ACS Nano, 8(5):5270–5281, 2014.

[54] Woong Choi, Mi Yeon Cho, Aniruddha Konar, Jong Hak Lee, Gi-Beom Cha, Soon Cheol Hong, Sangsig Kim, Jeongyong Kim, Debdeep Jena, Jinsoo Joo, et al. *High-detectivity Multilayer MoS_2 Phototransistors with Spectral Response from Ultraviolet to Infrared*. Adv. Mater., 24(43):5832–5836, 2012.

[55] Sanghyun Lee, Jinwoo Park, Yeojun Yun, Jaejin Lee, and Junseok Heo. *Enhanced Photoresponsivity of Multilayer MoS_2 Phototransistor Using Localized Au Schottky Junction Formed by Spherical-Lens Photolithography.* Adv. Mater. Interfaces, 6(8):1900053, 2019.

[56] Hee Sung Lee, Sung-Wook Min, Youn-Gyung Chang, Min Kyu Park, Taewook Nam, Hyungjun Kim, Jae Hoon Kim, Sunmin Ryu, and Seongil Im. *MoS2 nanosheet phototransistors with thickness-modulated optical energy gap.* Nano Lett., 12(7):3695–3700, 2012.

[57] Hyejin Jang, Christopher R Ryder, Joshua D Wood, Mark C Hersam, and David G Cahill. *3D Anisotropic Thermal Conductivity of Exfoliated Rhenium Disulfide.* Adv. Mater., 29(35):1700650, 2017.

[58] Mohammad Rahman, Kenneth Davey, and Shi-Zhang Qiao. *Advent of 2D rhenium disulfide (ReS2): fundamentals to applications.* Advanced Functional Materials, 27(10):1606129, 2017.

[59] Xiaobo Li, Chao Chen, Yang Yang, Zhibin Lei, and Hua Xu. *2D Re-Based Transition Metal Chalcogenides: Progress, Challenges, and Opportunities.* Adv. Sci., page 2002320, 2020.

[60] Erfu Liu, Yajun Fu, Yaojia Wang, Yanqing Feng, Huimei Liu, Xiangang Wan, Wei Zhou, Baigeng Wang, Lubin Shao, Ching-Hwa Ho, et al. *Integrated Digital Inverters Based on Two-Dimensional Anisotropic ReS_2 Field-Effect Transistors.* Nat. Commun., 6(1):1–7, 2015.

[61] Yanqing Feng, Wei Zhou, Yaojia Wang, Jian Zhou, Erfu Liu, Yajun Fu, Zhenhua Ni, Xinglong Wu, Hongtao Yuan, Feng Miao, et al. *Raman Vibrational Spectra of Bulk to Monolayer ReS_2 with Lower Symmetry.* Phys. Rev. B, 92(5):054110, 2015.

[62] K Dileep, R Sahu, Sumanta Sarkar, Sebastian C Peter, and Ranjan Datta. *Layer Specific Optical Band Gap Measurement at Nanoscale in MoS_2 and ReS_2 van der Waals Compounds by High Resolution Electron Energy Loss Spectroscopy.* J. Appl. Phys., 119(11):114309, 2016.

[63] Mathias Gehlmann, Irene Aguilera, Gustav Bihlmayer, Slavomír Nemsak, Philipp Nagler, Pika Gospodaric, Giovanni Zamborlini, Markus Eschbach, Vitaliy Feyer, Florian Kronast,

et al. *Direct Observation of the Band Gap Transition in Atomically Thin ReS$_2$*. Nano letters, 17(9):5187–5192, 2017.

[64] James L Webb, Lewis S Hart, Daniel Wolverson, Chaoyu Chen, Jose Avila, and Maria C Asensio. *Electronic Band Structure of ReS$_2$ by High-Resolution Angle-Resolved Photoemission Spectroscopy*. Phys. Rev. B, 96(11):115205, 2017.

[65] Hong-Xia Zhong, Shiyuan Gao, Jun-Jie Shi, and Li Yang. *Quasiparticle Band Gaps, Excitonic Effects, and Anisotropic Optical Properties of the Monolayer Distorted 1T Diamond-Chain Structures ReS$_2$ and ReSe$_2$*. Phys. Rev. B, 92(11):115438, 2015.

[66] JP Echeverry and IC Gerber. *Theoretical Investigations of the Anisotropic Optical Properties of Distorted 1T ReS$_2$ and ReSe$_2$ Monolayers, Bilayers, and in the Bulk Limit*. Phys. Rev. B, 97(7):075123, 2018.

[67] Surani M Gunasekera, Daniel Wolverson, Lewis S Hart, and Marcin Mucha-Kruczynski. *Electronic Band Structure of Rhenium Dichalcogenides*. Journal of Electronic Materials, 47(8):4314–4320, 2018.

[68] CM Fang, GA Wiegers, C Haas, and RA De Groot. *Electronic Structures of, and in the Real and the Hypothetical Undistorted Structures*. Journal of Physics: Condensed Matter, 9(21):4411, 1997.

[69] Yongjian Zhou, Nikhilesh Maity, Amritesh Rai, Rinkle Juneja, Xianghai Meng, Anupam Roy, Yanyao Zhang, Xiaochuan Xu, Jung-Fu Lin, Sanjay K Banerjee, et al. *Stacking-Order-Driven Optical Properties and Carrier Dynamics in ReS$_2$*. Adv. Mater., 32(22):1908311, 2020.

[70] Xiao-Fen Qiao, Jiang-Bin Wu, Linwei Zhou, Jingsi Qiao, Wei Shi, Tao Chen, Xin Zhang, Jun Zhang, Wei Ji, and Ping-Heng Tan. *Polytypism and Unexpected Strong Interlayer Coupling in Two-Dimensional Layered ReS$_2$*. Nanoscale, 8(15):8324–8332, 2016.

[71] Daniel A Chenet, O Burak Aslan, Pinshane Y Huang, Chris Fan, Arend M van der Zande, Tony F Heinz, and James C Hone. *In-Plane Anisotropy in Mono-and Few-Layer ReS$_2$ Probed by*

Raman Spectroscopy and Scanning Transmission Electron Microscopy. Nano Lett., 15(9):5667–5672, 2015.

[72] Qiannan Cui, Jiaqi He, Matthew Z Bellus, Mirzojamshed Mirzokarimov, Tino Hofmann, Hsin-Ying Chiu, Matthew Antonik, Dawei He, Yongsheng Wang, and Hui Zhao. *Transient Absorption Measurements on Anisotropic Monolayer ReS$_2$*. Small, 11(41):5565–5571, 2015.

[73] Ajjiporn Dathbun, Youngchan Kim, Seongchan Kim, Youngjae Yoo, Moon Sung Kang, Changgu Lee, and Jeong Ho Cho. *Large-Area CVD-Grown Sub-2V ReS$_2$ Transistors and Logic Gates.* Nano Lett., 17(5):2999–3005, 2017.

[74] Kai Xu, Hui-Xiong Deng, Zhenxing Wang, Yun Huang, Feng Wang, Shu-Shen Li, Jun-Wei Luo, and Jun He. *Sulfur Vacancy Activated Field Effect Transistors Based on ReS$_2$ Nanosheets.* Nanoscale, 7(38):15757–15762, 2015.

[75] Fucai Liu, Shoujun Zheng, Xuexia He, Apoorva Chaturvedi, Junfeng He, Wai Leong Chow, Thomas R Mion, Xingli Wang, Jiadong Zhou, Qundong Fu, et al. *Highly Sensitive Detection of Polarized Light Using Anisotropic 2D ReS$_2$*. Adv. Funct. Mater., 26(8):1169–1177, 2016.

[76] Wugang Liao, Wei Wei, Yu Tong, Wai Kin Chim, and Chunxiang Zhu. *Low-Frequency Noise in Layered ReS$_2$ Field Effect Transistors on HfO$_2$ and its Application for pH Sensing.* ACS Appl. Mater. Interfaces, 10(8):7248–7255, 2018.

[77] Aijun Yang, Jian Gao, Baichang Li, Jiawei Tan, Yu Xiang, Tushar Gupta, Lu Li, Shravan Suresh, Juan Carlos Idrobo, Toh-Ming Lu, et al. *Humidity Sensing Using Vertically Oriented Arrays of ReS$_2$ Nanosheets Deposited on an Interdigitated Gold Electrode.* 2d Mater., 3(4):045012, 2016.

[78] Erfu Liu, Mingsheng Long, Junwen Zeng, Wei Luo, Yaojia Wang, Yiming Pan, Wei Zhou, Baigeng Wang, Weida Hu, Zhenhua Ni, et al. *High Responsivity Phototransistors Based on Few-Layer ReS$_2$ for Weak Signal Detection.* Adv. Funct. Mater., 26(12):1938–1944, 2016.

[79] Jaewoo Shim, Aely Oh, Dong-Ho Kang, Seyong Oh, Sung Kyu Jang, Jaeho Jeon, Min Hwan Jeon, Minwoo Kim, Changhwan Choi, Jaehyeong Lee, et al. *High-Performance 2D Rhe-*

nium Disulfide (ReS$_2$) Transistors and Photodetectors by Oxygen Plasma Treatment. Adv. Mater., 28(32):6985–6992, 2016.

[80] Xiaobo Li, Fangfang Cui, Qingliang Feng, Gang Wang, Xiaosa Xu, Juanxia Wu, Nannan Mao, Xing Liang, Zhongyue Zhang, Jin Zhang, et al. *Controlled Growth of Large-Area Anisotropic ReS$_2$ Atomic Layer and Its Photodetector Application.* Nanoscale, 8(45):18956–18962, 2016.

[81] Kostya S Novoselov, D Jiang, F Schedin, TJ Booth, VV Khotkevich, SV Morozov, and Andre K Geim. *Two-dimensional Atomic Crystals.* Proceedings of the National Academy of Sciences, 102(30):10451–10453, 2005.

[82] Min Yi and Zhigang Shen. *A Review on Mechanical Exfoliation for the Scalable Production of Graphene.* J. Mater. Chem. A, 3(22):11700–11715, 2015.

[83] Rod Ruoff. *Calling All Chemists.* Nat. Nanotechnol., 3(1):10–11, 2008.

[84] Zhengyang Cai, Bilu Liu, Xiaolong Zou, and Hui-Ming Cheng. *Chemical Vapor Deposition Growth and Applications of Two-dimensional Materials and Their Heterostructures.* Chem. Rev., 118(13):6091–6133, 2018.

[85] Zongping Chen, Wencai Ren, Libo Gao, Bilu Liu, Songfeng Pei, and Hui-Ming Cheng. *Three-dimensional Flexible and Conductive Interconnected Graphene Networks Grown by Chemical Vapour Deposition.* Nat. Mater., 10(6):424–428, 2011.

[86] Libo Gao, Wencai Ren, Jinping Zhao, Lai-Peng Ma, Zongping Chen, and Hui-Ming Cheng. *Efficient Growth of High-quality Graphene Films on Cu Foils by Ambient Pressure Chemical Vapor Deposition.* Appl. Phys. Lett., 97(18):183109, 2010.

[87] Lewis Gomez De Arco, Yi Zhang, Cody W Schlenker, Koungmin Ryu, Mark E Thompson, and Chongwu Zhou. *Continuous, Highly Flexible, and Transparent Graphene Films by Chemical Vapor Deposition for Organic Photovoltaics.* ACS Nano, 4(5):2865–2873, 2010.

[88] Shanshan Wang, Youmin Rong, Ye Fan, Mercè Pacios, Harish Bhaskaran, Kuang He, and Jamie H Warner. *Shape Evolution*

of Monolayer MoS_2 Crystals Grown by Chemical Vapor Deposition. Chem. Mater., 26(22):6371–6379, 2014.

[89] Yeonjoon Jung, Eunji Ji, Andrea Capasso, and Gwan-Hyoung Lee. *Recent Progresses in the Growth of Two-dimensional Transition Metal Dichalcogenides.* J. Korean Ceram. Soc., 56(1):24–36, 2019.

[90] Dumitru Dumcenco, Dmitry Ovchinnikov, Kolyo Marinov, Predrag Lazic, Marco Gibertini, Nicola Marzari, Oriol Lopez Sanchez, Yen-Cheng Kung, Daria Krasnozhon, Ming-Wei Chen, et al. *Large-area Epitaxial Monolayer MoS_2.* ACS Nano, 9(4):4611–4620, 2015.

[91] AM Rinaldi and D Crippa. *CVD Technologies for Silicon: a Quick Survey.* In Semiconductors and Semimetals, volume 72, pages 1–50. Elsevier, 2001.

[92] Sina Najmaei, Zheng Liu, Wu Zhou, Xiaolong Zou, Gang Shi, Sidong Lei, Boris I Yakobson, Juan-Carlos Idrobo, Pulickel M Ajayan, and Jun Lou. *Vapour Phase Growth and Grain Boundary Structure of Molybdenum Disulphide Atomic Layers.* Nat. Mater., 12(8):754–759, 2013.

[93] Yifei Yu, Chun Li, Yi Liu, Liqin Su, Yong Zhang, and Linyou Cao. *Controlled Scalable Synthesis of Uniform, High-quality Monolayer and Few-layer MoS_2 Films.* Sci. Rep., 3:1866, 2013.

[94] Zeger Hens. *Fysische Chemie.* Universiteit Gent, 2010.

[95] Kibum Kang, Saien Xie, Lujie Huang, Yimo Han, Pinshane Y Huang, Kin Fai Mak, Cheol-Joo Kim, David Muller, and Jiwoong Park. *High-mobility three-atom-thick semiconducting films with wafer-scale homogeneity.* Nature, 520(7549):656–660, 2015.

[96] W Hao, C Marichy, and Catherine Journet. *Atomic Layer Deposition of Stable 2D Materials.* 2D Materials, 6(1):012001, 2018.

[97] Tania Roy, Mahmut Tosun, Jeong Seuk Kang, Angada B Sachid, Sujay B Desai, Mark Hettick, Chenming C Hu, and Ali Javey. *Field-Effect Transistors Built From All Two-Dimensional Material Components.* ACS Nano, 8(6):6259–6264, 2014.

[98] Yonghun Kim, Ah Ra Kim, Guoqing Zhao, Sun Young Choi, Soo Cheol Kang, Sung Kwan Lim, Kang Eun Lee, Jucheol Park,

Byoung Hun Lee, Myung Gwan Hahm, et al. *Wafer-Scale Integration of Highly Uniform and Scalable MoS$_2$ Transistors.* ACS Appl. Mater. Interfaces., 9(42):37146–37153, 2017.

[99] Kai Xu, Dongxue Chen, Fengyou Yang, Zhenxing Wang, Lei Yin, Feng Wang, Ruiqing Cheng, Kaihui Liu, Jie Xiong, Qian Liu, et al. *Sub-10 nm Nanopattern Architecture for 2D Material Field-effect Transistors.* Nano Lett., 17(2):1065–1070, 2017.

[100] Jonathan N Coleman, Mustafa Lotya, Arlene O'Neill, Shane D Bergin, Paul J King, Umar Khan, Karen Young, Alexandre Gaucher, Sukanta De, Ronan J Smith, et al. *Two-Dimensional Nanosheets Produced by Liquid Exfoliation of Layered Materials.* Science, 331(6017):568–571, 2011.

[101] Jonathan N Coleman. *Liquid Exfoliation of Defect-Free Graphene.* Acc. Chem. Res., 46(1):14–22, 2013.

[102] Valeria Nicolosi, Manish Chhowalla, Mercouri G Kanatzidis, Michael S Strano, and Jonathan N Coleman. *Liquid Exfoliation of Layered Materials.* Science, 340(6139):1226419, 2013.

[103] Jianfeng Shen, Yongmin He, Jingjie Wu, Caitian Gao, Kunttal Keyshar, Xiang Zhang, Yingchao Yang, Mingxin Ye, Robert Vajtai, Jun Lou, et al. *Liquid Phase Exfoliation of Two-Dimensional Materials by Directly Probing and Matching Surface Tension Components.* Nano Lett., 15(8):5449–5454, 2015.

[104] Benoit Mahler, Veronika Hoepfner, Kristine Liao, and Geoffrey A Ozin. *Colloidal Synthesis of 1T-WS$_2$ and 2H-WS$_2$ Nanosheets: Applications for Photocatalytic Hydrogen Evolution.* J. Am. Chem. Soc., 136(40):14121–14127, 2014.

[105] Donghee Son, Sue In Chae, Myungbin Kim, Moon Kee Choi, Jiwoong Yang, Kunsu Park, Vinayak S Kale, Ja Hoon Koo, Changsoon Choi, Minbaek Lee, et al. *Colloidal Synthesis of Uniform-Sized Molybdenum Disulfide Nanosheets for Wafer-Scale Flexible Nonvolatile Memory.* Adv. Mater., 28(42):9326–9332, 2016.

[106] Adam G Kelly, Toby Hallam, Claudia Backes, Andrew Harvey, Amir Sajad Esmaeily, Ian Godwin, João Coelho, Valeria Nicolosi, Jannika Lauth, Aditya Kulkarni, et al. *All-printed Thin-film Transistors from Networks of Liquid-exfoliated nanosheets.* Science, 356(6333):69–73, 2017.

[107] Francesco Bonaccorso, Antonino Bartolotta, Jonathan N Coleman, and Claudia Backes. *2D-crystal-based Functional Inks.* Adv. Mater., 28(29):6136–6166, 2016.

[108] J Scott Bunch, Yuval Yaish, Markus Brink, Kirill Bolotin, and Paul L McEuen. *Coulomb Oscillations and Hall Effect in Quasi-2D Graphite Quantum Dots.* Nano Lett., 5(2):287–290, 2005.

[109] Yenny Hernandez, Valeria Nicolosi, Mustafa Lotya, Fiona M Blighe, Zhenyu Sun, Sukanta De, IT McGovern, Brendan Holland, Michele Byrne, Yurii K Gun'Ko, et al. *High-Yield Production of Graphene by Liquid-Phase Exfoliation of Graphite.* Nat. Nanotechnol., 3(9):563, 2008.

[110] Shane D Bergin, Valeria Nicolosi, Philip V Streich, Silvia Giordani, Zhenyu Sun, Alan H Windle, Peter Ryan, N Peter P Niraj, Zhi-Tao T Wang, Leslie Carpenter, et al. *Towards Solutions of Single-Walled Carbon Nanotubes in Common Solvents.* Adv. Mater., 20(10):1876–1881, 2008.

[111] Mustafa Lotya, Paul J King, Umar Khan, Sukanta De, and Jonathan N Coleman. *High-Concentration, Surfactant-Stabilized Graphene Dispersions.* ACS Nano, 4(6):3155–3162, 2010.

[112] Graeme Cunningham, Mustafa Lotya, Clotilde S Cucinotta, Stefano Sanvito, Shane D Bergin, Robert Menzel, Milo SP Shaffer, and Jonathan N Coleman. *Solvent Exfoliation of Transition Metal Dichalcogenides: Dispersibility of Exfoliated Nanosheets Varies Only Weakly between Compounds.* ACS Nano, 6(4):3468–3480, 2012.

[113] J Marguerite Hughes, Damian Aherne, and Jonathan N Coleman. *Generalizing Solubility Parameter Theory to Apply to One-and Two-Dimensional Solutes and to Incorporate Dipolar Interactions.* J. Appl. Polym. Sci., 127(6):4483–4491, 2013.

[114] Michael Naguib, Murat Kurtoglu, Volker Presser, Jun Lu, Junjie Niu, Min Heon, Lars Hultman, Yury Gogotsi, and Michel W Barsoum. *Two-dimensional Nanocrystals Produced by Exfoliation of Ti_3AlC_2.* Adv. Mater., 23(37):4248–4253, 2011.

[115] Keith R Paton, Eswaraiah Varrla, Claudia Backes, Ronan J Smith, Umar Khan, Arlene O'Neill, Conor Boland, Mustafa Lotya, Oana M Istrate, Paul King, et al. *Scalable Production*

of Large Quantities of Defect-free Few-layer Graphene by Shear Exfoliation in Liquids. Nat. Mater., 13(6):624–630, 2014.

[116] Reza Rizvi, Emily P Nguyen, Matthew D Kowal, Wai H Mak, Sheikh Rasel, Md Akibul Islam, Ahmed Abdelaal, Anup S Joshi, Shahab Zekriardehani, Maria R Coleman, et al. *High-Throughput Continuous Production of Shear-Exfoliated 2D Layered Materials using Compressible Flows.* Adv. Mater., 30(30):1800200, 2018.

[117] Claudia Backes, Ronan J Smith, Niall McEvoy, Nina C Berner, David McCloskey, Hannah C Nerl, Arlene O'Neill, Paul J King, Tom Higgins, Damien Hanlon, et al. *Edge and Confinement Effects Allow In Situ Measurement of Size and Thickness of Liquid-exfoliated Nanosheets.* Nat. Commun., 5(1):1–10, 2014.

[118] Artur Ciesielski and Paolo Samori. *Graphene via Sonication Assisted Liquid-phase exfoliation.* Chem. Soc. Rev., 43(1):381–398, 2014.

[119] Changgu Lee, Hugen Yan, Louis E Brus, Tony F Heinz, James Hone, and Sunmin Ryu. *Anomalous Lattice Vibrations of Single-and Few-Layer MoS_2.* ACS Nano, 4(5):2695–2700, 2010.

[120] CBea Murray, David J Norris, and Moungi G Bawendi. *Synthesis and Characterization of Nearly Monodisperse CdE (E= Sulfur, Selenium, Tellurium) Semiconductor Nanocrystallites.* J. Am. Chem. Soc., 115(19):8706–8715, 1993.

[121] Xiaogang Peng, Michael C Schlamp, Andreas V Kadavanich, and A Paul Alivisatos. *Epitaxial Growth of Highly Luminescent CdSe/CdS Core/Shell Nanocrystals with Photostability and Electronic Accessibility.* J. Am. Chem. Soc., 119(30):7019–7029, 1997.

[122] Margaret A Hines and Philippe Guyot-Sionnest. *Synthesis and Characterization of Strongly Luminescing ZnS-capped CdSe Nanocrystals.* JPC, 100(2):468–471, 1996.

[123] Younan Xia, Peidong Yang, Yugang Sun, Yiying Wu, Brian Mayers, Byron Gates, Yadong Yin, Franklin Kim, and Haoquan Yan. *One-dimensional Nanostructures: Synthesis, Characterization, and Applications.* Adv. Mater., 15(5):353–389, 2003.

[124] S Ithurria, MD Tessier, B Mahler, RPSM Lobo, B Dubertret, and Al L Efros. *Colloidal Nanoplatelets with Two-dimensional Electronic Structure.* Nat. Mater., 10(12):936–941, 2011.

[125] Victor K LaMer and Robert H Dinegar. *Theory, Production and Mechanism of Formation of Monodispersed Hydrosols.* J. Am. Chem. Soc., 72(11):4847–4854, 1950.

[126] Yadong Yin and A Paul Alivisatos. *Colloidal Nanocrystal Synthesis and The Organic–Inorganic Interface.* Nature, 437(7059):664, 2004.

[127] Jonathan De Roo, Katrien De Keukeleere, Zeger Hens, and Isabel Van Driessche. *From Ligands to Binding Motifs and Beyond; the Enhanced Versatility of Nanocrystal Surfaces.* Dalton Trans., 45(34):13277–13283, 2016.

[128] Michael A Boles, Daishun Ling, Taeghwan Hyeon, and Dmitri V Talapin. *The Surface Science of Nanocrystals.* Nat. Mater., 15(2):141, 2016.

[129] Xiaogang Peng, Liberato Manna, Weidong Yang, Juanita Wickham, Erik Scher, Andreas Kadavanich, and A Paul Alivisatos. *Shape Control of CdSe Nanocrystals.* Nature, 404(6773):59, 2000.

[130] Kim De Nolf, Richard K Capek, Sofie Abe, Michael Sluydts, Youngjin Jang, Jose C Martins, Stefaan Cottenier, Efrat Lifshitz, and Zeger Hens. *Controlling the Size of Hot Injection Made Nanocrystals by Manipulating the Diffusion Coefficient of the Solute.* J. Am. Chem. Soc., 137(7):2495–2505, 2015.

[131] Jiang Tang, Kyle W Kemp, Sjoerd Hoogland, Kwang S Jeong, Huan Liu, Larissa Levina, Melissa Furukawa, Xihua Wang, Ratan Debnath, Dongkyu Cha, et al. *Colloidal-quantum-dot Photovoltaics using Atomic-ligand Passivation.* Nat. Mater., 10(10):765–771, 2011.

[132] Jong-Soo Lee, Maksym V Kovalenko, Jing Huang, Dae Sung Chung, and Dmitri V Talapin. *Band-like Transport, High Electron Mobility and High Photoconductivity in All-inorganic Nanocrystal Arrays.* Nat. Nanotechnol., 6(6):348–352, 2011.

[133] Jonathan De Roo, Isabel Van Driessche, José C Martins, and Zeger Hens. *Colloidal Metal Oxide Nanocrystal Cataly-*

sis by Sustained Chemically Driven Ligand Displacement. Nat. Mater., 15(5):517, 2016.

[134] Maria Ibanez, Rachel J Korkosz, Zhishan Luo, Pau Riba, Doris Cadavid, Silvia Ortega, Andreu Cabot, and Mercouri G Kanatzidis. *Electron Doping in Bottom-up Engineered Thermoelectric Nanomaterials through HCl-mediated Ligand Displacement.* J. Am. Chem. Soc., 137(12):4046–4049, 2015.

[135] Sohee Jeong, Dongwon Yoo, Jung-tak Jang, Minkyoung Kim, and Jinwoo Cheon. *Well-defined Colloidal 2-D Layered Transition-metal Chalcogenide Nanocrystals via Generalized Synthetic Protocols.* J. Am. Chem. Soc., 134(44):18233–18236, 2012.

[136] Jung-tak Jang, Sohee Jeong, Jung-wook Seo, Min-Cheol Kim, Eunji Sim, Yuhong Oh, Seunghoon Nam, Byungwoo Park, and Jinwoo Cheon. *Ultrathin Zirconium Disulfide Nanodiscs.* J. Am. Chem. Soc., 133(20):7636–7639, 2011.

[137] Dongwon Yoo, Minkyoung Kim, Sohee Jeong, Jeonghee Han, and Jinwoo Cheon. *Chemical Synthetic Strategy for Single-layer Transition-metal chalcogenides.* J. Am. Chem. Soc., 136(42):14670–14673, 2014.

[138] Sohee Jeong, Jae Hyo Han, Jung-tak Jang, Jung-wook Seo, Jin-Gyu Kim, and Jinwoo Cheon. *Transformative Two-Dimensional Layered Nanocrystals.* J. Am. Chem. Soc., 133(37):14500–14503, 2011.

[139] M Alam Khan and Yong-Mook Kang. *Synthesis and Electrochemical Performance of Colloidal MoS_2 Nanosheets as an Anode Material in Sodium Ion Battery.* J. Energy Storage, 7:252–257, 2016.

[140] Xu Li, Aiwei Tang, Jiantao Li, Li Guan, Guoyi Dong, and Feng Teng. *Heating-up Synthesis of MoS_2 Nanosheets and their Electrical Bistability Performance.* Nanoscale Res. Lett, 11(1):171, 2016.

[141] Yifan Sun, Yuanxi Wang, Du Sun, Bruno R Carvalho, Carlos G Read, Chia-hui Lee, Zhong Lin, Kazunori Fujisawa, Joshua A Robinson, Vincent H Crespi, et al. *Low-Temperature Solution Synthesis of Few-Layer $1T'$-$MoTe_2$ Nanostructures Exhibiting*

Lattice Compression. Angewandte Chemie, 128(8):2880–2884, 2016.

[142] Du Sun, Simin Feng, Mauricio Terrones, and Raymond E Schaak. *Formation and Interlayer Decoupling of Colloidal $MoSe_2$ Nanoflowers.* Chem. Mater., 27(8):3167–3175, 2015.

[143] Yifan Sun, Albert J Darling, Yawei Li, Kazunori Fujisawa, Cameron F Holder, He Liu, Michael J Janik, Mauricio Terrones, and Raymond E Schaak. *Defect-mediated Selective Hydrogenation of Nitroarenes on Nanostructured WS_2.* Chemical Science, 10(44):10310–10317, 2019.

[144] Pengshang Zhou, Gearoid A Collins, Zeger Hens, Kevin Michael Ryan, Hugh Geaney, and Shalini Singh. *Colloidal WSe_2 Nanocrystals as Anodes for Lithium-Ion Batteries.* Nanoscale, 2020.

[145] Beatriz Martín-García, Davide Spirito, Sebastiano Bellani, Mirko Prato, Valentino Romano, Anatolii Polovitsyn, Rosaria Brescia, Reinier Oropesa-Nuñez, Leyla Najafi, Alberto Ansaldo, et al. *Extending the Colloidal Transition Metal Dichalcogenide Library to ReS_2 Nanosheets for Application in Gas Sensing and Electrocatalysis.* Small, 15(52):1904670, 2019.

[146] Danielle A Henckel, Olivia M Lenz, Kannan M Krishnan, and Brandi M Cossairt. *Improved HER Catalysis through Facile, Aqueous Electrochemical Activation of Nanoscale WSe_2.* Nano Lett., 18(4):2329–2335, 2018.

[147] Wenxu Yin, Zhantong Ye, Xue Bai, Dong He, Xiaoyu Zhang, Hongwei Song, and W Yu William. *Low-temperature One-pot Synthesis of WS_2 Nanoflakes as Electrocatalyst for Hydrogen Evolution Reaction.* Nanotechnology, 30(4):045603, 2018.

[148] Maria S Sokolikova, Peter C Sherrell, Pawel Palczynski, Victoria L Bemmer, and Cecilia Mattevi. *Direct solution-phase Synthesis of $1T'$ WSe_2 Nanosheets.* Nature Commun., 10(1):1–8, 2019.

[149] Yifan Sun, Kazunori Fujisawa, Mauricio Terrones, and Raymond E Schaak. *Solution Synthesis of Few-layer WTe_2 and $Mo_xW_{1-x}Te_2$ Nanostructures.* J. Mater. Chem. C, 5(43):11317–11323, 2017.

[150] Yifan Sun, Kazunori Fujisawa, Zhong Lin, Yu Lei, Jared S Mondschein, Mauricio Terrones, and Raymond E Schaak. *Low-Temperature Solution Synthesis of Transition Metal Dichalcogenide Alloys with Tunable Optical Properties*. J. Am. Chem. Soc., 139(32):11096–11105, 2017.

[151] Junjun Zhang, Wenpei Kang, Miao Jiang, Yu You, Yulin Cao, Tsz-Wai Ng, YW Denis, Chun-Sing Lee, and Jun Xu. *Conversion of 1T-MoSe$_2$ to 2H-MoS$_{2x}$Se$_{2-2x}$ Mesoporous Nanospheres for Superior Sodium Storage Performance*. Nanoscale, 9(4):1484–1490, 2017.

[152] Christian Meerbach, Benjamin Klemmed, Daniel Spittel, Christoph Bauer, Young Jin Park, Rene Hubner, Hu Young Jeong, Denise Erb, Hyeon Suk Shin, Vladimir Lesnyak, et al. *General Colloidal Synthesis of Transition-Metal Disulfide Nanomaterials as Electrocatalysts for Hydrogen Evolution Reaction*. ACS Appl. Mater. Interfaces, 12(11):13148–13155, 2020.

[153] Joel H Hildebrand. *SOLUBILITY*. J. Am. Chem. Soc., 38(8):1452–1473, 1916.

[154] Kenneth S Pitzer. *Joel Henry Hildebrand 1881-1983. A Biographical Memoir by Kenneth S. Pitzer*. NAS, 1993.

[155] Michael Rubinstein, Ralph H Colby, et al. *Polymer Physics*, volume 23. Oxford university press New York, 2003.

[156] Paul J Flory. *Principles of Polymer Chemistry*. Cornell University Press, 1953.

[157] Paul J Flory and M Volkenstein. *Statistical Mechanics of Chain Molecules*. Biopolymers: Original Research on Biomolecules, 8(5):699–700, 1969.

[158] Carlo Cercignani. *The Boltzmann Equation*. In The Boltzmann equation and its applications, pages 40–103. Springer, 1988.

[159] Max Planck. *Treatise on Thermodynamics*. Courier Corporation, 2013.

[160] Donald Patterson and Andrée Robard. *Thermodynamics of Polymer Compatibility*. Macromolecules, 11(4):690–695, 1978.

[161] Shane D Bergin, Zhenyu Sun, David Rickard, Philip V Streich, James P Hamilton, and Jonathan N Coleman. *Multicompo-

nent Solubility Parameters for Single-walled Carbon Nanotube-Solvent Mixtures. ACS Nano, 3(8):2340–2350, 2009.

[162] George Scatchard. *Equilibria in Non-electrolyte Solutions in Relation to the Vapor Pressures and Densities of the Components.* Chemical Reviews, 8(2):321–333, 1931.

[163] Joel Henry Hildebrand et al. *Solubility of Non-electrolytes.* 1936.

[164] J Marguerite Hughes, Yenny Hernandez, Damian Aherne, Lukas Doessel, Klaus Mullen, Ben Moreton, Thomas W White, Cerianne Partridge, Giovanni Costantini, Aleksey Shmeliov, et al. *High Quality Dispersions of Hexabenzocoronene in Organic Solvents.* J. Am. Chem. Soc., 134(29):12168–12179, 2012.

[165] Charles M Hansen. *Hansen Solubility Parameters: a User's Handbook.* CRC Press, 2007.

[166] Wenjing Zhang, Jing-Kai Huang, Chang-Hsiao Chen, Yung-Huang Chang, Yuh-Jen Cheng, and Lain-Jong Li. *High-Gain Phototransistors Based on a CVD MoS_2 Monolayer.* Adv. Mater., 25(25):3456–3461, 2013.

[167] Ronan J Smith, Paul J King, Mustafa Lotya, Christian Wirtz, Umar Khan, Sukanta De, Arlene O'Neill, Georg S Duesberg, Jaime C Grunlan, Gregory Moriarty, et al. *Large-Scale Exfoliation of Inorganic Layered Compounds in Aqueous Surfactant Solutions.* Adv. Mater., 23(34):3944–3948, 2011.

[168] Eswaraiah Varrla, Claudia Backes, Keith R Paton, Andrew Harvey, Zahra Gholamvand, Joe McCauley, and Jonathan N Coleman. *Large-Scale Production of Size-Controlled MoS_2 Nanosheets by Shear Exfoliation.* Chem. Mater., 27(3):1129–1139, 2015.

[169] Yagang Yao, Ziyin Lin, Zhuo Li, Xiaojuan Song, Kyoung-Sik Moon, and Ching-ping Wong. *Large-Scale Production of Two-Dimensional Nanosheets.* J. Mater. Chem., 22(27):13494–13499, 2012.

[170] Jack R Brent, Nicky Savjani, Edward A Lewis, Sarah J Haigh, David J Lewis, and Paul O'Brien. *Production of Few-layer Phosphorene by Liquid Exfoliation of Black Phosphorus.* Chem. Comm., 50(87):13338–13341, 2014.

[171] Lewis Hart, Sara Dale, Sarah Hoye, James L Webb, and Daniel Wolverson. *Rhenium Dichalcogenides: Layered Semiconductors with Two Vertical Orientations.* Nano Lett., 16(2):1381–1386, 2016.

[172] Takeshi Fujita, Yoshikazu Ito, Yongwen Tan, Hisato Yamaguchi, Daisuke Hojo, Akihiko Hirata, Damien Voiry, Manish Chhowalla, and Mingwei Chen. *Chemically Exfoliated ReS$_2$ Nanosheets.* Nanoscale, 6(21):12458–12462, 2014.

[173] Joohoon Kang, Vinod K Sangwan, Joshua D Wood, Xiaolong Liu, Itamar Balla, David Lam, and Mark C Hersam. *Layer-by-Layer Sorting of Rhenium Disulfide via High-Density Isopycnic Density Gradient Ultracentrifugation.* Nano Lett., 16(11):7216–7223, 2016.

[174] Naktal Al-Dulaimi, Edward A Lewis, David J Lewis, Simon K Howell, Sarah J Haigh, and Paul O'Brien. *Sequential Bottom-Up and Top-Down Processing for the Synthesis of Transition Metal Dichalcogenide Nanosheets: the Case of Rhenium Disulfide (ReS$_2$).* Chem. Commun., 52(50):7878–7881, 2016.

[175] Qihua Jing, Hao Zhang, Hao Huang, Xingce Fan, Yumeng Zhang, Xiangyu Hou, Qingyu Xu, Zhenhua Ni, and Teng Qiu. *Ultrasonic Exfoliated ReS$_2$ Nanosheets: Fabrication and Use as Co-Catalyst For Enhancing Photocatalytic Efficiency of TiO$_2$ Nanoparticles Under Sunlight.* Nanotechnology, 30(18):184001, 2019.

[176] Zhao-Hua Miao, Lan-Xiang Lv, Kai Li, Pei-Ying Liu, Zhenglin Li, Huanjie Yang, Qingliang Zhao, Manli Chang, Liang Zhen, and Cheng-Yan Xu. *Liquid Exfoliation of Colloidal Rhenium Disulfide Nanosheets as a Multifunctional Theranostic Agent for In Vivo Photoacoustic/CT Imaging and Photothermal Therapy.* Small, 14(14):1703789, 2018.

[177] Yenny Hernandez, Mustafa Lotya, David Rickard, Shane D Bergin, and Jonathan N Coleman. *Measurement of Multicomponent Solubility Parameters for Graphene Facilitates Solvent Discovery.* Langmuir, 26(5):3208–3213, 2010.

[178] Jose A Carrasco, Andrew Harvey, Damien Hanlon, Vicent Lloret, Dave McAteer, Roger Sanchis-Gual, Andreas Hirsch, Frank Hauke, Gonzalo Abellán, Jonathan N Coleman, et al. *Liq-*

uid Phase Exfoliation of Carbonate-Intercalated Layered Double Hydroxides. Chem. Commun., 55(23):3315–3318, 2019.

[179] Yu Song, Siqi Hu, Miao-Ling Lin, Xuetao Gan, Ping-Heng Tan, and Jianlin Zhao. *Extraordinary Second Harmonic Generation in ReS$_2$ Atomic Crystals*. ACS Photonics, 5(9):3485–3491, 2018.

[180] Ozgur Burak Aslan, Daniel A Chenet, Arend M Van Der Zande, James C Hone, and Tony F Heinz. *Linearly Polarized Excitons in Single-and Few-Layer ReS$_2$ Crystals*. ACS Photonics, 3(1):96–101, 2016.

[181] CH Ho, YS Huang, and KK Tiong. *In-Plane Anisotropy of the Optical and Electrical Properties of ReS$_2$ and ReSe$_2$ Layered Crystals*. J. Alloys Compd., 317:222–226, 2001.

[182] Alan D McNaught, Andrew Wilkinson, et al. *Compendium of Chemical Terminology*, volume 1669. Blackwell Science Oxford, 1997.

[183] Andrew Harvey, Claudia Backes, Zahra Gholamvand, Damien Hanlon, David McAteer, Hannah C Nerl, Eva McGuire, Andres Seral-Ascaso, Quentin M Ramasse, Niall McEvoy, et al. *Preparation of Gallium Sulfide Nanosheets by Liquid Exfoliation and Their Application as Hydrogen Evolution Catalysts*. Chem. Mater., 27(9):3483–3493, 2015.

[184] Andrew Harvey, Xiaoyun He, Ian J Godwin, Claudia Backes, David McAteer, Nina C Berner, Niall McEvoy, Auren Ferguson, Aleksey Shmeliov, Michael EG Lyons, et al. *Production of Ni(OH)$_2$ Nanosheets by Liquid Phase Exfoliation: from Optical Properties to Electrochemical Applications*. J. Mater. Chem. A, 4(28):11046–11059, 2016.

[185] Elisa Petroni, Emanuele Lago, Sebastiano Bellani, Danil W Boukhvalov, Antonio Politano, Bekir Gürbulak, Songül Duman, Mirko Prato, Silvia Gentiluomo, Reinier Oropesa-Nuñez, et al. *Liquid-Phase Exfoliated Indium–Selenide Flakes and Their Application in Hydrogen Evolution Reaction*. Small, 14(26):1800749, 2018.

[186] Claudia Backes, Thomas M Higgins, Adam Kelly, Conor Boland, Andrew Harvey, Damien Hanlon, and Jonathan N Coleman. *Guidelines for Exfoliation, Characterization and Process-*

ing of Layered Materials Produced by Liquid Exfoliation. Chem. Mater., 29(1):243–255, 2017.

[187] Zeger Hens and Iwan Moreels. *Light Absorption by Colloidal Semiconductor Quantum Dots.* J. Mater. Chem., 22(21):10406–10415, 2012.

[188] Damien Hanlon, Claudia Backes, Thomas M Higgins, Marguerite Hughes, Arlene O'Neill, Paul King, Niall McEvoy, Georg S Duesberg, Beatriz Mendoza Sanchez, Henrik Pettersson, et al. *Production of Molybdenum Trioxide Nanosheets by Liquid Exfoliation and Their Application in High-Performance Supercapacitors.* Chem. Mater., 26(4):1751–1763, 2014.

[189] Mustafa Lotya, Aliaksandra Rakovich, John F Donegan, and Jonathan N Coleman. *Measuring the Lateral Size of Liquid-Exfoliated Nanosheets with Dynamic Light Scattering.* Nanotechnology, 24(26):265703, 2013.

[190] JM Urban, M Baranowski, A Kuc, A Surrente, Y Ma, D Włodarczyk, A Suchocki, D Ovchinnikov, T Heine, DK Maude, et al. *Non Equilibrium Anisotropic Excitons in Atomically Thin ReS_2.* 2d Mater., 6(1):015012, 2018.

[191] Amber McCreary, Jeffrey R Simpson, Yuanxi Wang, Daniel Rhodes, Kazunori Fujisawa, Luis Balicas, Madan Dubey, Vincent H Crespi, Mauricio Terrones, and Angela R Hight Walker. *Intricate Resonant Raman Response in Anisotropic ReS_2.* Nano Lett., 17(10):5897–5907, 2017.

[192] MA Vuurman, DJ Stufkens, A Oskam, and IE Wachs. *Structural Determination of Surface Rhenium Oxide On Various Oxide Supports (Al_2O_3, ZrO_2, TiO_2 and SiO_2).* J. Mol. Catal., 76(1-3):263–285, 1992.

[193] Biswanath Chakraborty, Achintya Bera, DVS Muthu, Somnath Bhowmick, Umesh V Waghmare, and AK Sood. *Symmetry-dependent Phonon Renormalization in Monolayer MoS_2 Transistor.* Phys. Rev. B, 85(16):161403, 2012.

[194] Jing-Kai Qin, Wen-Zhu Shao, Cheng-Yan Xu, Yang Li, Dan-Dan Ren, Xiao-Guo Song, and Liang Zhen. *Chemical Vapor Deposition Growth of Degenerate P-type Mo-Doped ReS_2 Films and Their Homojunction.* ACS Appl. Mater. Interfaces, 9(18):15583–15591, 2017.

[195] Na Zhang, Jingjing Lin, Shuqing Zhang, Shishu Zhang, Xiaobo Li, Dongyan Liu, Hua Xu, Jin Zhang, and Lianming Tong. *Doping Modulated In-Plane Anisotropic Raman Enhancement on Layered ReS$_2$*. Nano Research, 12(3):563–568, 2019.

[196] Juan Antonio Aliaga, Juan Francisco Araya, Harold Lozano, Eglantina Benavente, Gabriel Alonso-Nunez, and Guillermo González. *An Easy One-Pot Solvothermal Synthesis of Poorly Crystalline Solid ReS$_2$/C Microspheres*. Mater. Chem. Phys., 151:372–377, 2015.

[197] Sida Shen, Yu Chao, Ziliang Dong, Guanglin Wang, Xuan Yi, Guosheng Song, Kai Yang, Zhuang Liu, and Liang Cheng. *Bottom-Up Preparation of Uniform Ultrathin Rhenium Disulfide Nanosheets for Image-Guided Photothermal Radiotherapy*. Adv. Funct. Mater., 27(28):1700250, 2017.

[198] Jean-Charles Dupin, Danielle Gonbeau, Philippe Vinatier, and Alain Levasseur. *Systematic XPS Studies of Metal Oxides, Hydroxides and Peroxides*. Phys. Chem. Chem. Phys., 2(6):1319–1324, 2000.

[199] Victor Vega-Mayoral, Ruiyuan Tian, Adam G Kelly, Aideen Griffin, Andrew Harvey, Mino Borrelli, Katharina Nisi, Claudia Backes, and Jonathan N Coleman. *Solvent Exfoliation Stabilizes TiS$_2$ Nanosheets Against Oxidation, Facilitating Lithium Storage Applications*. Nanoscale, 11(13):6206–6216, 2019.

[200] Sheneve Z Butler, Shawna M Hollen, Linyou Cao, Yi Cui, Jay A Gupta, Humberto R Gutiérrez, Tony F Heinz, Seung Sae Hong, Jiaxing Huang, Ariel F Ismach, et al. *Progress, Challenges, and Opportunities in Two-Dimensional Materials Beyond Graphene*. ACS Nano, 7(4):2898–2926, 2013.

[201] Deep Jariwala, Vinod K Sangwan, Lincoln J Lauhon, Tobin J Marks, and Mark C Hersam. *Emerging Device Applications for Semiconducting Two-Dimensional Transition Metal Dichalcogenides*. ACS Nano, 8(2):1102–1120, 2014.

[202] Andrea C Ferrari, Francesco Bonaccorso, Vladimir Fal'Ko, Konstantin S Novoselov, Stephan Roche, Peter Bøggild, Stefano Borini, Frank HL Koppens, Vincenzo Palermo, Nicola Pugno, et al. *Science and Technology Roadmap for Graphene, Related*

Two-dimensional Crystals, and Hybrid Systems. Nanoscale, 7(11):4598–4810, 2015.

[203] Jonathan Owen. *The Coordination Chemistry of Nanocrystal Surfaces.* Science, 347(6222):615–616, 2015.

[204] Pengshang Zhou, Ivo Tanghe, Pieter Schiettecatte, Dries Van Thourhout, Zeger Hens, and Pieter Geiregat. *Ultrafast Carrier Dynamics in Colloidal WS_2 Nanosheets Obtained Through a Hot Injection Synthesis.* J. Chem. Phys., 151(16):164701, 2019.

[205] Zeger Hens and José C Martins. *A Solution NMR Toolbox for Characterizing the Surface Chemistry of Colloidal Nanocrystals.* Chem. Mater., 25(8):1211–1221, 2013.

[206] Diana Y Qiu, H Felipe, and Steven G Louie. *Optical Spectrum of MoS_2: Many-Body Effects and Diversity of Exciton States.* Phys. Rev. Lett., 111(21):216805, 2013.

[207] Zoran Rukelj, Antonio Štrkalj, and Vito Despoja. *Optical Absorption and Transmission in a Molybdenum Disulfide Monolayer.* Phys. Rev. B, 94(11):115428, 2016.

[208] Andrea C Ferrari, JC Meyer, Vittorio Scardaci, Cinzia Casiraghi, Michele Lazzeri, Francesco Mauri, Stefano Piscanec, Da Jiang, KS Novoselov, S Roth, et al. *Raman Spectrum of Graphene and Graphene Layers.* Phys. Rev. Lett., 97(18):187401, 2006.

[209] Patrick R Whelan, Bjarke S Jessen, Ruizhi Wang, Birong Luo, Adam C Stoot, David MA Mackenzie, Philipp Braeuninger-Weimer, Alex Jouvray, Lutz Prager, Luca Camilli, et al. *Raman Spectral Indicators of Catalyst Decoupling for Transfer of CVD Grown 2D Materials.* Carbon, 117:75–81, 2017.

[210] William Henry Bragg and William Lawrence Bragg. *The Reflection of X-rays by Crystals.* Proceedings of the Royal Society of London. Series A, Containing Papers of a Mathematical and Physical Character, 88(605):428–438, 1913.

[211] Tao Liang, Simon R Phillpot, and Susan B Sinnott. *Parametrization of a Reactive Many-body Potential for Mo–S Systems.* Phys. Rev. B, 79(24):245110, 2009.

[212] RR Chianelli, EB Prestridge, TA Pecoraro, and JP DeNeufville. *Molybdenum Disulfide in the Poorly Crystalline" Rag" Structure.* Science, 203(4385):1105–1107, 1979.

[213] P Joensen, ED Crozier, N Alberding, and RF Frindt. *A Study of Single-layer and Restacked MoS_2 by X-ray Diffraction and X-ray Absorption Spectroscopy.* Journal of Physics C: Solid State Physics, 20(26):4043, 1987.

[214] Louis De Broglie. *Waves and quanta.* Nature, 112(2815):540–540, 1923.

[215] Ernst Ruska. *The Development of the Electron Microscope and of Electron Microscopy.* Rev. Mod. Phys., 59(3):627, 1987.

[216] Kai Leng, Zhongxin Chen, Xiaoxu Zhao, Wei Tang, Bingbing Tian, Chang Tai Nai, Wu Zhou, and Kian Ping Loh. *Phase restructuring in transition metal dichalcogenides for highly stable energy storage.* ACS Nano, 10(10):9208–9215, 2016.

[217] Gerd Binnig, Calvin F Quate, and Ch Gerber. *Atomic Force Microscope.* Phys. Rev. Lett., 56(9):930, 1986.

[218] Brunero Cappella and Giovanni Dietler. *Force-distance Curves by Atomic Force Microscopy.* Surf. Sci. Rep., 34(1-3):1–104, 1999.

[219] Michael J Hostetler, Julia E Wingate, Chuan-Jian Zhong, Jay E Harris, Richard W Vachet, Michael R Clark, J David Londono, Stephen J Green, Jennifer J Stokes, George D Wignall, et al. *Alkanethiolate Gold Cluster Molecules with Core Diameters from 1.5 to 5.2 nm: Core and Monolayer Properties as a Function of Core Size.* Langmuir, 14(1):17–30, 1998.

[220] Iwan Moreels, Bernd Fritzinger, José C Martins, and Zeger Hens. *Surface Chemistry of Colloidal PbSe Nanocrystals.* J. Am. Chem. Soc., 130(45):15081–15086, 2008.

[221] Bernd Fritzinger, Richard K Capek, Karel Lambert, José C Martins, and Zeger Hens. *Utilizing Self-Exchange to Address the Binding of Carboxylic Acid Ligands to CdSe Quantum Dots.* J. Am. Chem. Soc., 132(29):10195–10201, 2010.

[222] Roberto Grisorio, Danila Quarta, Angela Fiore, Luigi Carbone, Gian Paolo Suranna, and Carlo Giansante. *The Dynamic Sur-*

face Chemistry of Colloidal Metal Chalcogenide Quantum Dots. Nanoscale Advances, 1(9):3639–3646, 2019.

[223] Emile Drijvers, Jonathan De Roo, Jose C Martins, Ivan Infante, and Zeger Hens. *Ligand Displacement Exposes Binding Site Heterogeneity on CdSe Nanocrystal Surfaces.* Chem. Mater., 2018.

[224] Zeger Hens, Iwan Moreels, and Jose C Martins. *In Situ 1H NMR Study on the Trioctylphosphine Oxide Capping of Colloidal InP Nanocrystals.* ChemPhysChem, 6(12):2578–2584, 2005.

[225] Jonathan S Owen, Jungwon Park, Paul-Emile Trudeau, and A Paul Alivisatos. *Reaction Chemistry and Ligand Exchange at Cadmium- Selenide Nanocrystal Surfaces.* J. Am. Chem. Soc., 130(37):12279–12281, 2008.

[226] Shalini Singh, Renu Tomar, Stephanie Ten Brinck, Jonathan De Roo, Pieter Geiregat, Jose C Martins, Ivan Infante, and Zeger Hens. *Colloidal CdSe nanoplatelets, a Model for Surface Chemistry/Optoelectronic Property Relations in Semiconductor Nanocrystals.* J. Am. Chem. Soc., 140(41):13292–13300, 2018.

[227] Iwan Moreels, Yolanda Justo, Bram De Geyter, Katrien Haustraete, José C Martins, and Zeger Hens. *Size-tunable, Bright, and Stable PbS Quantum Dots: a Surface Chemistry Study.* ACS Nano, 5(3):2004–2012, 2011.

[228] Antti Hassinen, Iwan Moreels, Celso de Mello Donegá, José C Martins, and Zeger Hens. *Nuclear Magnetic Resonance Spectroscopy Demonstrating Dynamic Stabilization of CdSe Quantum Dots by Alkylamines.* J. Phys. Chem. Lett., 1(17):2577–2581, 2010.

[229] François Ribot, Virginie Escax, Claire Roiland, Clément Sanchez, José C Martins, Monique Biesemans, Ingrid Verbruggen, and Rudolph Willem. *In Situ Evaluation of Interfacial Affinity in CeO_2 Based Hybrid Nanoparticles by Pulsed Field Gradient NMR.* Chem. Comm., (8):1019–1021, 2005.

[230] Raquel Gomes, Antti Hassinen, Agnieszka Szczygiel, Qiang Zhao, André Vantomme, José C Martins, and Zeger Hens. *Binding of Phosphonic Acids to CdSe Quantum dots: a Solution NMR Study.* J. Phys. Chem. Lett., 2(3):145–152, 2011.

[231] Valeriia Grigel, Laxmi Kishore Sagar, Kim De Nolf, Qiang Zhao, André Vantomme, Jonathan De Roo, Ivan Infante, and Zeger Hens. *The Surface Chemistry of Colloidal HgSe Nanocrystals, toward Stoichiometric Quantum Dots by Design.* Chem. Mater., 30(21):7637–7647, 2018.

[232] Jonathan De Roo, Maria Ibáñez, Pieter Geiregat, Georgian Nedelcu, Willem Walravens, Jorick Maes, Jose C Martins, Isabel Van Driessche, Maksym V Kovalenko, and Zeger Hens. *Highly Dynamic Ligand Binding and Light Absorption Coefficient of Cesium Lead Bromide Perovskite Nanocrystals.* ACS Nano, 10(2):2071–2081, 2016.

[233] Bernd Fritzinger, Iwan Moreels, Petra Lommens, Rolf Koole, Zeger Hens, and José C Martins. *In Situ Observation of Rapid Ligand Exchange in Colloidal Nanocrystal Suspensions using Transfer NOE Nuclear Magnetic Resonance Spectroscopy.* J. Am. Chem. Soc., 131(8):3024–3032, 2009.

[234] Ralph G Pearson. *Absolute Electronegativity and Hardness: Application to Inorganic Chemistry.* Inorganic Chemistry, 27(4):734–740, 1988.

[235] Jari Leemans, Shalini Singh, Chen Li, Stephanie Ten Brinck, Sara Bals, Ivan Infante, Iwan Moreels, and Zeger Hens. *Near-Edge Ligand Stripping and Robust Radiative Exciton Recombination in CdSe/CdS Core/Crown Nanoplatelets.* J. Phys. Chem. Lett., 11(9):3339–3344, 2020.

[236] Angang Dong, Xingchen Ye, Jun Chen, Yijin Kang, Thomas Gordon, James M Kikkawa, and Christopher B Murray. *A Generalized Ligand-exchange Strategy Enabling Sequential Surface Functionalization of Colloidal Nanocrystals.* J. Am. Chem. Soc., 133(4):998–1006, 2011.

[237] Charles M Hansen. *Hansen Solubility Parameters: a User's Handbook.* CRC press, 2002.

[238] Antonio Esau Del Rio Castillo, Vittorio Pellegrini, Haiyan Sun, Joka Buha, Duc Anh Dinh, Emanuele Lago, Alberto Ansaldo, Andrea Capasso, Liberato Manna, and Francesco Bonaccorso. *Exfoliation of Few-layer Black Phosphorus in Low-boiling-point Solvents and its Application in Li-ion Batteries.* Chem. Mater, 30(2):506–516, 2018.

[239] John B Boland, Ruiyuan Tian, Andrew Harvey, Victor Vega-Mayoral, Aideen Griffin, Dominik V Horvath, Cian Gabbett, Madeleine Breshears, Joshua Pepper, Yanguang Li, et al. *Liquid Phase Exfoliation of GeS Nanosheets in Ambient Conditions for Lithium Ion Battery Applications*. 2d Mater., 7(3):035015, 2020.

[240] John B Boland, Andrew Harvey, Ruiyuan Tian, Damien Hanlon, Victor Vega-Mayoral, Beata Szydlowska, Aideen Griffin, Tanja Stimpel-Lindner, Sonia Jaskaniec, Valeria Nicolosi, et al. *Liquid Phase Exfoliation of MoO_2 Nanosheets for Lithium Ion Battery Applications*. Nanoscale Advances, 1(4):1560–1570, 2019.

[241] João Coelho, Beatriz Mendoza-Sánchez, Henrik Pettersson, Anuj Pokle, Eva K McGuire, Edmund Long, Lorcan McKeon, Alan P Bell, and Valeria Nicolosi. *Manganese Oxide Nanosheets and a 2D Hybrid of Graphene–Manganese Oxide Nanosheets Synthesized by Liquid-Phase Exfoliation*. 2d Mater., 2(2):025005, 2015.

[242] Chuanfang John Zhang, Sang-Hoon Park, Sean E O'Brien, Andrés Seral-Ascaso, Meiying Liang, Damien Hanlon, Dileep Krishnan, Alison Crossley, Niall McEvoy, Jonathan N Coleman, et al. *Liquid Exfoliation of Interlayer Spacing-Tunable 2D Vanadium Oxide Nanosheets: High Capacity and Rate Handling Li-ion Battery Cathodes*. Nano Energy, 39:151–161, 2017.

[243] Kathleen Maleski, Vadym N Mochalin, and Yury Gogotsi. *Dispersions of Two-Dimensional Titanium Carbide MXene in Organic Solvents*. Chem. Mater., 29(4):1632–1640, 2017.

[244] Dimitrios Konios, Minas M Stylianakis, Emmanuel Stratakis, and Emmanuel Kymakis. *Dispersion Behaviour of Graphene Oxide and Reduced Graphene Oxide*. J. Colloid Interface Sci., 430:108–112, 2014.

[245] Damien Hanlon, Claudia Backes, Evie Doherty, Clotilde S Cucinotta, Nina C Berner, Conor Boland, Kangho Lee, Andrew Harvey, Peter Lynch, Zahra Gholamvand, et al. *Liquid Exfoliation of Solvent-Stabilized Few-layer Black Phosphorus for Applications Beyond Electronics*. Nat. Commun., 6(1):1–11, 2015.

[246] Christopher E Hamilton, Jay R Lomeda, Zhengzong Sun, James M Tour, and Andrew R Barron. *High-yield Organic Dis-*

persions of Unfunctionalized Graphene. Nano Lett, 9(10):3460–3462, 2009.

[247] Eadweard Muybridge. *The Science of the Horse's Motions.* Sci Am, 39:241, 1878.

[248] H Abraham and J Lemoine. *Disparition Instantanée du Phénomène de Kerr.* Compt. Rend.(Paris), 129:206–208, 1899.

[249] George-Na3240 Porter. *Flash Photolysis and Spectroscopy. A New Method for the Study of Free Radical Reactions.* Proceedings of the Royal Society of London. Series A. Mathematical and Physical Sciences, 200(1061):284–300, 1950.

[250] Theodore H Maiman. *Stimulated Optical Radiation in Ruby.* Nature, 187(4736):493–494, 1960.

[251] AJ DeMaria, DA Stetser, and H Heynau. *Self Mode-locking of Lasers with Saturable Absorbers.* Appl. Phys. Lett., 8(7):174–176, 1966.

[252] CV Shank and EP Ippen. *Subpicosecond Kilowatt Pulses from a Mode-Locked Cw Dye Laser.* Appl. Phys. Lett., 24(8):373–375, 1974.

[253] Richard L Fork, CH Brito Cruz, PC Becker, and Charles V Shank. *Compression of Optical Pulses to Six Femtoseconds by using Cubic Phase Compensation.* Opt. Lett., 12(7):483–485, 1987.

[254] David E Spence, P Np Kean, and Wilson Sibbett. *60-fsec Pulse Generation from a Self-mode-locked Ti:sapphire Laser.* Opt. Lett., 16(1):42–44, 1991.

[255] RR Alfano and SL Shapiro. *Emission in the Region 4000 to 7000 Å via Four-Photon Coupling in Glass.* Phys. Rev. Lett., 24(11):584, 1970.

[256] A Brodeur and SL Chin. *Band-Gap Dependence of the Ultrafast White-Light Continuum.* Phys. Rev. Lett., 80(20):4406, 1998.

[257] Bram De Geyter, Arjan J Houtepen, Sergio Carrillo, Pieter Geiregat, Yunan Gao, Sybren ten Cate, Juleon M Schins, Dries Van Thourhout, Christophe Delerue, Laurens DA Siebbeles, et al. *Broadband and Picosecond Intraband Absorption in Lead-*

based Colloidal Quantum Dots. ACS Nano, 6(7):6067–6074, 2012.

[258] Galan Moody, Chandriker Kavir Dass, Kai Hao, Chang-Hsiao Chen, Lain-Jong Li, Akshay Singh, Kha Tran, Genevieve Clark, Xiaodong Xu, Gunnar Berghäuser, et al. *Intrinsic Homogeneous Linewidth and Broadening Mechanisms of Excitons in Monolayer Transition Metal Dichalcogenides.* Nat. Commun., 6(1):1–6, 2015.

[259] DR Wake, HW Yoon, JP Wolfe, and H Morkoc. *Response of Excitonic Absorption Spectra to Photoexcited Carriers in GaAs Quantum Wells.* Phys. Rev. B, 46(20):13452, 1992.

[260] Sangwan Sim, Jusang Park, Jeong-Gyu Song, Chihun In, Yun-Shik Lee, Hyungjun Kim, and Hyunyong Choi. *Exciton Dynamics in Atomically Thin MoS_2: Interexcitonic Interaction and Broadening Kinetics.* Phys. Rev. B, 88(7):075434, 2013.

[261] Eva A A Pogna, Margherita Marsili, Domenico De Fazio, Stefano Dal Conte, Cristian Manzoni, Davide Sangalli, Duhee Yoon, Antonio Lombardo, Andrea C Ferrari, Andrea Marini, et al. *Photo-Induced Bandgap Renormalization Governs the Ultrafast Response of Single-Layer MoS_2.* ACS Nano, 10(1):1182–1188, 2016.

[262] Paul D Cunningham, Kathleen M McCreary, Aubrey T Hanbicki, Marc Currie, Berend T Jonker, and L Michael Hayden. *Charge Trapping and Exciton Dynamics in Large-Area CVD Grown MoS_2.* J. Phys. Chem. C., 120(10):5819–5826, 2016.

[263] Georgia Kime, Marina A Leontiadou, Jack R Brent, Nicky Savjani, Paul O'Brien, and David Binks. *Ultrafast Charge Dynamics in Dispersions of Monolayer MoS_2 Nanosheets.* J. Phys. Chem. C, 121(40):22415–22421, 2017.

[264] Victor Vega-Mayoral, Tetiana Borzda, Daniele Vella, Matej Prijatelj, Eva A A Pogna, Claudia Backes, Jonathan N Coleman, Giulio Cerullo, Dragan Mihailovic, and Christoph Gadermaier. *Charge Trapping and Coalescence Dynamics in Few Layer MoS_2.* 2d Mater., 5(1):015011, 2017.

[265] Haining Wang, Changjian Zhang, and Farhan Rana. *Ultrafast Dynamics of Defect-Assisted Electron–Hole Recombination in Monolayer MoS_2.* Nano Lett., 15(1):339–345, 2014.

[266] Hongyan Shi, Rusen Yan, Simone Bertolazzi, Jacopo Brivio, Bo Gao, Andras Kis, Debdeep Jena, Huili Grace Xing, and Libai Huang. *Exciton Dynamics in Suspended Monolayer and Few-layer MoS$_2$ 2D Crystals.* ACS Nano, 7(2):1072–1080, 2013.

[267] Xiaoping Hong, Jonghwan Kim, Su-Fei Shi, Yu Zhang, Chenhao Jin, Yinghui Sun, Sefaattin Tongay, Junqiao Wu, Yanfeng Zhang, and Feng Wang. *Ultrafast Charge Transfer in Atomically Thin MoS$_2$/WS$_2$ Heterostructures.* Nat. Nanotechnol., 9(9):682, 2014.

[268] Dominik Lembke, Simone Bertolazzi, and Andras Kis. *Single-Layer MoS$_2$ Electronics.* Acc. Chem. Res., 48(1):100–110, 2015.

[269] Mark A Lukowski, Andrew S Daniel, Fei Meng, Audrey Forticaux, Linsen Li, and Song Jin. *Enhanced Hydrogen Evolution Catalysis from Chemically Exfoliated Metallic MoS$_2$ Nanosheets.* J. Am. Chem. Soc., 135(28):10274–10277, 2013.

[270] Pieter Geiregat, Arjan Houtepen, Yolanda Justo, Ferdinand C Grozema, Dries Van Thourhout, and Zeger Hens. *Coulomb Shifts upon Exciton Addition to Photoexcited PbS Colloidal Quantum Dots.* J. Phys. Chem. C, 118(38):22284–22290, 2014.

[271] Edbert J Sie, Alexander Steinhoff, Christopher Gies, Chun Hung Lui, Qiong Ma, Malte Rosner, Gunnar Schonhoff, Frank Jahnke, Tim O Wehling, Y-H Lee, et al. *Observation of Exciton Redshift–Blueshift Crossover in Monolayer WS2.* Nano Lett., 17(7):4210–4216, 2017.

[272] Ss Schmitt-Rink, DS Chemla, and DAB Miller. *Linear and Nonlinear Optical Properties of Semiconductor Quantum Wells.* Advances in Physics, 38(2):89–188, 1989.

[273] S Schmitt-Rink, C Ell, and H Haug. *Many-body Effects in the Absorption, Gain, and Luminescence Spectra of Semiconductor Quantum-well Structures.* Phys. Rev. B, 33(2):1183, 1986.

[274] S. Schmitt-Rink, D. S. Chemla, and D. A B Miller. *Theory of Transient Excitonic Optical Nonlinearities in Semiconductor Quantum-Well Structures.* Phys. Rev. B, 32(10):6601–6609, 1985.

[275] Dezheng Sun, Yi Rao, Georg A Reider, Gugang Chen, Yumeng You, Louis Brezin, Avetik R Harutyunyan, and Tony F Heinz.

Observation of Rapid Exciton–Exciton Annihilation in Mono-layer Molybdenum Disulfide. Nano Lett., 14(10):5625–5629, 2014.

[276] Callum J Docherty, Patrick Parkinson, Hannah J Joyce, Ming-Hui Chiu, Chang-Hsiao Chen, Ming-Yang Lee, Lain-Jong Li, Laura M Herz, and Michael B Johnston. *Ultrafast Transient Terahertz Conductivity of Monolayer MoS_2 and WSe_2 Grown by Chemical Vapor Deposition.* ACS Nano, 8(11):11147–11153, 2014.

[277] Zhong Lin, Bruno R Carvalho, Ethan Kahn, Ruitao Lv, Rahul Rao, Humberto Terrones, Marcos A Pimenta, and Mauricio Terrones. *Defect Engineering of Two-Dimensional Transition Metal Dichalcogenides.* 2d Mater., 3(2):022002, 2016.

[278] KC Santosh, Roberto C Longo, Rafik Addou, Robert M Wallace, and Kyeongjae Cho. *Impact of Intrinsic Atomic Defects on the Electronic Structure of MoS_2 Monolayers.* Nanotechnology, 25(37):375703, 2014.

[279] Wu Zhou, Xiaolong Zou, Sina Najmaei, Zheng Liu, Yumeng Shi, Jing Kong, Jun Lou, Pulickel M Ajayan, Boris I Yakobson, and Juan-Carlos Idrobo. *Intrinsic Structural Defects in Monolayer Molybdenum Disulfide.* Nano Lett., 13(6):2615–2622, 2013.

[280] Péter Vancsó, Gábor Zsolt Magda, János Pető, Ji-Young Noh, Yong-Sung Kim, Chanyong Hwang, László P Biró, and Levente Tapasztó. *The Intrinsic Defect Structure of Exfoliated MoS_2 Single Layers Revealed by Scanning Tunneling Microscopy.* Sci. Rep., 6(1):1–7, 2016.

[281] Ronald Ulbricht, Euan Hendry, Jie Shan, Tony F. Heinz, and Mischa Bonn. *Carrier Dynamics in Semiconductors Studied with Time-Resolved Terahertz Spectroscopy.* Rev. Mod. Phys., 83:543–586, Jun 2011.

[282] James Lloyd-Hughes and Tae-In Jeon. *A Review of the Ter-ahertz Conductivity of Bulk and Nano-Materials.* J. Infrared Millim. Terahertz Waves, 33(9):871–925, 2012.

[283] Jannika Lauth, Aditya Kulkarni, Frank CM Spoor, Nicolas Renaud, Ferdinand C Grozema, Arjan J Houtepen, Juleon M Schins, Sachin Kinge, and Laurens DA Siebbeles. *Photogeneration and Mobility of Charge Carriers in Atomically Thin*

Colloidal InSe Nanosheets Probed by Ultrafast Terahertz Spectroscopy. J. Phys. Chem. Lett., 7(20):4191–4196, 2016.

[284] Peter W Atkins and Ronald S Friedman. *Molecular Quantum Mechanics.* Oxford university press, 2011.

[285] J Jadczak, J Kutrowska-Girzycka, T Smoleński, P Kossacki, YS Huang, and L Bryja. *Exciton Binding Energy and Hydrogenic Rydberg Series in Layered ReS$_2$.* Sci. Rep., 9(1):1–9, 2019.

[286] William Russell Hindmarsh, AD Petford, and Graham Smith. *Interpretation of Collision Broadening and Shift in Atomic Spectra.* Proceedings of the Royal Society of London. Series A. Mathematical and Physical Sciences, 297(1449):296–304, 1967.

[287] RCC Leite, Jagdeep Shah, and JP Gordon. *Effect of Electron-Exciton Collisions on the Free-Exciton Linewidth in Epitaxial GaAs.* Phys. Rev. Lett., 23(23):1332, 1969.

[288] L Schultheis, J Kuhl, A Honold, and CW Tu. *Ultrafast Phase Relaxation of Excitons via Exciton-Exciton and Exciton-Electron Collisions.* Phys. Rev. Lett., 57(13):1635, 1986.

[289] A Honold, L Schultheis, J Kuhl, and CW Tu. *Collision Broadening of Two-Dimensional Excitons in a GaAs Single Quantum Well.* Phys. Rev. B, 40(9):6442, 1989.

[290] D Hulin, A Mysyrowicz, A Antonetti, A Migus, WT Masselink, H Morkoc, HM Gibbs, and N Peyghambarian. *Well-size Dependence of Exciton Blue Shift in GaAs Multiple-quantum-well Structures.* Phys. Rev. B, 33(6):4389, 1986.

[291] Paul D Cunningham, Aubrey T Hanbicki, Kathleen M McCreary, and Berend T Jonker. *Photoinduced Bandgap Renormalization and Exciton Binding Energy Reduction in WS_2.* ACS Nano, 11(12):12601–12608, 2017.

[292] Claudia Ruppert, Alexey Chernikov, Heather M Hill, Albert F Rigosi, and Tony F Heinz. *The Role of Electronic and Phononic Excitation in the Optical Response of Monolayer WS_2 after Ultrafast Excitation.* Nano Lett., 17(2):644–651, 2017.

[293] Xiaoxi Wu, M Tuan Trinh, and X-Y Zhu. *Excitonic Many-body Interactions in Two-dimensional Lead Iodide Perovskite Quantum Wells.* J. Phys. Chem. C, 119(26):14714–14721, 2015.

[294] Alexander Steinhoff, M Rosner, Frank Jahnke, Tim O Wehling, and Christopher Gies. *Influence of Excited Carriers on the Optical and Electronic Properties of MoS$_2$*. Nano Lett., 14(7):3743–3748, 2014.

[295] Lutz Waldecker, Archana Raja, Malte Rösner, Christina Steinke, Aaron Bostwick, Roland J Koch, Chris Jozwiak, Takashi Taniguchi, Kenji Watanabe, Eli Rotenberg, et al. *Rigid Band Shifts in Two-Dimensional Semiconductors Through External Dielectric Screening*. Phys. Rev. Lett., 123(20):206403, 2019.

[296] TH Wood, CA Burrus, DAB Miller, DS Chemla, TC Damen, AC Gossard, and W Wiegmann. *High-speed Optical Modulation with GaAs/GaAlAs Quantum Wells in a p-i-n Diode Structure*. Appl. Pjys. Lett., 44(1):16–18, 1984.

[297] David AB Miller, DS Chemla, TC Damen, AC Gossard, W Wiegmann, TH Wood, and CA Burrus. *Electric Field Dependence of Optical Absorption Near the Band Gap of Quantum-well Structures*. Phys. Rev. B, 32(2):1043, 1985.

[298] JS Weiner, David AB Miller, Daniel S Chemla, TC Damen, CA Burrus, TH Wood, AC Gossard, and W Wiegmann. *Strong Polarization-Sensitive Electroabsorption in GaAs/AlGaAs Quantum Well Waveguides*. Appl. Phys. Lett., 47(11):1148–1150, 1985.

[299] Yu-Hsuan Kuo, Yong Kyu Lee, Yangsi Ge, Shen Ren, Jonathan E Roth, Theodore I Kamins, David AB Miller, and James S Harris. *Strong Quantum-Confined Stark Effect in Germanium Quantum-Well Structures on Silicon*. Nature, 437(7063):1334–1336, 2005.

[300] MG Shorthose and JF Ryan. *Photocurrent Measurements of Electric-field-induced Carrier Energy Shifts and Tunnelling in In1-xGaxAs/InP Quantum Wells*. Journal of Physics: Condensed Matter, 1(11):2041, 1989.

[301] RT Collins, K v Klitzing, and K Ploog. *Photocurrent Spectroscopy of GaAs/Al$_x$Ga$_{1-x}$As Quantum Wells in an Electric Field*. Phys. Rev. B, 33(6):4378, 1986.

[302] K Yamanaka, T Fukunaga, N Tsukada, KLI Kobayashi, and M Ishii. *Photocurrent Spectroscopic Observation of Interband*

Transitions in GaAs-AlGaAs Quantum Wells under an Applied High Electric Field. Surface Science, 174(1-3):250–254, 1986.

[303] Z Ikonic, V Milanovic, and Dimitrije Tjapkin. *Optical Transitions between Higher Levels in a Quantum Well in an Electric Field.* Journal of Physics C: Solid State Physics, 20(19):L425, 1987.

[304] A Shikanai, T Deguchi, T Sota, T Kuroda, A Tackeuchi, S Chichibu, and S Nakamura. *A Pump and Probe Study of Photoinduced Internal Field Screening Dynamics in an AlGaN/GaN Single-Quantum-Well Structure.* Appl. Phys. Lett., 76(4):454–456, 2000.

[305] Fei Chen, MC Cheung, Paul M Sweeney, WD Kirkey, M Furis, and AN Cartwright. *Ultrafast differential transmission spectroscopy of excitonic transitions in InGaN/GaN multiple quantum wells.* Journal of applied physics, 93(8):4933–4935, 2003.

[306] Fei Chen, WD Kirkey, M Furis, MC Cheung, and AN Cartwright. *Excitonic Field Screening and Bleaching in InGaN/GaN Multiple Quantum Wells.* Solid State Commun., 125(11-12):617–622, 2003.

[307] Kunimichi Omae, Yoichi Kawakami, Shigeo Fujita, Yukio Narukawa, and Takashi Mukai. *Effects of Internal Electrical Field on Transient Absorption in $In_xGa_{1-x}N$ Thin Layers and Quantum Wells with Different Thickness by Pump and Probe Spectroscopy.* Phys. Rev. B., 68(8):085303, 2003.

[308] Kunimichi Omae, Yoichi Kawakami, Shigeo Fujita, Motokazu Yamada, Yukio Narukawa, and Takashi Mukai. *Effects of Internal Electric Field and Carrier Density on Transient Absorption Spectra in a Thin GaN Epilayer.* Phys. Rev. B., 65(7):073308, 2002.

[309] David AB Miller, DS Chemla, TC Damen, AC Gossard, W Wiegmann, TH Wood, and CA Burrus. *Band-edge Electroabsorption in Quantum Well Structures: The Quantum-Confined Stark Effect.* Phys. Rev. Lett., 53(22):2173, 1984.

[310] Zaiyao Fei, Wenjin Zhao, Tauno A Palomaki, Bosong Sun, Moira K Miller, Zhiying Zhao, Jiaqiang Yan, Xiaodong Xu, and David H Cobden. *Ferroelectric Switching of a Two-dimensional metal.* Nature, 560(7718):336–339, 2018.

[311] AM Stoneham. *Shapes of Inhomogeneously Broadened Resonance Lines in Solids.* Rev. Mod. Phys., 41(1):82, 1969.

[312] Archana Raja, Lutz Waldecker, Jonas Zipfel, Yeongsu Cho, Samuel Brem, Jonas D Ziegler, Marvin Kulig, Takashi Taniguchi, Kenji Watanabe, Ermin Malic, et al. *Dielectric Disorder in Two-Dimensional Materials.* Nat. Nanotechnol., 14(9):832–837, 2019.

[313] Ali Jawaid, Dhriti Nepal, Kyoungweon Park, Michael Jespersen, Anthony Qualley, Peter Mirau, Lawrence F Drummy, and Richard A Vaia. *Mechanism for Liquid Phase Exfoliation of MoS_2.* Chem. Mater., 28(1):337–348, 2016.

[314] Ekaterina D Grayfer, Mariia N Kozlova, and Vladimir E Fedorov. *Colloidal 2D Nanosheets of MoS_2 and Other Transition Metal Dichalcogenides Through Liquid-phase Exfoliation.* Adv. Colloid Interface Sci, 245:40–61, 2017.

[315] Mark P Hendricks, Michael P Campos, Gregory T Cleveland, Ilan Jen-La Plante, and Jonathan S Owen. *A tunable library of substituted thiourea precursors to metal sulfide nanocrystals.* Science, 348(6240):1226–1230, 2015.

[316] Wiel H Evers, Juleon M Schins, Michiel Aerts, Aditya Kulkarni, Pierre Capiod, Maxime Berthe, Bruno Grandidier, Christophe Delerue, Herre SJ Van Der Zant, Carlo Van Overbeek, et al. *High Charge Mobility in Two-Dimensional Percolative Networks of PbSe Quantum Dots Connected by Atomic Bonds.* Nat. Commun., 6(1):1–8, 2015.

[317] Hsiang-Lin Liu, Chih-Chiang Shen, Sheng-Han Su, Chang-Lung Hsu, Ming-Yang Li, and Lain-Jong Li. *Optical Properties of Monolayer Transition Metal Dichalcogenides Probed by Spectroscopic Ellipsometry.* Appl. Phys. Lett., 105(20):201905, 2014.

[318] AR Beal and HP Hughes. *Kramers-Kronig Analysis of the Reflectivity Spectra of 2H-MoS_2, 2H-$MoSe_2$ and 2H-$MoTe_2$.* Journal of Physics C: Solid State Physics, 12(5):881, 1979.

[319] Susumu Ninomiya and Sadao Adachi. *Optical Properties of Cubic and Hexagonal CdSe.* Journal of Applied Physics, 78(7):4681–4689, 1995.

[320] Fuad I Alzakia, Wanxin Sun, Stephen J Pennycook, and Swee Ching Tan. *Introducing Normalized Centrifugation for a More Accurate Thermodynamic Analysis of Molybdenum Disulfide Dispersions: A Study on Mixed Solvents of Alcohols and Amines with Water.* ACS applied materials & interfaces, 12(2):3096–3103, 2019.

Nederlandse Samenvatting
–Summary in Dutch–

Hoofdstuk 2: Like Likes Like, Descriptoren voor Oplosbaarheid

Wetenschappelijke vooruitgang is vaak te danken aan het gebruik van eenvoudige conceptuele modellen om complexe verschijnselen te verklaren; een mentaal beeld helpt ons vaak ver vooruit. In dit inleidend hoofdstuk, bespreken we een binair roostermodel om het gedrag van mengsels te conceptualiseren, en geven we een algemeen overzicht van de oplossingstheorie voor mengsels binnen het raamwerk van een dergelijk roostermodel. Op deze manier zijn we in staat om abstracte thermodynamische concepten, zoals energie en entropie, te relateren aan *tastbare* interacties tussen moleculen onderling. Aangezien entropie betrekking heeft op het aantal manieren waarop een toestand kan worden gerealiseerd, bevorderen entropische effecten typisch het vormen van mengsels. We benadrukken in het bijzonder dat energetische veranderingen verband houden met het vormen en breken van moleculaire bindingen. Als zodanig hangt de oplosbaarheid af van een afweging tussen deze effecten - een resultaat dat duidelijk overstemt met onze chemische intuïtie.

Voor experimenteel onderzoek kunnen dergelijke energetische effecten het eenvoudigst worden uitgedrukt in termen van een verschil in de oplosbaarheidsparameters van de zuivere stoffen binnen het mengsel. Dientengevolge minimaliseert het overeenstemmen van de oplosbaarheidsparameters van individuele componenten in mengsels de energie van het mengen en maximaliseert daardoor de oplosbaarheid van een opgeloste stof in een oplosmiddel. Op deze manier biedt de oplosbaarheidsparameter een kwantitatieve beschrijving van het kwalitatieve begrip *like likes like*. De simpele notie van het *overeenstemmen van*

oplosbaarheidsparameters als centrale vereiste voor de vorming van stabiele mengsels zullen we talrijke keren gebruiken in het eerste deel van dit manuscript.

Hoofdstuk 3: Exfoliatie in de Vloeistoffase van ReS_2 door Optimalisatie van de Oplosbaarheidsparameters

Met behulp van de concepten die in hoofdstuk 2 zijn uiteengezet, hebben we de factoren onderzocht die de succesvolle *liquid-phase exfoliation* (exfoliatie in de vloeistoffase) van ReS_2 bepalen, en we hebben de belangrijkste kenmerken van de resulterende ReS_2 colloïden geanalyseerd. Door in een brede waaier aan oplosmiddelen te exfoliëren, hebben we aangetoond dat de omstandigheden voor LPE met een hoge opbrengst kunnen worden begrepen uit de thermodynamica van polymeeroplossingen, waarbij de meest optimale oplosmiddelen worden gekenmerkt door vergelijkbare Hildebrand en Hansen oplosbaarheidsparameters. Het bepalen van de oplosbaarheidsparameters van ReS_2 stelde ons in staat om ReS_2 te vergelijken met meer gevestigde geëxfolieerde 2D-materialen zoals grafeen of MoS_2. Gebruikmakend van N-methyl-2-pyrrolidon als een goed exfoliatieoplosmiddel, voerden we een gedetailleerde analyse uit van het geëxfolieerde ReS_2, waaruit bleek dat de door ons voorgestelde LPE-procedure anisotroopgestapelde en chemisch zuivere ReS_2 colloïden met een langdurige stabiliteit opleverde. Hieruit hebben we geconcludeerd dat LPE een geschikte methode is om ReS_2 colloïden te produceren.

Hoofdstuk 4: Oplosbaarheidsparameters als Descriptoren voor Stabiele Colloïdale MoS_2 Dispersies

Vertrekkend vanuit een reeks observaties, aangevuld met uitgebreide analyses, hebben we de thermodynamische benadering van oplossingen uitgebreid tot colloïdaal gesynthetiseerde TMD-systemen. Daarbij hebben we een reeks onderwerpen aangesneden, te beginnen met de synthese van MoS_2 met behulp van colloïdale chemie. Vanuit dit oogpunt hebben we eerst een gedetailleerde analyse van het geproduceerde MoS_2 uitgevoerd met behulp van een combinatie van UV-Vis-absorptiespectroscopie, Raman-spectroscopie, XRD, TEM en AFM. Door deze technieken te combineren, stelden we vast dat het gesynthetiseerd MoS_2 gemiddeld 3 monolagen bevat en de 2H-halfgeleidende fase aanneemt–de gewenste fase voor opto-elektronische toepassingen.

Uitgaande van de empirische waarneming dat de MoS_2 dispersies colloïdaal onstabiel zijn, hebben we eerst hun oppervlak bestudeerd door middel van NMR-spectroscopie. Door 1D- en 2D-NMR-technieken te combineren, hebben we vastgesteld dat liganden niet sterk gebonden zijn aan het MoS_2-oppervlak, maar een dynamisch adsorptie/desorptie-evenwicht ondergaan, waarbij ze uitwisselen tussen een vrije en een gebonden toestand. Hieruit concludeerden we dat dit gedrag waarschijnlijk de oorzaak is van hun beperkte colloïdale stabiliteit in conventionele oplosmiddelen, zoals hexaan en tolueen. Op basis van hun kristalstructuur, met uitgebreide zwavel oppervlakken, speculeerden we dat zachte metaalcomplexen de dispersies zouden kunnen stabiliseren door adhesie met behulp van donor-acceptor-interacties. Inderdaad, het toevoegen van een overmaat aan een metaalzout stabiliseerde de dispersies in conventionele oplosmiddelen. Echter, een conventionele cyclus van opeenvolgende precipitatie en herdispersie destabilseerde de colloïden. Met behulp van NMR-spectroscopie hebben we deze waarnemingen geïnterpreteerd als een manifestatie van een dynamische ligand-interactie.

Redenerend vanuit de waarneming dat de stabiliteit sterk afhankelijk is van de keuze van het oplosmiddel, hebben we de stabiliteit van colloïdale MoS_2 nanokristallen in een breed scala aan oplosmiddelen vergeleken. Vergelijkbaar aan ons werk in verband met de LPE van ReS_2 in hoofdstuk 3, tonen we aan dat dit gedrag kan worden begrepen vanuit de oplossings-thermodynamica, waarbij de oplosbaarheidsparameter van het oplosmiddel een succesvolle descriptor is om de oplosbaarheid van colloïdale MoS_2 nanokristallen te begrijpen. Het afstemmen van de oplosbaarheidsparameters stelde ons in staat colloïdaal MoS_2 te vergelijken met MoS_2 geproduceerd door LPE. De uitstekende overeenkomst tussen materialen geproduceerd met behulp van zeer verschillende methoden onderstreepte dat de stabiliteit van gesynthetiseerde TMDs te correleren is met de energie van het mengen, in plaats van een effect te zijn van elektrostatische ligandafstoting. Deze bevindingen waren een aanvulling op onze NMR-analyses, die liganden aantoonden met zeer weinig affiniteit voor het nanokristal-oppervlak. Belangrijk is dat deze bevindingen contrasteerden met andere laagdimensionale systemen die zijn gesynthetiseerd met behulp van colloïdale chemie, waarbij de sterisch/elektrostatische afstoting tussen liganden de belangrijkste drijvende kracht is die aggregatie voorkomt. Dientengevolge zijn colloïdale MoS_2 nanokristallen stabiel in oplosmiddelen met hogere oplosbaarheidsparameters dan die gewoonlijk

worden gebruikt om nanokristallen te verspreiden die zijn bereid door middel van hete injectie. Goede oplosmiddelen zijn hierbij aromatische oplosmiddelen met polaire groepen, zoals o-dichloorbenzeen, of zelfs polaire aprotische oplosmiddelen, zoals DMF. We concluderen dus dat olloïdale chemie MoS_2 nanokristallen oplevert met vergelijkbare oppervlakken als deze die geproduceerd worden door LPE. Deze bevinding biedt mogelijk het vooruitzicht om gevestigde procedures te gebruiken die zijn ontwikkeld voor LPE-nanomaterialen om bijvoorbeeld TMD-dispersies te verwerken als vloeibare inkten.

Hoofdstuk 5: Waarom is Exfoliatie in de Vloeistoffase van Van der Waals Gelaagde Vaste Stoffen Mogelijk in een Breed Spectrum aan Oplosmiddelen?

Experimentele gegevens verzameld voor een verscheidenheid aan Van der Waals-vaste stoffen, waaronder onze studies gepresenteerd in de hoofdstukken 3 en 4, gaven aan dat LPE mogelijk is in een veel breder scala aan oplosmiddelen dan de oplossingstheorie zou toestaan, op basis van de grootte van de gedispergeerde, of geëxfolieerde colloïden. Hieromtrent rijst de vraag of dergelijke experimentele resultaten verzoend kunnen worden met de oplossingstheorie, en zo ja, welke thermodynamische grootheden zouden effectief het experimentele venster van goede exfoliatie oplosmiddelen beschrijven?

Redenerend vanuit deze perspectieven hebben we eerst onze experimentele waarnemingen aangevuld met relevante literatuurgegevens. Ongeacht de kenmerken van het geëxfolieerde materiaal ontdekten we dat dit goede oplosmiddelvenster overeenkomt met een oplosbaarheidsparameterbereik van $4.5 - 6.8\,\mathrm{MPa}^{1/2}$ rond een optimale oplossingsparameter. Om de discrepanties tussen theorie en experiment beter te begrijpen, hebben we de meest algemeen toegepaste goede exfoliatieconditie opnieuw afgeleid, die voortbouwt op Flory-Huggins-theorie om de fractie van gedispergeerd of geëxfolieerd materiaal uit te drukken als een Gaussische functie van het verschil in oplosbaarheidsparameters, en de breedte van de Gauss naar het volume van een individuele verspreide colloïde. Daarbij hebben we benadrukt dat deze relatie alleen van toepassing is wanneer de vrije energie van Flory-Huggins een mengbaarheidskloof oplevert tussen het oplosmiddel en de opgeloste stof. Aangezien elk colloïde van een geëxfolieerd materiaal stabiel zou moeten zijn wanneer mengsels van een oplosmiddel en opgeloste stof stabiel zouden zijn bij

alle samenstellingen, hebben we de kritische uitwisselingsparameter $\chi_c = 0.5$ geïntroduceerd, waarboven een mengbaarheidskloof ontstaat, als een maatstaf voor het experimenteel exfoliatie venster. Interessant is dat we ontdekten dat het resulterende bereik van de oplosbaarheidsparameters nauw overeenkomt met experimenteel waargenomen goede exfoliatie-oplosmiddelvensters. We concludeerden daarom dat oplossings-thermodynamica geschikt is om goede exfoliatie oplosmiddelen te beschrijven, op voorwaarde dat het bereik van de oplosbaarheidsparameters gekoppeld is aan de kritische uitwisselingsparameter voor de (niet-)mengbaarheid van oplosmiddel/opgeloste stof.

Hoofdstuk 6: Het Proben van Ladingen & Optische Niet-Lineariteiten met Pump-Probe Spectroscopy

In het inleidende hoofdstuk van deel *II* hebben we de principes achter ultrasnelle *pump-probe* spectroscopie besproken. Door een aantal historische experimenten te belichten, hebben we benadrukt dat, om een schijnbaar continue beweging te meten, een nog snellere probe nodig is. Moderne *pump-probe* spectroscopie gedijt op dit idee en gebruikt twee gesynchroniseerde lichtpulsen om veranderingen in materiaaleigenschappen in kaart te brengen. Een optische *pump* excitatie induceert een verandering in een materiaaleigenschap, bijvoorbeeld de absorptie, en een vertraagde *probe* meet de foto-geïnduceerde verandering als een functie van energie en vertragingstijd. Op die manier kunnen we met behulp van femtoseconde lasers de halfgeleiderfysica ontwarren op anders ontoegankelijke tijdschalen. Zoals duidelijk zal worden in de hoofdstukken 7 en 8, zal een essentieel aspect de interpretatie zijn van spectrale effecten, geïnduceerd door foto-geëxciteerde dragers, die versleuteld zijn in de experimentele data. Met dit idee in gedachten hebben we een reeks spectrale effecten bekeken en besproken hoe ze tot uiting komen in een transiënte absorptiemeting.

Hoofdstuk 7: Ultrasnelle Carrier-Dynamica in Colloïdaal Molybdeendisulfide met Weinig Lagen

Gebruikmakend van de gevestigde colloïdale synthese beschreven in hoofdstuk 4, presenteerden we een gedetailleerde studie van de relaxatie van ladingsdragers in foto-geëxciteerde colloïdale MoS_2 nanosheets met behulp van femtoseconde transiënte absorptiespectroscopie op zichtbare en nabij-infrarode golflengten. We hebben aangetoond

dat de tijdelijke absorptie na foto-excitatie wordt veroorzaakt door
zowel een vermindering van de oscillatorsterkte van de overgangen
die de directe opening vormen, als een verschuiving van het volledige
absorptiespectrum naar lagere energie. We hebben deze kenmerken
toegeschreven aan respectievelijk het opvullen van de toestand en de
renormalisatie van de bandgap. Door spectrale deconvolutie zien we
dat in het bijzonder de A exciton bleach een sub-picoseconde ver-
val vertoont, wat we toeschrijven aan het snel invangen van gaten in
defecte midgap toestanden. Het verdwijnen van spectrale verschui-
vingen bij langere vertragingstijden weerspiegelt de relaxatie van de
ladingsdragerdistributie door verdere ladingsopvang- en recombina-
tiegebeurtenissen. Een vergelijking tussen de dynamica van fotogege-
nereerde ladingsdragers in het geval van colloïdale MoS_2 nanosheets
zoals hier gemeten en bestaande literatuur over CVD-gegroeide MoS_2
nanosheets wijst op een zeer vergelijkbare reeks van snelle trapping
van één type drager, gevolgd door capture van de resterende drager op
een langere tijdschaal. Dienovereenkomstig concluderen we dat collo-
ïdale synthese MoS_2 nanobladen van vergelijkbare kwaliteit oplevert,
zelfs als er een geheel andere chemie betrokken is bij de productie van
de TMD. Dit toont aan dat TMD's die met beide benaderingen zijn
gefabriceerd, baat kunnen hebben bij vergelijkbare strategieën voor
defectpassivering. om de levensduur van fotogenererende excitonen
te verlengen.

Hoofdstuk 8: Generatie van Vrije Ladingsdragers en Op-
tische Niet-lineariteiten in Rhenium Disulfide

Voortgaande op de concepten beschreven in hoofdstuk 7, bestudeer-
den we het verval van ladingsdragers in foto-geëxciteerde ReS_2 met
behulp van een combinatie van breedband femtoseconde transiënte ab-
sorptiespectroscopie en femtoseconde THz-spectroscopie. Met THz-
spectroscopie hebben we aangetoond dat optische excitaties vrije la-
dingsdragers genereren in ReS_2. In het bijzonder hebben we een ei-
genaardig samenspel waargenomen tussen verschillende optische niet-
lineariteiten in het TA-spectrum – lijnbreedteveranderingen en spec-
trale verschuivingen – en de evolutie van de foto-opgewekte populatie
van vrije ladingsdragers. Vanuit een conceptueel perspectief bespra-
ken we de consistentie van onze dataset met verschillende mechanis-
men die zouden kunnen leiden tot zo'n rijke fysica. Ten eerste ver-
breedde de aanwezigheid van vrije ladingen aanvankelijk de excitonre-
sonantie als gevolg van collisional broadening, en verschoof de absorp-

tie blauw vanwege screening van vrije ladingsdragers. In een tweede
fase verviel de populatie van vrije dragers, en dit verval viel samen met
een overgang van een blauwe naar een rode verschuiving geassocieerd
met roosterverwarming of bandgap-renormalisatie, en een verminde-
ring van de inhomogene lijnbreedte van het exciton. Behalve dat
deze studie inzicht verschaft in een reeks optische niet-lineariteiten,
is het genereren van mobiele ladingen in dergelijke ultradunne mate-
rialen vanuit praktisch oogpunt even interessant, aangezien mobiele
ladingsdragers zeer gewenst zijn voor fotovoltaïsche apparaten of fo-
todetectoren.